Mathematical Modelling and Investigation of Explosive Pinch, Friction and Shear Problems

Robert William Timms

A thesis submitted to the School of Mathematics at the University of East Anglia in partial fulfilment of the requirements for the degree of Doctor of Philosophy

School of Mathematics
University of East Anglia
August 2018

Abstract

The mechanisms which lead to the accidental ignition of explosive materials in response to low energy stimuli are still not well understood. It is widely agreed that localised regions of increased temperature, so-called 'hot spots', are responsible. Many mechanisms for hot spot generation have been suggested as a result of experimental studies, but the understanding of such processes remains incomplete. In this thesis, we use asymptotic and numerical techniques to investigate hot spot mechanisms, with a particular focus on those arising from impacts which pinch and shear explosives.

First, a model which accounts for the effect of friction as an explosive material is pinched between two flat plates is developed. An analytical solution is found by exploiting the small aspect ratio of the explosive sample. Numerical solution of the thermal part of the problem demonstrates that our model is able to predict important features observed in experiments, such as additional heating near to the plates.

We then go on to study how the presence of a chemical reaction affects the development of shear bands as explosive materials are deformed. Through a boundary layer analysis, we are able to extract key non-dimensional parameters which control the development of shear bands in explosives, and discuss how this may inform the design of materials that are less susceptible to accidental ignitions due to mechanical insults.

Finally, we investigate how molten layers of explosive, which can form between sliding surfaces during shear deformation, may act as a site for hot spot generation. In particular, we consider how the inhomogeneous nature of explosive materials affects the propagation of the melt front. Through a lubrication-type analysis, we demonstrate that the melt front is unstable to perturbations in the presence of a chemical reaction, and that material non-uniformities lead to localised heating within the molten layer.

Acknowledgements

First and foremost I would like to thank my supervisors Dr Richard Purvis and Dr John Curtis for their guidance, support and enthusiasm throughout this project; it has been invaluable in helping me to develop as a researcher. Richard, your continued passion for industrial and applied mathematics has instilled in me a desire to continue to apply mathematics in whatever I may go on to do in the future. John, thank you for all of the insight you have given me into the role of mathematics in industry, and for your honest advice throughout my studies. I am grateful for all of the exciting opportunities I have been afforded during my studies, and must also acknowledge colleagues at AWE, and John's collaborators elsewhere, for their useful comments. Thanks are also due to Professor Alexander Korobkin, without whom I probably would have never started this PhD.

I would like to thank all of those at the University of East Anglia who made my time studying here so enjoyable. Ruari, Mike, Keith, Robin, Peter, Julia, Jodie, Natasha, Jack, Alberto, Andy, George, Martin and everyone else in the office, thank you all for your support, shared frustrations and regular distractions. Thank you Mat, for the many years of friendship and often ill-timed discussions about science (at which point I should probably thank all those who have endured listening to me talk about my PhD!). I will be forever grateful to my parents and sister, Jennifer, for their love and encouragement which has helped me to get where I am today.

Finally, I must thank Abigail, my wife. For the past 8 years you have been an endless source of love, encouragement and laughter. A lot has changed in both of our lives since we first got together, but you have remained a constant inspiration for all that I do. Thank you.

Life is good. She is wonderful.

This work was funded by an Engineering and Physical Sciences Research Council industrial CASE partnership with AWE, both of whose support is gratefully acknowledged.

Contents

List of Figures

Chapter 1

Introduction

1.1 Motivation

The safe processing, handling and storage of high explosive materials requires a strong understanding of their behaviour in response to accidental mechanical or thermal loads. Unfortunately, while much is known about the behaviour of explosive materials during high speed deformation, the mechanisms responsible for the accidental ignition of such materials in response to low energy stimuli, referred to as 'insults' in the literature, are still not well understood. Two of the most likely insults are impacts, for instance drops or falls during transport, and thermal insults such as fires [5]. The consequences of ignition in response to an insult can be disastrous and carry a great cost, including tragic loss of life. Recently there has been an increase in the amount of work modelling accidental ignitions, with the primary goal of improving safety [33–35, 82–84]. However, the understanding of the mechanisms responsible for ignition, and of how the reaction grows, remains incomplete.

An idealised example of a mechanical stimulus is the impact of a cylindrical spigot upon a bare explosive. A number of experiments conducted at AWE aim to investigate such impacts, and it is found that the explosive may be subjected to localised pinch and/or shearing, depending on the geometry [5, 35, 59]. Modelling such impacts numerically using Lagrangian hydrocodes is typically only useful until the mesh becomes severely deformed, at which point there is either only a thin layer of explosive remaining or the deformation has localised into thin shear bands. The mesh does not deform when using Eulerian hydrocodes, but accurately tracking boundaries becomes more difficult. Typically, a very high spatial resolution is required to overcome these difficulties, but this comes at the cost of computational resources and time. Not only do many hydrocode models suffer from problems related to the mesh, it is sometimes the case that they fail to predict faithfully what is observed in experiments. The aim of this thesis is to develop analytical models of mechanical loads that are typical of accidental impacts. These models will add to the understanding of explosive response, with the hope of gaining a deeper understanding of the physical mechanisms which

lead to ignition. Such an understanding is a necessary prerequisite to the development of new hydrocode models that are capable of accurately capturing the behaviour of explosives undergoing severe deformation as a result of an insult.

It is in general believed that explosive ignition in response to insults is of thermal origin, with mechanical energy being converted into heat energy in localised regions, forming so-called 'hot spots' [48]. Many hot spot mechanisms have been proposed in the literature, but it is found that the explosive response is strongly dependent on the material properties, microstructure and type of insult, making it difficult to identify a single mechanism as dominant. The main mechanisms suggested for hot spot generation include adiabatic compression of trapped gas spaces, viscous heating of rapidly extruded material, friction between impacting surfaces, local adiabatic shear, and heating at crack tips. Note that this list is certainly not exhaustive, and many more mechanisms have been described in other studies [see 48, and references therein]. In Chapter 2 we discuss some of the main hot spot mechanisms, with reference to experiments and modelling found in the literature.

The general approach taken in this thesis will be to consider idealised geometries which allow for the investigation of a particular hot spot mechanism. The models developed will add to the understanding of High Explosive Violent Reaction (HEVR), with the ultimate goal of improving and validating hydrocode models.

1.2 Modelling of explosive materials

Explosives are, in general, composite materials, formed of independent granules held together with a polymeric binder. Typically, explosives are less than 15% binder by volume, and are constructed to have zero void volume (for solid propellants and certain UK explosives) or 2 to 5% void volume [81]. Consequently, the mechanical response of explosives shares many features with the granular behaviour exhibited by rocks and soils, as well as the rate dependency found in plastics. The complex behaviour of explosive materials in response to mechanical loads renders it difficult to make a confident choice of constitutive model. One often has to make a compromise by choosing an empirical law which encompasses the main behaviours, or resort to developing new constitutive laws – though the latter will be beyond the scope of this work.

A successful model requires an astute choice of constitutive law: one which accurately models the behaviour of the material in question, but which is simple enough to allow some mathematical tractability. Of course, it would be possible to pose a very complicated material, but this will often require solution through the use of large scale numerical simulations which are known to break down in the situations considered here. It is our aim to avoid such computations and to favour simpler models, which give a deeper understanding of the fundamental mechanisms involved. Explosive response is thermomechanical in nature, with additional self-heating due to

chemical reaction. Therefore an appropriate model for the chemistry is also required, to complement the material model.

Owing to the danger involved in conducting experiments on explosives, it is difficult to obtain detailed information about their constitutive behaviour. However, there is some experimental data available in the literature; in particular, unconfined compression tests have been used to obtain information about the stress-strain curve at a number of strain-rates [e.g. 59, 98]. These tests showed evidence of yield, with the material exhibiting a combination of elastic and plastic behaviour. A study group report [59] concerned with modelling explosive response during pinch suggested a number suitable rheologies, including perfect plasticity, viscoelasticity and thermo-viscoplasticity. Other models of hot spot mechanisms [e.g. 23, 24, 33, 34, 80] also treat the explosive material as behaving plastically, and it is therefore suggested that plasticity is a suitable model for explosives. In the following, we discuss the basic theory of elasticity and plasticity in general sense, giving a background on the modelling of different behaviours we might expect an explosive material to exhibit in response to an insult.

Perhaps the simplest constitutive law for solid behaviour is that of the linearly elastic solid, although such a choice does not capture many of the features observed in explosive material behaviour. To better describe the mechanical response of explosive materials, we may turn our attention to the theory of plasticity, which includes a diverse range of models constructed to describe a whole host of real-life behaviours. The list of such models is ever growing and becoming increasingly complex [62]. The most straightforward description of plastic behaviour, although not necessarily the most feature-rich, is that of perfect plasticity. More general theories include phenomena such as viscoelasticity and thermoelasticity, and are often characterised by the terms “elastic-plastic”, “viscoplastic”, “elasto-viscoplastic” etc. [62]. Explosives have been known to exhibit all of these behaviours, and require further models for strength, porosity, and so on [e.g. 59, 84].

Unlike elasticity, plasticity is characterised by deformations which are irreversible; such deformations occur when a stress threshold is exceeded. The existence of such a stress threshold is a defining property of plasticity, and the material response differs depending upon whether the stress state lies inside or on this threshold. Plastic media are supposed to behave elastically when the stress state lies inside the threshold. However when the stress state is on the threshold, the material behaviour differs greatly from that of the elastic solid and new laws must be formulated. In perfectly plastic materials the stress threshold is constant regardless of any change in strain, strain-rate, temperature etc. For non-perfectly plastic materials, the stress threshold is allowed to evolve with the loading, introducing further complications.

In a state of uniaxial loading the elastic limit or stress threshold can be described by a single number, which when exceeded the material ceases to behave elastically; the question is then how to measure the stress threshold for multi-axial stress states?

This may be achieved through the definition of a yield criterion, usually written in the form

$$f(\boldsymbol{\sigma}) = 0, \tag{1.2.1}$$

where $\boldsymbol{\sigma}$ is the stress tensor. For an assumed isotropic material it can be shown that the function f must be invariant under a change of axis, and as such must be a scalar valued isotropic function of the tensor $\boldsymbol{\sigma}$ [70]. Thus the yield criterion must depend only on the principal invariants of the stress tensor, i.e.

$$f(I_1(\boldsymbol{\sigma}), I_2(\boldsymbol{\sigma}), I_3(\boldsymbol{\sigma})) = 0, \tag{1.2.2}$$

where

$$I_1(\boldsymbol{\sigma}) = \operatorname{tr}\boldsymbol{\sigma} = \sigma_{ii}, \tag{1.2.3}$$

$$I_2(\boldsymbol{\sigma}) = \frac{1}{2}\{(\operatorname{tr}\boldsymbol{\sigma})^2 - \operatorname{tr}(\boldsymbol{\sigma})^2\} = \frac{1}{2}\{(\sigma_{kk}^2 - \sigma_{ij}\sigma_{ij}\}, \tag{1.2.4}$$

$$I_3(\boldsymbol{\sigma}) = \det\boldsymbol{\sigma} = \varepsilon_{ijk}\sigma_{i1}\sigma_{j2}\sigma_{k3}, \tag{1.2.5}$$

are the principal invariants of the stress tensor $\boldsymbol{\sigma}$.

In many cases, especially for metals, the influence of a mean pressure on the plastic deformation is negligible and the dependence of f on I_1 may be neglected [62]. Further we introduce the deviatoric stress tensor defined as

$$\mathbf{s} = \boldsymbol{\sigma} - \frac{1}{3}(\operatorname{tr}\boldsymbol{\sigma})\mathbf{I}, \quad \text{or} \quad s_{ij} = \sigma_{ij} - \frac{1}{3}\sigma_{kk}\delta_{ij}, \tag{1.2.6}$$

so that the yield criterion may be written in the form

$$f(J_2, J_3) = 0, \tag{1.2.7}$$

where $J_2 = \frac{1}{2}\{(\operatorname{tr}\mathbf{s})^2 - \operatorname{tr}(\mathbf{s})^2\}$ and $J_3 = \det\mathbf{s}$ are the second and third invariants of the deviatoric stress tensor, respectively.

There are a number of different yield criteria available in the literature [e.g. 60], so for now we give the two most simple examples. A criterion which gives good results for the case of pure metals is that of Tresca [95]. Also referred to as the *maximum-shear theory of loading*, the Tresca criterion states that plastic strain occurs when the maximum tangential stress attains a value $\tau_{\max} = k$. For principal stresses ordered as $\sigma_1 \geq \sigma_2 \geq \sigma_3$ this criterion may be formulated as

$$\frac{1}{2}(\sigma_1 - \sigma_3) \leq k. \tag{1.2.8}$$

The Tresca criterion is represented by a hexagonal cylinder in stress space. In the π–plane (the plane normal to the hydrostatic line) it is clear to observe the elastic domain being limited by a hexagon whose sides are parallel to the projection of the

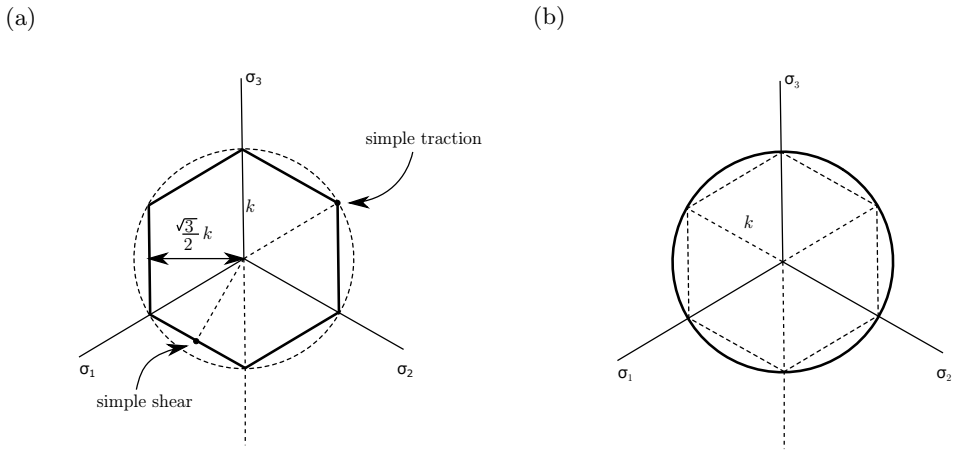

Figure 1.1: (a) Tresca and (b) von Mises yield criteria viewed down the hydrostatic axis.

axes, see Figure 1.1 (a).

An alternative to the Tresca criterion, commonly known as either the von Mises or *maximum distortion energy criterion*, was posed by Huber and von Mises, and offers a more simple geometric representation; that of a circular cylinder which circumscribes the hexagonal cylinder described by the Tresca criterion, see Figure 1.1 (b). The von Mises criterion is unusual in that it was suggested based on a purely mathematical basis [70]. The yield criterion takes the form

$$(\sigma_1 - \sigma_2)^2 + (\sigma_2 - \sigma_3)^2 + (\sigma_3 - \sigma_1)^2 \leq 6k^2, \tag{1.2.9}$$

with equality where the material is behaving plastically (i.e. where it has yielded). The von Mises criterion may be written more simply as

$$J_2(\mathbf{s}) = s_{ij}s_{ij} \leq \frac{2}{3}k^2, \tag{1.2.10}$$

suggesting that the material begins to yield when the second deviatoric stress invariant reaches some critical value [97].

When the stress threshold is reached, the material begins to deform plastically and we require a so-called flow rule. Plastic flow rules give a relation between the plastic strains ε_{ij}^p and the stresses σ_{ij} in terms of a plastic multiplier λ, and take the form

$$\mathrm{d}\varepsilon_{ij}^p = \mathrm{d}\lambda \frac{\partial g}{\partial \sigma_{ij}}, \tag{1.2.11}$$

where g is a scalar valued function known as the plastic potential. When the plastic potential g coincides with the yield criterion f the flow rule is said to be an associated flow rule, otherwise it is called a non-associated flow rule.

To continue with our earlier example, we find that the flow rule associated with

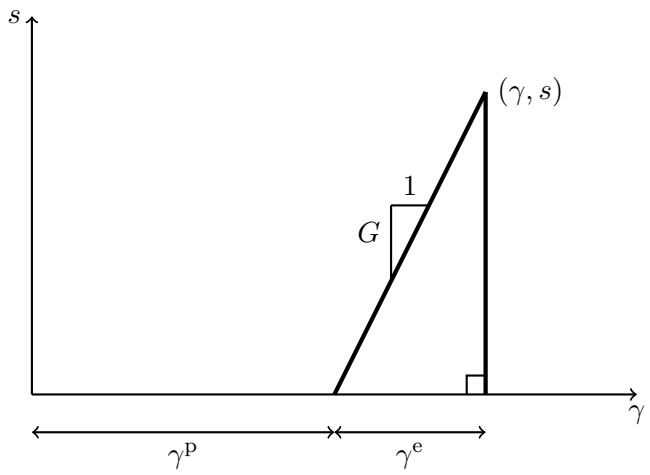

Figure 1.2: Decomposition of the total strain into elastic and plastic parts.

the von Mises yield criterion is

$$\mathrm{d}\varepsilon_1^p = \frac{2}{3}\,\mathrm{d}\lambda\left(\sigma_1 - \frac{1}{2}(\sigma_2+\sigma_3)\right), \tag{1.2.12}$$

$$\mathrm{d}\varepsilon_2^p = \frac{2}{3}\,\mathrm{d}\lambda\left(\sigma_2 - \frac{1}{2}(\sigma_1+\sigma_3)\right), \tag{1.2.13}$$

$$\mathrm{d}\varepsilon_3^p = \frac{2}{3}\,\mathrm{d}\lambda\left(\sigma_3 - \frac{1}{2}(\sigma_1+\sigma_2)\right), \tag{1.2.14}$$

known as the Levy-Mises flow rule.

The theories of Tresca and von Mises outlined above assume a constant yield stress, and are therefore examples of perfect plasticity. More generally, the yield stress may vary as a function of temperature, strain, strain-rate etc. A generalisation of the yield criterion (1.2.1) is given by

$$f(\boldsymbol{\sigma}; T, q_n) = 0, \tag{1.2.15}$$

where T is the temperature and q_n is a collection of state variables. Often, q_n is taken to be a variable, say K, which characterises the extent of work hardening [101].

As a simple one-dimensional example we may consider an elastic-plastic isotropic material undergoing a simple shear deformation. When considering elasticity and plasticity simultaneously it is useful to decompose the strain into an elastic and plastic part [62, 101]

$$\gamma = \gamma^{\mathrm{e}} + \gamma^{\mathrm{p}}, \quad \gamma^{\mathrm{e}} = s/G, \tag{1.2.16}$$

where s is the shear stress, and G is the elastic shear modulus. Note that it is always possible to decompose the total strain unambiguously into its elastic and plastic parts, even without knowledge of the stress-strain curve or stress history [101]. Figure 1.2 shows a graphical interpretation of the strain decomposition.

If we make the assumption that the material hardens isotropically, then the yield

function may be written $f(|s|;T,K) = \hat{f}(|s|,T) - K$ [101], which has the property

$$\hat{f}(|s|,T) \begin{cases} < K, & \text{elastic,} \\ = K, & \text{onset of yield,} \\ > K, & \text{plastic flow.} \end{cases} \tag{1.2.17}$$

In order to give a complete set of governing equations, one must provide constitutive laws for the plastic strain-rate $\dot{\gamma}^{\mathrm{p}}$ and hardening variable K [101]:

$$\dot{\gamma}^{\mathrm{p}} = \Gamma(|s|,T,K)\frac{|s|}{s}, \tag{1.2.18}$$

$$\dot{K} = \xi(|s|,T,K). \tag{1.2.19}$$

Since plastic deformation only occurs outside of the elastic region, the constitutive law for the plastic strain must have the property that it is zero for $\hat{f}(|s|,T) \leq K$ and positive for $\hat{f}(|s|,T) > K$. There exists a great number of models for the plastic strain-rate in the literature [e.g. 70, 101], many of which are empirical, aiming to describe qualitatively the key physics of the deformation process. Often, the constitutive laws for the plastic strain-rate and work hardening variable are combined into a single function: the so-called dynamic flow stress $s = \hat{s}(K,\dot{\gamma}^{\mathrm{p}},T)$ [8, 31, 101]. In contrast to the empirical approach, some plastic strain-rate laws are developed from more elementary arguments involving dislocation dynamics and then calibrated to experimental data [62, 101]. One such example of a viscoplastic flow stress is the power law model:

$$s = \pm s_0 |\gamma^{\mathrm{p}}|^n T^l |\dot{\gamma}^{\mathrm{p}}|^m, \tag{1.2.20}$$

used by many authors [e.g 54, 76, 101] to capture the effects of work and rate hardening, described by the exponents m and n, and thermal softening, described by the exponent l. The power law model suggests the generalisation

$$s = \pm K g(T) h(|\dot{\gamma}^{\mathrm{p}}|), \tag{1.2.21}$$

where the work hardening parameter K evolves according to some constitutive function. More complicated flow laws which account for different physical effects can be found in the literature [e.g. 101]. For instance, Zerilli-Armstrong models [105] are based on the argument that plastic slip is a thermally activated process, so the strain-rate should satisfy an Arrhenius law

$$\dot{\gamma}^{\mathrm{p}} = \Gamma_0 \exp(-E_{\mathrm{p}}/k_{\mathrm{B}}T), \tag{1.2.22}$$

where Γ_0 is a constant, E_{p} is an activation energy and k_{B} is Boltzmann's constant.

The flow stress is then split into an athermal and thermal part

$$s = s_{\mathrm{a}} + s_{\mathrm{th}}, \tag{1.2.23}$$

with the thermal part given by

$$s_{\mathrm{th}} = s_{\mathrm{th}_0} \exp(-\beta T), \tag{1.2.24}$$

where β depends on the strain-rate. The exact forms of the athermal stress component s_{a} and the thermal stress coefficient s_{th_0} are determined to be different for face-centred cubic and body-centered cubic materials [101, 105]. To extend this description into multiple dimensions, one must consider the constitutive laws for plastic strain-rate and hardening to be functions of the effective plastic strain and stress [62, 101]. A complete description of thermo-viscoplasticity is given in a thermodynamic framework in [101]. This reference also includes a discussion of a range of empirical models for plastic flow.

In reality, modelling of explosive materials should account for effects such as pressure dependence, rate dependence, compressibility, anisotropy, damage, etc. [2, 56, 59, 83], not to mention phase changes [3, 6, 51, 72] and microstructure [e.g. 9]. In this thesis we will favour simple material descriptions of explosives so that analytical progress can be made. Our modelling of solid explosives will be restricted to either rigid plastic materials or (elastic-)viscoplastic materials which account only for the physical effects of strain hardening, rate dependence and thermal softening through constitutive laws similar to (1.2.21).

1.3 Chemical decomposition models

The main focus of this work is to identify potential mechanisms which may contribute to thermal runaway. Although modelling of the chemistry is important to predict the temperature rise, the chemical reaction does not in itself lead to initial hot spot generation – the self heating due to a chemical reaction only serves to accelerate the heating to a violent level once sufficient heat has already been generated by other thermomechanical means. As such, we choose a simple model for the chemistry that captures the overall characteristics of the heating, whilst still offering some mathematical tractability. Here we present some simple chemical models often found in the literature.

First, the one stage Arrhenius model, expressed in terms of a mass fraction $\alpha(t)$ of the reaction products by

$$\frac{\mathrm{d}\alpha}{\mathrm{d}t} = A(1-\alpha)\exp\left(-\frac{E}{RT}\right), \tag{1.3.1}$$

where A is the pre-exponential factor, E is the activation energy, R is the molar gas

constant and T is the temperature, which may be a function of both space and time. Naturally, $\alpha = 0$ corresponds to an unreacted sample and $\alpha = 1$ corresponds to a fully reacted sample. It is well known that multiple reactions – some endothermic, some exothermic – are actually proceeding in parallel, but the one-step Arrhenius reaction serves as a preliminary model.

The one stage Arrhenius model may be extended to include multiple stages. For example, McGuire and Tarver [71] use a three-reaction model in their numerical study of the thermal explosion of HMX (cyclotetramethylene tetranitramine) and RDX (cyclotrimethylene trinitramine). The chemical decomposition model is

$$\mathbb{A} \to \mathbb{B} \to 2\mathbb{C} \to \mathbb{D}, \tag{1.3.2}$$

where $\mathbb{A}$ represents HMX or RDX, $\mathbb{B}$ represents $H_2C{=}N\text{-}NO_2$, $\mathbb{C}$ represents $CH_2O{=}N_2O$ or $HCN{+}HNO_2$ and $\mathbb{D}$ represents the final reaction products. For such a model the heat flow equation reads

$$\begin{aligned} -\kappa\nabla^2 T + \rho c\frac{\partial T}{\partial t} = {} & N_{\mathbb{A}}\Omega_1 A_1 \exp\left(-\frac{E_1}{RT}\right) + N_{\mathbb{B}}\Omega_2 A_2 \exp\left(-\frac{E_2}{RT}\right) \\ & + N_{\mathbb{C}}^2\Omega_3 A_3 \exp\left(-\frac{E_3}{RT}\right), \end{aligned} \tag{1.3.3}$$

where κ is the thermal conductivity, T is the temperature distribution, ρ is the density, c the specific heat capacity, $N_{\mathbb{A},\mathbb{B},\mathbb{C},\mathbb{D}}$ are the mole fractions such that $N_{\mathbb{A}} + N_{\mathbb{B}} + N_{\mathbb{C}} + N_{\mathbb{D}} = 1$, the Ω_i are the corresponding heats of reaction, the A_i are the frequency factors, and the E_i are the activation energies.

An alternative is the Prout-Tompkins model, which has the same exponential temperature dependence as the Arrhenius model but may allow a better fit to experimental data through the power law dependence on the mass fraction. The Prout-Tompkins model takes the form

$$\frac{\mathrm{d}\alpha}{\mathrm{d}t} = A\alpha^a(1 - b\alpha)^c \exp\left(-\frac{E}{RT}\right), \tag{1.3.4}$$

where a, b, c are the Prout-Tompkins model kinetics parameters [63], and α is the mass fraction as in (1.3.1). As with the Arrhenius model, the parameters need to be selected to provide a good fit to experimental data.

It is certainly possible to construct very detailed chemical models, either of the exponential form discussed above, or otherwise [e.g. 71]. However, since the focus of this work is the ignition mechanisms, and not accurate prediction of the temperature rise after the commencement of runaway, we will restrict ourselves to simple models which have solutions which behave like the physical chemical system.

1.4 Thesis outline

In Chapter 2 we continue our introduction, and discuss the main hot spot mechanisms found in the literature, with a particular focus on experimental evidence and numerical modelling. We highlight what we believe are the most important mechanisms and give an outline of how these are currently handled by hydrocode models used in industry. One of the key motivations for this project is to improve the understanding of hot spot mechanisms. Such mechanisms are, by definition, highly localised in space and it is therefore difficult for hydrocode models to give a satisfactory description before succumbing to issues such as severe mesh deformation [33, 34, 59]. We discuss the limitations of the hydrocode models and identify a number of hot spot mechanisms we wish to address in this thesis using analytical mathematical techniques. Following on from our overview of hot spot mechanisms, we detail the aims of the thesis.

The structure of the main body of this thesis was motivated by considering the response of an explosive material to a typical mechanical insult, such as being dropped or impacted upon by another object. Initially, the material is crushed and pinched, with friction and rapid plastic deformation playing an important role in mechanically heating the explosive. Owing to the inhomogeneous nature of the material, the deformation may subsequently localise into thin planar regions, known as shear bands. The development of shear bands leads to considerable localised heating due to plastic work. In some circumstances, the material within the shear band may melt as it continues to be heated further by plastic work and reaction, resulting in a molten layer of explosive trapped between two sliding surfaces. The work in the following four chapters chronologically follows the processes which occur as a result of a mechanical insult, starting with modelling the important effect of friction during pinch in Chapter 2, through to assessing how additional heating due to chemical reaction affects the development of shear bands in Chapters 4 and 5, and finally investigating the role of material inhomogeneity in the melting process in Chapter 6.

Motivated by the experimental and numerical test geometries discussed in Chapter 2, we develop a novel model for the pinching of an explosive material between two flat, rotating plates in Chapter 3. This model builds on the one-dimensional, free slip model in [33], and accounts for the effects of friction through boundary conditions on the shear stress, thus allowing for the identification of localised heating adjacent to the plates as seen in experiments. The model retains the rigid-plastic assumption of [33], so that the mechanical and thermal problems decouple and are solved sequentially. By assuming a large aspect ratio, a solution can be sought in a series expansion, and, under the quasi-steady assumption, the effect of varying the roughness of the plates can be investigated purely analytically. Further, we consider the effect of retaining the inertial terms in the governing equations. Once the mechanical problem is solved, we treat the thermal part of the problem numerically. The chapter concludes by discussing a simple

thermo-viscoplastic model and an idea for modelling hot spot generation during pinch due to (locally) periodic spatial variations in material properties or initial conditions.

In Chapter 4 we present a one-dimensional model for reactive shear bands. The model treats the material as elastic-plastic with a thermo-viscoplastic constitutive law for the plastic strain-rate. In order to demonstrate typical shear band behaviour in reactive materials we extend the numerical scheme for inert shear bands in [107] to account for a single-step Arrhenius reaction. The typical characteristics of a reactive shear band are discussed with the aid of numerical solutions. As a first approximation we then make the rigid-plastic assumption by taking the limit of infinite elastic shear modulus. Motivated by the numerical results, we seek an asymptotic description of the formation of a reactive shear band in a rigid-plastic which treats the band as a boundary layer. In the absence of strain hardening effects we are able to obtain a solution describing the initial growth (decay) of temperature (stress) within the band.

In Chapter 5 we return to the elastic-plastic model of a reactive shear band outlined in the previous chapter. The governing equations are nondimensionalised using a thermal length scale, allowing the thinness of the band compared with a typical sample size to be exploited. Using an exponential plastic strain-rate law [38] we are able to identify an asymptotic structure which consists of an inner region, away from which the plastic strain-rate decays exponentially, and an outer elastic region. These are matched together through an intermediate diffusive zone. In the analysis we describe three different approaches to obtaining a solution, each of which make slightly different assumptions about the timescales over which heating due to plastic work and chemical reaction are comparable, or dominate over one another. The first approach accounts for an early elastic stage and a subsequent stage during which heating due to plastic work and reaction are accounted for simultaneously. In the second approach, the slowly growing reaction is ignored in the early stages, and is only accounted for once some critical temperature threshold is reached. The third approach is based on an approximate thermal explosion theory [80], which essentially switches between heating due to plastic work and heating due to reaction at the time at which the two terms first become comparable in the energy equation. The three approaches are compared with one another, and the first approach is shown to give excellent agreement with results obtained using the numerical scheme described in Chapter 4. To account for strain hardening effects we propose a novel extension to the exponential plastic strain-rate law given in [38]. It is shown that the onset of shear banding can be delayed, or, in the most extreme cases, prevented entirely by strain hardening effects. Finally, the equations are recast in terms of new non-dimensional variables, and a criterion for the onset of shear banding in reactive materials is derived and discussed.

Chapter 6 develops a two-dimensional model which describes the melting and

ignition of an explosive sliding past a solid surface. A lubrication type model is formally derived which accounts for both heating due to viscous dissipation and chemical reaction within the liquid melt layer. In order to account for non-uniform melting, possibly due to locally varying material properties or inclusions, we perturb the shape of the melt front separating the liquid and solid explosive. It is demonstrated that melt front is linearly stable to perturbations in the absence of any chemical reaction, but becomes unstable upon the inclusion of an Arrhenius source term. Non-uniform melting is identified as a possible hot spot mechanism in heterogenous explosives, and predictions about how the shape of the melt front may affect the spatial dependence of the heating within the layer, and the time to runaway, are made. Further, we consider the effects of allowing the specific heat, viscosity and thermal conductivity to vary with temperature. In particular, it is shown that the temperature-dependent viscosity affects the shape of the velocity profile across the layer, and may therefore play an important role in the generation of localised hot spots. Finally, an idealised model for the presence of surface roughness, or grit in the sliding surface, is considered. A comparison between our model geometry of a wall sliding past a semi-infinite block of explosive and the geometry of an internal closed microcrack is discussed.

Finally, in Chapter 7 we conclude. We discuss some ideas for future work, and mention some other, less fruitful, modelling efforts that were made during this research.

1.5 Statement of originality

Chapter 2 is largely a literature review and is therefore not original.

The work in Chapter 3 substantially builds on the work of Curtis [33], addressing the important effect of friction. The mechanical part of the problem is solved using the approach described in [88]. The consideration of the combined squeezing and rotating motion is entirely novel. Further, the analysis which includes inertia is also original, as is the two-dimensional numerical solution of the thermal part of the problem which accounts for friction.

The one-dimensional model for shear banding used in Chapter 4 is standard in the literature [e.g. 101, 107]. The extension of the numerical scheme [107] to include heating due to chemical reaction is novel. A similar numerical solution to the rigid-plastic shear band problem, albeit in the configuration of torsion of a thin-walled specimen instead of unidirectional shearing of a slab, may be found in [24, 80]. The asymptotic analysis of the rigid-plastic shear band which includes a chemical reaction is original, though a similar analysis for an inert material is carried out in [42].

The boundary-layer analysis set out in Chapter 5 builds on the inert work [38]. Originality is claimed for the inclusion of a chemical reaction in the analysis. The first two approaches shown to solve the reactive shear band problem are novel, as is

the demonstration that the reactive shear band model reduces to an entirely different problem, which models the heating of a half-space of explosive material due to a heat flux at the boundary, in an appropriate limit. The final approach to modelling the onset of reactive shear bands is motivated by the thermal explosion theory [80], but arrives at the result through a different boundary layer argument. The postulated exponential plastic strain-rate law which accounts for strain hardening, and the following solution of the boundary-layer problem, are also original. To conclude the chapter a criterion for the onset of shear banding is derived and discussed. A similar criterion was developed for an inert analysis in [38], but we provide an original discussion on how a chemical reaction affects the tendency for a shear band to form.

The two-dimensional model for the melting and ignition of an explosive given in Chapter 6 is original work. A one-dimensional model was developed in an ad-hoc manner in [90], but we provide a formal derivation. The resulting analysis, both numerical and asymptotic, which considers a perturbed melt front width is entirely original, as is the consideration of temperature dependent material properties. The simple model for grit is also an original contribution.

Chapter 2

Hot Spot Mechanisms and Experiments

In this chapter we discuss the main hot spot mechanisms proposed in the literature, giving reference to both the experimental evidence and the modelling work which aims to understand the role such mechanisms play in accidental ignitions. As well as highlighting the experimental studies, we give an overview of the types of numerical models used to study the response of explosives to mechanical and/or thermal insults. We go on to discuss the limitations faced by such numerical hydrocode models, such as severe mesh deformation, and use these limitations to motivate the analytical approach of hot spot modelling preferred in this thesis. Further, we comment on how it is envisaged that the analytical modelling may inform and improve hydrocode models.

A series of papers by Field and colleagues at the Cavendish laboratory, Cambridge, [45–48, 58, 91] investigated the response of explosive materials to stress and impact, with a particular focus on the mechanisms of hot spot production. They conducted a range of experiments on samples in the form of single crystals, powder layers, pressed pellets, gels, PBXs (polymer bonded explosives) and propellants. The techniques used in the study will be discussed in the following section. The mechanisms suggested in [48] are:

(i) adiabatic compression of trapped gas spaces [16, 17, 26, 32, 89];

(ii) viscous/plastic heating of the surrounding matrix material during cavity collapse [52];

(iii) viscous heating of material rapidly extruded between the impacting surfaces of grains [13, 43, 57, 85];

(iv) friction between the impacting surfaces, the explosive crystals and/or grit particles in the explosive layer [14–16, 18, 25];

(v) localised adiabatic shearing [2, 51, 58, 91, 99];

(vi) heating at crack tips [45];

(vii) spark discharge [103];

(viii) triboluminescent discharge [45];

(ix) decomposition followed by Joule heating of metallic filaments [92].

We first give a brief overview of typical experimental set-ups, with some general comments on the constitutive behaviour of explosives, before addressing each of the mechanisms listed above in turn. Finally, we discuss hydrocode models and how the modelling of ignition is handled.

2.1 Experiments

In their paper, Field et al. [45] consider the behaviour of thin layers of explosive when impacted. They present evidence for ignition by a variety of mechanisms including adiabatic shear of the explosive, compression of trapped gas spaces, viscous flow, friction, fracture or shear of added particles, and triboluminescent discharge. The viability of each mechanism is assessed for different explosives and impact conditions via the means of photographic evidence.

In the experiments conducted at the Cavendish laboratory, explosive samples were impacted by a 5 kg weight dropped from a height of 1 m, see Figure 2.1. During the experiment the weight was allowed to fall freely, guided by metal rods, and impacted onto the toughened glass hammer. The anvil was also made from toughened glass so that the photographs could be captured in the transmitted light. In the drop-weight tests described in [45, 48] samples typically consisted of 10–25 mg of explosive in powder, pellet or liquid form. Some samples included additional particles in their formulation. The work [45] in particular contains a large number of photographic sequences, all of which were captured using an Atomic Weapons Research Establishment C4 rotating mirror framing camera with an inter-frame time of approximately 5 µs and a field of view of 20 mm. The transparent anvil and drop-weight arrangement shown in Figure 2.1 was originally used by Blackwood and Bowden [12]. It was observed that, in the early stages of the drop-weight experiment, the explosive sample was compressed and compacted, with its radial expansion progressing at a similar velocity to that of impact ($\approx 1\,\mathrm{m\,s^{-1}}$). This early stage was not illustrated by Field [45]. Early work [45–47, 58, 73, 74, 91] showed that initiation of the explosive sample typically took place after rapid radial flow (greater than approximately $100\,\mathrm{m\,s^{-1}}$) in the absence of sensitising grits. Such rapid flow can occur as a result of mechanical failure of the sample. However, if the material is weak and offers little resistance to the drop-weight it will deform at a constant volume, with large radial velocities being a natural outcome [48].

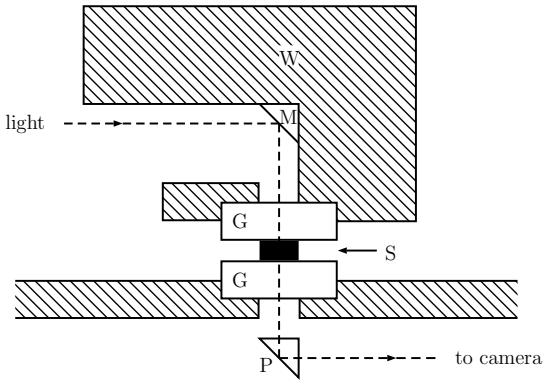

Figure 2.1: Experimental arrangement at instant of impact: W, drop-weight; G, glass blocks; M, mirror; P, Prism; S, sample. The upper glass block is attached to the weight.

The stage of the drop-weight tests during which the material strength is exceeded and the sample begins to deform plastically is referred to as the "pinch" regime. In the geometry depicted in Figure 2.1 it is important to note that, due to the confining effect of the anvils, the yield stress, denoted here by p_Y, is higher than the uniaxial yield stress Y [45]. Application of the von Mises yield criterion to a thin layer of height h and diameter d gives the Schroeder-Webster relation [86]

$$p_Y = Y\left(1 + \frac{d}{3\sqrt{3}h}\right). \tag{2.1.1}$$

Note the importance of the ratio d/h: the smaller the height, or greater the diameter, the higher the mean pressure. The relation (2.1.1) goes some way to explain the sample size effects found in impact ignition; for instance, it has been demonstrated that a 'critical mass' of explosive was required for ignition, with samples of small height showing little tendency to flow [58]. The variation of ignition probability with sample thickness is considered in detail in [2]. Once plastic flow commences, the sample expands rapidly in the radial direction at speeds of more than the critical $100\,\mathrm{m\,s^{-1}}$, and a subsequent ignition may observed [45]. In sufficiently strong materials, rapid deformation is a necessary prerequisite for ignition and it has been observed that the prevention of flow in an explosive sample decreases the sample sensitivity, i.e. the likelihood of ignition is reduced [2]. Stress-time traces obtained from the instrumented drop-weight machine substantiate this view [45, 48]. While ignition occurs after rapid flow, it is important to note that the rapid flow itself does not necessarily cause ignition; experimental evidence reveals that samples may deform rapidly, but fail to ignite [45].

For a number of explosive materials, e.g. PETN (pentaerythritol tetranitrate), RDX, AP (ammonium percholate), it is observed that the sample becomes transparent and flows very rapidly, at speeds exceeding $300\,\mathrm{m\,s^{-1}}$, before ignition. In PETN this transparency is due to the sample melting, with similar behaviour observed with RDX, whereas for AP the transparency is due to sintering of particles. This is evidenced by

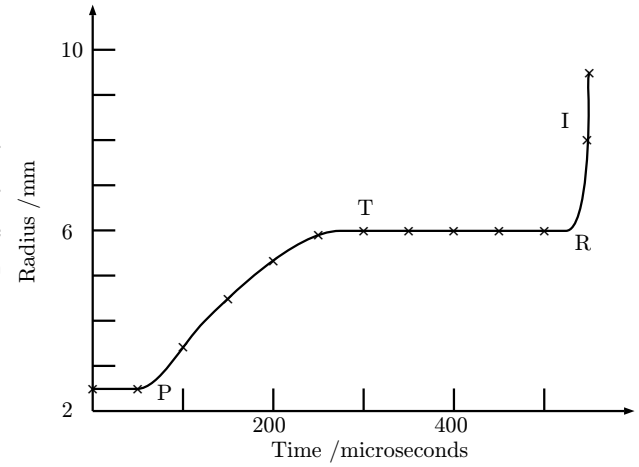

Figure 2.2: Sketch of radius against time for a pressed pellet of PETN. P,T,R and I denote the onset of plastic flow, transparency, rapid flow and ignition, respectively.

a static loading experiment with a sample of AP, in which the transparency occurs before the plastic flow and is partially lost during the plastic deformation stage [45]. After ignition occurs, fractures can be detected in the material ahead of the burning front [58].

Experiments were also made on an instrumented drop-weight machine, providing evidence on the relation between mechanical failure of the explosive sample and the time of ignition. During the test, strain gauges mounted on a hard steel roller allowed the stress on the sample to be monitored during impact. Full details of the instrumented drop-weight apparatus are given in [58]. Field and co-workers have presented results for impacts on a wide range of explosive and inert samples [45]. Figure 2.2 shows a sketch of the sample radius against time for a pressed 25 mg pellet of PETN during a drop-weight test from a height of 1 m. It is clear to observe the relation between mechanical failure and ignition, with ignition always occurring after failure.

Results for a range of PBXs in a miniaturised Hopkinson bar experiment are given in [46]. In a conventional Hopkinson bar experiment, the specimen is placed between two long, cylindrical rods [e.g. 65]. A stress wave is sent down the input bar, and the incident, reflected and transmitted waves are recorded by gauges, allowing the stress–strain behaviour to be obtained, typically at strain-rates of around 10^3 s^{-1}. A direct-impact miniaturised system, which removed the need for the input bar, was developed by Gorham [55] This particular system had the advantage of being able to conduct experiment at strain-rates of up to 10^5 s^{-1}. A number of other experimental techniques, such as the Brazilian test, are described in [48] and references therein.

More recent work [98] aimed to characterise the behaviour of PBXs through a series compressive tests performed at a temperature of 293 ± 2 K over a range of strain-rates from 10^{-8} to 10^3 s^{-1}, and at a strain-rate of 10^{-3} s^{-1} over a range of temperatures from 208 to 333 K. Results from a range of tests demonstrated

a strain-rate dependence of the compressive strength, with the strain at failure increasing from approximately 0.5% at the slowest strain-rates to 1% at the fastest strain-rates. Further evidence for the temperature dependence of the compressive strength, and shear banding, a phenomenon where the flow localises to narrow bands within the material, is also observed. Figure 4 of [98] shows typical stress-strain curves at an array of different strain-rates. In order to measure the stress corresponding to a linearly increasing strain, efforts were made to keep the strain-rate constant throughout the experiment. Interestingly the elastic modulus appears to be larger at higher strain-rates, and the strain corresponding to maximum stress only increased minimally with increasing strain-rate. After yielding we see a significant decrease in stress, i.e. we observe strain softening behaviour, which is indicative of possible shear banding in the sample. This highly localised flow may lead to hotspots and as such is identified as an important topic for further investigation [59].

The tests commonly used at AWE to examine explosive response include: impact sensitiveness (known as the Rotter test); response to incendive sparks (known as the Ease of Ignition test); response to prolonged flame exposure (known as the Train test); heat stability (known as the Temperature of Ignition test); sensitiveness to impact between a variety of surfaces (known as the Mallet Friction test); response to exposure to electrostatic discharges of different energies (known as the Spark test); impact with crush and pinch (known as the Steven test); and response due to penetration by a metal rod (known as the Small Scale Spigot test) [5]. The tests are designed to examine the response of the explosive to mechanical or thermal loads which are representative potential threats, or insults, it may encounter during typical use.

The tests conducted add to the understanding of a number of different hot spot mechanisms or accidental ignition scenarios. In the Steven test a small sample of explosive material is fixed between a base unit and covering plate, surrounded by a strong retaining ring, as shown in Figure 2.3. A curved projectile impacts on the covering plate in order to examine the response of the explosive to the insult. At an increased impact speed more energy is transferred to the explosive, thereby increasing the risk of detonation.

Another test currently in use is the so-called Spigot test, designed to represent a thin spigot impacting on a bare explosive charge with a semi-rigid back surface. The target consists of a 10 mm thick steel base and a polished perspex confining ring of height 25.5 mm which surrounds the explosive sample, see Figure 2.4. The perspex ring provides minimal mechanical confinement to the sample but still allows the explosive response to be viewed from a position normal to the impact axis. A 5 mm recess cut is made in the centre of the rear face of the steel base, which is designed to produce a steel flyer when the sample reacts. The velocity of the flyer is recorded using Photon Doppler Velocimetry [81]. A 28 mm long hardened steel spigot is fired from a smooth bore gas gun which, because of its length, can penetrate the full depth

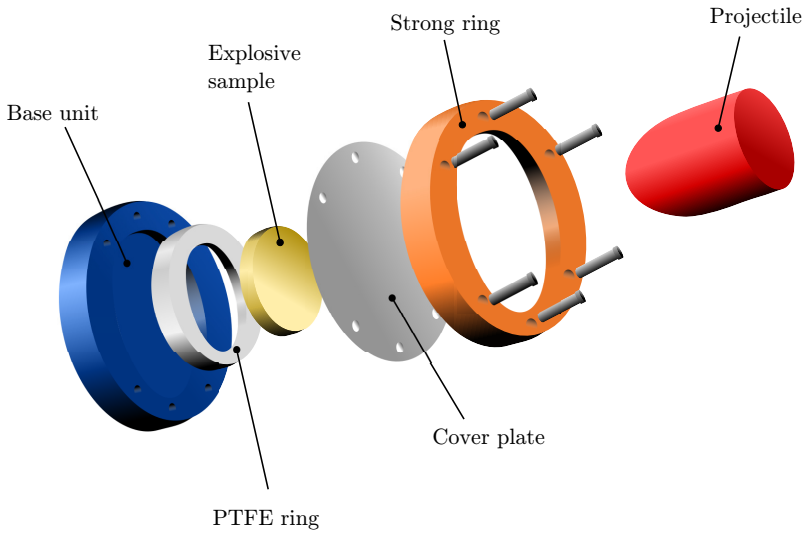

Figure 2.3: Configuration for the UK Steven test.

of the explosive sample. Two wire coils placed at the muzzle end of the gas gun allow reliable measurement of the muzzle velocity, regardless of the projectile shape.

Although the geometry of both the Steven test and the Spigot test is relatively simple compared to the real-world situation, it still remains too complex for the types of models we would like to develop here. In order to make some analytical progress we may wish to consider tests in more simple geometrical configurations. One such configuration is that of the so-called "Pinch-Test", in which a sample of explosive is squeezed between two parallel plates with no confining ring as seen in Steven test [59]. Although not currently conducted by AWE, the Pinch-Test is of interest due to its simple geometry. It is envisaged that in the AWE Pinch-Test the the upper plate is moved towards the stationary lower plate and the sample is freely allowed to expand laterally. Note that in the Pinch-Test there is no air gap between the upper plate and the sample, so air cushioning effects are not important. However, in other tests, such as the Spigot test, the air gap may play a crucial role [36]. A recent study group also highlighted the potential usefulness of experiments involving shear, in particular simple shear between two flat plates and cone rheometry [59].

2.2 Hot spot mechanisms

Although there are nine suggested hot spot mechanisms in [48], and several more in the literature [e.g. 2, 49, 53, 94, 96], most consideration is given to those numbered (i) and (iii)–(vi) in the list given at the start of this chapter. Here we give a discussion of what are to be considered the five most important hot spot mechanisms.

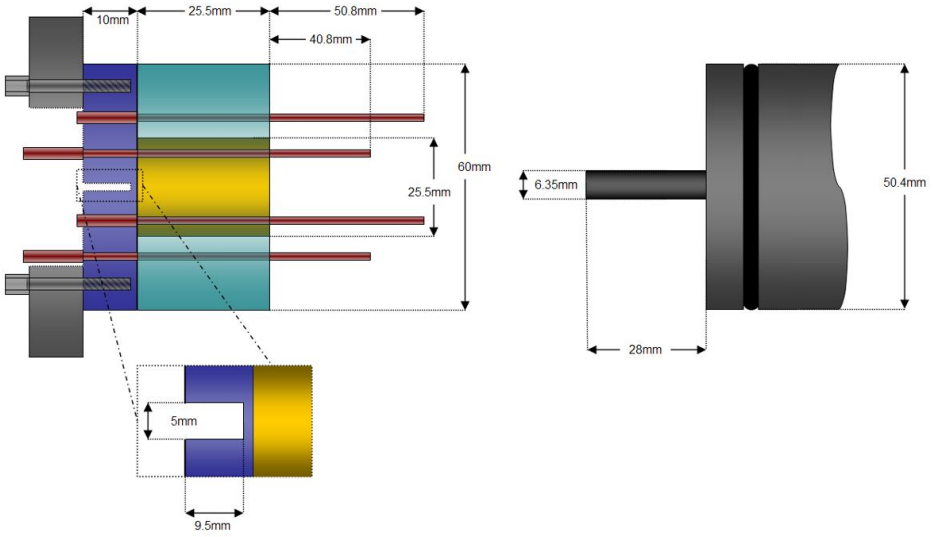

Figure 2.4: Spigot test design (not to scale). The explosive sample (yellow) is surrounded by a perspex ring (pale blue). Image courtesy of AWE.

2.2.1 Adiabatic compression of trapped gas spaces

Voids have long been known to sensitise explosive materials, leading to an increased likelihood of ignition due to impact or shock [48]. In some insensitive formulations, such as ammonium nitrate, artificial cavities are added to increase the sensitivity. It has been shown that the collapse of gas bubbles is a particularly important consideration for liquid explosives [16, 17, 32, 48, 104]. For solid explosives undergoing impact in the drop-weight test it was shown that the gas spaces also play an important role [16, 104], especially for annular layers of material. Results showed that the specific heat of the gas was an important factor during collapse, indicating adiabatic heating. This claim was criticised by some authors [2], who argued that at impact velocities on the order of $1\,\mathrm{m\,s^{-1}}$ the gas spaces were more likely to compress isothermally. However, later photographic evidence [45, 48, 58] showed that the material deformed rapidly in the radial direction ($\approx 100\,\mathrm{m\,s^{-1}}$) during the drop-weight test, adding more evidence to the argument for adiabatic heating of collapsing gas spaces. Another mechanism acting during the collapse of gas spaces is that of jetting; the cavity may collapse asymmetrically, producing a liquid jet [66].

2.2.2 Viscous and/or plastic heating

In the literature, viscous heating due to the flow of material between confining plates has been suggested as a potential ignition mechanism. Early work [43], which assumed laminar flow and Newtonian viscosity, showed that the maximum rate of

shear in a liquid film occurs near the outer edge of the sample, and is given by

$$\left(\frac{\partial v_r}{\partial z}\right)_{\max} = \frac{4v_r}{h}, \tag{2.2.1}$$

where v_r is the radial velocity, z is the vertical coordinate and h is the film thickness. In the absence of heat losses, the temperature rise is governed by

$$\frac{\partial T}{\partial t} = \frac{\mu}{\rho c}\left(\frac{\partial v_r}{\partial z}\right)^2, \tag{2.2.2}$$

where μ is the viscosity, ρ is the density and c is the specific heat. Despite the relatively simple governing equation, evaluation of the temperature rise is not as straightforward as it looks, since the viscosity is a function of pressure and temperature, and it is expected that some heat loss to the anvils occurs. Heavens [58] considered the temperature contribution from viscous heating in impacted thin layers of NG (nitroglycerine) and PETN. For NG, assuming a constant viscosity, a temperature rise of 650 K was obtained, compared with a change of only c. 100 K for cases where a variable viscosity was used. Similar calculations for the PETN only estimated a temperature rise of 10–20 K, owing to the much lower shear rate. It was concluded that viscous heating could be an important hot spot mechanism in liquid explosives, but is only likely to be significant in solid explosives when observed in conjunction with other effects, a view supported by evidence in [45, 48]. Further hot spot mechanisms associated with viscous heating include heating of the matrix material and heating produced by compression of material downstream of the impacting liquid jet [69].

2.2.3 Friction

As an ignition mechanism, frictional rubbing is well established in the literature [14–18, 96]. During rubbing contact between two solid bodies, the hot spot temperature is determined by the solid with the lower melting point – the lower melting point solid 'quenches' the hot spot temperature to the melting temperature. Bowden and Gurton [14, 15] were able to measure hot spot ignition temperatures for a wide range of explosives by choosing grits of different melting points and measuring the effect on the sensitivities of the explosives. The validity of this work has been questioned by Swallowe and Field [91], who show that although the model presented by Bowden and Gurton [14, 15] works well with hard, high melting point additives, it requires further validation, since soft, low melting point additives such as polymers can also act to sensitise explosives. Sensitising polymers are those which fail catastrophically by fracture or localised shear, and have low specific heat, latent heat and thermal conductivity. It has also been argued that stab-initiation of explosives is essentially due to frictional rubbing, see [25]. The needle used in the test collects a layer of

adhering crystals as it enters the explosive sample and the subsequent hot spot is caused by rubbing between the adhered layer and the other solid crystals.

2.2.4 Localised adiabatic shearing

A common description of shear localisation, or adiabatic shear banding, is as follows. Consider a material which exhibits strain hardening, strain-rate hardening and thermal softening behaviour being placed under a uniform shear stress. In the early stages the response will be that of uniform shear strain; the material will undergo homogeneous deformation. As the strain is increased so that the material enters into the plastic regime, material hardening behaviour is observed. This hardening behaviour will be exacerbated by any geometric discontinuity or material inhomogeneity – the strain-rate will be higher near the discontinuity, leading to further hardening behaviour. If the straining occurs at a high enough average strain-rate (typically greater than 10^2 s^{-1}) there is insufficient time for the generated heat to be conducted away [24]. The material softens due to the localised temperature increase and, if this softening process dominates over the strain hardening effects, the material strength decreases. The local net softening of the material serves to concentrate the deformation into thin planar regions, known as shear bands. It is hypothesised that the concentration of thermal energy within shear bands could trigger a localised reaction which may spread through the explosive material.

Shear localisation has been widely studied in inert materials, e.g. [7, 38, 101], but the majority of studies for explosive materials have been experimental. Evidence for localised shear within the explosive sample can be observed in recovered unexploded samples. Photographic evidence for adiabatic shear is given in [45], showing ignition and propagation occurring in a shear band in a sample of PETN. Notable work on shear localisation in explosive materials includes [19, 29, 37, 51, 61] and the substantial work [2], in which it is suggested that if plastic deformation is localised into thin bands of dimensions of the order of a micometre or more then hot spots may be formed, causing subsequent ignition. Further evidence for this claim is given in [45–47, 51, 75].

Other authors are less convinced that shear localisation alone is a sufficient hot spot mechanism. In [25] it is argued that shear, even if localised, is only a sufficient ignition mechanism when strains are high. The ability of brittle explosive crystals to sustain high enough strains is questioned, and it is concluded that friction is a more likely cause in solid explosives. Furthermore, in [51] it is argued that ordinary sliding friction and shear localisation are identical processes, when considered on a molecular level.

More recent mathematical studies by Caspar and Powers [24, 80] on shear localisation in explosive materials considered an idealised situation in which a thin-walled cylindrical specimen is subjected to a torsional pulse, as in experiments

using a torsional split Hopkinson bar (TSHB). The temperature, stress and strain-rate were computed numerically as the band developed, and some analytical estimates for the time to induction were calculated [80]. For the numerical simulations presented it was found that ignition was a direct consequence of shear localisation [23, 24, 80]. A sensitivity analysis concluded that shear localisation, and subsequently ignition, is far more sensitive to changes in mechanical properties, as opposed to thermomechanical properties. Interestingly, Powers [80] notes that spatially homogeneous models for strained explosive materials are adequate to predict ignition (for materials which react at temperatures near the temperature at which mechanical strength is lost) even in the presence of perturbations which can induce shear localisation. Powers writes: "...more concentrated reactive hot spots associated with possible shear localisation are simply harbingers of an already imminent ignition process, and not its cause.".

2.2.5 Heating at crack tips

The intense stress field at the tip of a propagating crack can cause plastic deformation, leading to increased heating and possibly hot spots. Evidence given in [45, 49] supports the claims that:

(i) fracture of a single explosive crystal along does not cause ignition;

(ii) fracture produces gaseous decomposition products which sensitises the explosive by producing trapped gas pockets which can be compressed, causing ignition;

(iii) the sensitivity of explosives with additives may be affected by hot spots caused by fracture of the additive.

Heating at crack tips is discussed in detail in [45], where it is concluded that it is unlikely to be a hot spot ignition mechanism in an explosive crystal. The main reason for this is that the energy of such a process is simply too low to generate a hot spot of sufficient size and temperature necessary to cause ignition [48].

2.3 Numerical modelling of hot spots

The physical experiments discussed above are complimented by numerical simulations. Numerical models for ignition are often based on large scale finite element codes, many of which are currently implemented using the multiphysics simulation package LS–DYNA, a Lagrangian Finite Element code developed by the Livermore Software Technology Corporation (LSTC).

Simulations which aim to describe HEVR must account for a number of different physical processes. When subjected to a mechanical insult, a region of explosive material near to the impact site becomes damaged. This damage creates surface area, through the generation of cracks and fragments, and increases porosity as a result of

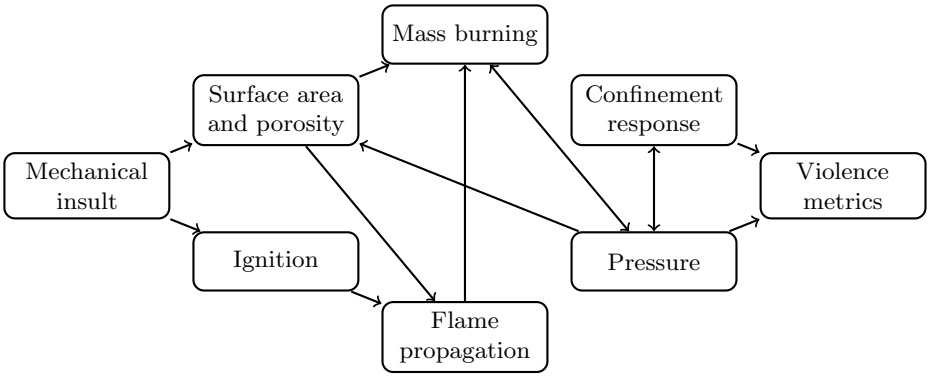

Figure 2.5: Interacting processes following a mechanical insult.

crack separation and isolation of fragments [83]. Subsequent to a localised ignition, a flame spreads through the damaged material, spreading rapidly through the open pores and igniting the newly created surface area. Where the surface area is locally increased there is a local increase in the mass burning rate, and the pressure rises until neither the mechanical strength nor confinement can contain it. This causes the confining structure to expand, reducing the pressure and potentially extinguishing the flame. The violence of the response is measured in many ways, including the extent of damage to the confinement, the velocity and fragment size distributions and the air blast [83]. Figure 2.5 shows the interactions of the various processes which follow a mechanical insult, as outlined in [83].

Understanding ignition is key to analysing whether a mechanical insult leads to HEVR. Therefore a strong understanding of the mechanisms which lead to ignition is necessary to devise an accurate ignition model for use in numerical simulations. Developed over the last decade as a joint venture between Lawrence Livermore National Laboratory (LLNL) and AWE, the High Explosive Violent Reaction Model HERMES (High Explosive Response to MEchanical Stimulus) is used to enable simulations of the mechanical – and subsequent energetic – response of explosive materials to a range of mechanical insults such as impacts, drops and falls [84]. The HERMES model is embedded into other numerical simulation software packages which solve the nonlinear large deformation equations of compressible fluid and solid flow. HERMES consists of a number of sub-models, including a constitutive model for strength, porosity and generation of surface area through fragmentation, an ignition model, an ignition front propagation model, and a model for material burning subsequent to ignition [81, 83, 84]. At present, HERMES is not used as a fully predictive model, and is instead best used as a guide for understanding and developing new experiments, and for identifying hot spot mechanisms [84].

Given that ignition is the critical factor in determining if HEVR will occur, development of a reliable and realistic ignition criterion is crucial if the model is to be a success. Some have used modified shock-to-detonation models for HEVR response, but this is contested on the grounds that HEVR is generally not a detonation. Even

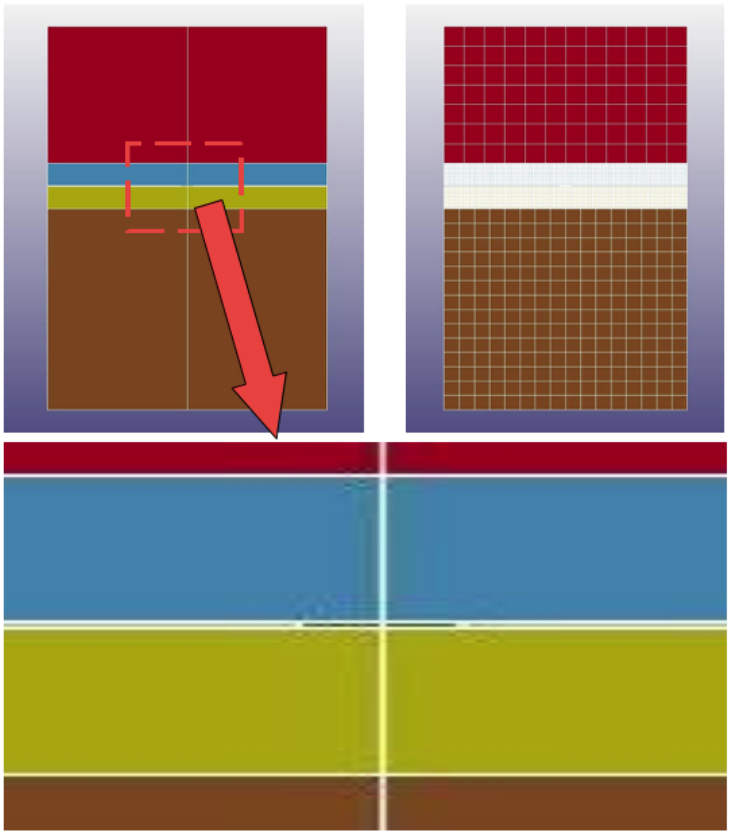

Figure 2.6: Geometry and mesh for the drop test. Image taken from [35], with permission.

when a violent event is recorded on blast gauges substantial amounts of unreacted explosive remain [81]. The ignition model used in the implementation of HERMES is based on the observation that ignition in low speed impacts is always preceded by significant shear deformation [84]. Although the shear localisation mechanism is not explicitly indicated, the properties of the stress tensor are used to identify areas of undergoing shear deformation. A purely mechanical ignition criterion is given as a time integral of a function of shear, equivalent stress, pressure, and strain:

$$I_{\mathrm{gn}} = \int_0^t \left(2 - \frac{27\,|s_1 s_2 s_3|}{2Y^3}\right)^5 \left(\frac{p + s_2/2}{p_0}\right)^{1/2} \dot{\varepsilon}_p \,\mathrm{d}t, \tag{2.3.1}$$

where $s_{1,2,3}$ are the principal stress deviators, $Y = \sqrt{\frac{3}{2}(s_{ij}s_{ij})}$ is the equivalent stress, p is the pressure, p_0 is a prescribed constant pressure, and $\dot{\varepsilon}_p$ is the plastic strain-rate. Ignition is considered to take place when I_{gn} reaches a particular value set by calibration with experiments. A comprehensive summary of the HERMES model, and its sub-models, can be found in [84].

Figure 2.6 shows the finite element mesh used in a hydrocode simulation of a simple drop-weight test [35], whose geometry is loosely based on the drop-weight tests at the Cavendish laboratory [45]. The sample is small, with a radius of 2.5 mm

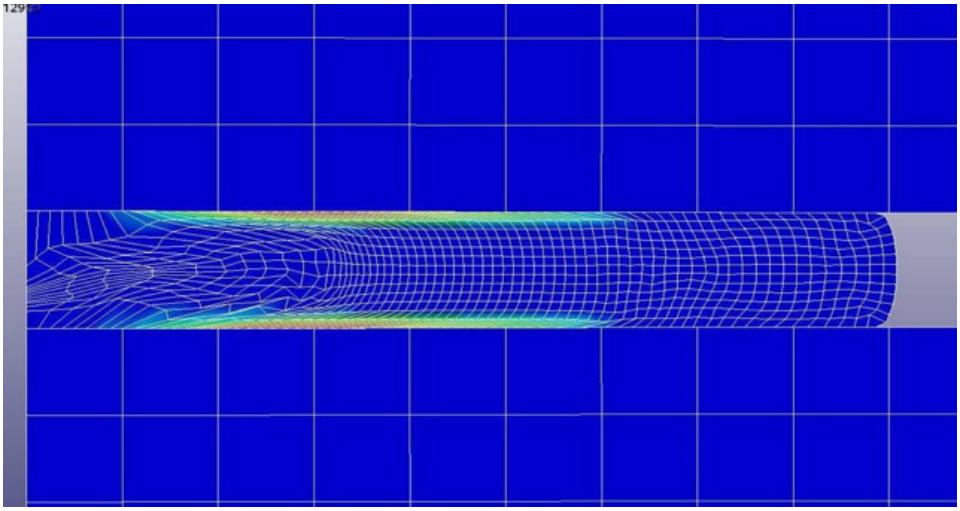

Figure 2.7: Contours of ignition parameter in PETN sample impacted at $1\,\mathrm{m\,s^{-1}}$, with minimum (blue, darker) 0.0 and maximum (red) 352.0 (in boundary layers). Note the mesh distortion, particularly in the boundary layers.. The image shows a slice through the r–z plane at the fixed time 120 µs. Image taken from [35], with permission.

and height of 0.5094 mm, so a very fine mesh is required; so fine that it is not visible at this scale, but can be observed in later plots showing the explosive sample. The adjacent meshes in the the hammer and anvil can be more coarse, allowing for a reasonable run time. Figure 2.7 shows contours of the HERMES ignition parameter at a time of 120 µs in a sample of PETN subjected to an impact corresponding to a typical drop height of 1 m [35, 45, 48]. As the explosive is pinched, it is observed that the highest values of the ignition parameter are associated with boundary layer shear. This highly deformed shear layer results from friction between the explosive and drop-hammer/anvil as the sample is squeezed out. By this time considerable mesh deformation has occurred, despite the simple geometry of the drop-weight test [35]. A simplified model, which replaced the drop-hammer and anvil with rigid moving walls, allowed for more detailed consideration of the explosive response while keeping run times low. This model broadly captured the same behaviour seen in the full formulation, which treated the drop-hammer and anvil explicitly, but the reaction was delayed somewhat. Figure 2.8 shows contours of the ignition parameter at 168 µs, and it is observed they are very similar to those shown in the full model at the earlier time of 120 µs, see Figure 2.7. This analysis in particular demonstrated that, while the model with rigid walls is useful in obtaining an idea of the likely explosive response, modelling the interaction of the explosive with the drop-hammer and anvil is likely important for accuracy.

There are clear benefits to using numerical models in terms of cost, safety and time. However, due to the very large deformations found in modelling a large number of tests, many numerical formulations suffer from severe mesh deformations [33–35]. Though useful in predicting potential experimental outcomes, numerical simulations do not always provide a great deal of insight into the underlying physical mechanisms

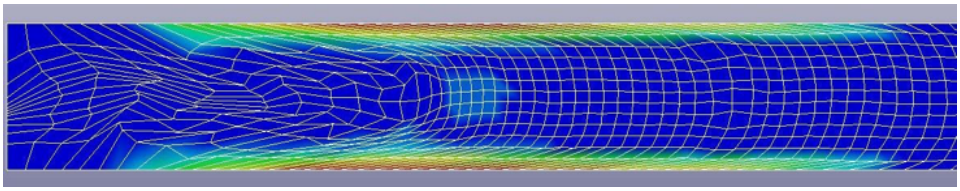

Figure 2.8: Contours of ignition parameter in PETN sample computed from simulation with rigid walls, with minimum (blue, darker) 0.0 and maximum (red) 352.0 (in boundary layers). The image shows a slice through the r–z plane at the fixed time 168 µs. Note the mesh distortion, particularly in the boundary layers. Image taken from [35], with permission.

at play. Consequently, there is a great need for analytical results to compliment and validate the numerical results. Some simple models of hot spot mechanisms include those of Curtis [33, 34], which study a rigid-plastic explosive subjected to pinch in a axisymmetric geometry, and shear in a planar geometry. Both models utilise simple material models, and ignore effects such as friction, so that substantial analytical progress can be made. These studies demonstrate the usefulness of simple models in adding to the understanding of ignition and HEVR.

2.4 Aims of thesis

The aim is to use asymptotic techniques to develop simplified models of a variety of hot spot mechanisms. The study of such models is motivated by two potential benefits: the formulation and solution of simplified models may be useful in providing test cases to validate the numerical solution; and the deeper understanding gained may help to inform the development of future numerical models. For instance, better knowledge of which hot spot mechanisms are important for ignition could lead to the inclusion of a more accurate, or sophisticated, ignition criterion for use in the HERMES model. As discussed in this chapter, explosive response to insults is incredibly complex, and a large number of potential hot spot mechanisms are suggested in the literature. In this thesis we will specifically develop models which aim to address the following:

(i) the effect of friction at the boundaries during pinch, with a particular focus on how this may generate boundary layers or similar localised heating;

(ii) localised shearing, either due to shear banding or other means of mechanical localisation;

(iii) viscous or plastic heating resulting from pinch and/or shear.

During the development of our models there will be a focus on the mechanical aspects of the problem. We will not be concerned with the modelling of thermal insults, and instead centre our attention on localised heating which results from mechanical insults.

Our primary motivation for studying hot spots in this manner is to add to the physical understanding of accidental ignitions due to insults. However, a possible further use of the type of simplified models we aim to develop would be as a sub-grid solution, so multiple length scales may be addressed in the hydrocode models. One such example of this is given in [20], where a physics-based multi-scale model of shear initiated reactions is developed. In this model it is assumed that within each sheared continuum cell there exists a shear band, located at the mid plane, thus allowing for the shear band behaviour on the order of microns to be captured on the continuum grid on the order of millimetres. It is hoped that the models developed in this thesis may inform the future generation of such sub-grid models, where appropriate.

Our main focus for the thesis will be on the explosive response to pinch, the onset and growth of reactive shear bands and the subsequent melting of a locally sheared explosive. The novel analytical progress we make extends simple models [e.g. 33, 33, 90], and primarily addresses the effects of friction and material heterogeneity, so that the localisation of heating can be observed and studied.

Chapter 3

A Rigid-Plastic Model for Explosive Pinch

It is well known that the pinching of an explosive between two flat surfaces can lead to initiation [33, 45]. However, the exact mechanisms by which this occurs are not well understood [59]. The large deformations which occur during pinching offer challenges to Lagrangian based hydrocode models, owing to severe mesh deformation [33, 35]. Further, it is difficult to obtain experimental data for this type of insult. As such, it is of interest to develop analytical models for the pinching of an explosive between two flat plates.

A novel *ad hoc* analytical method of the axial pinching of an explosive cylinder by two flat plates moving at constant speed is developed and discussed in [33]. In this formulation, it is assumed that as the material is compressed it is in perfect plastic flow under adiabatic conditions, and the explosive reaction is modelled using a simple Arrhenius Law. The heating of the explosive due to mechanical heating and self heating due to the reaction are calculated.

In the analysis presented in [33] there is no treatment of friction at the contact region between the plate and explosive. As a result of this simplification the dissipation calculated is constant throughout the sample. Sherwood and Durban [88] investigated the squeezing of a non-reactive viscoplastic solid in the presence of friction. In their paper a cylinder of height h is squeezed between two circular plates of radius R. It is assumed that the tangential stress at the contact between the plates and explosive is constant (a so-called "Tresca boundary condition" [44]) and is prescribed as some fixed fraction m of the yield stress of the material. A series solution is presented which exploits the small ratio of sample height to sample radius. This approach allows for the consideration of partial slip at the contact region, and therefore gives insight into the role of friction during the squeezing motion. It is suggested that their paper may form a strong basis to explore frictional effects in the configuration posed by Curtis [33]. In this chapter, motivated by our desire to understand the behaviour of explosive materials undergoing complex deformations, we develop a new model for

the pinching of an explosive between two rotating plates which move together at a constant speed. This model offers an extension to the model in [33] and solution in [88], both of which consider only a squeezing motion. Such combined deformations are likely to be more representative of the complex loadings which may be responsible for accidental ignition. This is achieved by application of a partial stress boundary condition, allowing for slip in both the radial and azimuthal directions. This type of boundary condition is typical of yield stress materials [44], and may be interpreted as a proxy for friction between the plates and the explosive material.

In Section 3.1 we describe the pinching configuration as set out in [88] with the addition of the rotating plates. Owing to the relatively simple rigid-plastic constitutive law, the mechanical and thermal problem decouple, allowing each part to be solved sequentially. The governing equations for the mechanical part of the problem are given in Section 3.2. In the case of negligible inertia we derive an asymptotic solution for the mechanical problem using the technique of Sherwood and Durban [88]. This allows for the mechanical dissipation within the explosive sample to be calculated analytically. We then account for inertial effects, and derive a set of two coupled partial differential equations for the corrections to the velocity components. Subsequently, the thermal problem is solved numerically in Section 3.3, and the effect of friction on the spatial distribution of the heating is considered.

3.1 Pinching configuration

We study the pinching of an explosive between two rotating flat plates, see Figure 3.1. A cylinder of explosive material with radius $\tilde{R}(\tilde{z},\tilde{t})$ is placed between two parallel plates. The plates at $\tilde{z}=\pm\tilde{h}/2$ approach one another with velocities $\mp V$, and rotate in opposite directions. It is assumed that V is constant. The axis of the cylinder coincides with the the $\tilde{z}$-axis and the full height of the sample at time $\tilde{t}$ is $\tilde{h}(\tilde{t})$. We consider the explosive sample to behave as a rigid-plastic, and impose a boundary condition on the shear stress, allowing slip to occur [88]. In reality the material behaviour of the explosive is more complex and it is likely elastic effects would need to be considered. However, the elastic modulus G of explosive materials such as HMX is typically on the order of 1–10 GPa compared with a yield stress in shear k on the order of 10–100 MPa [33, 72, 87, 93], so the rigid-plastic limit $G/k\to\infty$ provides a good approximation to the elastic-plastic behaviour [3, 72, 80, 101]. Following the work of Sherwood and Durban [88] we obtain a solution in the form of an expansion in $\tilde{h}/\tilde{r}$, where $\tilde{r}$ is the radial coordinate: such a solution is useful for $\tilde{r}$ large enough, but fails near the axis $\tilde{r}=0$.

As in [33, 88], it is assumed that the rigid-plastic solid has constant yield stress in shear $k=3^{-\frac{1}{2}}Y$, where Y is the compressive yield strength of the material. In order to account for partial-slip at the plates we apply boundary conditions on the shear stress, namely that the shear stresses in the radial and azimuthal directions

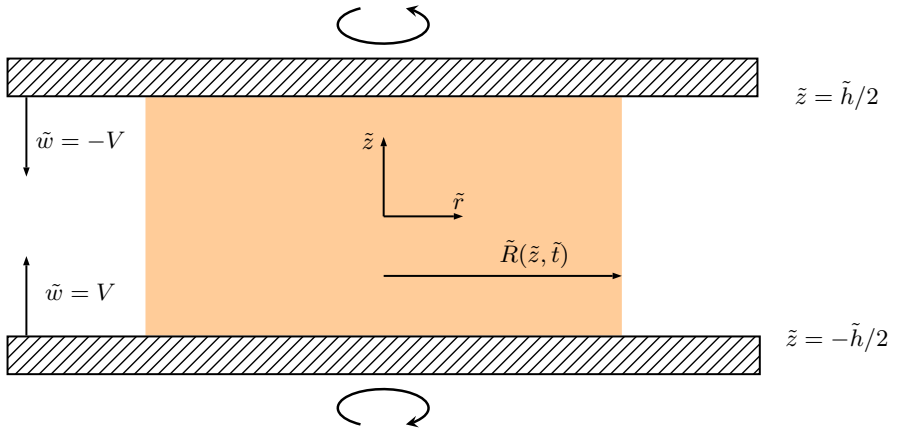

Figure 3.1: Schematic of the axial pinching of an explosive sample between two rotating flat plates.

are some fixed fraction – m and n, respectively – of the yield stress. In the case where the plates do not rotate ($n = 0$), the analysis is similar to Prandtl's cycloid solution (see [60] p. 232) for the plane two-dimensional compression of a rigid-plastic block between rough plates. For simplicity we impose the same stress fraction at both plates, so that the problem remains symmetric about the centre plane $\tilde{z} = 0$. However, the analysis could be extended to plates with differing stress fractions.

3.2 Rigid-Plastic analysis

In the absence of body forces the dimensional equations for continuity and momentum conservation in polar coordinates $(\tilde{r}, \tilde{\theta}, \tilde{z})$ are

$$\frac{1}{\tilde{r}}\frac{\partial(\tilde{r}\tilde{u})}{\partial\tilde{r}} + \frac{1}{\tilde{r}}\frac{\partial\tilde{v}}{\partial\tilde{\theta}} + \frac{\partial\tilde{w}}{\partial\tilde{z}} = 0, \tag{3.2.1}$$

$$\frac{\partial\tilde{\sigma}_{\tilde{r}\tilde{r}}}{\partial\tilde{r}} + \frac{1}{\tilde{r}}\frac{\partial\tilde{\sigma}_{\tilde{r}\tilde{\theta}}}{\partial\tilde{\theta}} + \frac{\partial\tilde{\sigma}_{\tilde{r}\tilde{z}}}{\partial\tilde{z}} + \frac{\tilde{\sigma}_{\tilde{r}\tilde{r}} - \tilde{\sigma}_{\tilde{\theta}\tilde{\theta}}}{\tilde{r}} = \rho\left(\frac{\partial\tilde{u}}{\partial\tilde{t}} + \tilde{u}\frac{\partial\tilde{u}}{\partial\tilde{r}} + \frac{\tilde{v}}{\tilde{r}}\frac{\partial\tilde{u}}{\partial\tilde{\theta}} - \frac{\tilde{v}^2}{\tilde{r}} + \tilde{w}\frac{\partial\tilde{u}}{\partial\tilde{z}}\right), \tag{3.2.2}$$

$$\frac{\partial\tilde{\sigma}_{\tilde{r}\tilde{\theta}}}{\partial\tilde{r}} + \frac{1}{\tilde{r}}\frac{\partial\tilde{\sigma}_{\tilde{\theta}\tilde{\theta}}}{\partial\tilde{\theta}} + \frac{\partial\tilde{\sigma}_{\tilde{\theta}\tilde{z}}}{\partial\tilde{z}} + 2\frac{\tilde{\sigma}_{\tilde{r}\tilde{\theta}}}{\tilde{r}} = \rho\left(\frac{\partial\tilde{v}}{\partial\tilde{t}} + \tilde{u}\frac{\partial\tilde{v}}{\partial\tilde{r}} + \frac{\tilde{v}}{\tilde{r}}\frac{\partial\tilde{v}}{\partial\tilde{\theta}} + \frac{\tilde{u}\tilde{v}}{\tilde{r}} + \tilde{w}\frac{\partial\tilde{v}}{\partial\tilde{z}}\right), \tag{3.2.3}$$

$$\frac{\partial\tilde{\sigma}_{\tilde{r}\tilde{z}}}{\partial\tilde{r}} + \frac{1}{\tilde{r}}\frac{\partial\tilde{\sigma}_{\tilde{\theta}\tilde{z}}}{\partial\tilde{\theta}} + \frac{\partial\tilde{\sigma}_{\tilde{z}\tilde{z}}}{\partial\tilde{z}} + \frac{\tilde{\sigma}_{\tilde{r}\tilde{z}}}{\tilde{r}} = \rho\left(\frac{\partial\tilde{w}}{\partial\tilde{t}} + \tilde{u}\frac{\partial\tilde{w}}{\partial\tilde{r}} + \frac{\tilde{v}}{\tilde{r}}\frac{\partial\tilde{w}}{\partial\tilde{\theta}} + \tilde{w}\frac{\partial\tilde{w}}{\partial\tilde{z}}\right), \tag{3.2.4}$$

where $\tilde{\sigma}_{ij}$ are the components of the stress tensor, ρ is the material density and $(\tilde{u}, \tilde{v}, \tilde{w})$ are the radial, azimuthal, and axial velocity components, respectively. Note that (3.2.2) implies that $\tilde{\sigma}_{\tilde{r}\tilde{r}} = \tilde{\sigma}_{\tilde{\theta}\tilde{\theta}}$ on the axis $\tilde{r} = 0$. The components of the plastic strain-rate $\tilde{\varepsilon}_{ij}$ are related to the velocity components in the usual way, written out explicitly as

$$\tilde{\varepsilon}_{\tilde{r}\tilde{r}} = \frac{\partial\tilde{u}}{\partial\tilde{r}}, \tag{3.2.5}$$

$$\tilde{\varepsilon}_{\tilde{\theta}\tilde{\theta}} = \frac{1}{\tilde{r}}\left(\frac{\partial \tilde{v}}{\partial \tilde{\theta}} + \tilde{u}\right), \tag{3.2.6}$$

$$\tilde{\varepsilon}_{\tilde{z}\tilde{z}} = \frac{\partial \tilde{w}}{\partial \tilde{z}}, \tag{3.2.7}$$

$$\tilde{\varepsilon}_{\tilde{r}\tilde{\theta}} = \frac{1}{2}\left(\frac{\partial \tilde{u}}{\partial \tilde{\theta}} + \frac{\partial \tilde{v}}{\partial \tilde{r}} - \frac{\tilde{v}}{\tilde{r}}\right), \tag{3.2.8}$$

$$\tilde{\varepsilon}_{\tilde{\theta}\tilde{z}} = \frac{1}{2}\left(\frac{\partial \tilde{v}}{\partial \tilde{z}} + \frac{\partial \tilde{w}}{\partial \tilde{\theta}}\right), \tag{3.2.9}$$

$$\tilde{\varepsilon}_{\tilde{r}\tilde{z}} = \frac{1}{2}\left(\frac{\partial \tilde{u}}{\partial \tilde{z}} + \frac{\partial \tilde{w}}{\partial \tilde{r}}\right). \tag{3.2.10}$$

It is assumed that the von-Mises yield criterion for plastic flow holds, given here in terms of the yield stress in shear k,

$$(\tilde{\sigma}_{\tilde{r}\tilde{r}} - \tilde{\sigma}_{\tilde{\theta}\tilde{\theta}})^2 + (\tilde{\sigma}_{\tilde{\theta}\tilde{\theta}} - \tilde{\sigma}_{\tilde{z}\tilde{z}})^2 + (\tilde{\sigma}_{\tilde{z}\tilde{z}} - \tilde{\sigma}_{\tilde{r}\tilde{r}})^2 + 6(\tilde{\sigma}^2_{\tilde{r}\tilde{\theta}} + \tilde{\sigma}^2_{\tilde{\theta}\tilde{z}} + \tilde{\sigma}^2_{\tilde{r}\tilde{z}}) = 6k^2. \tag{3.2.11}$$

The plastic strain-rate $\tilde{\varepsilon}_{ij}$ is then related to the deviatoric stress $\tilde{s}_{ij} = \tilde{\sigma}_{ij} - \frac{1}{3}\delta_{ij}\tilde{\sigma}_{kk}$ by the coaxiality relation

$$\tilde{\varepsilon}_{ij} = \tilde{\lambda}\tilde{s}_{ij}, \tag{3.2.12}$$

where the proportionality factor is given by

$$\tilde{\lambda} = \frac{(\tilde{\varepsilon}_{ij}\tilde{\varepsilon}_{ij})^{1/2}}{2^{1/2}k}. \tag{3.2.13}$$

The governing equations (3.2.1)–(3.2.13) should be supplemented by initial conditions, boundary conditions on the upper and lower plates, and free surface boundary conditions on the outer edge of the cylinder. These conditions will be discussed later.

In the absence of friction at the top and bottom plates, the governing equations (though not the initial conditions) are satisfied by a uniform straining motion

$$\tilde{u} = V\tilde{r}/\tilde{h}, \quad \tilde{v} = 0, \quad \tilde{w} = -2V\tilde{z}/\tilde{h}. \tag{3.2.14}$$

This solution satisfies the boundary condition $\hat{w} = \mp V$ on the upper and lower plates. In order to account for the effects of partial slip at the plates we impose a boundary condition of the form $\tilde{\sigma}_{\tilde{r}\tilde{z}} = \mp mk$, $\tilde{\sigma}_{\tilde{\theta}\tilde{z}} = nk$ at $\tilde{z} = \pm\tilde{h}/2$, where the stress fractions m and n vary from 0 to 1. From (3.2.11) it is found that we must satisfy the inequality $m^2 + n^2 < 1$. The case $m = 0 = n$ corresponds to free-slip at the plates. It is important to note the distinction between the stress boundary condition imposed here compared with a boundary condition on the velocity, particularly in the azimuthal direction. This boundary condition has the somewhat artificial physical interpretation that the plates are rotating in such a way as to impose a constant shear stress in the $\tilde{\theta}$–$\tilde{z}$ direction on the material. Such a condition may be difficult replicate exactly in experiments; nonetheless this condition allows for analytical

progress to be made and offers insight on how friction may affect the heating within the sample. In the case of no rotation ($n = 0$), the stress fraction m has the more intuitive physical interpretation that $m = 0$ corresponds to perfectly smooth plates, and $m = 1$ corresponds to perfectly rough plates. Although experiments which aim to replicate this type of boundary condition explicitly have not been conducted it is expected from a comparison with the literature [e.g. 83] that a moderate value of $m \approx 0.3$ would be typical. The advantages of this type of boundary condition in plastic and viscoplastic flow problems have been demonstrated in several studies [40, 41]. However, it is important to note that alternative boundary conditions may be more suitable, depending on the material used [44, 88].

We introduce the following non-dimensional variables

$$r = \tilde{r}/h_0, \quad z = \tilde{z}/h_0, \quad u = \tilde{u}/V, \quad v = \tilde{v}/V, \quad w = \tilde{w}/V,$$
$$t = \frac{V}{h_0}\tilde{t}, \quad \sigma_{ij} = \tilde{\sigma}_{ij}/Y, \quad \lambda = \frac{Yh_0}{V}\tilde{\lambda},$$

where h_0 is the initial sample height, V is the plate speed and Y is the compressive yield stress of the material. Note that in contrast to lubrication-type models we do not introduce disparate length scales (see [44] for a comprehensive review of the different approaches used in modelling squeeze flow type problems). However, we will later exploit the typically large aspect ratio, and identify the ratio of sample-height to sample-radius as a small parameter.

In terms of the dimensionless variables the incompressibility condition is

$$\frac{1}{r}\frac{\partial(ru)}{\partial r} + \frac{1}{r}\frac{\partial v}{\partial \theta} + \frac{\partial w}{\partial z} = 0, \tag{3.2.15}$$

and the momentum equations are

$$\frac{\partial \sigma_{rr}}{\partial r} + \frac{1}{r}\frac{\partial \sigma_{r\theta}}{\partial \theta} + \frac{\partial \sigma_{rz}}{\partial z} + \frac{\sigma_{rr} - \sigma_{\theta\theta}}{r} = \mathcal{R}\dot{u}, \tag{3.2.16}$$
$$\frac{\partial \sigma_{r\theta}}{\partial r} + \frac{1}{r}\frac{\partial \sigma_{\theta\theta}}{\partial \theta} + \frac{\partial \sigma_{\theta z}}{\partial z} + 2\frac{\sigma_{r\theta}}{r} = \mathcal{R}\dot{v}, \tag{3.2.17}$$
$$\frac{\partial \sigma_{rz}}{\partial r} + \frac{1}{r}\frac{\partial \sigma_{\theta z}}{\partial \theta} + \frac{\partial \sigma_{zz}}{\partial z} + \frac{\sigma_{rz}}{r} = \mathcal{R}\dot{w}, \tag{3.2.18}$$

where the dimensionless number $\mathcal{R} = \rho V^2/Y$ is the ratio of inertial effects to yield stress, and we have used an overdot to denote the material time derivative. Written out in full, the Levy-Mises equations relating strain-rate to stress are

$$\varepsilon_{rr} = \frac{\partial u}{\partial r} = \frac{\lambda}{3}(2\sigma_{rr} - \sigma_{\theta\theta} - \sigma_{zz}), \tag{3.2.19}$$
$$\varepsilon_{\theta\theta} = \frac{1}{r}\left(\frac{\partial v}{\partial \theta} + u\right) = \frac{\lambda}{3}(2\sigma_{\theta\theta} - \sigma_{rr} - \sigma_{zz}), \tag{3.2.20}$$
$$\varepsilon_{zz} = \frac{\partial w}{\partial z} = \frac{\lambda}{3}(2\sigma_{zz} - \sigma_{rr} - \sigma_{\theta\theta}), \tag{3.2.21}$$

$$\varepsilon_{r\theta} = \frac{1}{2}\left(\frac{\partial u}{\partial \theta} + \frac{\partial v}{\partial r} - \frac{v}{r}\right) = \lambda \sigma_{r\theta}, \tag{3.2.22}$$

$$\varepsilon_{\theta z} = \frac{1}{2}\left(\frac{\partial v}{\partial z} + \frac{\partial w}{\partial \theta}\right) = \lambda \sigma_{\theta z}, \tag{3.2.23}$$

$$\varepsilon_{rz} = \frac{1}{2}\left(\frac{\partial u}{\partial z} + \frac{\partial w}{\partial r}\right) = \lambda \sigma_{rz}. \tag{3.2.24}$$

Finally, we have the non-dimensional form of the von-Mises yield criterion

$$(\sigma_{rr} - \sigma_{\theta\theta})^2 + (\sigma_{\theta\theta} - \sigma_{zz})^2 + (\sigma_{zz} - \sigma_{rr})^2 + 6(\sigma_{r\theta}^2 + \sigma_{\theta z}^2 + \sigma_{rz}^2) = 2. \tag{3.2.25}$$

The governing equations (3.2.15)–(3.2.25) are to be solved subject to the boundary conditions

$$\sigma_{rz} = \mp 3^{-1/2} m, \quad \sigma_{\theta z} = 3^{-1/2} n \quad \text{and} \quad w = \mp 1 \quad \text{at} \quad z = \pm h/2, \tag{3.2.26}$$

on the upper and lower pates. Typically, the outer edge is taken to be stress free in squeeze flow type experiments [44]. The exact boundary condition used on the free surface will be discussed later, as will initial conditions when we consider the problem which accounts for inertia.

3.2.1 Negligible inertia solution

We first present the solution for the case of negligible inertia. Typically the yield stress of the materials considered is in the range 10–100 MPa, and their density is on the order of magnitude of $1000\,\mathrm{kg\,m^{-3}}$. Thus for a typical plate speed $V \sim 10\,\mathrm{m\,s^{-1}}$ we estimate $\mathcal{R} \sim O(10^{-2})$, and safely neglect the inertial terms in (3.2.16)–(3.2.18).

In order to satisfy the partial-slip boundary conditions on the plates we modify the uniform straining motion, and look for a velocity field of the form

$$u = \frac{r}{h} - h w_1'(z) - w_2'(z)\frac{h^2}{r} + \cdots, \tag{3.2.27}$$

$$v = v_0(z) + v_1(z)\frac{h}{r} + \cdots, \tag{3.2.28}$$

$$w = -\frac{2z}{h} + w_1(z)\frac{h}{r} + \cdots, \tag{3.2.29}$$

where the prime represents the derivative of a function of only one variable (here the w_i and v_i are functions of z only). Note the absence of an $O(r/h)$ term in our expansion for v. Such a term corresponds to the azimuthal velocity field obtained when a no-slip condition is applied on v at the plates, and dominates in the yield criterion, forcing $\sigma_{rz} = 0$ to leading order. Thus, the boundary condition (3.2.26) would not be satisfied for $m \neq 0$. We wish to consider the case where there is a combined squeezing and rotating motion which gives changes in σ_{rz} and $\sigma_{\theta z}$ at the same order in h/r. We therefore reject the possibility of an $O(r/h)$ term in v, this

being the most substantial difference between a typical no-slip condition and the constant shear stress boundary condition applied here.

The strain-rates corresponding to (3.2.27)–(3.2.29) are

$$\varepsilon_{rr} = \frac{1}{h} + w_2'(z)\frac{h^2}{r^2} + \cdots, \tag{3.2.30}$$

$$\varepsilon_{\theta\theta} = \frac{1}{h} - w_1'(z)\frac{h}{r} - w_2'(z)\frac{h^2}{r^2} + \cdots, \tag{3.2.31}$$

$$\varepsilon_{zz} = -\frac{2}{h} + w_1'(z)\frac{h}{r} + \cdots, \tag{3.2.32}$$

$$\varepsilon_{r\theta} = \frac{1}{2}\left[-\frac{1}{r}v_0(z) - 2\frac{h}{r^2}v_1(z) + \cdots\right], \tag{3.2.33}$$

$$\varepsilon_{\theta z} = \frac{1}{2}\left[v_0'(z) + \frac{h}{r}v_1'(z) + \cdots\right], \tag{3.2.34}$$

$$\varepsilon_{rz} = \frac{1}{2}\left[-hw_1''(z) - w_2''(z)\frac{h^2}{r} - w_1(z)\frac{h}{r^2} + \cdots\right]. \tag{3.2.35}$$

Subtracting the circumferential strain-rate (3.2.31) from the radial strain-rate (3.2.30), recalling the Levy-Mises relations (3.2.19) and (3.2.20), provides

$$\lambda(\sigma_{rr} - \sigma_{\theta\theta}) = w_1'(z)\frac{h}{r} + 2w_2'(z)\frac{h^2}{r^2}, \tag{3.2.36}$$

while the definition of the Levy-Mises proportionality factor gives

$$\lambda = 3^{1/2}\left[\frac{3}{h^2} + \frac{(hw_1'')^2}{4} + \frac{(v_0')^2}{4}\right]^{1/2} + O(h/r). \tag{3.2.37}$$

Substituting (3.2.37) into (3.2.36) we observe that the stress field is triaxial, i.e. $\sigma_{rr} = \sigma_{\theta\theta} \neq \sigma_{zz}$, to leading order. The Levy-Mises equations related to the axial and shear strain-rates, (3.2.21)–(3.2.24), now read

$$-\frac{1}{h} + \frac{hw_1'(z)}{2r} = \frac{\lambda}{3}(\sigma_{zz} - \sigma_{rr}) + \frac{\lambda}{6}(\sigma_{rr} - \sigma_{\theta\theta}), \tag{3.2.38}$$

and

$$-\frac{1}{r}v_0(z) - 2\frac{h}{r^2}v_1(z) = 2\lambda\sigma_{r\theta}, \tag{3.2.39}$$

$$v_0'(z) + \frac{h}{r}v_1'(z) = 2\lambda\sigma_{\theta z}, \tag{3.2.40}$$

$$-hw_1''(z) - \frac{h^2w_2''(z)}{r} - \frac{hw_1(z)}{r^2} = 2\lambda\sigma_{rz}, \tag{3.2.41}$$

respectively. Dropping terms $O(r^{-1})$ and smaller, the constitutive relations take the simplified forms

$$\frac{1}{h} = \frac{\lambda}{3}(\sigma_{rr} - \sigma_{zz}), \tag{3.2.42}$$

$$0 = \sigma_{r\theta}, \tag{3.2.43}$$

$$v_0'(z) = 2\lambda\sigma_{\theta z}, \tag{3.2.44}$$

$$-hw_1''(z) = 2\lambda\sigma_{rz}, \tag{3.2.45}$$

and the von-Mises criteria becomes

$$(\sigma_{zz} - \sigma_{rr})^2 + 3(\sigma_{rz}^2 + \sigma_{\theta z}^2) = 1. \tag{3.2.46}$$

We introduce the variable ψ so that the yield criterion is identically satisfied

$$\sigma_{rz}^2 + \sigma_{\theta z}^2 = \frac{1}{3}\sin^2\psi, \tag{3.2.47}$$

$$\sigma_{rr} - \sigma_{zz} = \cos\psi. \tag{3.2.48}$$

Eliminating λ from the above we obtain

$$\tan^2\psi = \frac{h^2}{3}\left[\frac{(hw_1'')^2}{4} + \frac{(v_0')^2}{4}\right]. \tag{3.2.49}$$

Substituting the shear stress into the radial momentum equation (3.2.16), and integrating with respect to r gives

$$\sigma_{rr} = -r\sigma_{rz}' + s(z), \tag{3.2.50}$$

where $s(z)$ is an unknown function of integration. This gives axial stress

$$\sigma_{zz} = -r\sigma_{rz}' + s(z) - \cos\psi, \tag{3.2.51}$$

which is substituted into (3.2.18) to give

$$-r\sigma_{rz}'' + s'(z) - (\cos\psi)' + \frac{\sigma_{rz}}{r} = 0. \tag{3.2.52}$$

For large r we may drop the last term in (3.2.52), and consider separately terms of $O(r/h)$ and $O(r/h)^0$, leading to two straightforward differential equations

$$\sigma_{rz}'' = 0, \tag{3.2.53}$$

$$s'(z) - (\cos\psi)' = 0. \tag{3.2.54}$$

It is assumed that the stress fractions m and n are identical on the two plates at $z = \pm h/2$. The problem is therefore symmetric about the centre plane $z = 0$, and the shear stress σ_{rz} is antisymmetric in z, with $\sigma_{rz} = \mp 3^{-1/2}m$ on $z = \pm h/2$. Integration of (3.2.53) readily gives

$$\sigma_{rz} = -\frac{2mz}{3^{1/2}h}. \tag{3.2.55}$$

By considering the momentum balance in the θ direction (3.2.17) we obtain the

simple differential equation

$$\sigma'_{\theta z} = 0, \tag{3.2.56}$$

which has solution $\sigma_{\theta z} = 3^{-1/2}n$. To find the unknown function $s(z)$ we note that the shear stress components σ_{rz} and $\sigma_{\theta z}$ may be substituted into (3.2.47) to give $\sin^2\psi$ explicitly in terms of z. This is then used to replace $\cos\psi$ in (3.2.54) with a known function of z. The result is then integrated directly to give

$$s(z) = (1 - n^2 - 4m^2z^2/h^2)^{1/2} + B, \tag{3.2.57}$$

where B is a constant of integration. The normal stress components now read

$$\sigma_{rr} = \sigma_{\theta\theta} = \frac{2mr}{3^{1/2}h} + (1 - n^2 - 4m^2z^2/h^2)^{1/2} + B, \tag{3.2.58}$$

$$\sigma_{zz} = \frac{2mr}{3^{1/2}h} + B. \tag{3.2.59}$$

In a squeeze-flow test, the outer boundary $r = R$ is usually stress free [44]. In the case $m = n = 0$ we may satisfy this exactly through the choice $B = -1$. However, for non-zero m and/or n it is impossible to satisfy this condition at $r = R$ exactly. It can be shown that for a thin sample, the boundary condition to be satisfied is the average condition

$$\int_{-h/2}^{h/2} \sigma_{rr}\,\mathrm{d}z = 0 \quad \text{at } r = R. \tag{3.2.60}$$

Such a condition is typical in squeeze flow problems (e.g. [44, 60]), and in this case requires

$$B = -\frac{1}{2}\left[(1 - m^2 - n^2)^{1/2} + \frac{1 - n^2}{m}\sin^{-1}\left(\frac{m}{(1 - n^2)^{1/2}}\right)\right] - \frac{2mR}{3^{1/2}h}.$$

Hence

$$\begin{aligned}\sigma_{zz} = &-\frac{2m}{3^{1/2}}\frac{(R - r)}{h} \\ &-\frac{1}{2}\left[(1 - m^2 - n^2)^{1/2} + \frac{1 - n^2}{m}\sin^{-1}\left(\frac{m}{(1 - n^2)^{1/2}}\right)\right],\end{aligned} \tag{3.2.61}$$

$$\sigma_{rr} = \sigma_{\theta\theta} = \sigma_{zz} + (1 - n^2 - 4m^2z^2/h^2)^{1/2}. \tag{3.2.62}$$

It now remains to find the corrections to the radial and azimuthal velocity components w_1 and v_0. From (3.2.45)

$$\begin{aligned}w_1''(z) &= -\frac{2}{h}\lambda\sigma_{rz}, \\ &= -\frac{2}{h}\left(3^{1/2}\left[\frac{3}{h^2} + \frac{(hw_1'')^2}{4} + \frac{(v_0')^2}{4}\right]^{1/2}\right)\left(-\frac{2mz}{3^{1/2}h}\right),\end{aligned}$$

$$= \frac{6}{3^{1/2}h^2}\frac{(\sin^2\psi - n^2)^{1/2}}{\cos\psi}, \tag{3.2.63}$$

where we have used the definition of $\tan^2\psi$, along with the relation

$$\left(\frac{2mz}{h}\right)^2 + n^2 = \sin^2\psi, \tag{3.2.64}$$

which comes from substituting the solutions for the shear stress components into (3.2.47). Integration of (3.2.63) gives

$$w_1'(z) = -\frac{3^{1/2}}{mh}(1 - n^2 - 4m^2z^2/h^2)^{1/2} + C, \tag{3.2.65}$$

and a further integration gives

$$w_1(z) = -\frac{3^{1/2}}{4m}\left[\frac{1-n^2}{m}\sin^{-1}\left(\frac{2mz}{h(1-n^2)^{1/2}}\right) + \frac{2z}{h}(1 - n^2 - 4m^2z^2/h^2)^{1/2}\right] + Cz + G, \tag{3.2.66}$$

where the constants C and G are chosen to make $w_1 = 0$ on $z = \pm h/2$:

$$G = 0,$$
$$C = \frac{3^{1/2}}{2mh}\left[(1 - n^2 - m^2)^{1/2} + \frac{1-n^2}{m}\sin^{-1}\left(\frac{m}{(1-n^2)^{1/2}}\right)\right].$$

Now, we find v_0. From (3.2.44)

$$v_0'(z) = 2\lambda\sigma_{\theta z} = \frac{6n}{3^{1/2}h}\frac{1}{\cos\psi}, \tag{3.2.67}$$

which integrates to give

$$v_0(z) = \frac{3^{1/2}n}{m}\sin^{-1}\left(\frac{2mz}{h(1-n^2)^{1/2}}\right), \tag{3.2.68}$$

where we have used the condition $v_0(0) = 0$.

The velocity components read

$$u = \frac{r}{h} + \frac{3^{1/2}}{m}(1 - n^2 - 4m^2z^2/h^2)^{1/2} - \frac{3^{1/2}}{2m}\left[(1 - n^2 - m^2)^{1/2} + \frac{1-n^2}{m}\sin^{-1}\left(\frac{m}{(1-n^2)^{1/2}}\right)\right] + O(h/r), \tag{3.2.69}$$

$$v = \frac{3^{1/2}n}{m}\sin^{-1}\left(\frac{2mz}{h(1-n^2)^{1/2}}\right) + O(h/r), \tag{3.2.70}$$

$$w = -\frac{2z}{h} - \frac{3^{1/2}h}{4mr}\left[\frac{1-n^2}{m}\sin^{-1}\left(\frac{2mz}{h(1-n^2)^{1/2}}\right) + \frac{2z}{h}(1 - n^2 - 4m^2z^2/h^2)^{1/2}\right]$$

$$+\frac{3^{1/2}z}{2mr}\left[(1-n^2-m^2)^{1/2}+\frac{1-n^2}{m}\sin^{-1}\left(\frac{m}{(1-n^2)^{1/2}}\right)\right]+O((h/r)^2). \tag{3.2.71}$$

Note that the radial velocity on $z=\pm h/2$ is

$$u=\frac{r}{h}-\frac{3^{1/2}}{2m}\left[(1-n^2-m^2)^{1/2}+\frac{1-n^2}{m}\sin^{-1}\left(\frac{m}{(1-n^2)^{1/2}}\right)\right]+O(h/r), \tag{3.2.72}$$

and it is observed that slip occurs at the walls, even when $m=1$ and $n=0$ (i.e. in the case of the pinching of a material between two perfectly rough plates).

For $m^2+n^2=1$ the first two terms of (3.2.72) predict negative wall velocities for $r/h<3^{1/2}\pi/4$, and the next term in the expansion does not change this. Physically it is expected that the slip at the plates is opposed by the constant shear stresses (3.2.26). As a result, we must conclude that the solution gives unphysical results when r/h is sufficiently small. In [88] the analysis with $n=0$ is continued to the next order in the expansion. However, this does not resolve the issue of predicted negative velocities at the plates.

Figure 3.2 shows the corrections to the radial and azimuthal velocity components. As expected, increasing m results in a reduction in the radial velocity adjacent to the plates, with a corresponding increase in radial velocity towards the centreline $z=0$. In contrast, increasing n corresponds to an increase in the boundary shear stress in the θ–z direction, i.e. an increase in the rotating motion. As such we see an increase in the azimuthal velocity adjacent to the plates with increasing n. By symmetry, the azimuthal velocity (and its correction) must be zero along the centreline $z=0$.

The rate of dissipation of mechanical energy is calculated to be

$$\begin{aligned}\Phi&=\varepsilon_{ij}\sigma_{ij}=\varepsilon_{rr}\sigma_{rr}+\varepsilon_{\theta\theta}\sigma_{\theta\theta}+\varepsilon_{zz}\sigma_{zz}+2\varepsilon_{rz}\sigma_{rz}+2\varepsilon_{\theta z}\sigma_{\theta z},\\&=\left(1-n^2-4m^2z^2/h^2\right)^{1/2}\left(\frac{2}{h}-w_1'\frac{h}{r}\right)\\&\quad+\left(\frac{8m^2z^2}{3^{1/2}h^2}+\frac{2n^2}{3^{1/2}}\right)\left[\frac{3}{h^2}+\frac{(hw_1'')^2}{4}+\frac{(v_0')^2}{4}\right]^{1/2}.\end{aligned} \tag{3.2.73}$$

Interestingly, the effect on the mechanical heating due to application of the constant shear stress boundary condition $\sigma_{rz}=\mp 3^{-1/2}m$ is confined to a region relatively near to the plates, whereas application of the constant shear stress boundary condition $\sigma_{\theta z}=3^{-1/2}n$ has a more significant effect on the heating in the bulk of the material, as seen in Figure 3.3. As m is increased with $n=0.3$ held fixed, see Figure 3.3 (a), we observe additional heating due to mechanical dissipation adjacent to the plates, but the dissipation remains unchanged around $z=0$. However, as n is increased with $m=0.3$ held fixed, see Figure 3.3 (b), the heating due to mechanical dissipation increases throughout the sample.

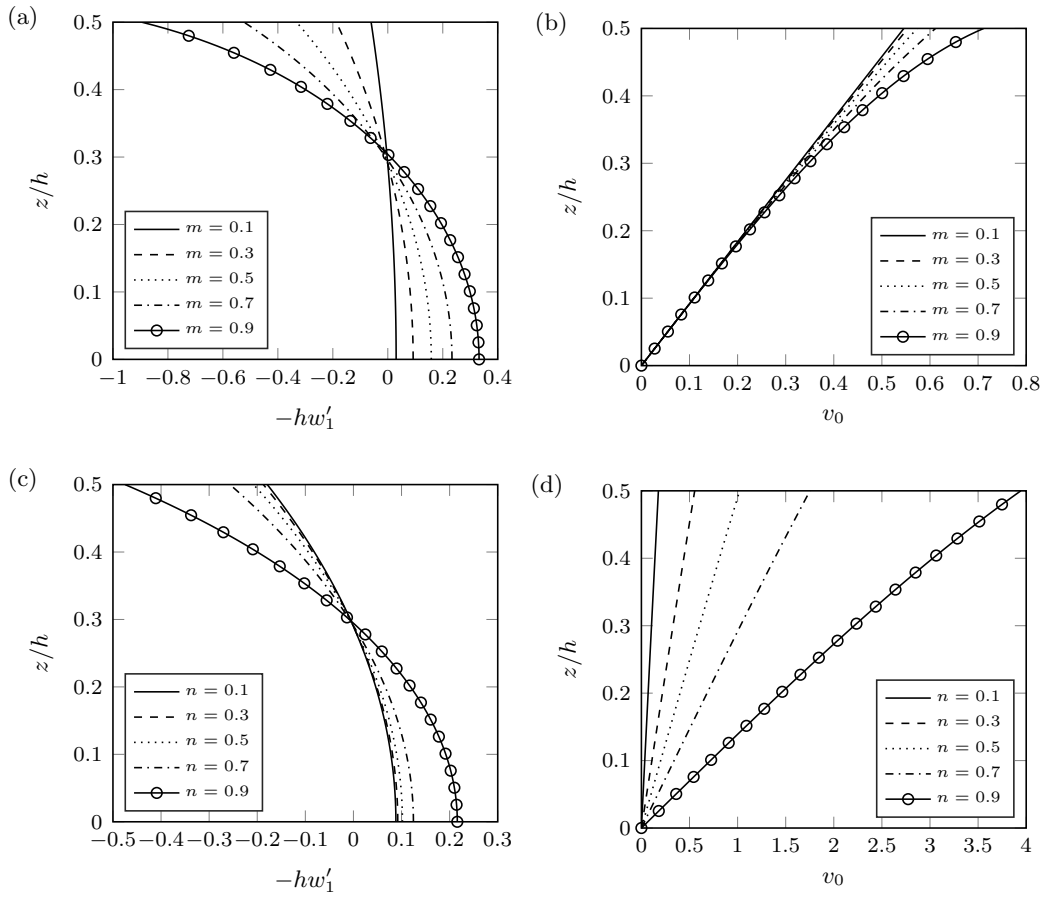

Figure 3.2: Corrections to the non-dimensional radial (a,c) and azimuthal (b,d) velocity components as a function of z/h for: (a,b) various m, $n = 0.3$; and (c,d) $m = 0.3$, various n.

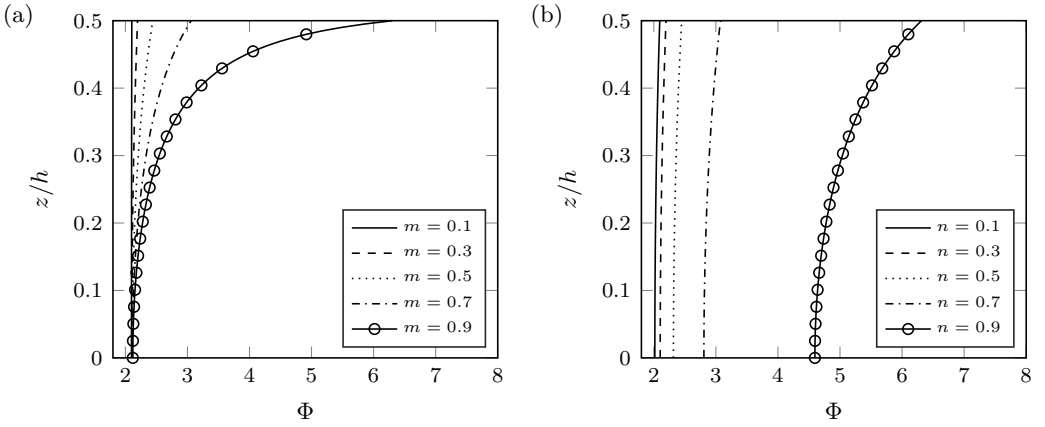

Figure 3.3: The non-dimensional mechanical dissipation as a function of z/h for: (a) various m, $n = 0.3$; and (b) $m = 0.3$, various n.

In the limit $m, n \to 0$ we find the mechanical dissipation may be expanded as

$$\Phi = \frac{2}{h} + \frac{3^{1/2}m}{6r}(1 - 12z^2/h^2) + \frac{2n}{h} + \cdots , \tag{3.2.74}$$

and we see that the contribution arising from the boundary condition on $\sigma_{\theta z}$ is spatially independent, whereas the contribution arising from the boundary condition on σ_{rz} is a function of z. It is interesting to note that as $m \to 0$ we actually see a decrease in dissipation near the plates, unlike for moderate m (approximately $m > 0.1$) for which the dissipation is increased near the plates. The dissipation has the unphysical behaviour of being singular as $h \to 0$. Such a singularity would be removed by considering compressibility effects which would prevent full pinch from occurring.

3.2.2 Inertial effects

We now consider the effects of retaining the inertial terms in the momentum equations (3.2.16)–(3.2.18). As in the previous section, we look for a correction to the velocity field similar to (3.2.27)–(3.2.29). However, the correction functions may now depend explicitly on time so that we write

$$u = \frac{r}{h(t)} - h(t)\frac{\partial w_1}{\partial z}(z,t) - \frac{\partial w_2}{\partial z}(z,t)\frac{(h(t))^2}{r} + \cdots , \tag{3.2.75}$$

$$v = v_0(z,t) + v_1(z,t)\frac{h(t)}{r} + \cdots , \tag{3.2.76}$$

$$w = -\frac{2z}{h(t)} + w_1(z,t)\frac{h(t)}{r} + \cdots . \tag{3.2.77}$$

The analysis proceeds in the same way, and the simplified relations (3.2.42)–(3.2.45) still hold, but with partial derivatives in z replacing the ordinary derivatives. This gives

$$\frac{1}{h} = \frac{\lambda}{3}(\sigma_{rr} - \sigma_{zz}), \tag{3.2.78}$$

$$0 = \sigma_{r\theta}, \tag{3.2.79}$$

$$\frac{\partial v_0}{\partial z} = 2\lambda\sigma_{\theta z}, \tag{3.2.80}$$

$$-h\frac{\partial^2 w_1}{\partial z^2} = 2\lambda\sigma_{rz}, \tag{3.2.81}$$

$$(\sigma_{zz} - \sigma_{rr})^2 + 3(\sigma_{rz}^2 + \sigma_{\theta z}^2) = 1, \tag{3.2.82}$$

to leading order in h/r. As in Section 3.2.1, we introduce the function ψ, satisfying equations (3.2.47) and (3.2.48). Substitution of the shear stress and velocity components into the radial momentum equation and integrating with respect to r

gives

$$\sigma_{rr}+r\frac{\partial\sigma_{rz}}{\partial z}=\mathcal{R}\left(\frac{3r^2}{2h^2}+r\frac{\partial w_1}{\partial z}+2rz\frac{\partial^2 w_1}{\partial z^2}-rh\frac{\partial^2 w_1}{\partial z\partial t}\right)+s(z,t)+O(h/r). \quad (3.2.83)$$

By equation (3.2.48) we find the axial stress

$$\sigma_{zz}=-r\frac{\partial\sigma_{rz}}{\partial z}+\mathcal{R}\left(\frac{3r^2}{2h^2}+r\frac{\partial w_1}{\partial z}+2rz\frac{\partial^2 w_1}{\partial z^2}-rh\frac{\partial^2 w_1}{\partial z\partial t}\right)+s(z,t)-\cos\psi, \quad (3.2.84)$$

correct up to leading order in h/r. Substituting the normal stress σ_{zz} into (3.2.18) we find

$$\begin{aligned}-r\frac{\partial^2\sigma_{rz}}{\partial z^2}+\mathcal{R}\left(r\frac{\partial^2 w_1}{\partial z^2}+2r\frac{\partial^3 w_1}{\partial z^3}+2rz\frac{\partial^2 w_1}{\partial z^2}-rh\frac{\partial^3 w_1}{\partial z^2\partial t}\right)\\ +\frac{\partial}{\partial z}\left(s(z,t)-\cos\psi\right)=0. \quad (3.2.85)\end{aligned}$$

Considering separately terms in $O(r/h)$ and $O(r/h)^0$, we obtain two partial differential equations

$$-\frac{\partial^2\sigma_{rz}}{\partial z^2}+\mathcal{R}\left(\frac{\partial^2 w_1}{\partial z^2}+2\frac{\partial^3 w_1}{\partial z^3}+2z\frac{\partial^2 w_1}{\partial z^2}-h\frac{\partial^3 w_1}{\partial z^2\partial t}\right)=0, \quad (3.2.86)$$

$$\frac{\partial}{\partial z}\left(s(z,t)-\cos\psi\right)=0, \quad (3.2.87)$$

the second of which may be integrated directly to give $s(z,t)=\cos\psi+c_1(t)$. From the azimuthal momentum equation (3.2.17) we find

$$\frac{\partial\sigma_{\theta z}}{\partial z}=\mathcal{R}\left(\frac{\partial v_0}{\partial t}+\frac{v_0}{h}-\frac{2z}{h}\frac{\partial v_0}{\partial z}\right)+O(h/r). \quad (3.2.88)$$

By (3.2.80) and (3.2.81), the stress components may be eliminated from the governing differential equations (3.2.86) and (3.2.88), giving

$$\frac{\partial w_1}{\partial t}=\frac{1}{2\mathcal{R}}\frac{1}{\lambda}\frac{\partial^2 w_1}{\partial z^2}+\frac{2z}{h}\frac{\partial w_1}{\partial z}-\frac{1}{h}w_1+c_2(t)z+c_3(t), \quad (3.2.89)$$

$$\frac{\partial v_0}{\partial t}=\frac{1}{2\mathcal{R}}\frac{\partial}{\partial z}\left(\frac{1}{\lambda}\frac{\partial v_0}{\partial z}\right)-\frac{v_0}{h}+\frac{2z}{h}\frac{\partial v_0}{\partial z}, \quad (3.2.90)$$

where the functions $c_2(t)$ and $c_3(t)$, which come from integrating (3.2.86) twice with respect to z, are fixed using the boundary condition $w_1(\pm h/2,t)=0$, and λ is given by (3.2.37). The partial-slip boundary conditions on the shear stress components may be recast in terms of the velocity corrections as

$$\frac{\partial w_1}{\partial z}=-\frac{1}{2\mathcal{R}}\frac{1}{\lambda}\frac{2\sqrt{3}}{h^2}(1-m^2-n^2)^{-1/2}m, \quad \text{and} \quad \frac{\partial v_0}{\partial z}=\frac{2\sqrt{3}}{h}(1-m^2-n^2)^{-1/2}n, \quad (3.2.91)$$

at $z = \pm h/2$. Equations (3.2.89)–(3.2.90) are supplemented by the initial conditions

$$w_1(t=0) = 0 \quad \text{and} \quad v_0(t=0) = 0, \tag{3.2.92}$$

which states that the velocity corrections are initially zero. Owing to the small ratio of sample-height to sample-radius, the largest contribution to the inertial effects comes from the rapid radial velocity.

To allow for convenient numerical solution of (3.2.89)–(3.2.90) we introduce the variable $\hat{z} = z/h$, which maps the problem onto the fixed spatial domain $-1/2 \leq \hat{z} \leq 1/2$ (see Appendix A). In terms of the new computational variables the equations read

$$\frac{\partial w_1}{\partial t} = \frac{1}{2h^2\mathcal{R}}\frac{1}{\lambda}\frac{\partial^2 w_1}{\partial \hat{z}^2} + 2\hat{z}\left(\frac{1}{h}-1\right)\frac{\partial w_1}{\partial \hat{z}} - \frac{1}{h}w_1 + c_2(t)\hat{z}h + c_3(t), \tag{3.2.93}$$

$$\frac{\partial v_0}{\partial t} = \frac{1}{2h^2\mathcal{R}}\frac{\partial}{\partial \hat{z}}\left(\frac{1}{\lambda}\frac{\partial v_0}{\partial \hat{z}}\right) - \frac{v_0}{h} + 2\hat{z}\left(\frac{1}{h}-1\right)\frac{\partial v_0}{\partial \hat{z}}, \tag{3.2.94}$$

with the time dependent functions $c_2(t)$ and $c_3(t)$ given by

$$c_2(t) = \frac{1}{h}\left\{-\frac{2m}{\sqrt{3}h\mathcal{R}} + \left(1-\frac{1}{h}\right)\left(\left.\frac{\partial w_1}{\partial \hat{z}}\right|_{\hat{z}=1/2} + \left.\frac{\partial w_1}{\partial \hat{z}}\right|_{\hat{z}=-1/2}\right)\right\}, \tag{3.2.95}$$

$$c_3(t) = \frac{1}{2}\left(1-\frac{1}{h}\right)\left(\left.\frac{\partial w_1}{\partial \hat{z}}\right|_{\hat{z}=1/2} - \left.\frac{\partial w_1}{\partial \hat{z}}\right|_{\hat{z}=-1/2}\right), \tag{3.2.96}$$

to ensure the boundary condition $w_1(\hat{z} = 1/2, t) = 0$ is satisfied. In the transformed coordinates the partial-slip boundary conditions are

$$\frac{\partial w_1}{\partial \hat{z}} = -\frac{1}{2\mathcal{R}}\frac{1}{\lambda}2\sqrt{3}(1-m^2-n^2)^{-1/2}m, \quad \text{and} \quad \frac{\partial v_0}{\partial \hat{z}} = 2\sqrt{3}(1-m^2-n^2)^{-1/2}n, \tag{3.2.97}$$

at $\hat{z} = \pm 1/2$. The spatial derivatives in (3.2.93)–(3.2.94) are discretised using second-order finite differences, and marched forward in time using an adaptive Runge-Kutta scheme. Once the velocity corrections w_1 and v_0 have been computed the mechanical dissipation may be calculated semi-analytically, here in terms of the original z, as

$$\Phi = (1-3\sigma_{rz}^2-3\sigma_{\theta z}^2)^{1/2}\left(\frac{2}{h} - \frac{\partial w_1}{\partial z}\frac{h}{r}\right) + \frac{6}{h}(1-3\sigma_{rz}^2-3\sigma_{\theta z}^2)^{-1/2}\left(\sigma_{rz}^2+\sigma_{\theta z}^2\right), \tag{3.2.98}$$

with the stress components given by (3.2.80) and (3.2.81). The normal stress components may be recovered using (3.2.83) and (3.2.84) to calculate the radial and axial stress components, respectively. The unknown function $c_1(t)$ introduced by integration of (3.2.87) may be fixed by again imposing the condition that the outer boundary in the squeeze flow is stress free (on average).

Figures 3.4–3.7 show the numerically computed corrections to the radial and axial

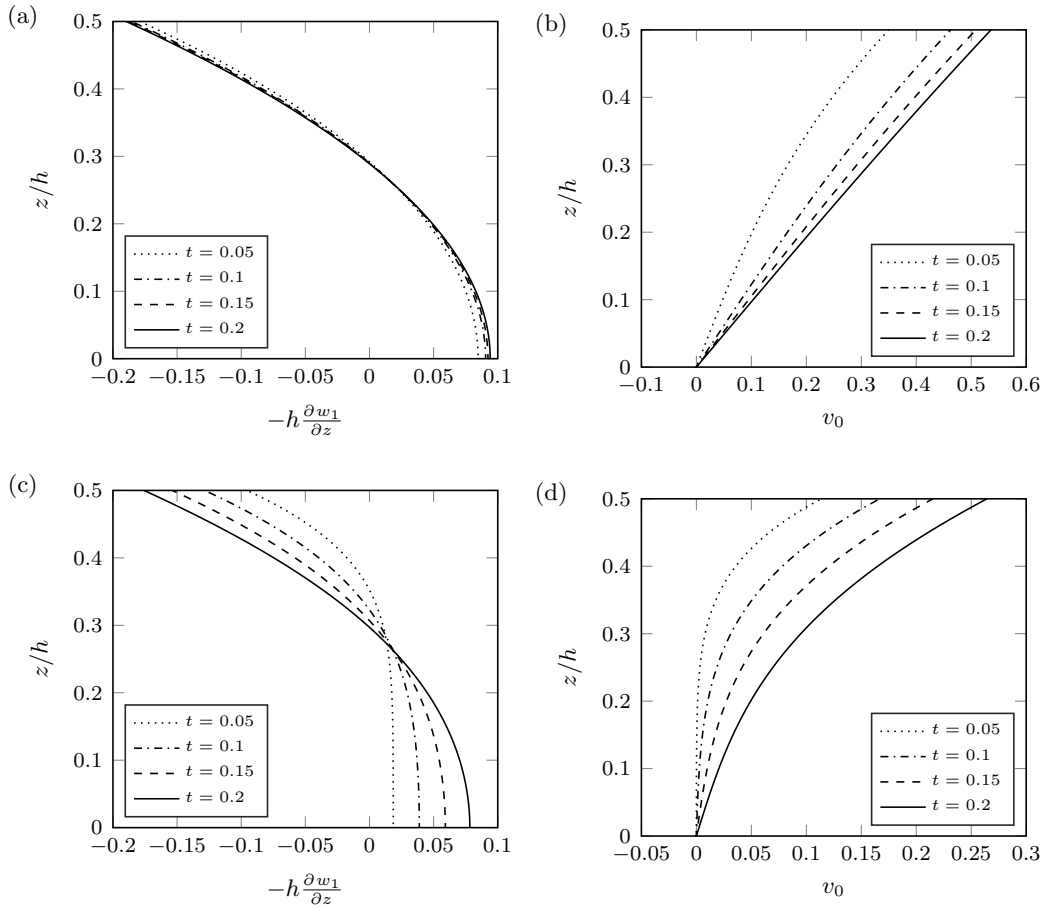

Figure 3.4: Corrections to the non-dimensional radial (a,c) and azimuthal (b,d) velocity components as a function of z/h, with fixed $m = 0.3 = n$, for: (a,b) $\mathcal{R} = 0.1$; and (c,d) $\mathcal{R} = 1$. Plots are shown at non-dimensional times $t = 0.05, 0.1, 0.15, 0.2$. Full pinch is achieved at $t = 0.5$.

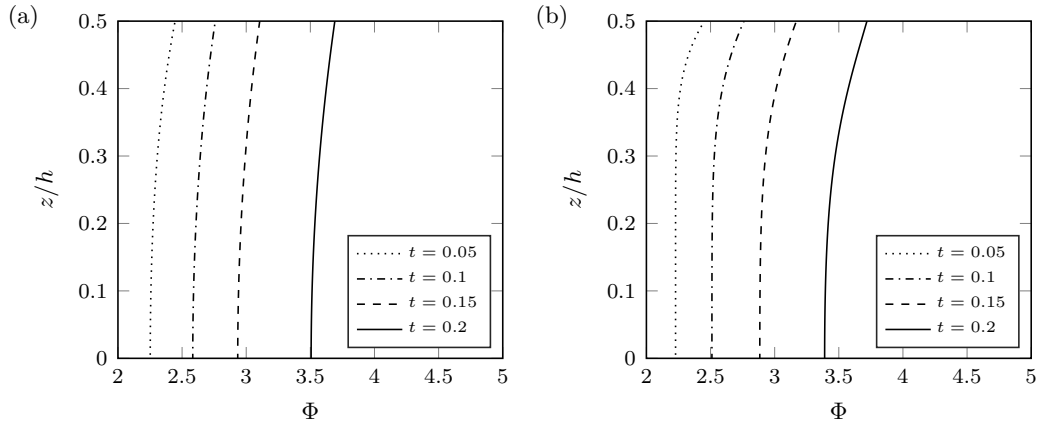

Figure 3.5: The non-dimensional mechanical dissipation as a function of z/h, with fixed $m = 0.3 = n$, for: (a) $\mathcal{R} = 0.1$; and (b) $\mathcal{R} = 1$. Plots are shown at non-dimensional times $t = 0.05, 0.1, 0.15, 0.2$. Full pinch is achieved at $t = 0.5$.

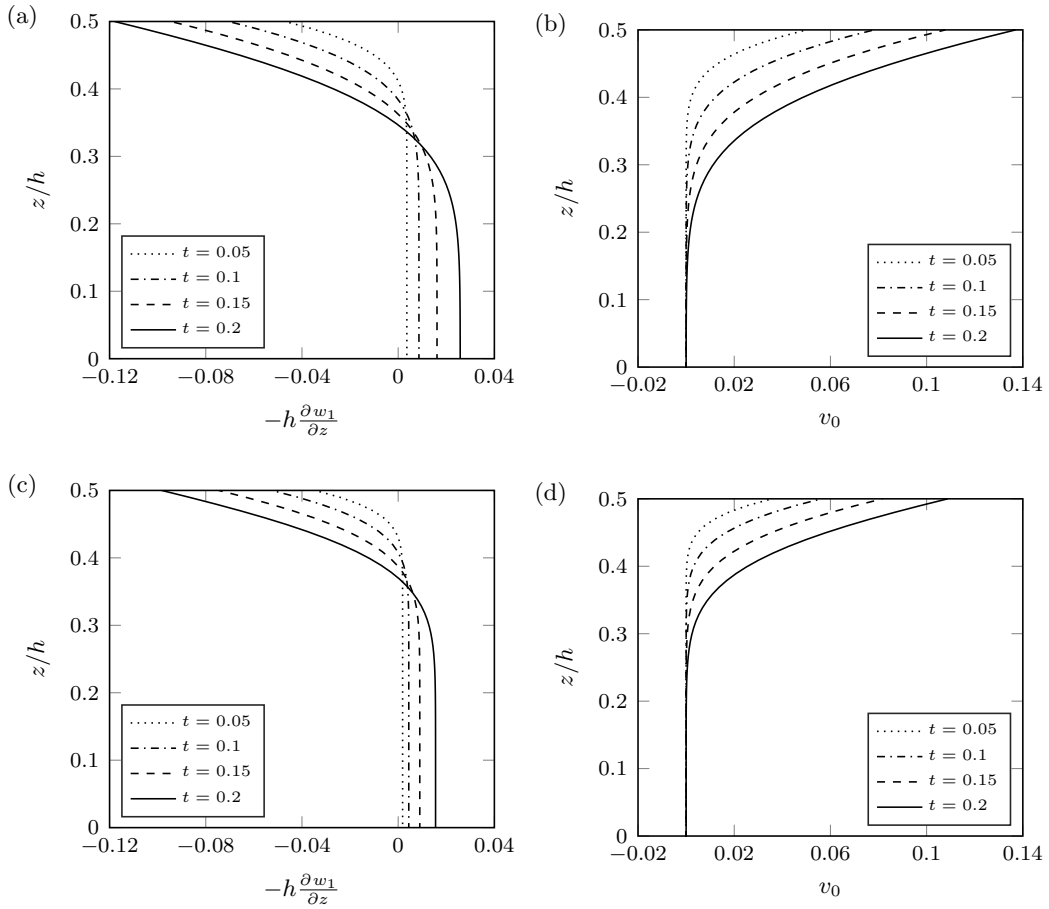

Figure 3.6: Corrections to the non-dimensional radial (a,c) and azimuthal (b,d) velocity components as a function of z/h, with fixed $m = 0.3 = n$, for: (a,b) $\mathcal{R} = 5$; and (c,d) $\mathcal{R} = 10$. Plots are shown at non-dimensional times $t = 0.05, 0.1, 0.15, 0.2$. Full pinch is achieved at $t = 0.5$.

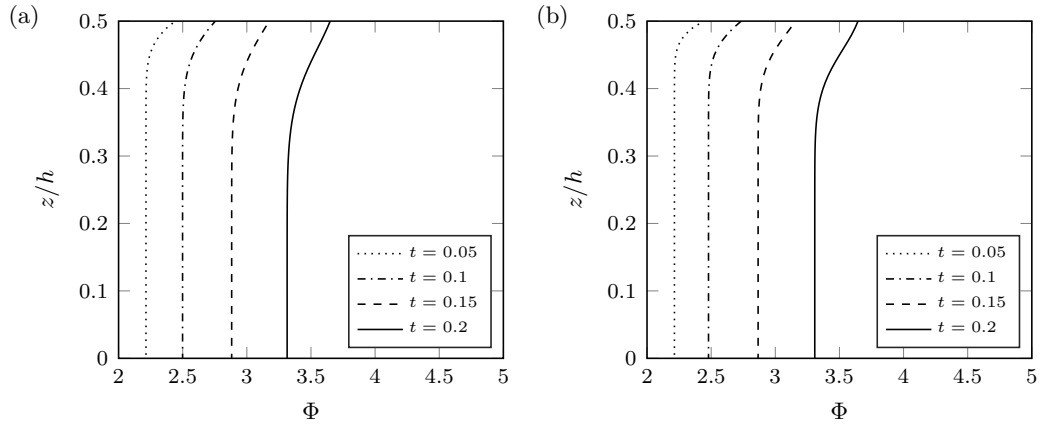

Figure 3.7: The non-dimensional mechanical dissipation as a function of z/h, with fixed $m = 0.3 = n$, for: (a) $\mathcal{R} = 5$; and (b) $\mathcal{R} = 10$. Plots are shown at non-dimensional times $t = 0.05, 0.1, 0.15, 0.2$. Full pinch is achieved at $t = 0.5$.

velocity components, as well as the dissipation, as functions of z/h for various values of $\mathcal{R}$. For small values of $\mathcal{R}$ we observe a parabolic profile to the radial velocity correction, as in the quasi-steady case. As time is increased with $\mathcal{R}$ small the correction to the azimuthal velocity approaches the linear profile predicted by the analysis with $\mathcal{R} = 0$. However, as $\mathcal{R}$ is increased, to say $\mathcal{R} \approx 5$, we observe that both the radial and azimuthal velocity corrections are initially approximately constant across the sample, except in a region near the plates. As $\mathcal{R}$ is increased further the inertial effects become more important, and the size of the region in which the velocity correction changes from the constant value in the bulk to the value at the wall is decreased. Over time, the viscous effect near the plates penetrates towards the centre, and the region over which the radial (azimuthal) velocity correction increases (decreases) to the value in the bulk increases in size, eventually relaxing towards the parabolic profile. As a result of this viscous boundary layer type behaviour, we find a region of increased mechanical dissipation near the plates. This extra heating near the plates due to inertia is in addition to the heating caused by the partial slip boundary condition.

3.3 Thermal model

In this section we solve the thermal part of the problem. Since the localised heating is driven by the mechanical heating, we restrict our full numerical solution of the thermal part of the problem to the negligible inertia case. This allows us to see how the mechanical heating drives localised reactions, and the conclusions of the numerical solution may be easily extended to problem which includes inertial effects by comparing the form of the mechanical dissipation found in Sections 3.2.1 and 3.2.2. Further, for the materials of interest in this study it is found that $\mathcal{R} \sim O(10^{-2})$, so we are typically in a regime where the analytical results for the velocities, stresses and dissipation calculated in Section 3.2.1 are relevant. The initial dimensional temperature $\tilde{T}_0$ of the explosive is specified, and the temperature $\tilde{T}(\tilde{r}, \tilde{z}, \tilde{t})$ increases due to mechanical dissipation and subsequent chemical reaction. To model the reaction, we employ a single step Arrhenius reaction expressed in terms of the (dimensionless) mass fraction α of gaseous products by

$$\dot{\alpha} = \frac{\partial \alpha}{\partial \tilde{t}} + \tilde{u}\frac{\partial \alpha}{\partial \tilde{r}} + \frac{\tilde{v}}{\tilde{r}}\frac{\partial \alpha}{\partial \tilde{\theta}} + \tilde{w}\frac{\partial \alpha}{\partial \tilde{z}} = A(1-\alpha)\exp\left(-\frac{E}{R\tilde{T}}\right), \tag{3.3.1}$$

where A is the dimensional pre-exponential factor, E is the activation energy and R is the molar gas constant. The temperature growth is governed by the equation of conservation of energy

$$\rho c\dot{\tilde{T}} = \rho c\left(\frac{\partial \tilde{T}}{\partial \tilde{t}} + \tilde{u}\frac{\partial \tilde{T}}{\partial \tilde{r}} + \frac{\tilde{v}}{\tilde{r}}\frac{\partial \tilde{T}}{\partial \tilde{\theta}} + \tilde{w}\frac{\partial \tilde{T}}{\partial \tilde{z}}\right) = \kappa\tilde{\nabla}^2\tilde{T} + \tilde{\Phi} + \rho\Omega\dot{\alpha}, \tag{3.3.2}$$

where c is the specific heat at constant volume, κ is the thermal conductivity, Ω is the specific heat of the reaction described by (3.3.1), and $\tilde{\Phi}$ is the dimensional rate of mechanical dissipation. Note that due symmetry in the azimuthal direction, the θ derivatives in (3.3.1) and (3.3.2) are zero. To non-dimensionalise the thermal part of the problem we scale the temperature by a typical temperature difference ΔT and scale the pre-exponential factor, which has units s^{-1}, using the timescale given by the ratio of the initial sample height to the velocity h_0/V. Recall that the mass fraction α is already dimensionless.

In non-dimensional variables the Arrhenius and energy equation read

$$\dot{\alpha} = \hat{A}(1-\alpha)\exp\left(-\frac{\hat{E}}{T}\right), \tag{3.3.3}$$

and

$$\dot{T} = \frac{1}{\mathrm{Pe}}\nabla^2 T + \frac{\mathrm{Ec}}{\mathcal{R}}\Phi + \hat{\Omega}\dot{\alpha}, \tag{3.3.4}$$

respectively. Here we have introduced the non-dimensional constants $\hat{A} = Ah_0/V$, $\hat{E} = E/R(\Delta T)$ and $\hat{\Omega} = \Omega/(c\,\Delta T)$, which are the counterparts of the pre-exponential factor, activation energy and heat of reaction, respectively. We have also introduced two dimensionless groupings: the Eckert number

$$\mathrm{Ec} = \frac{V^2}{c\,\Delta T}, \tag{3.3.5}$$

which characterises the dissipation; and the Péclet number

$$\mathrm{Pe} = \frac{h_0 V}{\kappa/\rho c}, \tag{3.3.6}$$

which is the ratio of the advective transport rate to the diffusive transport rate. Alternatively, the Péclet number may be recognised as the product of the generalised Reynolds number and the Prandtl number, i.e. $\mathrm{Pe} = \mathcal{R}\,\mathrm{Pr}$, where $\mathrm{Pr} = c(Yh_0/V)/\kappa$ is the ratio of momentum diffusion to thermal diffusivity. Similarly, the product of the Eckert and Prandtl number may be recognised as the Brinkman number, $\mathrm{Br} = \mathrm{Ec}\,\mathrm{Pr}$, which is the ratio of heat production by viscous dissipation to the heat transport by conduction. The thermal conductivity of polymer bonded explosives is found to be in the range $0.1 < \kappa < 0.6\ \mathrm{W\,m^{-1}\,K^{-1}}$ [10], so we estimate the Péclet number to be $O(10^8)$, and thus neglect the effects of diffusion in the following analysis.

3.4 Numerical solution

For ease of computation we write (3.3.3) and (3.3.4) in terms of the computational variables $(\hat{r}, \hat{z})$ using the formulas for the derivatives given in Appendix A. This

recovers a fixed grid, on which we solve the equations

$$\frac{\partial\hat{\alpha}}{\partial t}+\frac{\hat{r}}{\hat{R}}\left[\frac{\hat{u}}{\hat{r}}-\frac{\partial\hat{R}}{\partial t}+\frac{1}{h}\left(\frac{\mathrm{d}h}{\mathrm{d}t}\hat{z}-\hat{w}\right)\frac{\partial R}{\partial\hat{z}}\right]\frac{\partial\hat{\alpha}}{\partial\hat{r}}+\frac{1}{h}\left[\hat{w}-\frac{\mathrm{d}h}{\mathrm{d}t}\hat{z}\right]\frac{\partial\hat{\alpha}}{\partial\hat{z}}$$
$$=\hat{A}(1-\hat{\alpha})\exp\left(-\frac{\hat{E}}{\hat{T}}\right), \tag{3.4.1}$$

and

$$\frac{\partial\hat{T}}{\partial t}+\frac{\hat{r}}{\hat{R}}\left[\frac{\hat{u}}{\hat{r}}-\frac{\partial\hat{R}}{\partial t}+\frac{1}{h}\left(\frac{\mathrm{d}h}{\mathrm{d}t}\hat{z}-\hat{w}\right)\frac{\partial R}{\partial\hat{z}}\right]\frac{\partial\hat{T}}{\partial\hat{r}}+\frac{1}{h}\left[\hat{w}-\frac{\mathrm{d}h}{\mathrm{d}t}\hat{z}\right]\frac{\partial\hat{T}}{\partial\hat{z}}$$
$$=\frac{\mathrm{Ec}}{\mathcal{R}}\hat{\Phi}+\hat{\Omega}\dot{\hat{\alpha}}, \tag{3.4.2}$$

for the mass fraction and temperature, respectively.

Equations (3.4.1) and (3.4.2) are solved numerically using a Crank-Nicolson (C-N) scheme. Since the material properties are assumed independent of temperature, the shape of the free surface $\hat{R}(\hat{z},t)$ has been computed ahead of time and stored for use at each time step of the C-N routine. At each time step the velocities and mechanical dissipation are updated to account for the deformation of the explosive sample. Since thermal runaway commences much before α approaches 1 (the theoretical point at which 100% of the sample converted to gaseous products), it is reasonable to assume there is always plenty of material to react. In running the simulations, it is found that the variation in α is very small throughout the explosive sample up until the time at which thermal runaway has commenced.

It was assumed that the upper and lower surfaces of the explosive were insulated, as well as the outer surface. Perhaps a more realistic condition at the contact region between the sample and plates would be a source term corresponding to frictional heating. However, an insulated condition will allow us to observe what effect varying the stress fractions m and n has on the heating due to mechanical dissipation. A source term will only serve to exacerbate any additional heating that is observed at the walls due to the relaxation of the perfect slip condition. To obtain an estimate of the size of the frictional heating term, denoted q_{f}, we use the formula given by [28], which states that the surface heat flux is determined by the frictional shear stress s_{f} and the relative velocity between the two interfaces v_{rel}:

$$q_{\mathrm{f}}=c_{\mathrm{f}}\cdot|s_{\mathrm{f}}|\cdot|v_{\mathrm{rel}}|. \tag{3.4.3}$$

Note that this gives a heat source term per unit area, unlike the mechanical dissipation and Arrhenius reaction, which are given per unit volume in (3.3.2). In this definition,

c_f is the fraction of frictional heat flux into the explosive, and is given by

$$c_\mathrm{f} = \frac{\sqrt{(\kappa\rho c)_E}}{\sqrt{(\kappa\rho c)_E} + (\kappa\rho c)_P}, \tag{3.4.4}$$

where subscripts E and P refer to the explosive and plate, respectively. Using the values in Table 3.1 for HMX, a representative temperature of 600 K, and scalings consistent with the typical values used to obtain our non-dimensional variables we find the following order of magnitude estimates for the heat source terms corresponding to friction, mechanical dissipation and reaction, respectively:

$$\begin{aligned} q_\mathrm{f} \sim c_\mathrm{f} Y V \sim 10^5\,\mathrm{W\,m^{-2}}, \quad q_\mathrm{D} \sim \frac{YV}{h_0} \sim 10^{10}\,\mathrm{W\,m^{-3}}, \\ q_\mathrm{R} \sim \rho\Omega A \exp\left(-\frac{E}{R\cdot 660\,\mathrm{K}}\right) \sim 10^{10}\,\mathrm{W\,m^{-3}}. \end{aligned} \tag{3.4.5}$$

In the calculation of c_f we have assumed that the plates are made of steel to represent the base plate in the Steven test, with material properties $\kappa = 50\,\mathrm{W\,m^{-1}\,K^{-1}}$, $\rho = 8000\,\mathrm{kg\,m^{-3}}$ and $c = 500\,\mathrm{J\,kg^{-1}\,K^{-1}}$.

At $r = 0$ the symmetry of the problem suggests that the normal derivative of the temperature vanishes on the axis. However, it is noted that our series expansion in h/r breaks down near $r = 0$, so in order to avoid singularities the computational domain is restricted to $\hat{r}_\mathrm{min} \le \hat{r} \le 1$, where $\hat{r}_\mathrm{min} = 3^{1/2}(\pi/4)(h_0/R_0)$ is chosen to ensure that the radial velocity remains positive at the upper and lower contact regions, regardless of the choice of stress fraction. Here h_0 and R_0 denote the initial sample height and radius respectively. Note that we may obtain a solution in a greater area of the sample for larger aspect ratios, for example with an aspect ratio of 10, and using the simulation parameters in Table 3.2, the minimum radial coordinate is $\hat{r}_{min} = 0.1360$. This allows for solution in a reasonably large portion of the explosive sample. Future work may look to obtain a solution for small r/h which would match on to the solution provided here, and allow the full sample to be modelled. Here we apply the no flux condition on the temperature at $\hat{r} = \hat{r}_\mathrm{min}$. The condition applied at $\hat{r}_\mathrm{min}$ is unrealistic since we expect heat transfer between the computational domain and the neglected inner core region. An alternative would be to apply an isothermal condition at $\hat{r}_\mathrm{min}$. This could be motivated by the possible existence of an unyielded core region in which no heating due to plastic work takes place [44]. In the following Section results with both boundary conditions at the core will be presented and compared. Regardless of the boundary condition used the results sufficiently far away from the centre of the explosive sample should still provide insight into the physical problem. In the formulation the diffusion of temperature was neglected, so any extreme or erroneous temperatures calculated near $\hat{r} = 0$ should have a minimal effect on the solution away from the axis.

The computation can proceed if we choose $\hat{r}_\mathrm{min}$ to be smaller than the value given

Explosive Property	HMX-based	Ex-MS
Activation Energy E /J mol^{-1}	2.2×10^5	1.966×10^5
Molar Gas Constant R /J mol^{-1} K^{-1}	8.314	8.314
Pre-Exponential Constant A /s^{-1}	$5.011872336 \times 10^{19}$	$6.309573445 \times 10^{19}$
Density ρ /kg m^{-3}	1800	1700
Specific Heat c /J kg^{-1} K^{-1}	1255.2	1090.0
Heat of Reaction Ω /J kg^{-1}	5.02×10^6	6.38×10^6
Dynamic Compressive Strength Y /MPa	16	200

Table 3.1: Material properties for a HMX-based explosive and Ex-MS [33].

above and, as expected, doing so has no discernible effect on the solution away from $\hat{r} = 0$. With a reduced $\hat{r}_{\min}$ we observe an area of significant heating in the centre of the explosive sample and reduced heating where the unphysical negative velocities are predicted near the plates. This region of particularly high heating near the centre may be unphysical and therefore give incorrect predictions regarding the time to runaway.

3.5 Results

The partial-slip model outlined in the previous sections has been used to simulate two explosives: a HMX-based PBX and a more sensitive formulation, Ex-MS, whose properties are given in Table 3.1. The Ex-MS is more sensitive than HMX, but the explosive properties are all of a similar order of magnitude. For instance, Ex-MS has a lower activation energy of 1.966×10^5 J mol^{-1} compared with 2.2×10^5 J mol^{-1} for HMX, but both are $O(10^5)$. Many of the mechanical properties are also of a similar order of magnitude, and both materials have a similar thermal mass ($\rho c \approx 2 \times 10^6$ for both the HMX and Ex-MS). However, the compressive strength of Ex-MS is 200 MPa compared with just 16 MPa for HMX. This is the most significant difference between the two materials and, since the dissipation scales with the yield stress, we predict that heating due to mechanical dissipation of the Ex-MS will be 10 times that of the HMX. Subsequently, the Ex-MS can reach the critical temperature required for reaction more easily than the HMX during the pinching deformation. The initial sample width was chosen to be wider than typically used in drop-weight experiments in order to maximise the size of the computational domain. The simulation parameters are given in Table 3.2.

The results for the two explosives differ greatly. For the Ex-MS it was found that either the temperature invariably exceeded the stopping temperature 1000 K or the rate of temperature increase due to reaction become so rapid that the minimum timestep was reached before the sample become fully pinched. However, for HMX the response was much less violent, with a relatively modest increase in temperature during the pinching process. Figure 3.8 (Figure 3.9) shows the maximum dimensional

Simulation Parameter	Value
Impact Speed V /m s^{-1}	10-50
Initial Height of Explosive Cylinder h_0 /mm	25.4
Initial Radius of Explosive Cylinder R_0 /mm	254
Start Time t_0 /s	0
Initial Temperature T_0 /K	298-523

Table 3.2: Simulation parameters used for the pinch model.

temperature rise $\tilde{T}_{\max}$ in Ex-MS and HMX as a function of time for fixed $n = 0.3$ ($m = 0.3$) and various values of m (n). It is clear to observe that even in the early stages of the process the Ex-MS is heating rapidly when compared with the HMX.

The free-slip model [33] indicated that the temperature rise of Ex-MS became dominated by the reaction at a greater range of initial temperature compared with the HMX-based explosive. In the simulations for the HMX based explosive it was found that the main source of heating during the pinching process was mechanical dissipation, except when the initial temperature was increased to 523 K. For lower initial temperatures it was found that the HMX became fully pinched with only a small amount of material reacted. In contrast, it was found that for Ex-MS there was always a time at which the reaction became the dominant heat source. Figure 3.10 shows the height at which the reaction first became the dominant heat source for Ex-MS. The partial-slip model presented here shows good agreement with the model of Curtis as $m, n \to 0$ for Ex-MS. As the stress fractions are increased there is additional heating due to mechanical dissipation, which drives a more rapid reaction. As a result we find that the reaction dominates sooner as the stress fractions are increased. In the simulations for HMX the partial-slip model predicted that the dominant heating source was dissipation, even as the initial temperature was increased to 523 K. The rapid rise in temperature in the HMX at around 508 microseconds is due to the singular form of the dissipation as $h \to 0$.

As expected, increasing m and n causes the temperature to rise more rapidly. For a fixed n we see that varying m between 0 and 0.5 leads to a relatively modest decrease in time to runaway. However, as m is increased further the time to runaway decreases dramatically, see Figure 3.8. When m is held fixed we see that increasing n has a more noticeable effect on the time to runaway, especially for Ex-MS, see Figure 3.9. Perhaps the most interesting comparison to draw comes from considering how varying m and n affects the spatial distribution of the temperature throughout the sample, as shown in Figure 3.11. Panels (a,c,e) show heatmaps in the $\hat{r}$–$\hat{z}$ plane for: $m = 0.3 = n$; $m = 0.9$, $n = 0.3$; and $m = 0.3$, $n = 0.9$, respectively. Panels (b,d,e) show vertical slices through the heatmaps at fixed $\hat{r} = 0.6$ at a series of increasing times. For moderate m and n, panels (a) and (b), we observe a slight increase in temperature near the plates, becoming more pronounced as the reaction progresses. When we increase m to 0.9, panels (c) and (d), we observe an area of

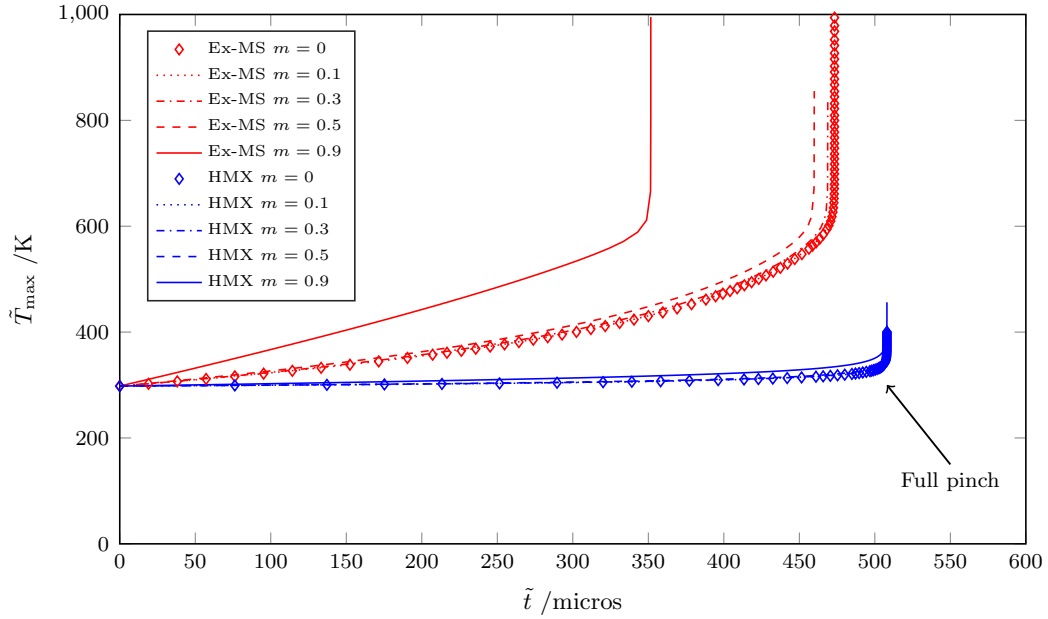

Figure 3.8: Maximum dimensional temperature rise $\tilde{T}_{\max}$ in Ex-MS (red) and HMX (blue) subject to a plate speed $V = 25\mathrm{m\,s^{-1}}$ for fixed $n = 0.3$ and various values of m.

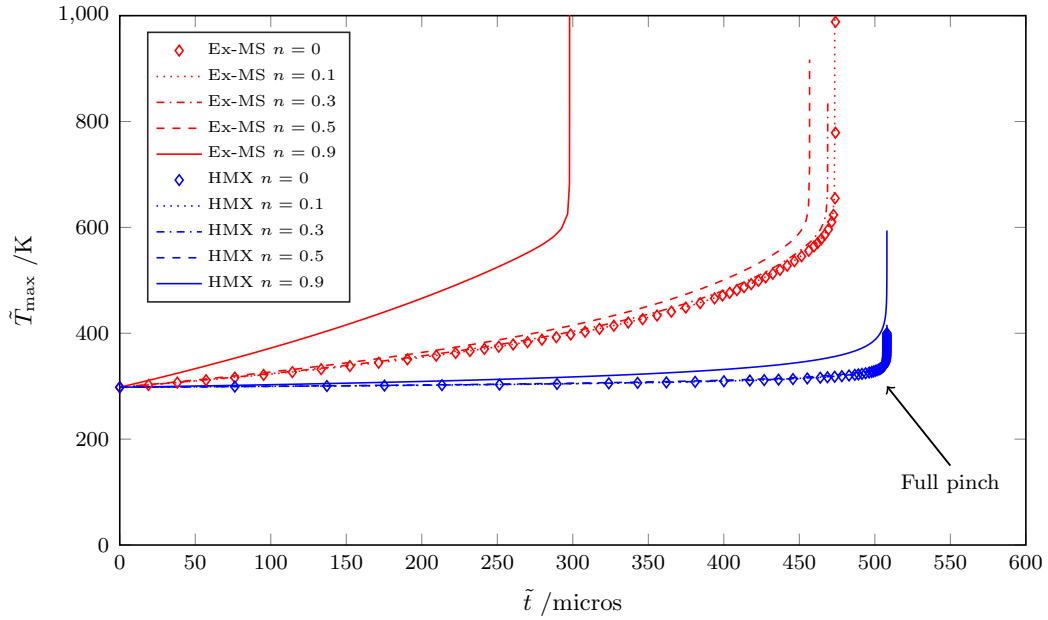

Figure 3.9: Maximum dimensional temperature rise $\tilde{T}_{\max}$ in Ex-MS (red) and HMX (blue) subject to a plate speed $V = 25\mathrm{m\,s^{-1}}$ for fixed $m = 0.3$ and various values of n.

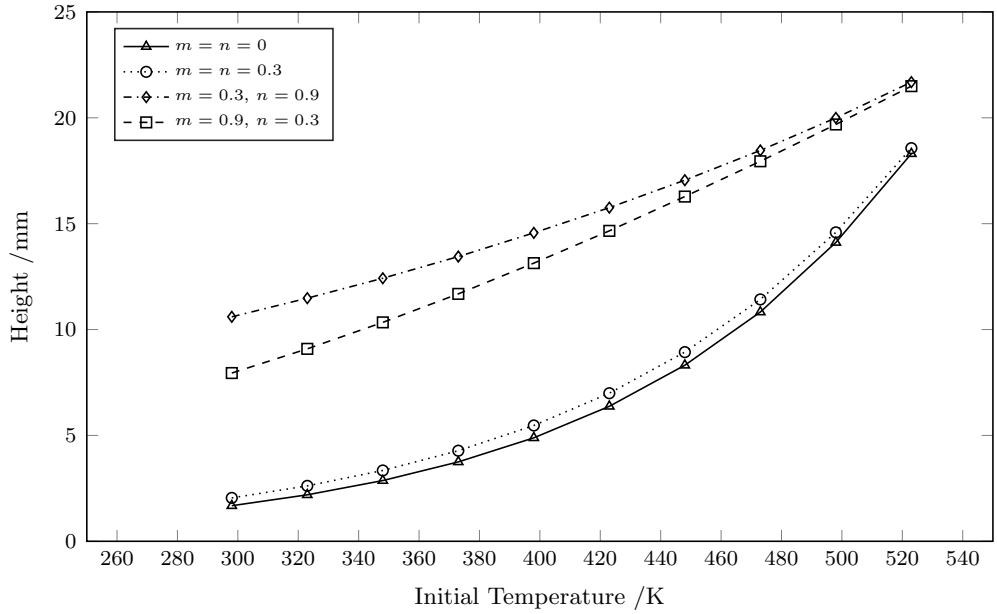

Figure 3.10: Height at which heating by reaction first dominates heating by mechanical dissipation for Ex-MS. The figure shown results from this study for Ex-MS with: $m = n = 0.3$; $m = 0.3$, $n = 0.9$; and $m = 0.9$, $n = 0.3$. For comparison results from the free-slip model [33] are shown.

localised temperature increase adjacent to the plates, with the temperature difference between the plates and centreline exceeding 150 K at a time of 95% to runaway. In contrast, we see that when we increase n to 0.9, panels (e) and (f), the temperature gradient in the $\hat{z}$ direction is much smaller, i.e. we see that the heating is distributed more evenly throughout the sample. In this case the temperature difference between the plates and centreline at a time of 95% to runaway is around 75 K, half that observed in the case of increased m. Figure 3.12 shows the same results but with an isothermal boundary condition at $\hat{r}_{\min}$. The results are shown at exactly the same times as in Figure 3.11, and we observe that while there is an obvious difference in the temperature adjacent to the core region, there is no noticeable difference in the solution away from the core. In fact, when looking at the vertical temperature profiles taken at $\hat{r} = 0.6$ the results with the adiabatic and isothermal boundary conditions are indistinguishable, and we conclude that our choice of boundary condition at the core has little effect on our solution in the bulk of the material.

Figure 3.13 shows contours of the time to ignition in microseconds for Ex-MS n the m-n plane. For moderate values of m and n the contours are roughly circular, and the effect on the ignition time is similar for increases in either stress fraction. However, for larger values the time to ignition decreases more rapidly with increasing n compared to increasing m, as can be seen from the asymmetry in the contours.

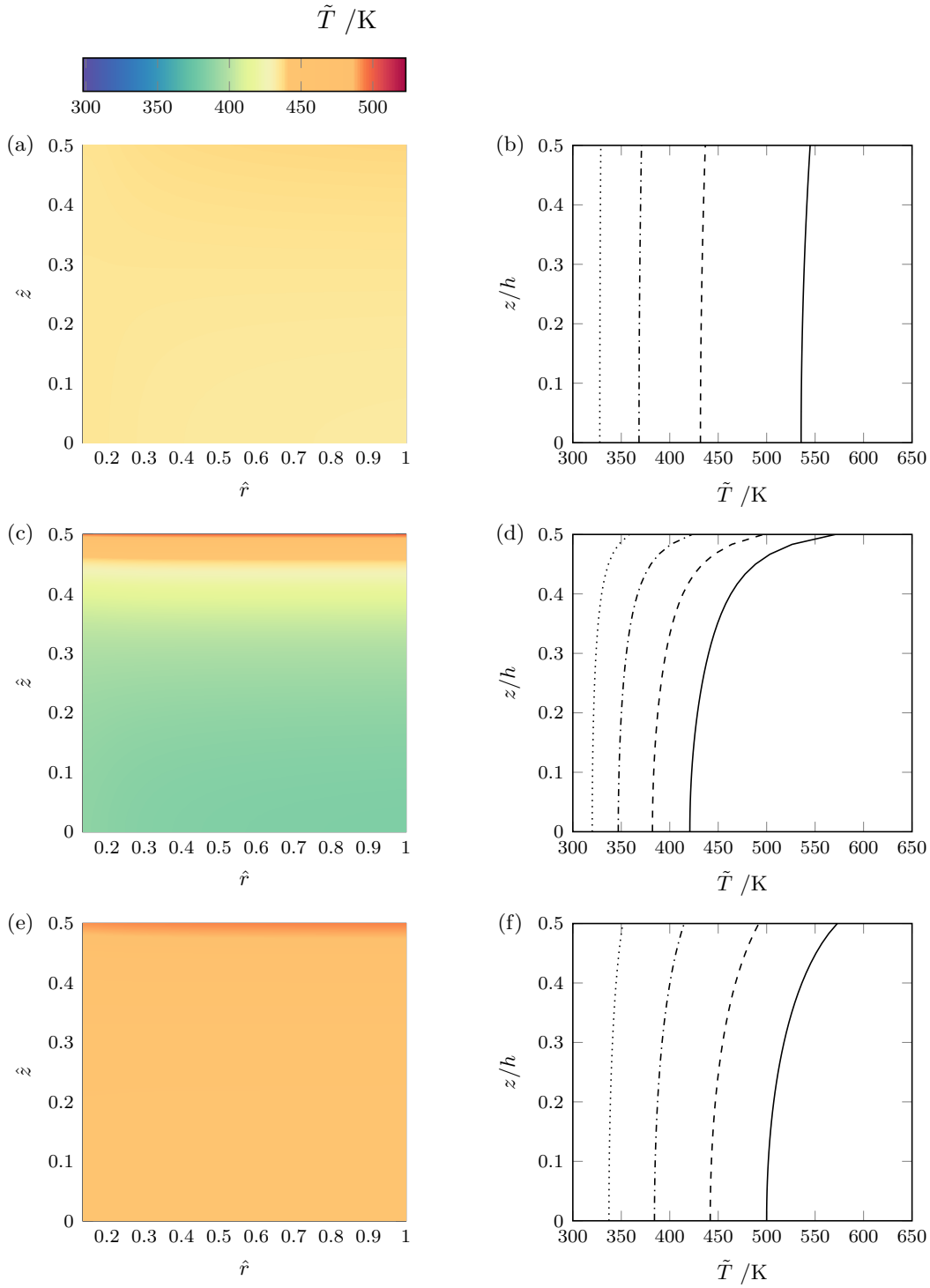

Figure 3.11: Left panels show the dimensional temperature $\tilde{T}$ in the $\hat{r}$–$\hat{z}$ plane for Ex-MS at 75% of time to runaway, corresponding to dimensional times: (a) $\tilde{t} = 351$ micro s; (c) $\tilde{t} = 254$ micro s; and (e) $\tilde{t} = 223$ micro s. Right panels show the dimensional temperature as a function of $\hat{z}$ at fixed $\hat{r} = 0.6$ for times $t = 25\%$, 50%, 75% and 95% of time to runaway, corresponding to dimensional times: (b) $\tilde{t} = 117$, 234, 351, 445 micro s; (d) $\tilde{t} = 88$, 176, 254, 334 micro s; and (f) $\tilde{t} = 74$, 149, 223, 283 micro s . The values of m and n used were: (a,b) $m = 0.3 = n$; (c,d) $m = 0.9$, $n = 0.3$; and (e,f) $m = 0.3$, $n = 0.9$. Note that in order to allow useful comparison between results with different values of stress fractions the same colourbar has been used for the plots in (a,c,e). As a result it appears that panel (a) shows a constant temperature throughout the sample. However, there is a slight increase in temperature with increasing z, as more readily observed in panel (b).

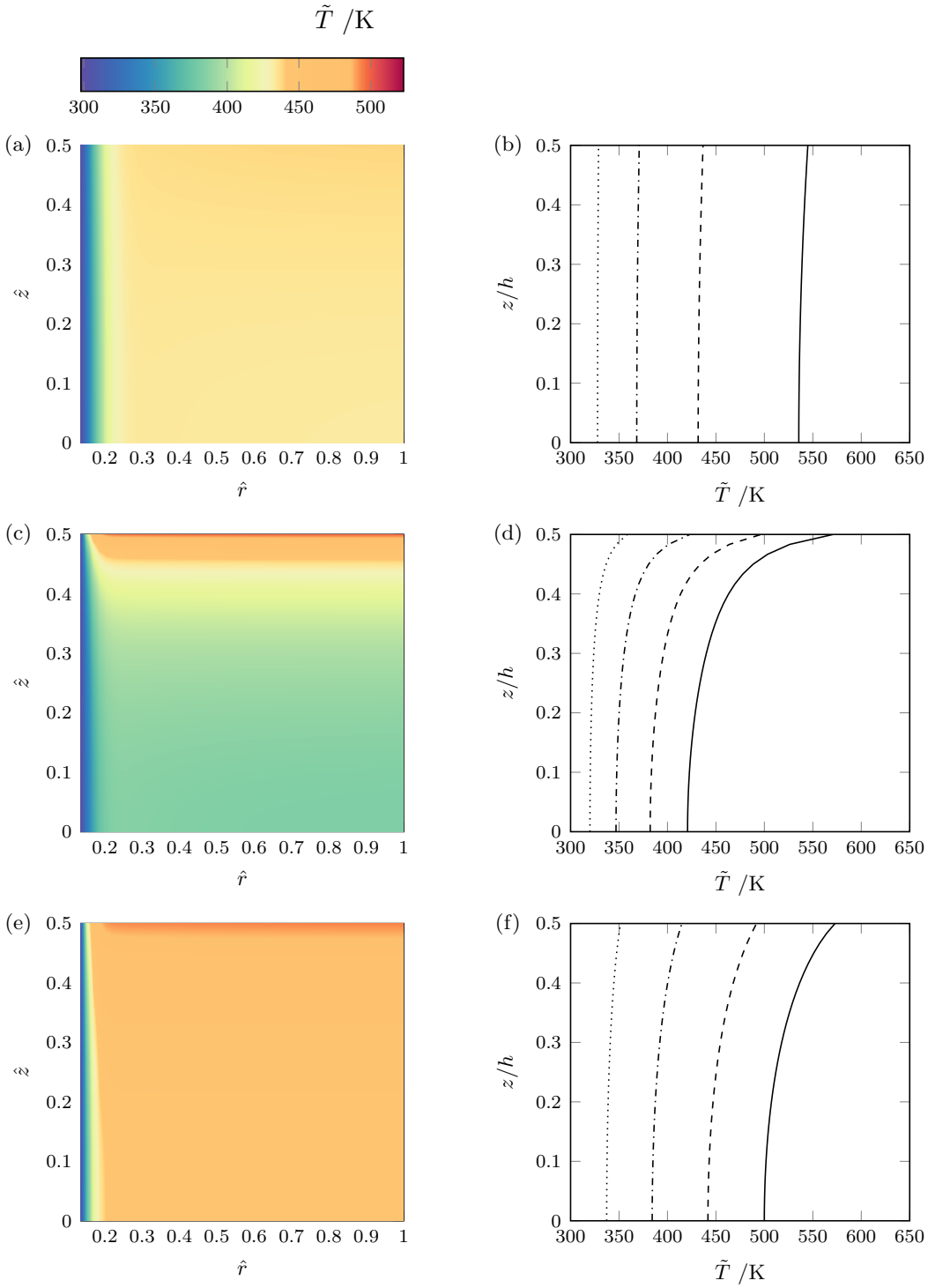

Figure 3.12: Left panels show the dimensional temperature $\tilde{T}$ in the $\hat{r}$–$\hat{z}$ plane for Ex-MS with an isothermal boundary condition at $\hat{r} = \hat{r}_{\min}$, shown at dimensional times: (a) $\tilde{t} = 351$ micro s; (c) $\tilde{t} = 254$ micro s; and (e) $\tilde{t} = 223$ micro s. Right panels show the dimensional temperature as a function of $\hat{z}$ at fixed $\hat{r} = 0.6$ for dimensional times: (b) $\tilde{t} = 117$, 234, 351, 445 micro s; (d) $\tilde{t} = 88$, 176, 254, 334 micro s; and (f) $\tilde{t} = 74$, 149, 223, 283 micro s. The values of m and n used were: (a,b) $m = 0.3 = n$; (c,d) $m = 0.9$, $n = 0.3$; and (e,f) $m = 0.3$, $n = 0.9$. Note that in order to allow useful comparison between results with different values of stress fractions the same colourbar has been used for the plots in (a,c,e). As a result it appears that panel (a) shows a constant temperature throughout the bulk of the sample away from the axis $\hat{r} = 0$. However, there is a slight increase in temperature with increasing z, as more readily observed in panel (b).

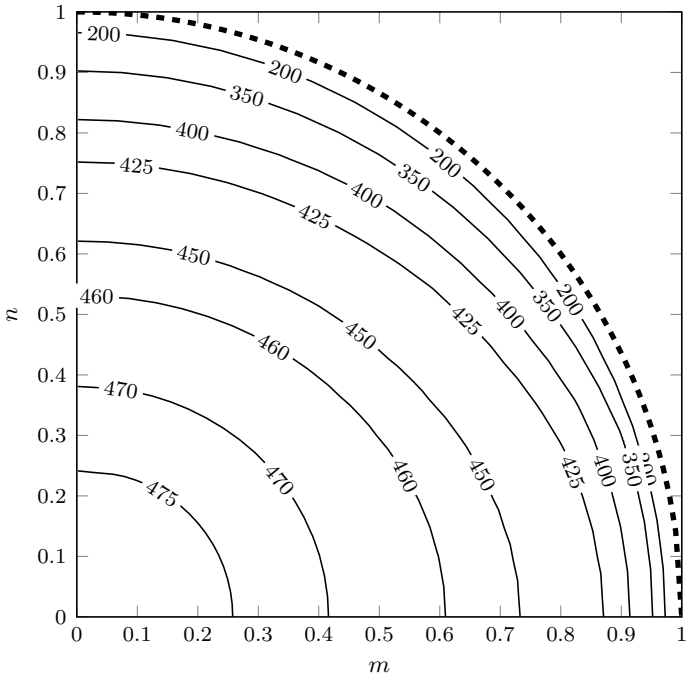

Figure 3.13: Contours of time to ignition in microseconds for Ex-MS in the m–n plane for a sample of Ex-MS subject to a plate speed $V = 25\mathrm{m\,s^{-1}}$.

3.6 Discussion

The analytical solution for the squeezing motion of a plastic material between two plates presented here has extended the analysis of [88] to account for a Tresca boundary condition in both the r–z and θ–z directions, shedding light on the response of a rigid-plastic material to a more complicated deformation which applies shear in multiple ways. Further, we have also been able to account for the effects of inertia when the ratio of inertial effects to yield stress is $\mathcal{R} \sim O(1)$. The usefulness of this analysis in terms of understanding hot spot mechanisms has been to investigate how accounting for the effects of friction, here via partial-slip boundary conditions, affects the spatial distribution of heating due to mechanical dissipation within the material. It was demonstrated that increased friction on the plates leads to increased dissipation, and ultimately earlier onset of reaction. Such additional heating adjacent to the contact region between the explosive and the impacting material is consistent with experimental findings [4], and with the numerical results discussed in Chapter 2. In particular, we have been able to demonstrate that an analytical model, such as our partial slip boundary condition squeeze model, has the ability to at least qualitatively predict the additional heating seen near boundaries in experiments, and may therefore be useful in informing hydrocode models. It should be remembered that the additional heating described here is due to changes in the velocity field which result from the boundary conditions on the shear stress, and is *not* due to friction as a heat source at the contact between the plates and the material. Frictional heating

could certainly be important, especially if a large surface area of explosive is in contact with the impacting body. The relative size of the frictional heating compared with heating due to mechanical dissipation and chemical reaction can be estimated by (3.4.5). Accounting for heating due to friction at the surface would likely be a worthwhile extension to this model.

The approach used in this chapter gives a solution in a series in h/r which fails near the axis $r = 0$. Although it was demonstrated that the boundary condition applied at our artificial core $r = r_{\min}$ had a minimal effect on the results in the bulk of the material, future work should look to address how to deal with the core region in a more rigorous way. In the analysis of viscoplastic squeeze flow it is found that there exists an unyielded zone which includes the axis of symmetry, predicting that the central plane moves as a rigid plug [44]. Near to this axis the flow must be essentially shear free, which invalidates the assumptions made in the lubrication approximation (see [44] and references therein). In [67] it is shown that the lubrication approximation provides a good first-order estimate for the squeeze flow of viscoplastic materials, and through a rescaling of the variables in the core region a self-consistent solution with a small deformation rate in the core is obtained. They argue that the problem requires a singular perturbation instead of the regular perturbation used in the lubrication approximation. Although we did not use the lubrication approximation in our analysis, we did exploit the fact that $h \ll r$, so perhaps a similar rescaling in the core region, or singular perturbation analysis, may be useful to obtain a solution which is valid near the central axis.

As an extension to the rigid-plastic model for pinch an alternative viscoplastic model was considered, which accounts for the effects of strain-rate sensitivity, work hardening and strain softening [e.g. 54, 101]. In the simplest case of free-slip boundary conditions the equations of motion are still satisfied by a uniform biaxial extension, and a simple ODE for the temperature can be obtained as in [33]. Numerical solution allowed for the investigation of how various thermomechanical properties affected the time to runaway. A similar sensitivity analysis for the explosive material LX-14 undergoing shear in [24] revealed that the localisation of shear (and therefore heating) is much more sensitive to changes in mechanical properties than to most thermochemical properties.

The implementation of a viscoplastic model which only accounts for the uniform straining motion lacks the spatial dependence necessary to observe the generation of hot spots. One interesting approach may be to consider a viscoplastic material undergoing a leading-order uniform straining motion and assume some small (possibly periodic) variations in the initial temperature, stress, strain etc., or material properties (e.g. yield stress, density). In [21] an approximate linear stability analysis of shear band formation in a metal undergoing uniform shear is conducted. Multiple time scales are identified corresponding to an "inertial" and "viscous" time, and the asymptotic method of multiple scales is utilised to obtain integrals which control

the growth rates of the perturbations to the leading-order motion. Crucially, these integrals are known in terms of the assumed constitutive behaviour of the material. Such an approach was attempted for the squeezing motion, but analytical progress became prohibitively complex due to the complicated spatial relations between various properties. With some necessary additional assumptions, such an approach may be worthwhile, and shed light on how the microstructure of an explosive may lead to instabilities on the macroscale.

Chapter 4

Modelling of Reactive Shear Bands

Shear localisation is often suggested as a potential ignition mechanism in explosive materials [2, 19, 24, 29, 37, 51, 61, 80], backed up by experimental evidence [e.g. 45, 98]. The phenomenon of shear banding is well-studied in a general context, often with a particular focus on metals [7, 38, 39, 42, 54, 100–102, 107]. However, there have been comparatively few studies on the development of shear bands in explosive materials. A comprehensive review of the modelling of shear bands can be found in [101]. The majority of models of shear banding are one-dimensional, owing to the large aspect ratio observed in experiments. Examples of shear band models developed specifically for explosive materials are less common in the literature, and are most often concerned with how the addition of a chemical heat source term affects the tendency for a shear band to form [24, 37, 80].

A one-dimensional model which aimed to address the likelihood of both friction and shear banding as accidental ignition mechanisms is developed in [51]. The model predicts the existence of a maximum obtainable temperature in the absence of reaction, which depends on the pressure and shear velocity. Upon introduction of chemical heating, the shear rate required to achieve a thermal explosion decreases rapidly as the pressure increases. The model can track the developing shear band, but requires numerical solution to determine the velocity profile across the sheared layer. A more simple model, which considers the shear band as a localised region of uniform straining, is developed in [37]. The work extends the so-called Frank-Kamenetskii analysis [50], which describes the process of self-ignition, to account for mechanical heating. The stability of the steady shear banding solution is studied, and predictions for the maximum temperature at the centre of the band as a function of the plastic work are made. The analysis demonstrates how the mechanical process of shear banding may combine with the thermochemical process of self-ignition to increase the mechanical sensitivity of explosive materials. Caspar and Powers [23, 24, 80] studied a thin-walled, cylindrical, rigid-plastic specimen of the explosive material LX-14.

Experimental studies were performed on an inert simulant, Mock 900-20, in order to characterise the effects of strain and strain-rate hardening. The studies go on to use both numerical and analytical techniques to study how an inhomogeneity in the sample thickness can trigger the onset of a shear band. Further, shear localisation in LX-14 was shown to be sensitive to changes in mechanical properties, specific heat and activation energy, but relatively insensitive to changes in the thermal conductivity and kinetic rate constant.

In this chapter we consider a one-dimensional model for a reactive shear band, which accounts for heating due to plastic work and chemical reaction. Our main aim is to illustrate typical shear band behaviour found in explosive materials. In Section 4.1 we give the governing equations for a slab of explosive material undergoing a shearing motion. The material is treated as an elastic-plastic, with an as-yet unspecified constitutive law for the plastic strain-rate. As in [39, 42, 80], we use a perturbation in the initial temperature as the stimulus for localised plastic deformation. Physically, the shear band may be triggered in a number of different ways, most of which result from non-uniformities in the material [101]. Some authors have used an inhomogeneity in the heat flux [38] or sample width [24]. In practice, since the initial perturbation is small, the development and growth of the shear band is not affected by the choice of stimulus. In Section 4.2 we extend the so-called "cohesive" numerical scheme given in [107] to account for heating due to chemical reaction. The governing equations are then solved, and results illustrating the development of a shear band are discussed. In particular, we note how the ratio of elastic modulus to shear yield strength is large, so that a rigid-plastic model may be appropriate. In Section 4.3 we take the limit of infinite elastic modulus, and formally recover a one-dimensional, rigid-plastic model for reactive shear bands, equivalent to the axisymmetric model considered in [23, 24, 80]. The governing equations are solved numerically and compared with elastic-plastic results from the previous section.

The numerical solutions demonstrate that the plastic strain localises into a thin zone centred about our initial temperature perturbation. Motivated by this observation, we seek an asymptotic solution in Section 4.3.2, in which the outer solution is used as the leading-order term in the shear band region. In order to make analytical progress in the inner region, we restrict ourselves to the case of no strain hardening. This analysis extends the inert work [42] to account for an Arrhenius source term. Later, in Chapter 5, we will consider a more detailed analytical study of the formation and growth of shear bands in a reactive material. Through a more systematic asymptotic argument, we will develop an analytical model for shear banding which accounts for strain and strain-rate effects, thermal softening, and heating due to both plastic work and chemical reaction.

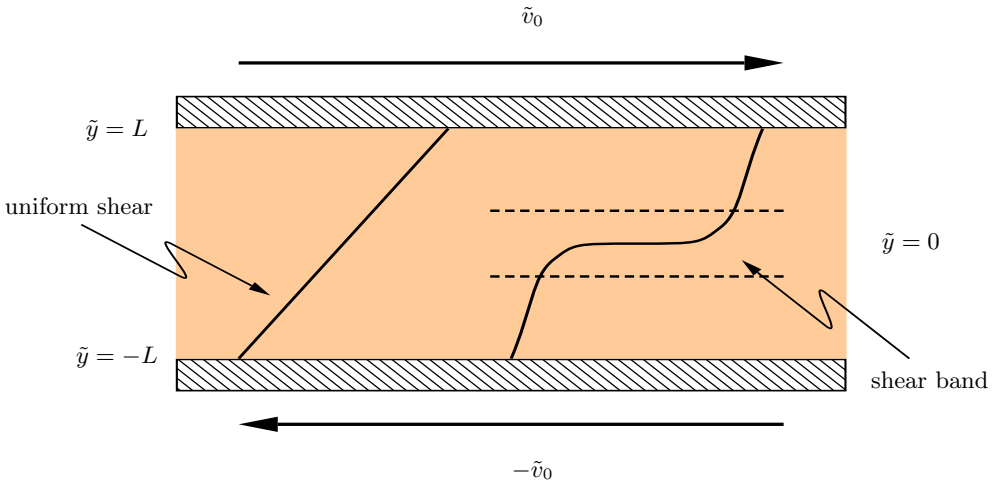

Figure 4.1: Schematic of uniform shearing vs. a shear band centered about $\tilde{y} = 0$.

4.1 Shear Band model

We consider a two-dimensional slab of explosive material of height $2L$ subject to an applied uniform shearing motion, see Figure 4.1. The sample is loaded at time $\tilde{t} = 0$ such that the constant velocity at $\tilde{y} = \pm L$ is $\pm\tilde{v}_0$. In the absence of any inhomogeneity in the material properties, or in the initial or boundary conditions, it is assumed that the velocity profile is linear for $-L < \tilde{y} < L$. However, perturbations may be introduced which will allow for localisation to occur. Since the shear banding process in an example of an instability, the form of these perturbations is not of great importance; we are more concerned with how the instability grows or decays in time. For now, it is assumed that such perturbations will be uniform in the direction of shearing so that a one dimensional model is appropriate. The explosive material is assumed to behave as an elastic-plastic, with a constitutive law which accounts for strain hardening, strain-rate sensitivity and thermal softening effects. The heating of the material due to plastic work is modelled, as well as the subsequent self-heating due to exothermic reaction. The reaction is modelled using a one-step Arrhenius law.

In dimensional form the governing equations read:

$$\rho\tilde{v}_{\tilde{t}} = \tilde{s}_{\tilde{y}}, \qquad \text{momentum balance;} \qquad (4.1.1)$$

$$\rho c\tilde{T}_{\tilde{t}} = \kappa\tilde{T}_{\tilde{y}\tilde{y}} + \beta\tilde{s}\dot{\Gamma} + \rho\Omega A\exp(-E/(R\tilde{T})), \qquad \text{energy balance;} \qquad (4.1.2)$$

$$\tilde{s}_{\tilde{t}} = G(\tilde{v}_{\tilde{y}} - \dot{\Gamma}), \qquad \text{elastic relationship;} \qquad (4.1.3)$$

$$\dot{\Gamma} = \dot{\Gamma}(\tilde{s}, \tilde{T}, \Gamma), \qquad \text{plastic flow law;} \qquad (4.1.4)$$

$$\Gamma = \int_0^{\tilde{t}} \dot{\Gamma}(t')\,\mathrm{d}t', \qquad \text{plastic strain.} \qquad (4.1.5)$$

Here the dependent variables are velocity $\tilde{v}(\tilde{y}, \tilde{t})$, stress $\tilde{s}(\tilde{y}, \tilde{t})$, temperature $\tilde{T}(\tilde{y}, \tilde{t})$, and plastic strain-rate $\dot{\Gamma}(\tilde{y}, \tilde{t})$. The plastic strain $\Gamma(\tilde{y}, \tilde{t})$ is determined by integration

of the plastic strain-rate. The material constants ρ, G, c, κ, β, Ω, A, E and R, are the density, elastic shear modulus, specific heat, thermal conductivity, Taylor-Quinney coefficient, heat of reaction, rate constant, activation energy and molar gas constant, respectively. In this model it is assumed that the material is initially free of stress or plastic strain, and is shearing under a uniform strain-rate $\dot{\Gamma}_0$. We will use an inhomogeneity in the initial temperature profile as the stimulus for the formation of a shear band, and the ends of the slab are assumed to be insulated. The effects of the boundary conditions in the one-dimensional shear band model are discussed in [107]. It is found that the development of shear bands is identical when using either insulated or periodic boundary conditions with a constant boundary velocity. However, if the insulated boundary conditions are replaced with isothermal conditions at the ends of the slab, the shear band develops at a slightly earlier time. The corresponding initial and boundary conditions are

$$\tilde{v}(\pm L,\tilde{t}) = \pm\tilde{v}_0, \quad \tilde{v}(\tilde{y},0) = \dot{\Gamma}_0\tilde{y}, \quad \Gamma(\tilde{y},0) = 0, \quad \dot{\Gamma}(\tilde{y},0) = \dot{\Gamma}_0, \tag{4.1.6}$$

$$\tilde{T}_{\tilde{y}}(\pm L,\tilde{t}) = 0, \quad \tilde{T}(\tilde{y},0) = \tilde{T}_0(1+\varepsilon\tilde{f}(\tilde{y}/(\varepsilon L)), \tag{4.1.7}$$

with appropriate compliance of the stress. Here the small parameter ε and function $\tilde{f}(\tilde{y}/(\varepsilon L))$ describe the size and shape of the initial temperature perturbation, respectively, and $\tilde{T}_0$ is a dimensional initial bulk temperature. Typically $\tilde{T}_0$ will be taken to be room temperature ($\sim 298\,\mathrm{K}$).

We introduce non-dimensional variables, which are related to the dimensional variables by

$$\begin{gathered} t = \tilde{t}/t^*, \quad y = \tilde{y}/L, \quad v = \tilde{v}/\tilde{v}_0, \quad s = \tilde{s}/s^*, \\ \dot{\gamma} = \dot{\Gamma}/\dot{\Gamma}_0, \quad \gamma = \Gamma/\Gamma_0, \quad T = \tilde{T}/\tilde{T}_0, \end{gathered} \tag{4.1.8}$$

where s^* is a representative stress, $t^* = L/\tilde{v}_0$ is a typical timescale, $\dot{\Gamma}_0 = \tilde{v}_0/L$ is a typical strain-rate, and $\Gamma_0 = t^*\dot{\Gamma}_0$ is a typical strain. These scalings result in the non-dimensional groupings

$$\begin{gathered} \mathcal{R} = \frac{\rho\tilde{v}_0^2}{s^*}, \quad \hat{G} = \frac{G}{s^*}, \quad \mathrm{Pe} = \frac{\rho c\tilde{v}_0 L}{\kappa}, \quad \mathrm{Ec} = \frac{\beta\tilde{v}_0^2}{c\tilde{T}_0} \\ \hat{E} = \frac{E}{R\tilde{T}_0}, \quad \hat{\Omega} = \frac{\Omega}{c\tilde{T}_0}, \quad \hat{A} = At^*. \end{gathered} \tag{4.1.9}$$

As is typical [e.g. 101], we take $\beta = 1$ in the analysis to follow.

In terms of the non-dimensional variables, the governing equations are

$$\mathcal{R}v_t = s_y \tag{4.1.10}$$

$$T_t = \frac{1}{\mathrm{Pe}}T_{yy} + \frac{\mathrm{Ec}}{\mathcal{R}}s\dot{\gamma} + \hat{\Omega}\hat{A}\exp(-\hat{E}/T), \tag{4.1.11}$$

$$s_t = \hat{G}(v_y - \dot{\gamma}), \tag{4.1.12}$$

$$\dot{\gamma} = \dot{\gamma}(s, t, \gamma). \tag{4.1.13}$$

$$\gamma = \int_0^t \dot{\gamma}(t')\,\mathrm{d}t'. \tag{4.1.14}$$

These are supplemented by the boundary and initial conditions

$$v(\pm 1, t) = \pm 1, \quad T_y(\pm 1, t) = 0, \tag{4.1.15}$$

$$v(y, 0) = y, \quad \gamma(y, 0) = 0, \quad \dot{\gamma}(y, 0) = 1, \quad T(y, 0) = 1 + \varepsilon f(y/\varepsilon), \tag{4.1.16}$$

with appropriate compliance of the stress.

4.2 Numerical solution

In this section we give details of the numerical scheme for shear banding proposed by Zhou et al. [107]. The mechanical part of the problem remains unchanged from [107], but we adapt the thermal part of the solver to account for heating due to chemical reaction. Despite being the same as in [107], the procedure for the solution of the mechanical part of the problem is included so that this section gives a self contained exposition of the full numerical scheme. The governing equations (4.1.10)–(4.1.11) are of mixed hyperbolic-parabolic type, with the constitutive equation (4.1.13) closing the system. The partial differential equations are integrated in time, switching between the hyperbolic and parabolic parts of the problem, a procedure which is common for problems of this type [107]. First, the temperature is assumed known, and the mechanical equations (4.1.10) and (4.1.12), along with the constitutive laws (4.1.13) and (4.1.14), are solved. These variables, along with the known temperature T, may be used to compute the plastic strain γ and strain-rate $\dot{\gamma}$. We exploit the fact that the characteristics of the mechanical system are straight lines, allowing for efficient advancement to the next timestep. With all mechanical variables regarded as known, we advance equation (4.1.11) forward in time. For the inert problem, it is claimed that, due to the smoothness of thermal diffusion compared with stress wave propagation, the decoupled approach gives accurate results provided the mechanical step can be solved accurately [107]. In order to accurately capture the rapid heating due to the chemical reaction we iterate the computation between the mechanical and thermal stage. This approach gives satisfactory results provided that the integration timestep is sufficiently small.

4.2.1 Characteristics for mechanical equations

The governing equations (4.1.10)–(4.1.14) have characteristics which are straight lines in the $y - t$ plane:

$$\frac{\mathrm{d}y}{\mathrm{d}t} = \pm S, 0, \tag{4.2.1}$$

where $S = \sqrt{\hat{G}/\mathcal{R}}$ is the non-dimensional elastic shear wave speed. Along these lines, the mechanical characteristic equations are

$$\mathrm{d}s \mp \mathcal{R}S\,\mathrm{d}v + \hat{G}\dot{\gamma}(y,t)\,\mathrm{d}t = 0, \quad \mathrm{d}\gamma = \dot{\gamma}\,\mathrm{d}t. \tag{4.2.2}$$

The spatial domain $-1 \leq y \leq 1$ is discretised into N segments of equal length $\Delta y = 1/N$, and the integration time step is fixed as $\Delta t = \Delta y/S$. Thus, the $y-t$ plane is divided into a rectangular mesh, with each of the nodes being linked by the characteristic lines $\mathrm{d}y/\mathrm{d}t = S, -S, 0$.

The independent variables on the node $(i, t+\Delta t)$ may be computed using information from nodes $(i-1,t)$, (i,t) and $(i+1,t)$. Since $\mathcal{R}$ and S are constant, equations (4.2.2) may be integrated along the characteristic lines as:

$$\Delta s - \mathcal{R}S\Delta v + \hat{G}\bar{\dot{\gamma}}_{+}\Delta t = 0, \qquad \text{along} \quad \Delta y = S\Delta t, \tag{4.2.3}$$

$$\Delta s + \mathcal{R}S\Delta v + \hat{G}\bar{\dot{\gamma}}_{-}\Delta t = 0, \qquad \text{along} \quad \Delta y = -S\Delta t, \tag{4.2.4}$$

where

$$\bar{\dot{\gamma}}_{+} \equiv \frac{\int_t^{t+\Delta t} \dot{\gamma}(y_{i-1} + St', t')\,\mathrm{d}t'}{\Delta t} \quad \text{and} \quad \bar{\dot{\gamma}}_{-} \equiv \frac{\int_t^{t+\Delta t} \dot{\gamma}(y_{i+1} - St', t')\,\mathrm{d}t'}{\Delta t}, \tag{4.2.5}$$

define the average values of the plastic-strain-rate $\dot{\gamma}$ along the two integration paths.

4.2.2 Pseudo-cohesive nodes

Making use of the relation $\hat{G}\Delta t = \pm\mathcal{R}S\Delta y$ we obtain the following two difference equations:

$$(s_i^{t+\Delta t} - s_{i-1}^t) - \mathcal{R}S(v_i^{t+\Delta t} - v_{i-1}^t) + \mathcal{R}S\Delta y\frac{\dot{\gamma}_{i-1}^t + \dot{\gamma}_i^{t+\Delta t}}{2} = 0, \tag{4.2.6}$$

$$(s_i^{t+\Delta t} - s_{i+1}^t) + \mathcal{R}S(v_i^{t+\Delta t} - v_{i+1}^t) - \mathcal{R}S(-\Delta y)\frac{\dot{\gamma}_{i+1}^t + \dot{\gamma}_i^{t+\Delta t}}{2} = 0. \tag{4.2.7}$$

These two equations are used in combination with the flow law (4.1.13) to determine the three unknown quantities $v_i^{t+\Delta t}$, $s_i^{t+\Delta t}$ and $\dot{\gamma}_i^{t+\Delta t}$.

As in [107], we adopt the concept of *pseudo-cohesive nodes*. This has many benefits: it makes for a very efficient scheme, allowing for a fine mesh to be used throughout the sample; the integration is carried out along the elastic characteristic lines, so that stress waves can be accurately tracked; and it separates the deformation into an elastic and viscoplastic part [107]. Since the *pseudo-cohesive* scheme treats plastic deformation as a jump across a nodal pair, it can handle severe deformations like those observed in shear bands. The scheme may also be used to model cracking and fragmentation in brittle materials [e.g. 106]. We begin by rewriting equations (4.2.6)

and (4.2.7) as

$$(s_i^{t+\Delta t} - s_{i-1}^t) - \mathcal{R}S\left\{\left[v_i^{t+\Delta t} - \frac{\Delta y}{2}\dot{\gamma}_i^{t+\Delta t}\right] - \left[v_{i-1}^t + \frac{\Delta y}{2}\dot{\gamma}_{i-1}^t\right]\right\} = 0, \tag{4.2.8}$$

$$(s_i^{t+\Delta t} - s_{i+1}^t) + \mathcal{R}S\left\{\left[v_i^{t+\Delta t} + \frac{\Delta y}{2}\dot{\gamma}_i^{t+\Delta t}\right] - \left[v_{i+1}^t + \frac{\Delta y}{2}\dot{\gamma}_{i+1}^t\right]\right\} = 0, \tag{4.2.9}$$

and splitting the nodal velocity into two parts defined as

$$v_{i^-} \equiv v_i - \dot{\gamma}_i\frac{\Delta y}{2}, \quad v_{i^+} \equiv v_i + \dot{\gamma}_i\frac{\Delta y}{2}. \tag{4.2.10}$$

The split nodal velocities v_{i^-} and v_{i^+} are now treated as separate independent variables, so that the nodal velocity and plastic strain-rate may be written

$$v_i = \frac{v_{i^-} + v_{i^+}}{2}, \quad \dot{\gamma}_i = \frac{v_{i^+} - v_{i^-}}{\Delta y}. \tag{4.2.11}$$

Equations (4.2.8) and (4.2.9) are rewritten as

$$(s_i^{t+\Delta t} - s_{i-1}^t) - \mathcal{R}S(v_{i^-}^{t+\Delta t} - v_{(i-1)^+}^t) = 0, \tag{4.2.12}$$

$$(s_i^{t+\Delta t} - s_{i+1}^t) + \mathcal{R}S(v_{i^+}^{t+\Delta t} - v_{(i+1)^-}^t) = 0, \tag{4.2.13}$$

and the five equations (4.1.13), (4.1.14), $(4.2.11)_2$, (4.2.12) and (4.2.13) can be solved for the quantities $v_{i^-}^{t+\Delta t}$, $v_{i^+}^{t+\Delta t}$, $s_i^{t+\Delta t}$, $\gamma_i^{t+\Delta t}$ and $\dot{\gamma}_i^{t+\Delta t}$.

By splitting the nodal velocity, the plastic deformation is treated as a jump across the the nodal couple through the relation $(4.2.11)_2$, and the momentum is transmitted through the material by elastic stress waves which propagate between neighbouring nodes: $(i-1)^+ \leftrightarrow i^-$ and $i^+ \leftrightarrow (i+1)^-$. The plastic flow stress can be considered analogous to a cohesive stress s_{coh} and we can define an equivalent cohesive displacement $\delta_{\text{coh}} \equiv \gamma\Delta y$. The core feature of this approach is that the process is separated into a nonlinear cohesive law (viscoplastic flow) and linear elastic wave propagation. The stress waves are treated explicitly along characteristic lines, which makes the scheme extremely efficient. Figure 4.2 shows an interpretation of the cohesive scheme. It should be noted that the cohesive model requires no additional physical assumptions, and is purely an adaptation of the material's constitutive relationship.

4.2.3 Numerical integration

The difference equations (4.2.12) and (4.2.13) may be added to yield

$$s_i^{t+\Delta t} = \frac{s_{i-1}^t + s_{i+1}^t}{2} + \frac{\mathcal{R}S}{2}\left[v_{(i+1)^-}^t - v_{(i-1)^+}^t\right] - \frac{\mathcal{R}S\Delta y}{2}\dot{\gamma}_i^{t+\Delta t}, \tag{4.2.14}$$

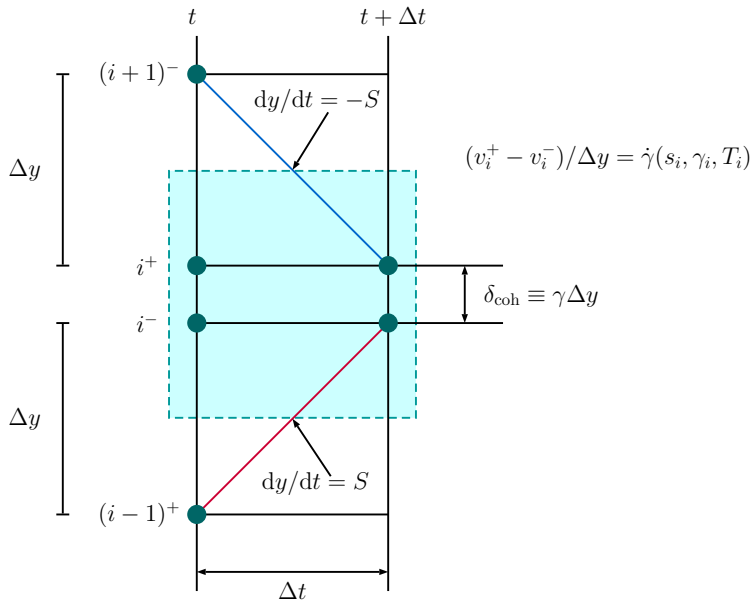

Figure 4.2: Schematic of the "cohesive" numerical scheme used by Zhou et al. [107].

where we have used equation $(4.2.11)_2$ to reintroduce the plastic strain-rate. Equation (4.2.14) is to be solved along with the plastic strain-rate function

$$\dot{\gamma}_i^{t+\Delta t} = \dot{\gamma}(s_i^{t+\Delta t}, T_i^t, \gamma_i^{t+\Delta t}), \tag{4.2.15}$$

and a second-order expression for the plastic strain

$$\gamma_i^{t+\Delta t} = \gamma_i^t + \frac{\Delta t}{2}\left[\dot{\gamma}_i^{t+\Delta t} + \dot{\gamma}_i^t\right], \tag{4.2.16}$$

using a Newton-Raphson scheme.

Once the mechanical equations have converged, the thermal part of the problem is solved using a discretised version of (4.1.11):

$$T_i^{t+\Delta t} = T_i^t + \Delta t \frac{1}{\mathrm{Pe}}\left(\frac{T_{i+1}^t - 2T_i^t + T_{i-1}^t}{\Delta y^2}\right) + \Delta t \frac{\mathrm{Ec}}{\mathcal{R}}\left(\frac{s_i^t + s_i^{t+\Delta t}}{2}\right)\left(\frac{\dot{\gamma}_i^t + \dot{\gamma}_i^{t+\Delta t}}{2}\right) + \Delta t\, \hat{\Omega}\hat{A} \exp\left(-\frac{2\hat{E}}{T_i^t + T_i^{t+\Delta t}}\right). \tag{4.2.17}$$

The above equation, which uses a second order midpoint rule for the heat generation terms, is iterated with the mechanical part of the problem until the temperature has converged. In the early stages of the problem, this iteration stage is not required since the temperature changes on a timescale much shorter than the timescale required by the mechanical part of the scheme. However, as the temperature is increased the heating due to reaction becomes important, and the updated value of the temperature may be used to solve an updated version of the mechanical equations (4.2.14)–(4.2.15). Such an iteration process is repeated until a solution is obtained to within a specified

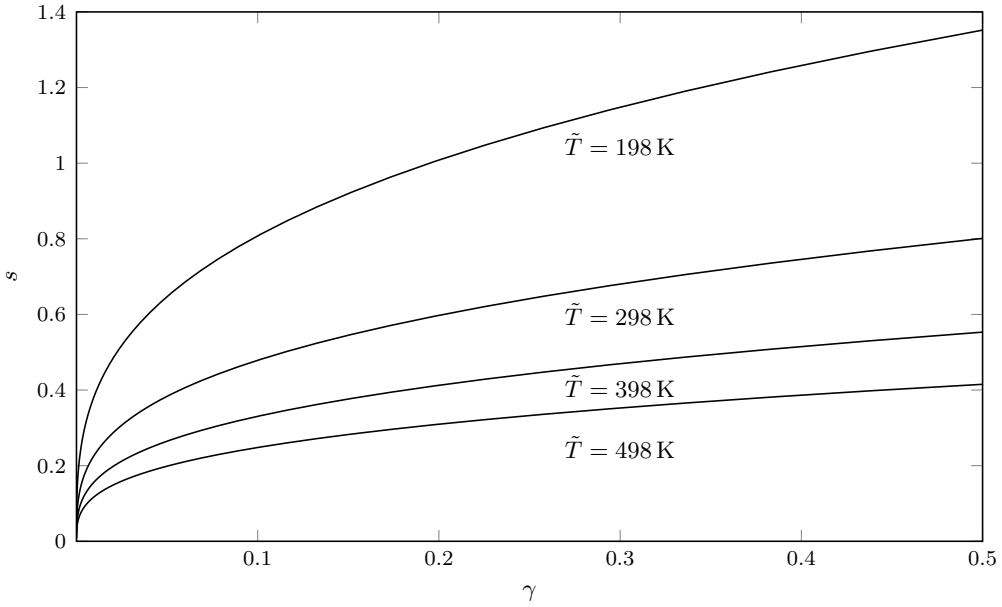

Figure 4.3: Isothermal stress–strain curves plotted from (4.2.23) at a range of temperatures with fixed strain rate $\dot{\Gamma} = \dot{\Gamma}_0$, and parameter values taken from [80].

tolerance.

The above scheme applies to all internal nodes $0 < i < N$. For the updated boundary nodes we use:

$$v_0^{t+\Delta t} = v_0, \qquad v_N^{t+\Delta t} = v_0, \tag{4.2.18}$$

$$s_0^{t+\Delta t} = s_1^t - \mathcal{R}S\left[-v_0 + \frac{\Delta y}{2}\dot{\gamma}_0^{t+\Delta t} - v_{1^-}^t\right], \tag{4.2.19}$$

$$s_N^{t+\Delta t} = s_{N-1}^t + \mathcal{R}S\left[v_0 - \frac{\Delta y}{2}\dot{\gamma}_N^t - v_{(N-1)^+}^t\right], \tag{4.2.20}$$

$$T_0^{t+\Delta t} = T_1^{t+\Delta t} \qquad T_N^{t+\Delta t} = T_{N-1}^{t+\Delta t}. \tag{4.2.21}$$

4.2.4 Results

In this section we present the results of the numerical simulations of the one-dimensional shearing problem. For simplicity we initially choose to neglect hardening effects [102, 107], allowing the typical structure of a shear band to be demonstrated and discussed. We then present results which include the effect of strain hardening, and compare the physical characteristics of the shear band and its formation.

The numerical method outlined above can deal with general models of viscoplasticity [107], but to fix ideas we focus on a particular constitutive relationship. We assume a power law model for the stress as a function of strain, strain-rate and temperature. This simple model, which combines both strain hardening and rate hardening, used by [e.g 54, 76, 101], may be written in

LX-14 Material Properties & Simulation Parameters	
Density ρ /kg m^{-3}	1849
Elastic Shear Modulus G /Pa	3.52×10^9
Yield Stress in Shear k /Pa	4.24×10^7
Specific Heat c /J kg^{-1} K^{-1}	1130
Thermal Conductivity κ /W m^{-1} K^{-1}	0.439
Activation Energy E /J mol^{-1}	2.206×10^5
Heat of Reaction Ω /J kg^{-1}	5.95×10^6
Molar Gas Constant R /J mol^{-1} K^{-1}	8.314
Pre-Exponential Constant A /s^{-1}	5×10^{19}
Strain-rate exponent m	0.08
Strain hardening exponent n	0.32
Thermal softening exponent l	-1.28
Sample length L /m	2.5×10^{-3}
Boundary velocity $\tilde{v}_0$ /m s^{-1}	7
Nominal strain-rate $\dot{\Gamma}_0$ /s^{-1}	2800
Initial temperature $\tilde{T}_0$ /K	298

Table 4.1: Material properties for LX-14 taken from [3, 72, 80, 87, 93], and simulation parameters used in the reactive shear band model.

dimensional form as

$$\tilde{s} = \tilde{s_0} \left(\frac{\tilde{T}}{\tilde{T_0}} \right)^l \Gamma^n \left(\frac{\dot{\Gamma}}{\dot{\Gamma}_0} \right)^m , \tag{4.2.22}$$

where $\tilde{s}_0$ is a stress constant. If we choose our representative stress to be this stress constant, i.e. $s^* = \tilde{s}_0$, then the non-dimensional stress reads

$$s = T^l \gamma^n \dot{\gamma}^m. \tag{4.2.23}$$

Here terms with exponents l, n and m describe the thermal softening, strain, and strain-rate effects, respectively. As written, the flow stress shows no definite yield. However, if the exponent n is small, the stress-strain curve has a sharp knee which approximates yield [101]. Figure 4.3 shows isothermal stress–strain curves plotted from (4.2.23) at a range of temperatures with fixed strain rate $\dot{\Gamma} = \dot{\Gamma}_0$. An in-depth discussion of simple phenomenological and physical models for plastic flow can be found in [101]. For a PBX we typically find $l \sim O(1)$, $m \sim O(10^{-2})$, and $n \sim O(10^{-1})$ [e.g. 24, 80]. In [80] the above power law model is used for LX-14, with parameter values $\tilde{s}_0 = 42\,\text{MPa}$, $\tilde{T}_0 = 298\,\text{K}$, $\dot{\Gamma}_0 = 2800\,\text{s}^{-1}$, $l = -1.28$, $m = 0.08$ and $n = 0.32$.

Before presenting our results, we will comment on the mesh dependency of the scheme. A full discussion is given in Appendix A of [107], in which it is demonstrated that the centreline temperature and stress, and the jumps in velocity and displacement, are all found to be independent of the mesh size. However, the centreline strain and strain-rate in the shear band are found to vary with grid size, because the

mechanical size of the banding zone reaches the minimal mesh size. In the modelling of a fully-formed shear band, the narrow zone of localisation is considered as a line of discontinuity over which there are jumps in the velocity and displacement [39, 101, 107]. Figure 4.4 shows the centreline temperature and stress, as well as the plastic strain-rate throughout the sample, computed using our power law for the stress (4.2.23). Results are shown for an increasing number of nodes N, and the parameter values used are those given in Table 4.1. As discussed in [107], we observe that the temperature and stress at the centre of the band converge with an increasing number of nodes N, but the strain-rate varies with mesh size. In numerical calculations of shear banding, the strain-rate is regularised by the mesh [101]. In the following, all of the results are presented were computed with $N = 1001$ nodes.

Figure 4.5 shows the velocity, plastic strain-rate, shear stress, and temperature at a series of increasing times for a sample of LX-14 subject to a uniform shear in the absence of strain hardening effects (i.e. with $n = 0$). It is important to note that the constitutive law (4.2.22) was calibrated whilst accounting for strain hardening [24], so it may the case that the other fitting parameters l, m, and $\tilde{s}_0$ require some adjustment in order to give accurate quantitative predictions. Despite this, the solution obtained by simply setting $n = 0$ will still faithfully demonstrate the qualitative characteristics of the onset of shear banding in the absence of strain hardening effects. The results shown demonstrate the initial formation of a shear band. Initially, the velocity profile is linear and the temperature uniform, apart from near $y = 0$ where an initial perturbation, see (4.1.7), has been introduced in order to trigger the formation of a shear band. The velocity remains near to the linear, uniform shearing profile, for approximately 2 ms, see Figure 4.5 (a). As the shearing motion continues the material begins to deform plastically in the centre, owing to our initial temperature perturbation. The temperature in the centre then increases more rapidly due to plastic work, and thermal softening causes a drop in stress, with the plastic strain localising into a thin band in the centre. As is typical of shear bands [101], the characteristic length over which the plastic strain-rate is elevated is smaller than the characteristic thermal length scale, see Figure 4.5 (d,h). For the final time shown, the centreline plastic strain-rate exceeds 10^5 s^{-1}, and the temperature in the band is some 150 K greater than the temperature in the bulk of the material. The increased plastic strain-rate correspondingly gives a steeper velocity gradient, and we observe a velocity profile typical of shear band formation [101], see Figure 4.5 (a,b). As the temperature continues to increase, the material in the band is heated further due to chemical reaction, leading to more extreme localisation. The stress in the sample appears to be independent of y, at least to leading order. This is not surprising since our non-dimensional density is small $\mathcal{R} \sim O(10^{-2})$, so we could justifiably make the quasi-steady approximation $s_y = 0$, where the left had side of the momentum equation (4.1.1) is set to zero. The governing equations (4.1.1)–(4.1.5) admit steady solutions, where it is found that, due to momentum

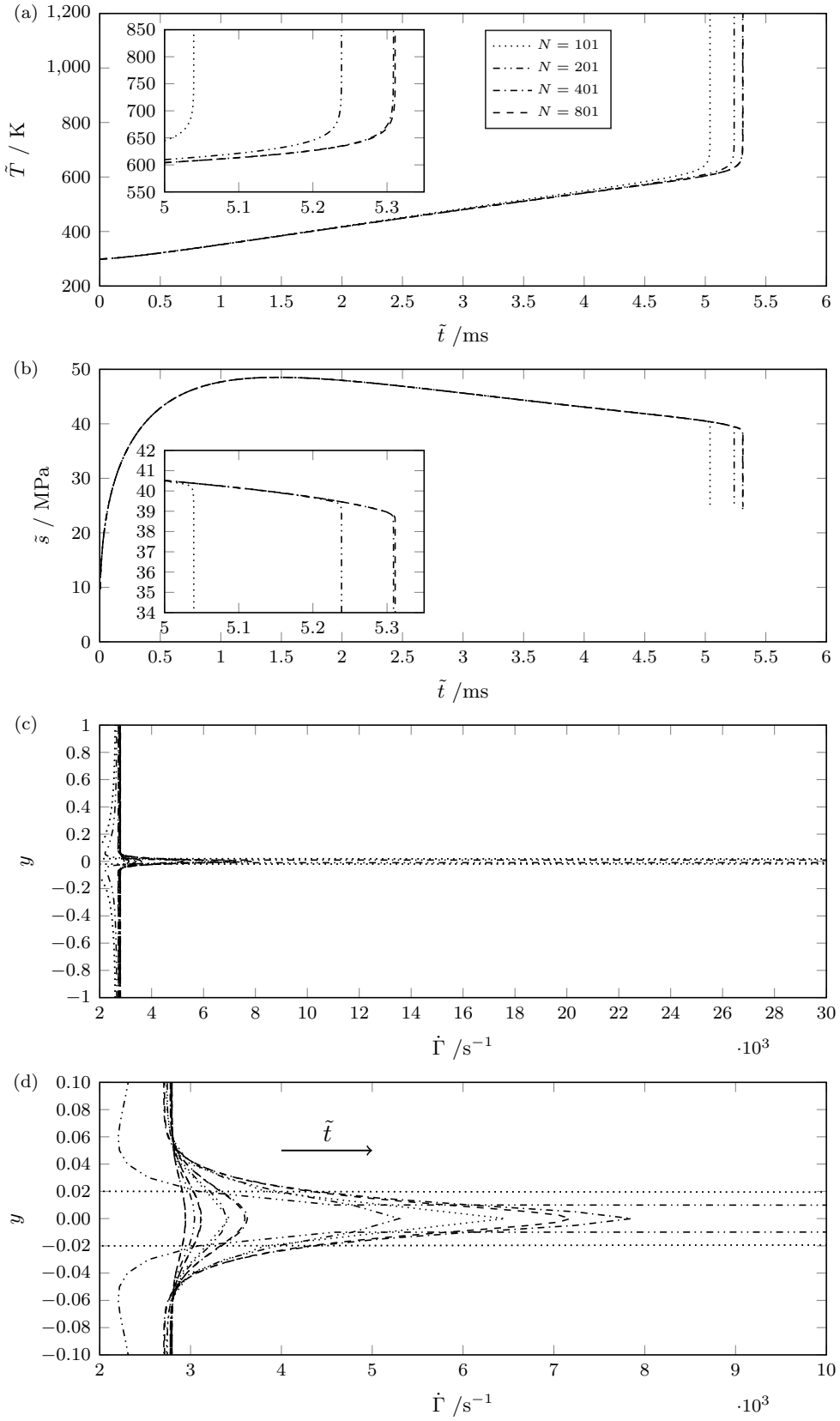

Figure 4.4: (a) Centreline temperature; (b) centreline stress; (c) strain-rate across the entire sample; and (d) strain-rate across the middle 10% of the sample. Plots are shown with an increasing number of grid points $N = 101$ ($\cdots$), 201 ($- \cdot\cdot$), 401 ($-\cdot$) and 801 ($--$). The strain-rate is shown as a function of sample height, and is plotted at a number of increasing times: $\tilde{t} = 4.5$, 5.0, 5.2 and 5.3 ms

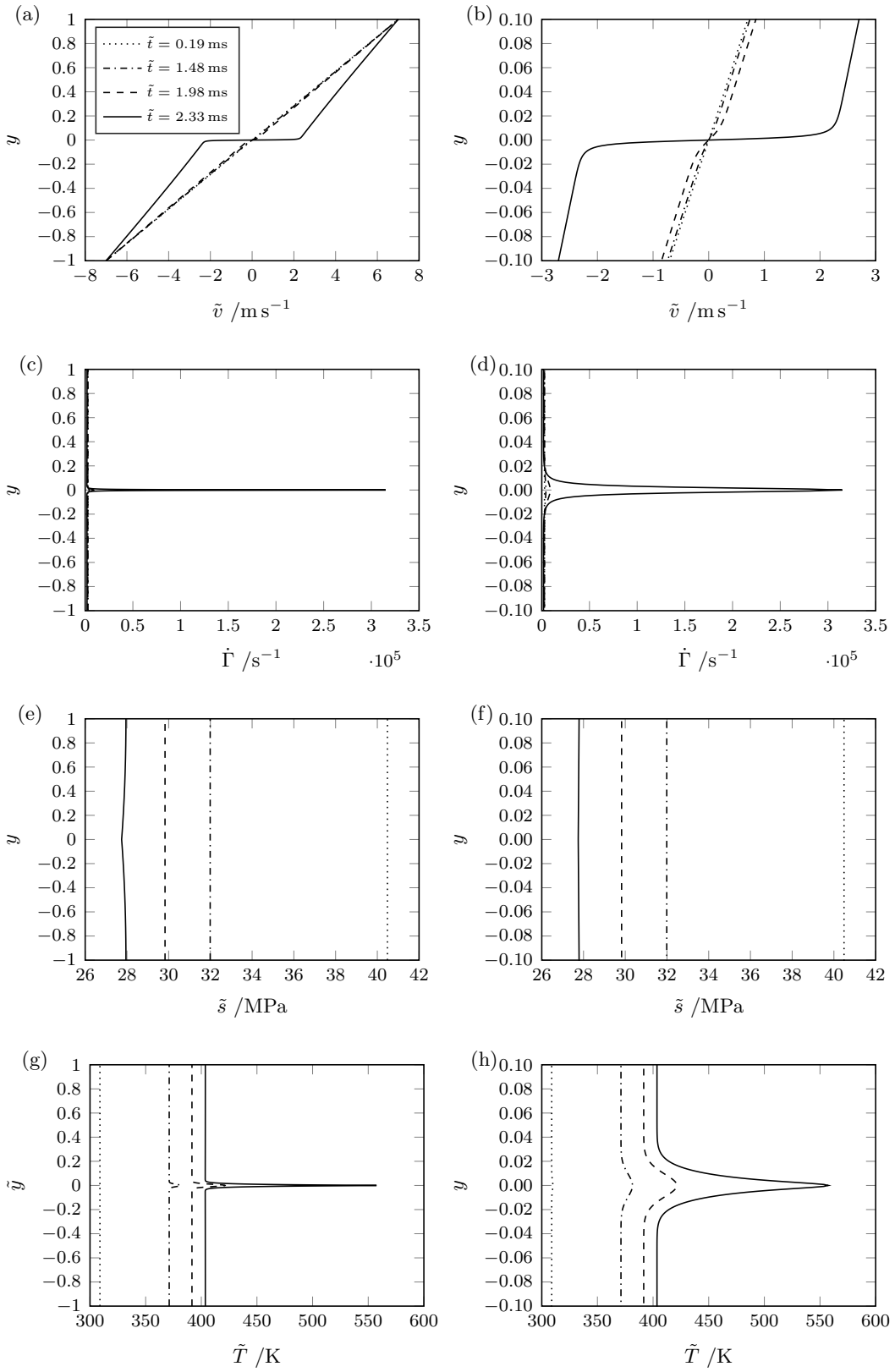

Figure 4.5: Numerical results for the elastic-plastic reactive shear band model in the absence of strain-hardening effects. Results show the: (a,b) velocity; (c,d) plastic strain-rate; (e,f) stress; and (g,h) temperature, at a series of increasing times $\tilde{t} = 0.19$, 1.48, 1.98 and 2.33 ms. The left panels (a,c,e,g) show the variables as a function of the non-dimensional sample height y. The right panels (b,d,f,h) depict the same results but zoomed in to show the middle 10% of the sample.

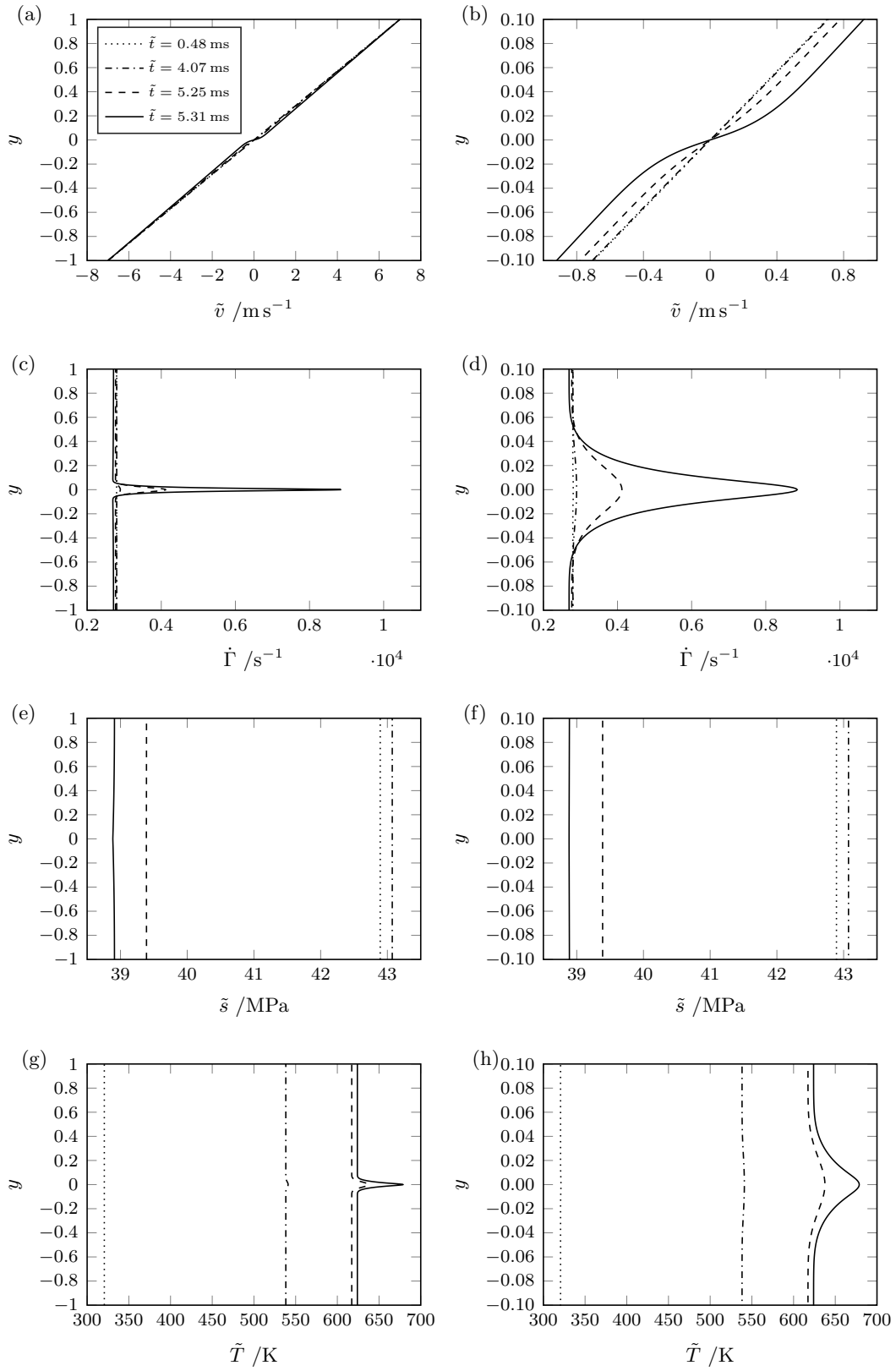

Figure 4.6: Numerical results for the elastic-plastic reactive shear band model, including strain-hardening effects. Results show the: (a,b) velocity; (c,d) plastic strain-rate; (e,f) stress; and (g,h) temperature, at a series of increasing times $\tilde{t} = 0.48$, 4.07, 5.25 and 5.31 ms. The left panels (a,c,e,g) show the variables as a function of the non-dimensional sample height y. The right panels (b,d,f,h) depict the same results but zoomed in to show the middle 10% of the sample.

balance, the stress must be constant. In this case the elastic strain-rate vanishes and the total strain-rate is equal to the plastic strain-rate. Such steady solutions are useful in revealing the structure of shear bands, and are discussed by Wright [101].

Figure 4.6 shows the same results with strain hardening effects included ($n = 0.32$). The most important differences to note are the much longer timescales, and much wider zone of plastic strain-rate localisation. The final snapshot shown in Figure 4.6 is taken at $\tilde{t} = 5.31\,\text{ms}$, and the centreline plastic strain-rate is only $O(10^4)$ s^{-1}, compared with a centreline plastic strain-rate of $O(10^5)$ s^{-1} at time $\tilde{t} = 2.33\,\text{ms}$ in the simulation which neglects hardening. Since thermal softening effects must now outweigh strain-rate dependence and strain hardening, the onset of shear banding is delayed. However, it should be remembered that the constitutive parameters were not calibrated in the absence of hardening, so the difference in timescales could be due to simply setting $n = 0$ in (4.2.23).

4.3 Rigid-Plastic approximation

Since the elastic modulus is much larger than the yield stress in shear, often by two orders of magnitude [3, 72, 80, 101], the assumed elastic-plastic behaviour of the material is well approximated by treating it as though it were a rigid-plastic. In the limit of infinitely large elastic modulus we find, by (4.1.12),

$$\lim_{\hat{G}\to\infty} \frac{s_t}{\hat{G}} = 0 \quad \Rightarrow \quad \dot{\gamma} = v_y, \tag{4.3.1}$$

i.e. the plastic strain-rate is given exactly by the gradient of the velocity. In this section we will give numerical and asymptotic results for the onset of shear bands in a rigid-plastic material which uses the power law model for the stress given by (4.2.22).

Under the assumption of large elastic modulus (i.e. rigid-plastic), and with a power law model for the stress, the non-dimensional governing equations are

$$\mathcal{R} v_t = s_y \tag{4.3.2}$$

$$u_t = v, \tag{4.3.3}$$

$$T_t = \frac{1}{\text{Pe}} T_{yy} + \frac{\text{Ec}}{\mathcal{R}} s v_y + \hat{\Omega}\hat{A}\exp(-\hat{E}/T), \tag{4.3.4}$$

$$s = T^l u_y^n v_y^m, \tag{4.3.5}$$

where we have explicitly written out the plastic strain and strain-rate as $\gamma = u_y$ and $\dot{\gamma} = v_y$, respectively.

4.3.1 Numerical results

The system of equations (4.3.2)–(4.3.5) and the accompanying boundary and initial conditions (4.1.15)–(4.1.16) are solved using a method-of-lines approach. The spatial derivatives are discretised using a second order accurate scheme, and the resulting system of ordinary differential equations is integrated in time using the stiff solver `ode15s` built into Matlab. This scheme is used in [23] to study shear banding in a thin-walled, cylindrical specimen of LX-14. A number of test problems are also solved, in order to validate the method. Figure 4.7 demonstrates the mesh dependency of the centreline temperature and stress, and the strain rate throughout the sample. As was the case in the cohesive scheme, the temperature and stress and the centre of the band converge as the number of grid points increases, see Figure 4.7 (a,b). However, the strain-rate increases at the centre as the grid size reduces. As the mechanical size of the band approaches the minimum grid spacing, the growth of the strain-rate is inversely proportional to the grid size. Figure 4.7 (c,d) shows the results for the strain-rate obtained with a number of different grid points. For each fixed N, the strain-rate is plotted at a number of increasing times, and we observe that the mesh dependence of the results becomes more of an issue at larger strain-rates. In the asymptotic analysis to follow, we will only be concerned with comparing our results for the temperature and stress, and not the strain-rate. As with the elastic-model, the following results were all computed using $N = 1001$ grid points.

Figure 4.9 shows the velocity, shear stress, displacement and temperature at a series of increasing times for a sample of LX-14 subject to a uniform shear, whereas Figure 4.8 shows results for the special case $n = 0$, corresponding to no strain hardening. The snapshots in the plots are taken at the same times as the results presented for the elastic-plastic model, see Figures 4.5 and 4.6. The development of the shear band shares the same qualitative characteristics as before: we initially observe that the stress rises uniformly throughout the sample, and the velocity profile is nearly linear, then, owing to the initial perturbation in the temperature, a shear band begins to develop about $y = 0$.

While the general behaviour is well captured by the rigid-plastic model, we do see some discrepancies, particularly in the later stages of the band formation. The jump in velocity across the band at the final time shown is smaller in the case of the rigid-plastic, but interestingly only noticeably so in the absence of hardening. However, this could be due to the mesh dependency of the centreline strain-rate.

The numerical simulations can continue to run beyond the final time plotted in Figures 4.8 and 4.9, but the velocity profile takes an extreme (likely unphysical) shape – by this time the material may well have failed [101]. However, the numerical results clearly demonstrate that there exists a thin zone in which the independent variables change rapidly, suggesting a boundary layer approach may be useful for describing the onset of shear banding.

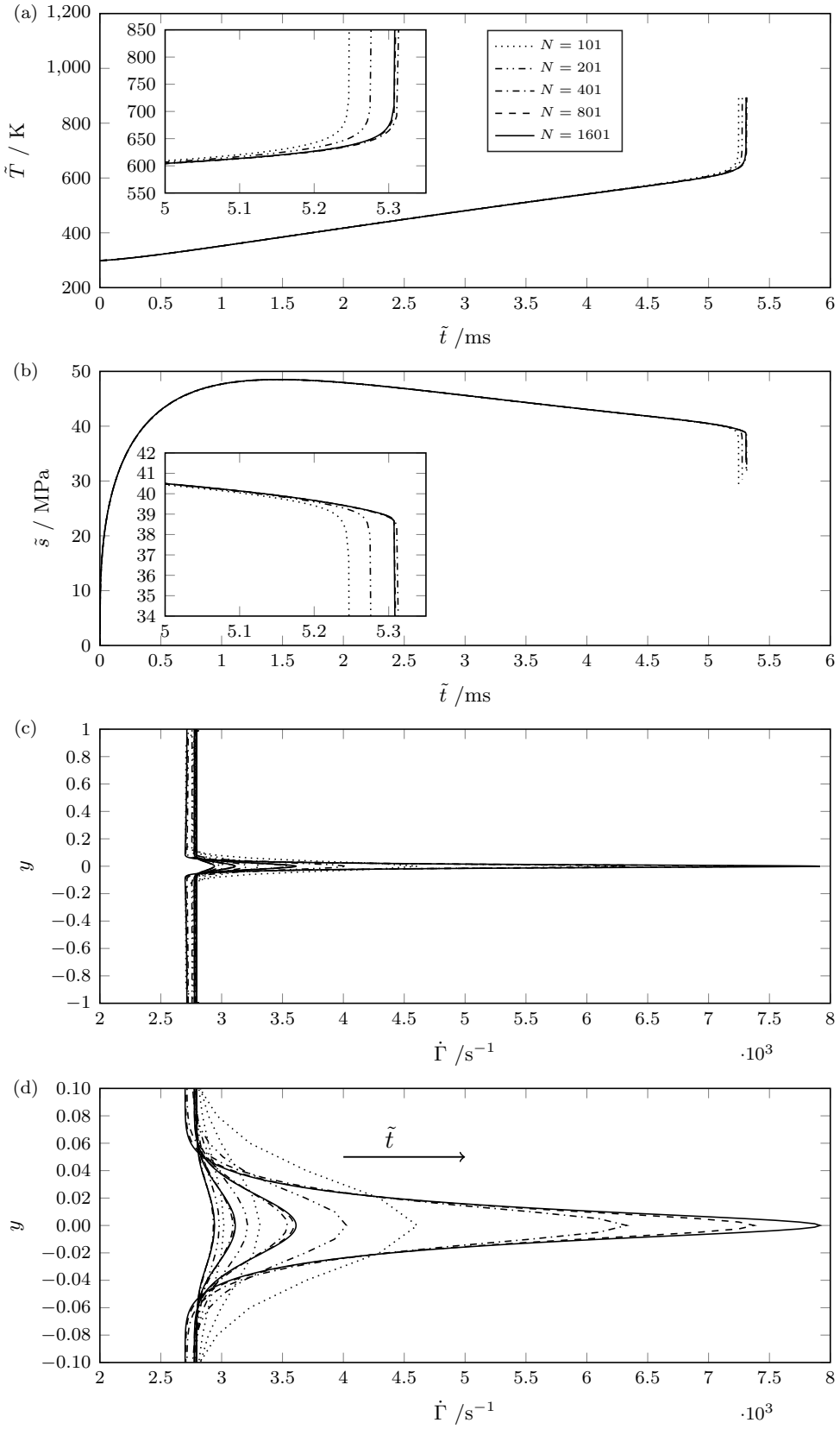

Figure 4.7: (a) Centreline temperature; (b) centreline stress; (c) strain-rate across the entire sample; and (d) strain-rate across the middle 10% of the sample. Plots are shown with an increasing number of grid points $N = 101$ ($\cdots$), 201 ($- \cdot\cdot$), 401 ($-\cdot$), 801 ($--$) and 1601 ($-$). The strain-rate is shown as a function of sample height, and is plotted at a number of increasing times: $\tilde{t} = 4.5$, 5.0, 5.2 and 5.3 ms

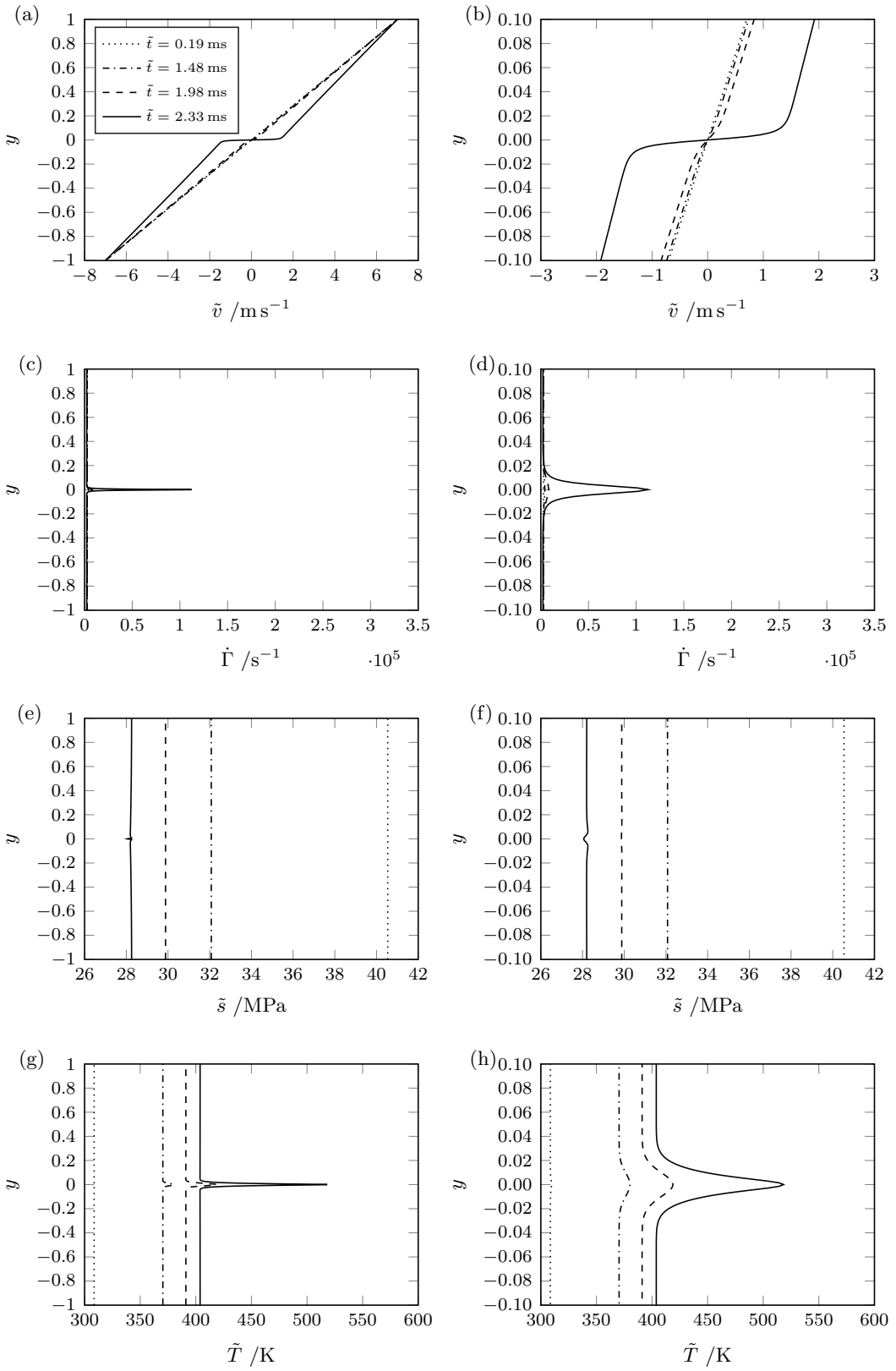

Figure 4.8: Numerical results for the rigid-plastic reactive shear band model in the absence of strain-hardening effects. Results show the: (a,b) velocity; (c,d) strain-rate; (e,f) stress; and (g,h) temperature, at a series of increasing times $\tilde{t} = 0.19$, 1.48, 1.98 and 2.33 ms. The left panels (a,c,e,g) show the variables as a function of the non-dimensional sample height y. The right panels (b,d,f,h) depict the same results but zoomed in to show the middle 10% of the sample.

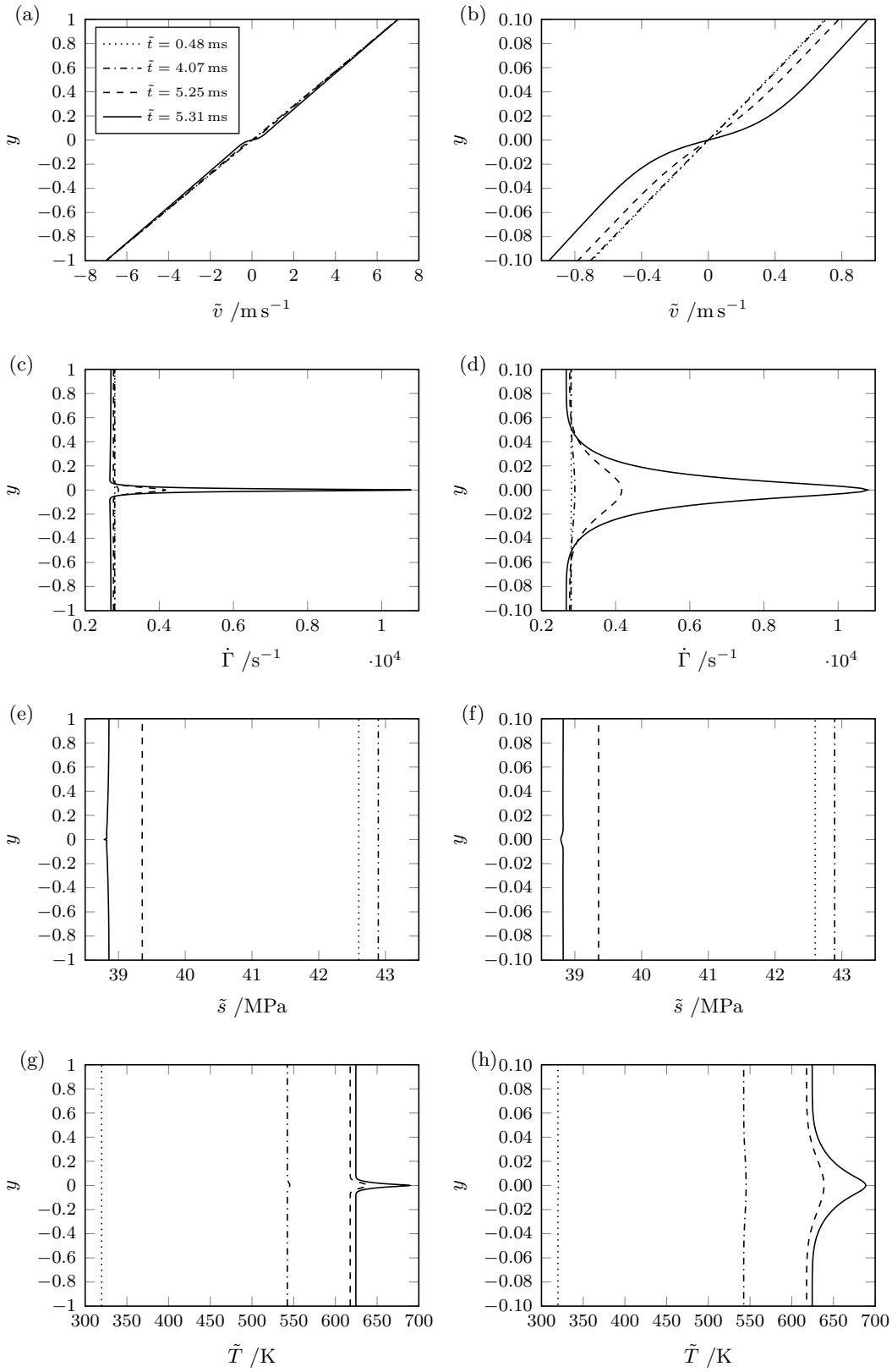

Figure 4.9: Numerical results for the rigid-plastic reactive shear band model, including strain-hardening effects. Results show the: (a,b) velocity; (c,d) strain-rate; (e,f) stress; and (g,h) temperature, at a series of increasing times $\tilde{t} = 0.48$, 4.07, 5.25 and 5.31 ms. The left panels (a,c,e,g) show the variables as a function of the non-dimensional sample height y. The right panels (b,d,f,h) depict the same results but zoomed in to show the middle 10% of the sample.

For many materials which exhibit shear banding, the Péclet number is typically large and it is sometimes argued that the effects of diffusion may be ignored [e.g. 42, 100], at least to leading-order, when modelling shear bands. Figure 4.10 shows a comparison of the dimensional centreline temperature $\tilde{T}(0,t)$ with and without the effects of diffusion for $n = 0$ and $n = 0.32$. Further, in order to compare our reactive shear band model with the more widely studied inert shear band model [e.g. 38, 39, 42, 100, 101] we also show the centreline temperature with and without reaction. As discussed, the shear band develops more rapidly when the effects of strain hardening are not accounted for. For all the results with $n = 0$ we see rapid temperature increase at or before $\tilde{t} \sim 2.5\,\text{ms}$. This time is increased to around $\tilde{t} \sim 5\,\text{ms}$ for the hardening results with reaction and increasing further still when the effects of heating due to chemical reaction are neglected. As expected, in the absence of diffusion the temperature in the centre of the band rises more rapidly as there are no heat losses to the surrounding material. This difference in the rate of heating is most apparent in the results for which strain hardening was included but the reaction was not. When comparing the results with and without reaction there is a notable difference depending on whether or not strain hardening is accounted for. For $n = 0$ we observe that there is no significant difference in the heating rate with or without the inclusion of the reaction; it is apparent that diffusion plays an important role in the absence of hardening. In the absence of diffusion the time taken for the centreline temperature to exceed 1000 K is reduced by just less than 1 ms. The minimal effect of the reaction is due to the fact that the localisation occurs over such a short timescale that the temperature in the band has already begun to increase at an extreme rate by the time the activation temperature $\sim 530\,\text{K}$ [24] has been reached. The inset figure shows the later stages of the process where the effect of the reaction is more apparent. In contrast, with $n = 0.32$ we see that in the inert case the rate of temperature increase is comparatively moderate at a temperature of around 530 K. As a result, the inclusion of the Arrhenius source term has a substantial effect on the time taken for the temperature to exceed 1000 K in the case of strain hardening.

4.3.2 Asymptotic analysis of the rigid-plastic model

Motivated by the numerical results we seek an asymptotic solution to the system of equations (4.3.2)–(4.3.5). We choose to impose a temperature perturbation that is even in y, and exploit the symmetry to redefine the problem on $0 \leq y \leq 1$ with the boundary conditions (4.1.15) being replaced by

$$v(0,t) = 0, \quad v(1,t) = 1, \quad T_y(0,t) = 0, \quad T_y(1,t) = 0. \tag{4.3.6}$$

In this model an $O(\varepsilon)$ inhomogeneity in the initial temperature is used as the stimulus to initiate a shear band. Physically, this corresponds to a band of slightly

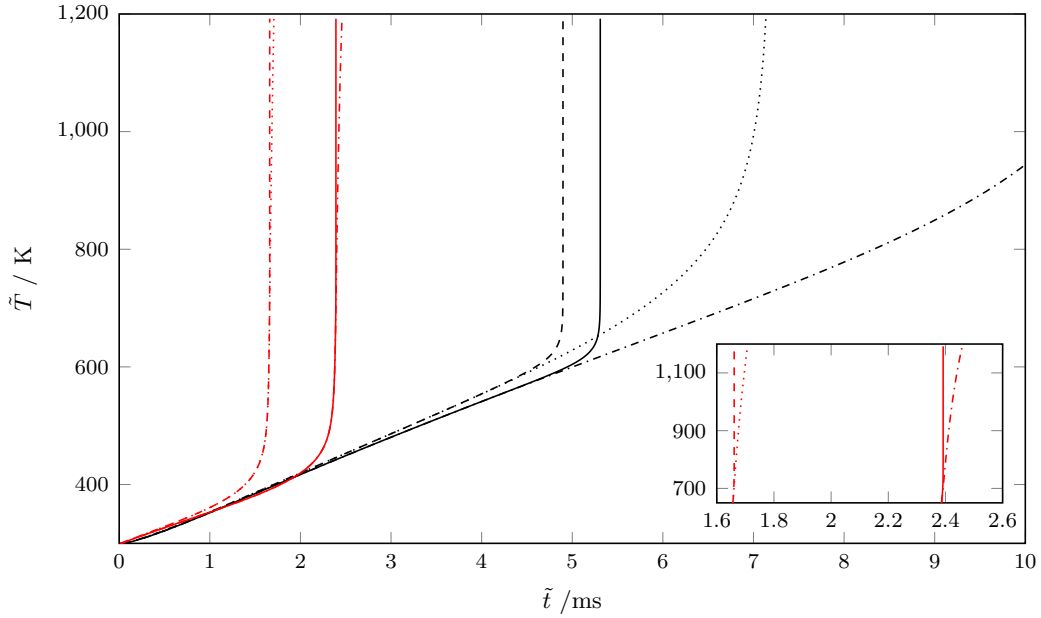

Figure 4.10: Comparison of centreline temperature with: no diffusion and no reaction (··); diffusion and no reaction (−·); no diffusion and reaction (−−); and both diffusion and reaction (−). The black lines show the results including strain hardening ($n = 0.32$), while the red lines show results for no strain hardening ($n = 0$). In the case of no strain hardening, diffusion greatly affects the centreline temperature and the results with and without reaction are virtually indistinguishable up until the later stages (inset).

increased temperature within the material. Such a local temperature rise would likely be due to locally differing mechanical or thermal properties. As discussed, PBXs are heterogenous in nature, and it is not unreasonable to assume one region may heat more quickly when the material is subject to an insult. In practice, the stimulus to trigger the band is not of great importance; since it is small its effect on the development of the band in time is negligible. We could similarly choose to initiate a shear band by perturbing any of the other variables, e.g. stress, or even in the sample geometry. For example, in [24] the behaviour of thin walled cylindrical specimen of explosive material is modelled, and a perturbation in the cylinder thickness is used to trigger a shear band.

Before proceeding with the asymptotic analysis, we must consider how best to relate the small parameter ε to the model parameters in order to facilitate useful physical interpretation. In some analyses of shear banding the effects of diffusion are neglected [e.g. 42, 100]. Such an assumption is justified provided that the initial temperature perturbation evolves on a length scale which is longer than the $O(\mathrm{Pe}^{-1/2})$ diffusion length scale. When this is the case the diffusion term in (4.3.4) is invariably smaller in magnitude than the other terms in the equation. However, during the formation of a shear band it is observed that the band narrows over time [100, 101] (at least until the unloading stage, when it is found that the band widens [39]) and therefore perturbations having length scales smaller than $O(\mathrm{Pe}^{-1/2})$ may well form. The Péclet number is typically large, so we define the small parameter ε through the

relation $\varepsilon^2 = 1/\mathrm{Pe}$. In doing so we ensure that the width of the initial temperature perturbation is of the correct diffusion scale.

4.3.3 The outer solution

We begin by solving the problem in the outer region away from the spatial inhomogeneity in the initial temperature. Following the analysis of the inert model for shear bands [42], we introduce the following expansions

$$(v, u, T, s) = (v_0, u_0, T_0, s_0) + \varepsilon^2(v_2, u_2, T_2, s_2) + o(\varepsilon^2). \tag{4.3.7}$$

Note that the expansion for the stress may be computed in terms of the expansions for the remaining variables by means of the constitutive law (4.3.5). However, in the interest of clarity, we retain the notation s_i for the terms in the expansion of the stress.

Substitution of the expansions into the governing equations gives

$$\mathcal{R}(v_{0_t} + \varepsilon^2 v_{2_t}) = s_{0_y} + \varepsilon^2 s_{2_y}, \tag{4.3.8}$$

$$u_{0_t} + \varepsilon^2 u_{2_t} = v_0 + \varepsilon^2 v_2, \tag{4.3.9}$$

$$\begin{aligned} T_{0_t} + \varepsilon^2 T_{2_t} = \varepsilon^2 T_{0_{yy}} + \frac{\mathrm{Ec}}{\mathcal{R}}[s_0 v_{0_y} + \varepsilon^2(s_2 v_{0_y} + s_0 v_{2_y})] \\ + \hat{\Omega}\hat{A}\exp\left(-\hat{E}/T_0\right)\left[1 + \varepsilon^2 \hat{E}\frac{T_2}{T_0^2}\right], \end{aligned} \tag{4.3.10}$$

$$s_0 + \varepsilon^2 s_2 = T_0^l u_{0_y}^n v_{0_y}^m \left[1 + \varepsilon^2\left(l\frac{T_2}{T_0} + n\frac{u_{2_y}}{u_{0_y}} + m\frac{v_{2_y}}{v_{0_y}}\right)\right], \tag{4.3.11}$$

with leading-order boundary and initial conditions

$$v_0(1,t) = 1, \quad T_{0_y}(1,t) = 0, \tag{4.3.12}$$

$$u_0(y,0) = 0, \quad v_0(y,0) = y, \quad T_0(y,0) = 1. \tag{4.3.13}$$

The leading-order terms in our expansion are satisfied by the uniform shearing solution, i.e. $v_0 = y$, $u_0 = yt$ and $s_0 = T_0^l t^n$. The leading-order temperature can then be computed through numerical solution of the energy equation (4.3.10) to $O(1)$, that is

$$T_{0_t} = \frac{\mathrm{Ec}}{\mathcal{R}} T_0^l t^n + \hat{\Omega}\hat{A}\exp\left(-\hat{E}/T_0\right). \tag{4.3.14}$$

In the special case of vanishing reaction rate $\hat{A} = 0$, corresponding to no chemical reaction, we have the exact leading-order outer solution

$$T_0 = \left[\frac{\mathrm{Ec}}{\mathcal{R}}\frac{1-l}{n+1}t^{n+1} + 1\right]^{\frac{1}{1-l}}. \tag{4.3.15}$$

Figure 4.11 shows the leading-order outer temperature and stress with and without

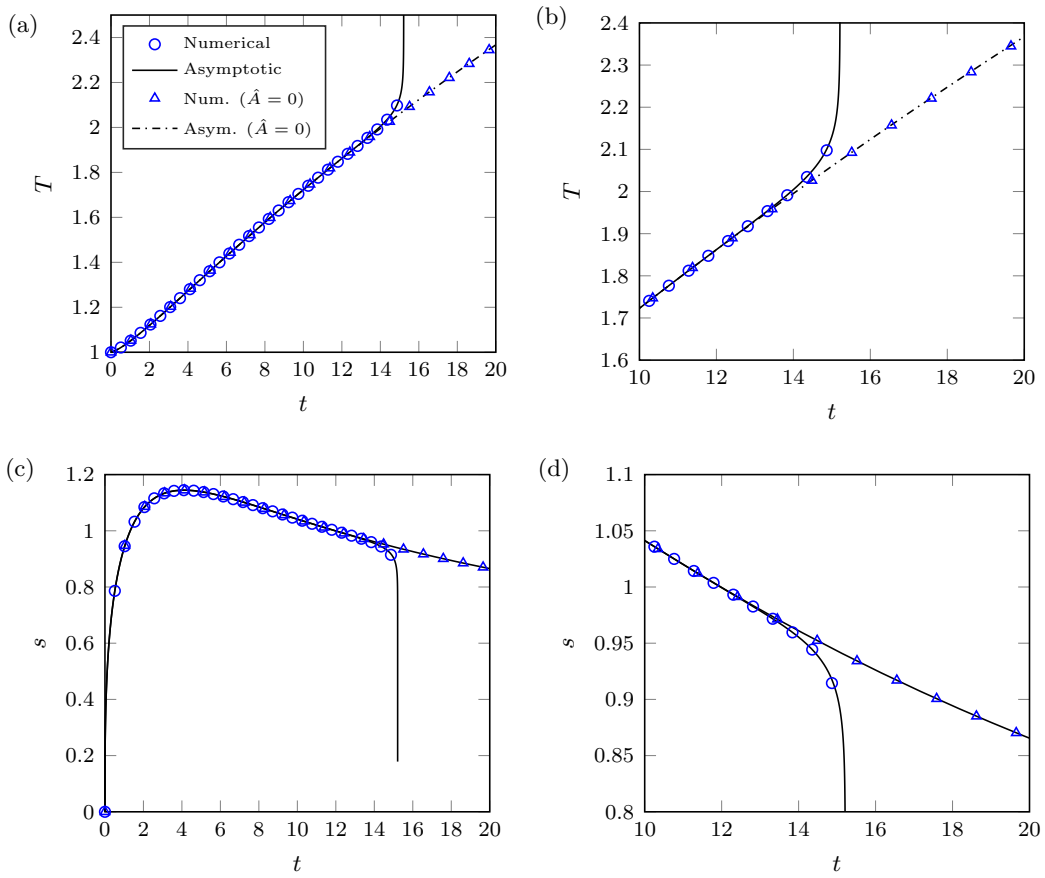

Figure 4.11: Comparison of the outer asymptotic solution and numerical solution for the temperature (a,b), and stress (c,d). Panels (b) and (d) show the later stages of the process.

reaction compared with the full numerical solution. Both the temperature and stress are well captured by the asymptotic solutions, even in the later stages, when the reaction commences.

4.3.4 The inner solution with strain hardening

Our initial disturbance is introduced at $y = 0$, so we expect a shear band to form near the centreline. The shear band will be treated as a boundary layer and we introduce the boundary layer variables

$$Y = \frac{y}{\varepsilon}, \quad v = \hat{v}(Y,t), \quad u = \hat{u}(Y,t), \quad T = \hat{T}(Y,t), \quad s = \hat{s}(Y,t). \tag{4.3.16}$$

The governing equations for the inner problem read

$$\mathcal{R}\hat{v}_t = \frac{1}{\varepsilon}\hat{s}_Y, \tag{4.3.17}$$

$$\hat{u}_t = \hat{v}, \tag{4.3.18}$$

$$\hat{T}_t = \hat{T}_{YY} + \frac{1}{\varepsilon}\frac{\mathrm{Ec}}{\mathcal{R}}\hat{s}\hat{v}_Y + \hat{\Omega}\hat{A}\exp\left(-\frac{\hat{E}}{\hat{T}}\right), \tag{4.3.19}$$

$$\hat{s} = \frac{1}{\varepsilon^{m+n}} \hat{T}^l \hat{u}_Y^n \hat{v}_Y^m, \tag{4.3.20}$$

with boundary and initial conditions

$$\hat{v}(0,t) = 0, \quad \hat{T}_Y(0,t) = 0, \tag{4.3.21}$$

$$\hat{u}(Y,0) = 0, \quad \hat{v}(Y,0) = \varepsilon Y, \quad \hat{T}(Y,0) = 1 + \varepsilon f(Y). \tag{4.3.22}$$

As in [42], when constructing our inner expansions we note that the leading-order outer solution T_0 satisfies all of the necessary boundary and initial conditions, so we do not expect any $O(1)$ variation in $\hat{T}$. Further, the outer analysis reveals that the velocity, and hence displacement and stress, is correct to $O(\varepsilon)$. Thus, in the inner region we use the expansions

$$\hat{v}(Y,t) = \varepsilon Y + \varepsilon^2 \hat{v}_2(Y,t) + \varepsilon^3 \hat{v}_3(Y,t) + o(\varepsilon^3), \tag{4.3.23}$$

$$\hat{u}(Y,t) = \varepsilon Y t + \varepsilon^2 \hat{u}_2(Y,t) + \varepsilon^3 \hat{u}_3(Y,t) + o(\varepsilon^3), \tag{4.3.24}$$

$$\hat{T}(Y,t) = T_0(t) + \varepsilon \hat{T}_1(Y,t) + \varepsilon^2 \hat{T}_2(Y,t) + o(\varepsilon^2), \tag{4.3.25}$$

$$\hat{s}(Y,t) = s_0(t) + \varepsilon \hat{s}_1(Y,t) + \varepsilon^2 \hat{s}_2(Y,t) + o(\varepsilon^2). \tag{4.3.26}$$

Substitution of the inner expansions into equations (4.3.17)–(4.3.20) gives the following equations for the first corrections to the inner solution

$$\varepsilon^2 \mathcal{R} \hat{v}_{2_t} = \hat{s}_{1_Y} + \varepsilon \hat{s}_{2_Y} + \varepsilon^2 \hat{s}_{3_Y}, \tag{4.3.27}$$

$$\varepsilon^2 \hat{u}_{2_t} = \varepsilon^2 \hat{v}_2, \tag{4.3.28}$$

$$\varepsilon \hat{T}_{1_t} = \varepsilon \left[\hat{T}_{1_{YY}} + \frac{\mathrm{Ec}}{\mathcal{R}} \left(s_0 \hat{v}_{2_Y} + \hat{s}_1 \right) + \hat{\Omega} \hat{A} \exp\left(-\frac{\hat{E}}{T_0} \right) \hat{E} \frac{\hat{T}_1}{T_0^2} \right], \tag{4.3.29}$$

$$\varepsilon \hat{s}_1 = \varepsilon T_0^l t^n \left(l \frac{\hat{T}_1}{T_0} + \frac{n}{t} \hat{u}_{2_Y} + m \hat{v}_{2_Y} \right), \tag{4.3.30}$$

with boundary and initial conditions

$$\hat{v}_2(0,t) = 0, \quad \hat{T}_{1_Y}(0,t) = 0, \tag{4.3.31}$$

$$\hat{u}_2(Y,0) = 0, \quad \hat{v}_2(Y,0) = 0, \quad \hat{T}_1(Y,0) = f(Y). \tag{4.3.32}$$

From (4.3.27) we observe that the correction to the stress is a function of time only, that is

$$\hat{s}_1(t) = T_0^l t^n \left(l \frac{\hat{T}_1}{T_0} + \frac{n}{t} \hat{u}_{2_Y} + m \hat{v}_{2_Y} \right). \tag{4.3.33}$$

However, we note that our $O(\varepsilon)$ disturbance in the temperature decays away from the shear band, thus we expect no disturbance in the outer solution for the temperature to this order. Further, our displacement and velocity profiles are correct to $O(\varepsilon^2)$, so we conclude that $\hat{s}_1$ must be zero in order to match with the outer solution to

$O(\varepsilon^2)$. Substituting $s_0 = T_0^l t^n$ and $\hat{s}_1 = 0$ into the governing equations for the inner problem gives

$$\varepsilon^2 \mathcal{R} \hat{v}_{2_t} = \varepsilon \hat{s}_{2_Y}(Y,t) + \varepsilon^2 \hat{s}_{3_Y}(Y,t), \tag{4.3.34}$$

$$\hat{u}_{2_t} = \hat{v}_2, \tag{4.3.35}$$

$$\hat{T}_{1_t} = \hat{T}_{1_{YY}} + \frac{\mathrm{Ec}}{\mathcal{R}} T_0^l t^n \hat{v}_{2_Y} + \hat{\Omega}\hat{A} \exp\left(-\frac{\hat{E}}{T_0}\right) \hat{E} \frac{\hat{T}_1}{T_0^2}. \tag{4.3.36}$$

In order to continue with this asymptotic solution we must consider further terms in our expansions (4.3.23)–(4.3.26). By (4.3.34) we find that the $O(\varepsilon^2)$ correction to the stress is a function of time only $\hat{s}_2 = \hat{s}_2(t)$, but depends on the higher order corrections $\hat{u}_3$, $\hat{v}_3$ and $\hat{T}_2$. In order to determine this correction to the stress we must then consider the $O(\varepsilon^2)$ outer problem in (4.3.8)–(4.3.11) and perform asymptotic matching between the two solutions. Unfortunately, it is found that the equation which would likely provide a solvability condition is too complicated to allow further analytical progress to be made. This problem is a result of including hardening effects; in the absence of strain hardening, the correction to the strain-rate $\hat{v}_{2_Y}$ in (4.3.36) may be replaced with the temperature correction $\hat{T}_1$ by means of (4.3.33), allowing the temperature to be determined prior to calculating the velocity correction. Noting that the absence of hardening corresponds to $n = 0$, the correction $\hat{v}_{2_Y}$ may be given by (4.3.33) using the known temperature correction $\hat{T}_1$.

4.3.5 The inner solution without strain hardening

With $n = 0$ the first-order correction to the stress is

$$\hat{s}_1(t) = T_0^l \left(l \frac{\hat{T}_1}{T_0} + m \hat{v}_{2_Y} \right) = 0, \tag{4.3.37}$$

which cannot be satisfied by the initial conditions (4.3.32). This prompts us to consider an initial layer in time during which $\hat{v}_2$ adjusts to satisfy (4.3.37). As in [42], we look for a solution in terms of the stretched time $\tau = t/\varepsilon^2$ of the form

$$\hat{v} = \varepsilon Y + \varepsilon^2 V(Y,\tau) + o(\varepsilon^2), \tag{4.3.38}$$

$$\hat{u} = \varepsilon^2 U(Y,\tau) + o(\varepsilon^2), \tag{4.3.39}$$

$$\hat{T} = 1 + \varepsilon \Theta(Y,\tau) + o(\varepsilon), \tag{4.3.40}$$

$$\hat{s} \sim \Sigma(Y,\tau). \tag{4.3.41}$$

Substitution into (4.3.17)–(4.3.20) gives the governing equations

$$\varepsilon \mathcal{R} V_\tau = \Sigma_Y, \tag{4.3.42}$$

$$U_\tau = 0, \tag{4.3.43}$$

$$\frac{1}{\varepsilon}\Theta_\tau = \varepsilon\Theta_{YY} + \frac{\mathrm{Ec}}{\mathcal{R}}\Sigma\,(1+\varepsilon V_Y) + \hat{\Omega}\hat{A}\exp(-\hat{E})(1+\varepsilon\hat{E}\Theta), \tag{4.3.44}$$

$$\Sigma = 1 + \varepsilon(l\Theta + mV_Y), \tag{4.3.45}$$

with boundary and initial conditions

$$V(0,\tau) = 0, \quad \Theta_Y(0,\tau) = 0, \tag{4.3.46}$$

$$U(Y,0) = 0, \quad V(Y,0) = 0, \quad \Theta(Y,0) = f(Y). \tag{4.3.47}$$

By (4.3.43) and (4.3.44) we find that the corrections to the displacement and temperature are independent of τ, and we therefore only require an initial layer in the velocity. Substituting the stress (4.3.45) into the momentum equation (4.3.42) we arrive at a partial differential equation governing the correction to the velocity

$$V_\tau = \frac{1}{\mathcal{R}}(lf(Y) + mV_Y)_Y. \tag{4.3.48}$$

Motivated by [42], we make the substitution

$$h(Y,\tau) = V + \frac{l}{m}F(Y), \quad F(Y) = \int_0^Y f(s)\,\mathrm{d}s, \tag{4.3.49}$$

which transforms (4.3.48) to

$$h_\tau = Dh_{YY}, \quad D = \frac{m}{\mathcal{R}}, \tag{4.3.50}$$

which must be solved subject to

$$h(0,\tau) = 0, \quad h(Y,0) = \frac{l}{m}F(Y). \tag{4.3.51}$$

The solution to (4.3.50)–(4.3.51) may be found using a Green's function, and is given in [42] as

$$V(Y,\tau) = -\frac{l}{m}\Bigg[F(Y) - \frac{1}{2\sqrt{D\pi\tau}}\int_0^\infty F(s)\Bigg\{\exp\left[-\frac{(Y-s)^2}{4D\tau}\right] - \exp\left[-\frac{(Y+s)^2}{4D\tau}\right]\Bigg\}\,\mathrm{d}s\Bigg]. \tag{4.3.52}$$

Asymptotic matching between V as $\tau \to \infty$ and $\hat{v}_2$ as $t \to 0$ provides the following conditions

$$\hat{v}_2(Y,0) = -\frac{l}{m}F(Y), \quad F(0) = 0, \tag{4.3.53}$$

which now allow (4.3.37) to be satisfied at $t = 0$. Using the $n = 0$ result for the stress (4.3.37) we may eliminate $\hat{v}_{2_Y}$ from (4.3.36), giving a PDE for the temperature

correction in the inner layer

$$\hat{T}_{1_t} = \hat{T}_{1_{YY}} + \frac{\mathrm{Ec}}{\mathcal{R}}\left(-\frac{l}{m}\hat{T}_1 T_0^{l-1}\right) + \hat{\Omega}\hat{A}\exp\left(-\frac{\hat{E}}{T_0}\right)\hat{E}\frac{\hat{T}_1}{T_0^2}. \tag{4.3.54}$$

Once this equation is solved for the temperature, the corrections to the velocity and displacement may be subsequently calculated using (4.3.37) and (4.3.28). As with the outer solution, if we neglect the effects of diffusion and chemical reaction we may write down an explicit solution. In the inner region this exact solution is correct to $O(\varepsilon)$ and is given in terms of the original variables by

$$\hat{T}(t) = T_0 + \varepsilon f(y/\varepsilon)T_0^{-l/m}, \tag{4.3.55}$$

with $T_0(t)$ given by (4.3.15).

Figure 4.12 shows a comparison of numerical and asymptotic dimensional centreline temperature $\tilde{T}(0,t)$ with: no diffusion and no reaction; diffusion and no reaction; no diffusion and reaction; and both diffusion and reaction. In each case the numerical solution, asymptotic solution correct up to $O(\varepsilon)$, leading-order asymptotic solution, and first-order correction are shown. In all cases the asymptotic solution gives an excellent agreement with the numerical solution in the early stages. Unfortunately, for the parameter values used for LX-14, we find that the reaction only becomes important at a non-dimensional temperature $T \sim 2$, by which time the temperature growth due to plastic work is so great that the solution in the centre of band is no longer near the solution away from the band. Since our asymptotic approach uses the outer temperature as the leading-order term, it is unable to accurately describe the stage during which the reaction is important where we see an $O(1)$ departure from the leading-order solution, not an $O(\varepsilon)$ correction. This is not to say that the reaction is unimportant, but simply that our approach taken here is unable to describe the reaction stage well for the parameter values used. In particular, it is worth noting that in the results which include strain hardening, the reaction takes place much later and we observe that the temperature at which significant plastic work takes place is similar to the HMX reaction initiation temperature $\tilde{T} \sim 530\,\mathrm{K}$, see Figure 4.10. Since the results with strain hardening included are the ones calibrated with the experimental data [24], we may conclude that in our model with $n = 0$, the onset of significant plastic work occurs much earlier than observed in experiments, and therefore at a much lower temperature. By reducing the activation energy we can cause the reaction to commence sooner, allowing us to obtain an example result in which the heating due to plastic work and reaction both become significant at a similar time. Figure 4.13 shows the centreline temperature predicted by the rigid-plastic shear band model with the (dimensional) activation energy decreased to $E = 1.324 \times 10^5\ \mathrm{J\,mol^{-1}}$. Panels (a) and (b) show results with no reaction ($\hat{A} = 0$), while panels (c) and (d) show results which account for the Arrhenius reaction term.

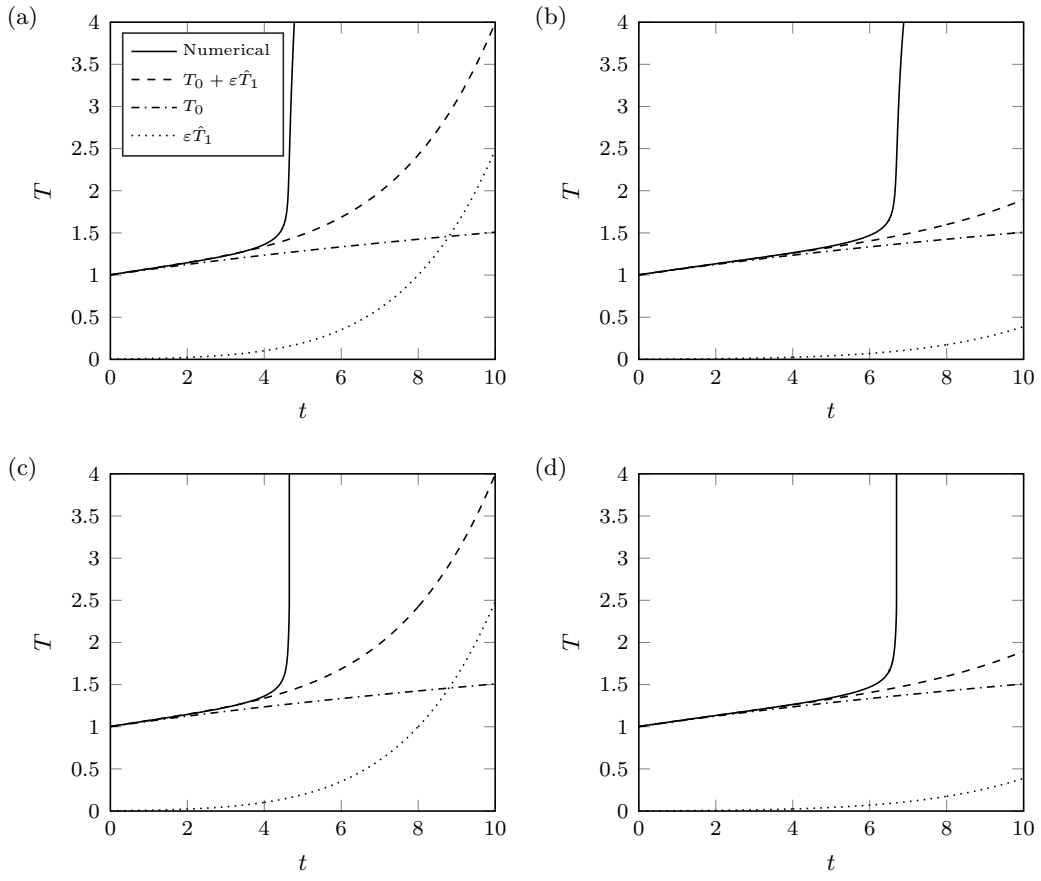

Figure 4.12: Comparison of centreline temperature in the rigid-plastic shear band model with: (a) no diffusion and no reaction; (b) diffusion and no reaction; (c) no diffusion and reaction; and (d) both diffusion and reaction. The results shown in each panel are: numerical ($-$); asymptotic $T_0 + \varepsilon\hat{T}_1$ ($--$); leading-order asymptotic T_0 ($-\cdot$); and first-order correction $\varepsilon\hat{T}_1$ ($\cdot\cdot$).

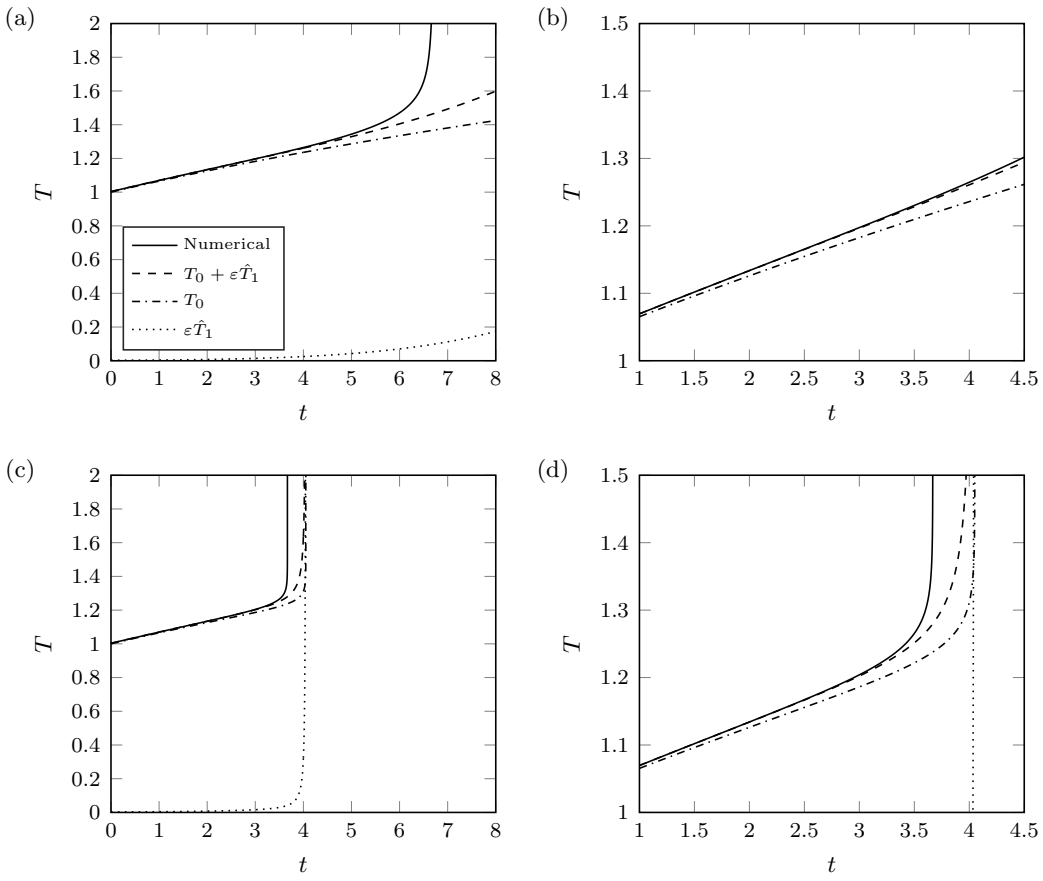

Figure 4.13: Comparison of centreline temperature in the rigid-plastic shear band model with reduced activation energy. Results are shown with: (a,b) diffusion and no reaction; and (c,d) diffusion and reaction. The results shown in each panel are: numerical ($-$); asymptotic $T_0 + \varepsilon\hat{T}_1$ ($--$); leading-order asymptotic T_0 ($-\cdot$); and first-order correction $\varepsilon\hat{T}_1$ ($\cdot\cdot$). Panels (b) and (d) show close-ups of the later stages of panels (a) and (c), respectively.

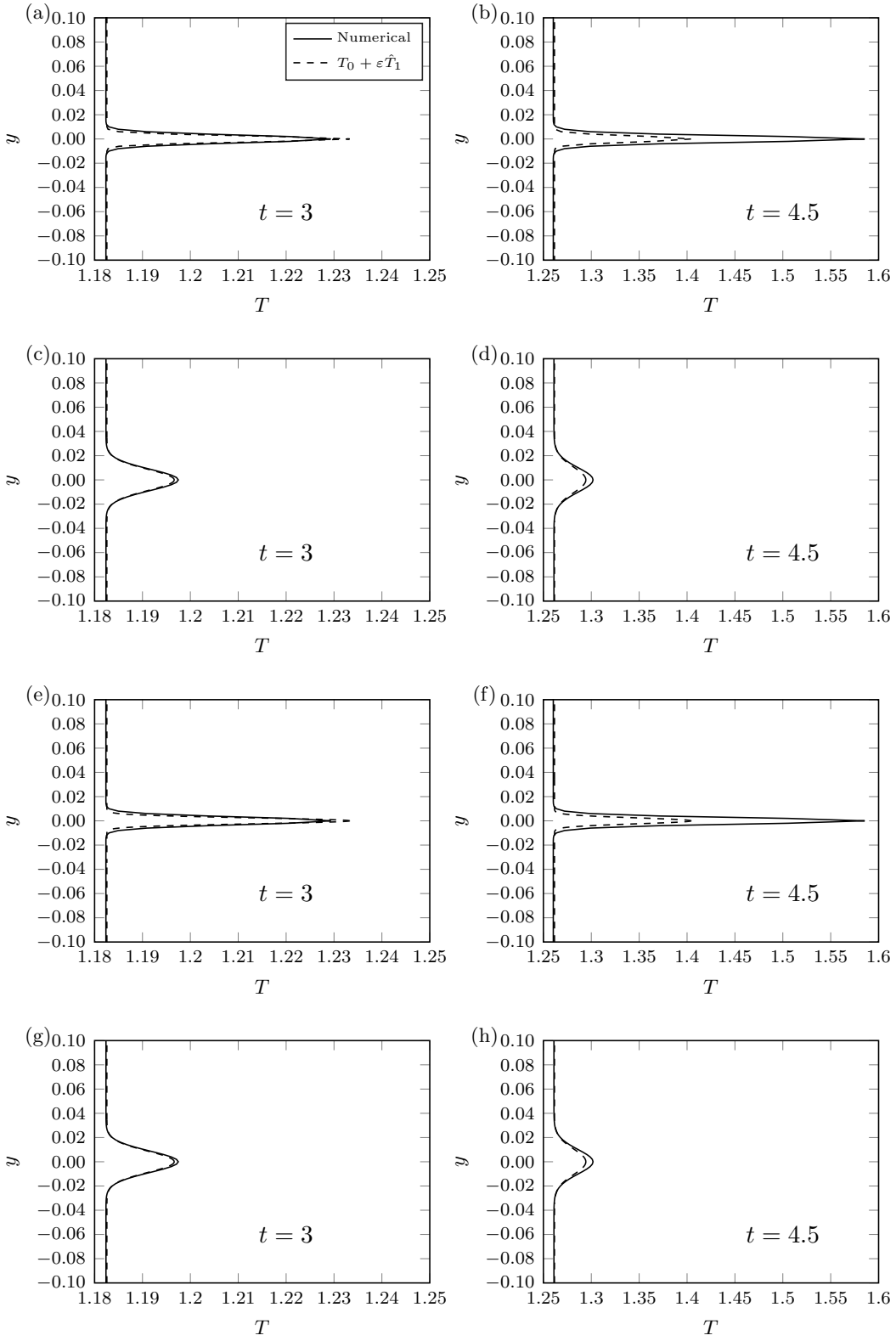

Figure 4.14: Comparison of temperature profiles predicted by the numerical and asymptotic rigid-plastic reactive shear band models with: (a) no diffusion and no reaction; (b) diffusion and no reaction; (c) no diffusion and reaction; and (d) both diffusion and reaction. The results shown in each panel are: numerical (−) and asymptotic $T_0 + \varepsilon \hat{T}_1$ (−−).

Both of the results shown account for diffusion. In this case we see that the the reaction occurs before we observe an $O(1)$ change in the temperature due to plastic work. In particular, this example shows the ability of our asymptotic analysis to capture the onset of shear banding due to chemical reaction, see Figure 4.13 (d).

Figure 4.14 shows a comparison between the temperature predicted by the asymptotic and numerical solutions with/without reaction and diffusion, using the material properties in Table 4.1. The snapshots in the left panels are taken at time $t = 3$, where we see a good agreement in all cases. The snapshots in the right panels are taken at the later time $t = 4.5$. Here we see a better agreement in the cases which include diffusion compared to those which do not. This is due to the fact that the temperature in the band increases more slowly and the temperature gradient is more smoothed out, so that the centreline temperature is nearer to that in the bulk. Thus, as expected, the asymptotic results show better agreement for a longer time when we account for diffusion.

4.4 Summary

The onset of shear banding in a reactive material has been investigated numerically for an elastic-plastic material. We have presented a useful extension to the numerical scheme described in [107] which accounts for the self-heating due to chemical reaction, and demonstrated the usefulness of the scheme in the study of shear localisation in reactive materials. A particular benefit of the elastic-plastic model coupled with the cohesive scheme is its efficiency; in this formulation the mechanical equations are readily solved using the method of characteristics, and all of the viscoplastic behaviour is lumped into the nodal jumps [107]. Such a method allows for an extremely fine mesh, and may therefore be a good candidate for a sub-grid model to be used in boundary or shear layers in larger numerical hydrocode models, as discussed in Chapter 2. Further, the low storage requirements of the method allow for a fine mesh to be used over a relatively large region, so may be used effectively to model the interaction of multiple shear bands [107]. This may be particularly useful in an improved model in which shear bands are triggered by the inhomogeneous structure of the explosive, and not by an imposed perturbation. Since the cohesive numerical scheme allows for a very fine mesh, and can handle large deformations and cracking, it could also be used to investigate other hot spot mechanisms discussed in Chapter 2 such as heating at crack tips, or frictional heating between explosive grains.

A comparison of numerical results has demonstrated the differences between the elastic-plastic model and rigid-plastic approximation used in other models of reactive shear bands [e.g. 23, 24, 80]. Both the elastic- and rigid-plastic models capture the key characteristics of the shear band formation, and both models have their benefits: the elastic model allows one to exploit the nature of the elastic stress waves

to give an efficient numerical scheme, whereas the rigid-plastic model affords the simplification that the plastic and total strain-rate are equivalent. Through the use of a simple one-dimensional model we have been able to qualitatively compare different constitutive models for explosive materials in a computationally efficient way, and, through the asymptotic analysis of Section 4.3.2 and that to follow in Chapter 5, have also been able to validate these results. The viscoplastic model used in this analysis was purposefully kept very general, and it is likely the model presented in this section could provide an excellent framework for investigating different constitutive laws to try and better understand which physical behaviours are most important for ignition. This approach could be extremely useful in aiding the development of future numerical ignition models, such as HERMES, described in Chapter 2.

Asymptotic analysis of the rigid-plastic model allowed for the solution in the band to be determined as a correction to the temperature in the bulk, away from the shear band. Unfortunately, this was only possible upon setting $n = 0$, corresponding to no strain hardening. Simply setting $n = 0$ in the constitutive law for the stress resulted in the early onset of plastic work compared with experiments. In the following chapter, we will analyse the elastic-plastic model using similar asymptotic techniques, and show that results can be obtained even in the presence of hardening.

Chapter 5

Boundary Layer Analysis for the Initiation of Reactive Shear Bands

In this chapter we present a boundary layer analysis to describe the onset of shear localisation in a reactive material. Thermal softening effects play a key role in the initiation and development of shear bands, and so it is reasonable to assume that the additional heating due to chemical reactions occurring in the material will affect the rate of plastic work in the material, which in turn increases the tendency for a shear band to form. Models of shear localisation in reactive materials typically resort to numerical solution [e.g. 3, 24]. However, in [80] a so-called "Thermal Explosion Theory" is developed for a rigid-plastic material under the assumption that most variables are spatially homogenous. This allows for the identification of three distinct periods: an induction stage, a reaction stage, and a post-reaction stage. In the initial stage the plastic work, which is assumed spatially homogenous, causes the temperature to increase to that required for a significant reaction. The process then enters the reaction stage, in which heating due to chemical reaction dominates. Once the reaction has reached completion, the process enters the final stage where the temperature increase is dominated by plastic work once again. Estimates for the induction time are given from this approximate theory, and from a more rigorous asymptotic analysis where the strain hardening parameter takes on special values corresponding to no strain hardening and a linear dependence of stress with strain [80]. In the asymptotic analysis the large activation energy is exploited in order to determine the perturbation to the temperature.

Here, we exploit the large activation energy in conjunction with the asymptotic analysis of inert shear bands in [38] in order to develop an asymptotic theory for shear bands which accounts for the effects of heating due to mechanical dissipation and chemical reaction simultaneously. In Section 5.1 we give the appropriate boundary conditions to supplement the one-dimensional model for reactive shear

bands presented in Chapter 4, and take the constitutive law for the strain-rate to be that in [38], which is convenient for the asymptotic analysis that follows. The governing equations are recast in non-dimensional form using a thermal length scale, which is typically much shorter than the sample width. This allows us to make the simplifying assumption that the plates are effectively an infinite distance from the shear band, consistent with the physical observation that the shear band width is typically much smaller than the size of the slab. Motivated by [38] we use an inhomogeneity in the heat flux as the stimulus for localised plastic deformation, and treat the problem as a perturbation to the elastic solution.

In Section 5.2 the thin zone of localisation is treated as a boundary layer, and scalings for the plastic strain-rate and activation energy are introduced. In Section 5.2.1 the solution for the early-time elastic stage is given analytically in terms of the imposed heat flux inhomogeneity. In Section 5.2.2 the simultaneous onset of significant plastic work and reaction within the localisation zone is considered. The asymptotic analysis reduces the problem to a pair of coupled nonlinear equations which govern the perturbations to the temperature and stress in the band. These are solved in conjunction with an auxiliary equation which determines a critical reaction timescale. In Section 5.2.3 we make the assumption that the reaction is considered to be asymptotically zero during the initial stages of heating resulting in a three-stage problem, similar to [80]. However, our three stages correspond to the early elastic stage, an induction stage where heating is dominated by plastic work, and a reaction stage where, in contrast to [80], both heating due to plastic work and reaction are accounted for. We adapt our model to replicate the approximate analysis in [80], and make comparisons between our boundary layer approaches and the thermal explosion theory in Section 5.2.4.

In Section 5.2.5 we consider the case where the heating due to plastic work is asymptotically zero for the entire duration of the shear banding process. In this limit it is shown that our reactive shear band model is equivalent to a model for the ignition of a half space due to heating at the boundary [78]. Strain hardening effects are considered for an inert model in Section 5.3. In Section 5.4 the results from the boundary layer solution are compared with the numerical solution found using the cohesive scheme described in Chapter 4. In Section 5.5 the equations from the boundary layer analysis are expressed in terms of three new non-dimensional parameters which govern the growth of the perturbations to the temperature and stress in the centre of the band. The results are compared with the inert case [38] and a criterion for the initiation of reactive shear bands is discussed.

5.1 Reactive shear band model

The governing equations are those in the previous section (4.1.1)–(4.1.5), which we restate here,

$$\rho\tilde{v}_{\tilde{t}} = \tilde{s}_{\tilde{y}}, \qquad \text{momentum balance;} \tag{5.1.1}$$

$$\rho c\tilde{T}_{\tilde{t}} = \kappa\tilde{T}_{\tilde{y}\tilde{y}} + \beta\tilde{s}\dot{\Gamma} + \rho\Omega A\exp(-E/(R\tilde{T})), \qquad \text{energy balance;} \tag{5.1.2}$$

$$\tilde{s}_{\tilde{t}} = G(\tilde{v}_{\tilde{y}} - \dot{\Gamma}), \qquad \text{elastic relationship;} \tag{5.1.3}$$

$$\dot{\Gamma} = \dot{\Gamma}(\tilde{s}, \tilde{T}, \Gamma), \qquad \text{plastic flow law;} \tag{5.1.4}$$

$$\Gamma = \int_0^{\tilde{t}} \dot{\Gamma}(t')\,\mathrm{d}t', \qquad \text{plastic strain.} \tag{5.1.5}$$

On the top and bottom of the slab we impose the boundary conditions

$$\tilde{v}(\pm L, \tilde{t}) = \pm\tilde{v}_0, \quad \tilde{T}(\pm L, \tilde{t}) = \tilde{T}_0, \tag{5.1.6}$$

with appropriate compliance of the stress. The initial conditions are taken to correspond to the uniform shearing solution with a constant boundary temperature, given by

$$\tilde{v}(\tilde{y}, 0) = \omega\tilde{y}, \quad \tilde{s}(\tilde{y}, 0) = \tilde{s}_0, \quad \dot{\Gamma}(\tilde{y}, 0) = \omega, \quad \Gamma(\tilde{y}, 0) = 0, \quad \tilde{T}(\tilde{y}, 0) = \tilde{T}_0, \tag{5.1.7}$$

where ω is the nominal strain-rate. Specification of an initial stress $\tilde{s}_0 > 0$ corresponds to starting the physical problem nearer to the onset of plastic deformation [38].

In order to initiate a shear band it is necessary to introduce some external localised stimulus. For this we consider an inhomogeneity in the heat flux placed at $\tilde{y} = 0$ as in [38], though other choices are available [e.g. 24, 39, 42, 80]. The heat flux disturbance is introduced as

$$\kappa\tilde{T}_{\tilde{y}}(0^-, \tilde{t}) = -\kappa\tilde{T}_{\tilde{y}}(0^+, \tilde{t}) = Q(\tilde{t}) \geq 0, \quad \tilde{t} > 0, \tag{5.1.8}$$

where κ is the thermal conductivity and $Q(\tilde{t})$ is assumed to be of small magnitude and short duration. Owing to symmetry considerations, we treat only the upper half plane, and solve the governing equations subject to the following conditions on the velocity and stress along the centreline

$$\tilde{v}(0, \tilde{t}) = 0, \quad \tilde{s}_{\tilde{y}}(0, \tilde{t}) = 0, \quad \tilde{t} > 0. \tag{5.1.9}$$

In the following we choose to adopt a strain-rate model which depends only on the stress and temperature. The analysis may be extended to account for hardening effects, but this introduces additional complexities; a discussion of the effects of hardening can be found in Section 5.3. In the interest of obtaining a clear insight into how the reaction affects the onset of shear bands, and to allow for a more direct

comparison with [38], the effects of strain hardening are not considered here. We use the model proposed in [38] which accounts for thermal softening and strain-rate dependence, and takes the following exponential form

$$\dot{\Gamma}(\tilde{s},\tilde{T}) = \dot{\Gamma}^* \exp\{-[B_1^{-1}(\tilde{T}_\mathrm{p} - \tilde{T}) + B_2^{-1}(\tilde{s}_\mathrm{p} - \tilde{s})]\}, \tag{5.1.10}$$

where $\dot{\Gamma}^*$ is a dimensional reference strain-rate, and the constants $\tilde{T}_\mathrm{p}$ and $\tilde{s}_\mathrm{p}$ are the critical values of temperature and stress below which the plastic strain-rate is exponentially small. It is required that $\tilde{T}_\mathrm{p} > \tilde{T}_0$ and $\tilde{s}_\mathrm{p} > \tilde{s}_0$ so that the problem is started in the elastic stage in which plastic strain is initially negligible. The parameters B_1 and B_2 are related to strain-rate sensitivity M and thermal sensitivity P via the definitions

$$M \equiv \frac{1}{\tilde{s}_\mathrm{p}} \frac{\partial \tilde{s}}{\partial \log \dot{\Gamma}} = \frac{B_2}{\tilde{s}_\mathrm{p}}, \quad P \equiv -\frac{\tilde{T}_\mathrm{p}}{\tilde{s}_\mathrm{p}} \frac{\partial \tilde{s}}{\partial \tilde{T}} = \left(\frac{B_2}{\tilde{s}_\mathrm{p}}\right) \Big/ \left(\frac{B_1}{\tilde{T}_\mathrm{p}}\right). \tag{5.1.11}$$

This strain-rate model is a good approximation of more typically adopted power law models, but offers a form which is much more convenient for the boundary layer analysis to follow. The exponential law (5.1.10) is compared with a power law model in Appendix B.

We introduce non-dimensional variables, which are related to the dimensional variables by

$$\begin{gathered} t = \tilde{t}/t^*, \quad y = \tilde{y}/l, \quad v = \tilde{v}/\tilde{v}_0, \quad s = \tilde{s}/\tilde{s}_0, \\ \dot{\gamma} = \dot{\Gamma}/\dot{\Gamma}_0, \quad T = \tilde{T}/\tilde{T}_0, \quad q = Q/q_0, \end{gathered} \tag{5.1.12}$$

and the parameters

$$\begin{gathered} t^* = \frac{\tilde{s}_0}{G\dot{\Gamma}_0}, \quad l = \left(\frac{\kappa \tilde{s}_0}{\rho c G \dot{\Gamma}_0}\right)^{1/2}, \quad \dot{\Gamma}_0 = \frac{\tilde{v}_0}{l}, \quad \Gamma_0 = t^* \dot{\Gamma}_0, \quad \hat{\omega} = \frac{\omega}{\dot{\Gamma}_0}, \\ \hat{\rho} = \frac{\kappa \dot{\Gamma}_0}{c \tilde{s}_0}, \quad \lambda = \frac{\beta \tilde{s}_0^2}{\rho c G \tilde{T}_0}, \quad \hat{E} = \frac{E}{R\tilde{T}_0}, \quad \hat{\Omega} = \frac{\Omega}{c\tilde{T}_0}, \quad \hat{A} = At^*, \quad q_0 = \frac{\kappa \tilde{T}_0}{l}. \end{gathered} \tag{5.1.13}$$

The choice of the thermal length scale $l \ll L$ places the rigid boundaries at $y = \pm L/l$. We choose to exploit the physical observation that shear bands are typically very thin compared with the sample size, taking the limit $L/l \to \infty$ so that the material sample occupies the space $-\infty < y < \infty$ [38].

To fix ideas we give typical values of the material properties for LX-14. Using parameter values found in [3, 72, 80, 87, 93], we have $\rho = 1.849 \times 10^3\,\mathrm{kg\,m^{-3}}$, $G \approx 3 \times 10^9\,\mathrm{Pa}$, $c = 1.130 \times 10^3\,\mathrm{J\,kg^{-1}\,K^{-1}}$, $\kappa = 4.390 \times 10^{-1}\,\mathrm{W\,m^{-1}\,K^{-1}}$, $M \approx 0.1$, $P \approx 1$, $\beta = 1$, $\omega = 10 \times 10^3\,\mathrm{s^{-1}}$, $L = 3.47 \times 10^{-3}\,\mathrm{m}$, $\tilde{T}_0 = 3 \times 10^2\,\mathrm{K}$, $\tilde{s_0} \approx 4 \times 10^7\,\mathrm{Pa}$, $\Omega = 5.950 \times 10^6\,\mathrm{J\,kg^{-1}}$, $A = 5 \times 10^{19}\,\mathrm{s^{-1}}$, $E = 2.206 \times 10^5\,\mathrm{J\,mol^{-1}}$ and $R = 8.314\,\mathrm{J\,mol^{-1}\,K^{-1}}$. This gives the following order of magnitude estimates for

the parameters:

$$t^* \sim 10^{-12}\,\mathrm{s}, \quad l \sim 10^{-9}\,\mathrm{m}, \quad \dot{\Gamma}_0 \sim 10^9\,\mathrm{s}^{-1}, \quad \Gamma_0 \sim 10^{-2}, \quad \hat{\omega} \sim 10^{-7},$$
$$\hat{\rho} \sim 10^{-2}, \quad \lambda \sim 10^{-3}, \quad \hat{E} \sim 10^2, \quad \hat{\Omega} \sim 10, \quad \hat{A} \sim 10^8, \quad q_0 \sim 10^{11}. \tag{5.1.14}$$

The material LX-14 is HMX based, and we expect the above estimates to be typical of most HMX based explosives. Choosing a representative strain-rate based on the thermal length scale l gives an extremely high value of $\dot{\Gamma}_0 \sim 10^9\,\mathrm{s}^{-1}$. While this may be typical of the strain-rate in a fully-formed band [e.g. 107], a more typical value of the strain-rate found within a developing shear band would be in the range $\dot{\Gamma}_0 \sim 10^3$ to $10^6\,\mathrm{s}^{-1}$ [38, 101, 107]. In [38, 39] the scaling for the strain-rate is selected to be representative of that within a shear band, and is independent from the length scale. In the following boundary layer analysis we will exploit this freedom in choosing our scaling for the strain-rate in order to achieve the designated scalings for some of our non-dimensional parameters.

The non-dimensional governing equations for the shearing problem in the upper-half plane read

$$\hat{\rho} v_t = s_y, \tag{5.1.15}$$

$$T_t = T_{yy} + \lambda s \dot{\gamma} + \hat{\Omega}\hat{A} \exp\left(-\frac{\hat{E}}{T}\right), \tag{5.1.16}$$

$$s_t = v_y - \dot{\gamma}, \tag{5.1.17}$$

$$\dot{\gamma} = \frac{\dot{\Gamma}^*}{\dot{\Gamma}_0} \exp\left\{-\left[\frac{\tilde{T}_0}{B_1}(T_\mathrm{p} - T) + \frac{\tilde{s}_0}{B_2}(s_\mathrm{p} - s)\right]\right\}, \tag{5.1.18}$$

where $T_\mathrm{p} = \tilde{T}_\mathrm{p}/\tilde{T}_0 > 1$ and $s_\mathrm{p} = \tilde{s}_\mathrm{p}/\tilde{s}_0 > 1$ are the non-dimensional critical temperature and stress, respectively. Since we are neglecting hardening effects (i.e. strain dependence), the non-dimensional counterpart of (5.1.5) has been omitted.

5.2 Boundary layer analysis

We seek a solution of (5.1.15)–(5.1.18) in the form of a perturbation to the elastic ($\dot{\gamma} = 0$) solution. In the following analysis, a thin zone centred around $y = 0$ in which significant plastic work and reaction take place is identified. Outside of this region both the heating due to plastic work and heating due to reaction are exponentially small, and far from the centre of the localisation zone the elastic solution remains valid. The solution in the thin zone around $y = 0$ is matched on to the elastic solution via an intermediate diffusive zone. The equations governing the behaviour of the perturbations to the elastic stress and temperature along the centreline will be obtained.

By differentiating (5.1.15) with respect to y and integrating the result with respect

to t we obtain an expression for v_y in terms of the stress. This is substituted into the elastic relationship (5.1.17) to give a single equation relating the stress and strain-rate. The governing equations then read

$$s_t = \hat{\rho}^{-1} \int_0^t s_{yy}(y,t')\,\mathrm{d}t' + \hat{\omega} - \dot{\gamma}, \tag{5.2.1}$$

$$T_t = T_{yy} + \lambda s\dot{\gamma} + \hat{\Omega}\hat{A}\exp\left(-\frac{\hat{E}}{T}\right), \tag{5.2.2}$$

where the velocity has been eliminated using the initial condition $v(y,0) = \hat{\omega}y$. The plastic strain-rate is still given by (5.1.18). These equations are to be solved subject to the initial and boundary conditions

$$s(y,0) = 1, \qquad T(y,0) = 1, \tag{5.2.3}$$

$$s_y(0,t) = 0, \qquad T_y(0,t) = -q(t), \qquad T(\infty,t) = 1. \tag{5.2.4}$$

In order to proceed with the boundary layer analysis, we must identify a small parameter ε. This is introduced through the ratios B_1/T_0 and B_2/s_0 by the relations

$$\frac{B_1}{\tilde{T}_0} = \beta_1^{-1}\varepsilon, \quad \frac{B_2}{\tilde{s}_0} = \beta_2^{-1}\varepsilon, \quad 0 < \varepsilon \ll 1, \tag{5.2.5}$$

where β_1 and β_2 are $O(1)$ constants. Such a scaling is typical of materials which exhibit shear banding [38]. It is assumed that the plastic strain-rate function can be multiplicatively scaled [38], so that

$$\frac{\dot{\Gamma}^*}{\dot{\Gamma}_0} = \dot{\gamma}_0\varepsilon^{-1/2}, \tag{5.2.6}$$

and the plastic strain-rate takes the non-dimensional form

$$\dot{\gamma}(s,T) = \dot{\gamma}_0\varepsilon^{-1/2}\exp\{-\varepsilon^{-1}[\beta_1(T_\mathrm{p} - T) + \beta_2(s_\mathrm{p} - s)]\}, \tag{5.2.7}$$

where $\dot{\gamma}_0$ is $O(1)$. The non-dimensional parameter $\hat{\rho} = \kappa\dot{\Gamma}_0/c\tilde{s}_0$ is typically small in materials which exhibit shear banding effects; for LX-14 we find $\hat{\rho} \sim 10^{-2}$. In order to take advantage of this, we introduce the scaling

$$\hat{\rho} = \varepsilon\hat{\rho}_0, \tag{5.2.8}$$

where $\hat{\rho}_0$ is $O(1)$.

We also exploit the largeness of the product of the pre-exponential factor $\hat{A}$ and heat of reaction $\hat{\Omega}$ by setting

$$\hat{\Omega}\hat{A} = \hat{A}_0\frac{\hat{E}^{1/2}}{T_\mathrm{R}}\exp\left(\frac{\hat{E}}{T_\mathrm{R}}\right), \tag{5.2.9}$$

where T_{R} is the (known) non-dimensional critical reaction temperature, i.e. the temperature at which significant reaction first occurs. The parameter $\hat{A}_0$ is $O(1)$. The reaction temperature will later be used to identify a reaction time scale t_{R}. As in high activation energy asymptotic analyses [e.g. 68], the small parameter ε, non-dimensional activation energy and the critical reaction temperature are related by

$$\varepsilon = \frac{T_{\mathrm{R}}^2}{\hat{E}}. \tag{5.2.10}$$

The assumed asymptotic scalings (5.2.5), (5.2.6), (5.2.8) and (5.2.9) are selected for facilitation of the asymptotic analysis and are qualitatively consistent with data found in the literature [3, 72, 80, 87, 93]. As discussed in the previous section, the representative strain-rate $\dot{\Gamma}_0$ may be used to bring the parameter values closer to their designated scalings. For instance, assuming $T_{\mathrm{R}} \sim T_{\mathrm{p}}$ and varying $\dot{\Gamma}_0$ between 10^3 and 10^6 gives $t^* \sim 10^{-9}$ to 10^{-6}, $l \sim 10^{-9}$, $\Gamma_0 \sim 10^{-2}$, $\hat{\omega} \sim 10^{-4}$ to 1, $\hat{\rho} \sim 10^{-7}$ to 10^{-4}, $\lambda \sim 10^{-3}$, $\hat{E} \sim 10^2$ to 10^3, $\hat{\Omega} \sim 10$, $\hat{A} \sim 10^{10}$ to 10^{14}, $q_0 \sim 10^{11}$.

Both relations (5.2.5) and (5.2.10) are consistent when we consider materials in which onset of significant plastic work and onset of significant reaction occur over similar timescales, these we refer to as "reactive shear bands". For materials in which localisation of plastic work occurs well before significant reaction (or vice-versa) these relations should be adjusted so that the appropriate dominant plastic or reaction properties are related through different powers of ε.

5.2.1 Elastic stage

In the initial stages of deformation the plastic strain-rate is initially exponentially small. This remains the case until the stress and temperature have risen sufficiently to make the argument of the exponent in (5.2.7) positive. Additionally, the Arrhenius source term is exponentially small until the critical reaction temperature T_{R} is reached. Thus, for early times the solution must satisfy

$$s_t = \hat{\omega}, \quad s(y,0) = 1, \tag{5.2.11}$$

$$T_t = T_{yy}, \quad T(y,0) = 1, \quad T_y(0,t) = -q(t), \quad T(\infty,1) = 1. \tag{5.2.12}$$

Equation (5.2.11) may be integrated directly to give the elastic stress

$$s_{\mathrm{e}}(y,t) = 1 + \hat{\omega}t, \tag{5.2.13}$$

which we label using a subscript 'e'. The method we use to solve (5.2.12) can be found in [22], but we outline the the key steps here. We look for a solution $T_{\mathrm{e}} = 1 + \theta(y,t)$, where θ satisfies the more simple problem of heat flow in a semi-infinite solid with

zero initial temperature and time-dependent heat flux at the origin, i.e.

$$\theta_t = \theta_{yy}, \quad \theta(y,0) = 0, \quad \theta_y(0,t) = -q(t), \quad \theta(\infty,1) = 0. \tag{5.2.14}$$

If we then consider the flux $F = -\theta_y$, we observe it satisfies $F_t = F_{yy}$ with $F(0,t) = q(t)$. In the simplest case $q(t) = 1$ this has the standard solution [e.g. 22]

$$F^{\mathrm{c}} = \operatorname{erfc} \frac{y}{2\sqrt{t}}, \tag{5.2.15}$$

where the superscript 'c' denotes the solution with constant heat flux at the boundary. By integration, the corresponding solution to (5.2.14) with $q(t) = 1$ is

$$\theta^{\mathrm{c}} = \int_y^\infty \operatorname{erfc} \frac{y'}{2\sqrt{t}} \, \mathrm{d}y'. \tag{5.2.16}$$

In order to find the solution for a time dependent flux at the boundary we appeal to Duhamel's theorem [22], which states that if $F = F^c(y,t)$ represents the temperature at y at time t for a solid in which the initial temperature is zero with unit boundary temperature, then the solution where the boundary temperature is a function of time only, in our case $q(t)$, is

$$F(y,t) = \int_0^t q(t') \frac{\partial}{\partial t} F^{\mathrm{c}}(y, t-t') \, \mathrm{d}t'. \tag{5.2.17}$$

Thus, the solution $\theta(y,t)$ with heat flux $q(t)$ is

$$\begin{aligned}
\theta(y,t) &= \int_0^t q(t') \frac{\partial}{\partial t} \theta^{\mathrm{c}}(y, t-t') \, \mathrm{d}t', && (5.2.18)\\
&= \int_0^t q(t') \frac{\partial}{\partial t} \int_y^\infty \operatorname{erfc} \frac{y'}{2\sqrt{(t-t')}} \, \mathrm{d}y' \, \mathrm{d}t', && (5.2.19)\\
&= \int_0^t q(t') \int_y^\infty \frac{y'}{2\sqrt{\pi (t-t')^3}} e^{-\frac{y'^2}{4(t-t')}} \, \mathrm{d}y' \, \mathrm{d}t', && (5.2.20)\\
&= \int_0^t q(t') \frac{e^{-\frac{y^2}{4(t-t')}}}{\sqrt{\pi (t-t')}} \, \mathrm{d}t'. && (5.2.21)
\end{aligned}$$

Finally, the inert elastic solution is given by

$$T_{\mathrm{e}}(y,t) = 1 + \delta \int_0^t h(t') \frac{e^{-\frac{y^2}{4(t-t')}}}{[\pi (t-t')]^{1/2}} \, \mathrm{d}t', \tag{5.2.22}$$

where the heat flux inhomogeneity is represented as

$$q(t) = \delta h(t), \quad 0 \le h(t) \le 1. \tag{5.2.23}$$

The scaling of the heat flux is such that $0 < \varepsilon \ll \delta \ll 1$, so that δ is sufficiently large to introduce localisation, but still small enough to be negligible in comparison with physical factors that control the evolution of the shear band. The ordering of the small parameters has the physical interpretation that the thermal stimulus is sufficiently strong to cause the onset of plastic localisation, but is not so strong that it causes a rapid departure from the elastic response of the material. This early time solution will be used as the basis of our asymptotic analysis.

5.2.2 Onset of reactive shear band – Approach I

In this section we develop a boundary layer analysis which splits the problem into an elastic stage and a plastic-reactive stage, where the latter simultaneously accounts for heating due to plastic work and reaction. For ease of later discussion this will be referred to as Approach I.

Beyond the critical plastic threshold, $\dot{\gamma}$ becomes large due to the multiplicative scaling. This motivates the definition of a critical time scale $t_{\rm p}$ at which the onset of significant plastic work occurs, i.e. the time at which the exponential in (5.2.7) becomes $O(1)$. Therefore $t_{\rm p}$ is defined by the smallest solution of

$$\beta_1[T_{\rm p} - T_{\rm e}(0, t_{\rm p})] + \beta_2[s_{\rm p} - s_{\rm e}(0, t_{\rm p})] = 0. \tag{5.2.24}$$

Given that the stimulus for the shear band is placed along the centreline, the plastic work first becomes significant near $y = 0$, and occurs at time $t = t_{\rm p}$. At this stage the solution will be a perturbation of the elastic solution (5.2.22)–(5.2.13). The temperature in the shear band will increase due to plastic work, until the critical reaction temperature is reached. As previously discussed, we consider the case where the subsequent reaction occurs on a similar timescale to the growth of the plastic work term. It is possible to consider a model in which the plastic and reactive behaviour occur on disparate timescales, but we restrict ourselves to the most critical case.

We introduce new independent variables ξ and τ such that

$$y = \varepsilon\xi, \quad t = t_{\rm p} + \varepsilon\tau, \quad \xi > 0, \quad \tau > -\frac{t_{\rm p}}{\varepsilon} \to -\infty, \tag{5.2.25}$$

which are appropriate to describe the inner solution in the boundary layer near $y = 0$, where the localised plastic straining first begins to occur. In order to identify the onset of the reaction we define a critical reaction timescale $\tau_{\rm R}$ (related to the "original time" by $t_{\rm R} = t_{\rm p} + \varepsilon\tau_{\rm R}$) as the solution of

$$T_{\rm R} = T_{\rm e}(0, t_{\rm p} + \varepsilon\tau_{\rm R}) + \varepsilon T_1(0, \tau_{\rm R}) + o(\varepsilon), \tag{5.2.26}$$

where the function T_1 is still to be determined as part of the solution.

In the inner layer we expand the temperature and stress in powers of ε as

$$T = T_{\rm e}(\varepsilon\xi, t_{\rm p} + \varepsilon\tau) + \varepsilon T_1(\xi,\tau) + \varepsilon^{3/2} T_2(\xi,\tau) + \cdots, \tag{5.2.27}$$

$$s = s_{\rm e}(\varepsilon\xi, t_{\rm p} + \varepsilon\tau) + \varepsilon s_1(\xi,\tau) + \varepsilon^{3/2} s_2(\xi,\tau) + \cdots. \tag{5.2.28}$$

Physically we expect the solution in the shear band to be driven by plastic work and the chemical reaction. The chosen scalings in the expansion allow for the appropriate balance between the plastic work and reaction terms in the governing equations (5.2.1)–(5.2.2). We expand the elastic parts of the solution as

$$T_{\rm e}(\varepsilon\xi, t_{\rm p} + \varepsilon\tau) = T_{\rm e}(0, t_{\rm p}) + \varepsilon(a\tau - b\xi) + o(\varepsilon), \tag{5.2.29}$$

$$s_{\rm e}(\varepsilon\xi, t_{\rm p} + \varepsilon\tau) = s_{\rm e}(0, t_{\rm p}) + \varepsilon\hat{\omega}\tau + o(\varepsilon), \tag{5.2.30}$$

where

$$a = T_{{\rm e}_t}(0, t_{\rm p}) = \delta \int_0^{t_{\rm p}} [\pi(t_{\rm p} - t')]^{-1/2} h'(t')\,{\rm d}t', \tag{5.2.31}$$

$$b = -T_{{\rm e}_y}(0, t_{\rm p}) = \delta h(t_{\rm p}). \tag{5.2.32}$$

Substitution of the expansions for the temperature and stress into (5.2.1)–(5.2.2) gives

$$\left[s_1 + \varepsilon^{1/2} s_2 + \cdots\right]_\tau = \hat{\rho}_0^{-1} \int_{-\infty}^{\tau} \left[\varepsilon^{-1} s_1 + \varepsilon^{-1/2} s_2 + \cdots\right]_{\xi\xi} {\rm d}\tau' - \dot{\gamma}, \tag{5.2.33}$$

$$\begin{aligned}\left[T_1 + \varepsilon^{1/2} T_2 + \cdots\right]_\tau = {} & \left[\varepsilon^{-1} T_1 + \varepsilon^{-1/2} T_2 + \cdots\right]_{\xi\xi} \\ & + \lambda\left[s_{\rm e} + \varepsilon s_1 + \cdots\right]\dot{\gamma} + \hat{\Omega}\hat{A}\exp\left(-\frac{\hat{E}}{T}\right),\end{aligned} \tag{5.2.34}$$

where the expansions of the plastic strain-rate and Arrhenius source term are given by

$$\dot{\gamma} = \dot{\gamma}_0 \varepsilon^{-1/2} \left\{\exp[\beta_3\tau - \beta_1 b\xi + \beta_1 T_1 + \beta_2 s_1] + o(1)\right\}, \tag{5.2.35}$$

and

$$\begin{aligned}\hat{\Omega}\hat{A}\exp\left(-\frac{\hat{E}}{T}\right) &= \hat{A}_0 \frac{\hat{E}^{1/2}}{T_{\rm R}} \exp\left(\frac{\hat{E}}{T_{\rm R}} - \frac{\hat{E}}{T}\right) \\ &= \hat{A}_0 \varepsilon^{-1/2} \exp\left\{\frac{T_{\rm R}}{\varepsilon}\left(1 - \frac{T_{\rm R}}{T_{\rm e}(0,t_{\rm p}) + \varepsilon(a\tau - b\xi + T_1) + o(\varepsilon)}\right)\right\},\end{aligned} \tag{5.2.36}$$

respectively. Here $\beta_3 = \beta_1 a + \beta_2\hat{\omega} > 0$, justified by the observation that $\beta_2\hat{\omega} > 0$ and $a \sim O(\delta)$ is negligible. Using (5.2.26) we may rewrite the temperature expansion as

a correction to the reaction temperature T_{R}, that is

$$\begin{aligned} T &= T_{\mathrm{e}}(0,t_{\mathrm{p}}) + \varepsilon(a\tau - b\xi + T_1) + o(\varepsilon), \\ &= T_{\mathrm{e}}(0,t_{\mathrm{p}}) + \varepsilon(a\tau_{\mathrm{R}} + T_1(0,\tau_{\mathrm{R}})) + \varepsilon(a(\tau-\tau_{\mathrm{R}}) - b\xi + T_1 - T_1(0,\tau_{\mathrm{R}})) + o(\varepsilon), \\ &= T_{\mathrm{R}} + \varepsilon(a(\tau-\tau_{\mathrm{R}}) - b\xi + T_1 - T_1(0,\tau_{\mathrm{R}})) + o(\varepsilon), \end{aligned} \tag{5.2.37}$$

so that (5.2.36) reads

$$\hat{\Omega}\hat{A}\exp\left(-\frac{\hat{E}}{T}\right) = \hat{A}_0\varepsilon^{-1/2}\exp\left\{a(\tau-\tau_{\mathrm{R}}) - b\xi + T_1 - T_1(0,\tau_{\mathrm{R}}) + o(1)\right\}, \tag{5.2.38}$$

and we observe that the onset of reaction is delayed by the shift in time τ_{R}.

We now solve the sequence of boundary value problems which arise from considering powers of ε. At $O(\varepsilon^{-1})$ we have the problem

$$\int_{-\infty}^{\tau} s_{1_{\xi\xi}}\,\mathrm{d}\tau = 0, \quad s_{1_\xi}(0,\tau) = 0, \quad s_1(\xi,-\infty) = 0, \tag{5.2.39}$$

$$T_{1_{\xi\xi}} = 0, \quad T_{1_\xi}(0,\tau) = 0, \quad T_1(\xi,-\infty) = 0. \tag{5.2.40}$$

Integrating both equations twice with respect to ξ and applying the boundary conditions at $\xi = 0$ reveals that the solutions must be functions of time τ only:

$$T_1(\xi,\tau) = f_1(\tau), \quad f_1(-\infty) = 0, \quad s_1(\xi,\tau) = g_1(\tau), \quad g_1(-\infty) = 0, \tag{5.2.41}$$

where $f_1(\tau)$ and $g_1(\tau)$ are to be determined by matching with the outer solution. We next solve the problem at $O(\varepsilon^{-1/2})$:

$$\int_{-\infty}^{\tau} s_{2_{\xi\xi}}\,\mathrm{d}\tau = \hat{\rho}_0\dot{\gamma}_0\exp[\beta_3\tau - \beta_1 b\xi + \beta_1 f_1 + \beta_2 g_1], \tag{5.2.42}$$

$$s_{2_\xi}(0,\tau) = 0, \quad s_2(\xi,-\infty) = 0, \tag{5.2.43}$$

$$\begin{aligned} T_{2_{\xi\xi}} = {} & -\lambda\dot{\gamma}_0(1+\hat{\omega}t_{\mathrm{p}})\exp[\beta_3\tau - \beta_1 b\xi + \beta_1 f_1 + \beta_2 g_1] \\ & - \hat{A}_0\exp[a(\tau-\tau_{\mathrm{R}}) - b\xi + f_1(\tau) - f_1(\tau_{\mathrm{R}})], \end{aligned} \tag{5.2.44}$$

$$T_{2_\xi}(0,\tau) = 0, \quad T_2(\xi,-\infty) = 0. \tag{5.2.45}$$

Differentiating (5.2.42) with respect to τ, integrating the result twice with respect to ξ and applying boundary the boundary condition at $\xi = 0$ gives

$$s_2(\xi,\tau) = \frac{\hat{\rho}_0\dot{\gamma}_0}{\beta_1 b}\left(\xi + \frac{\exp(-\beta_1 b\xi)}{\beta_1 b}\right) \times \frac{\mathrm{d}}{\mathrm{d}\tau}\{\exp[\beta_3\tau + \beta_1 f_1(\tau) + \beta_2 g_1(\tau)]\} + g_2(\tau), \tag{5.2.46}$$

where g_2 is an as-yet undetermined function of τ which must decay as $\tau \to -\infty$. Similarly, integrating (5.2.44) twice with respect to ξ and applying the boundary

condition gives

$$T_2(\xi,\tau) = -\frac{\lambda\dot{\gamma}_0(1+\hat{\omega}t_\mathrm{p})}{\beta_1 b}\left(\xi + \frac{\exp(-\beta_1 b\xi)}{\beta_1 b}\right)\exp[\beta_3\tau + \beta_1 f_1(\tau) + \beta_2 g_1(\tau)] \\ - \frac{\hat{A}_0}{b}\left(\xi + \frac{\exp(-\beta_1 b\xi)}{\beta_1 b}\right)\exp[a(\tau-\tau_\mathrm{R}) - b\xi + f_1(\tau) - f_1(\tau_\mathrm{R})] + f_2(\tau), \tag{5.2.47}$$

with $f_2(-\infty) = 0$. The functions $f_2(\tau)$ and $g_2(\tau)$ are to be determined through matching with the outer solution.

In order to satisfy the boundary conditions away from the shear band we consider an outer layer, in which the appropriate independent variables are

$$y = \varepsilon^{1/2}Y, \quad t = t_\mathrm{p} + \varepsilon\tau, \quad Y > 0, \quad \tau > -\frac{t_\mathrm{p}}{\varepsilon} \to -\infty. \tag{5.2.48}$$

In this region both the plastic straining and reaction are negligible. Motivated by achieving a balance between the time derivative and diffusive terms in the governing equations [38], we introduce the expansions

$$T = T_\mathrm{e}(\varepsilon^{1/2}Y, t_\mathrm{p} + \varepsilon\tau) + \varepsilon T_1^O(Y,\tau) + \varepsilon^{3/2}T_2^O(Y,\tau) + \cdots, \tag{5.2.49}$$

$$s = s_\mathrm{e}(\varepsilon^{1/2}Y, t_\mathrm{p} + \varepsilon\tau) + \varepsilon s_1^O(Y,\tau) + \varepsilon^{3/2}s_2^O(Y,\tau) + \cdots. \tag{5.2.50}$$

For the analysis here we only require the leading-order governing equations in the outer layer, which read

$$s_{1_\tau}^O = \hat{\rho}_0^{-1}\int_{-\infty}^{\tau} s_{1_{YY}}^O \,\mathrm{d}\tau', \quad s_1^O(\infty,\tau) = 0, \quad s_1^O(Y,-\infty) = 0, \tag{5.2.51}$$

$$T_{1_\tau}^O = T_{1_{YY}}^O, \quad T_1^O(\infty,\tau) = 0, \quad T_1^O(Y,-\infty) = 0. \tag{5.2.52}$$

No boundary conditions are imposed at $Y = 0$. Instead we must perform an asymptotic matching between the inner and outer solutions. The inner expansion is expressed in terms of the outer variables and equated to the outer expansion in order to derive matching relations at $Y = 0$. The result is

$$\varepsilon T_1^O(Y,\tau) + \varepsilon^{3/2}T_2^O(Y,\tau) + \cdots = \varepsilon T_1(\varepsilon^{-1/2}Y,\tau) + \varepsilon^{3/2}T_2(\varepsilon^{-1/2}Y,\tau) + \cdots \\ = \varepsilon\Bigg[f_1(\tau) - \frac{\lambda\dot{\gamma}_0(1+\hat{\omega}t_\mathrm{p})Y}{\beta_1 b}\exp(\beta_3\tau + \beta_1 f_1(\tau) + \beta_2 g_1(\tau)) \\ - \frac{\hat{A}_0 Y}{b}\exp(a(\tau-\tau_\mathrm{R}) - b\xi + f_1(\tau) - f_1(\tau_\mathrm{R}))\Bigg] + O(\varepsilon^{3/2}), \tag{5.2.53}$$

$$\varepsilon s_1^O(Y,\tau) + \varepsilon^{3/2}s_2^O(Y,\tau) + \cdots = \varepsilon s_1(\varepsilon^{-1/2}Y,\tau) + \varepsilon^{3/2}s_2(\varepsilon^{-1/2}Y,\tau) + \cdots \\ = \varepsilon\left[g_1(\tau) + \frac{\hat{\rho}_0\dot{\gamma}_0 Y}{\beta_1 b}\frac{\mathrm{d}}{\mathrm{d}\tau}\exp(\beta_3\tau + \beta_1 f_1(\tau) + \beta_2 g_1(\tau))\right] + O(\varepsilon^{3/2}), \tag{5.2.54}$$

which provides the boundary conditions

$$T_1^O(0,\tau) = f_1(\tau), \quad s_1^O(0,\tau) = g_1(\tau), \tag{5.2.55}$$

$$T_{1_Y}^O(0,\tau) = -\frac{\lambda\dot{\gamma}_0(1+\hat{\omega}t_\mathrm{p})}{\beta_1 b}\exp(\beta_3\tau + \beta_1 f_1(\tau) + \beta_2 g_1(\tau)) - \frac{\hat{A}_0}{b}\exp(a(\tau-\tau_\mathrm{R}) + f_1(\tau) - f_1(\tau_\mathrm{R})), \tag{5.2.56}$$

$$s_{1_Y}^O(0,\tau) = \frac{\hat{\rho}_0\dot{\gamma}_0}{\beta_1 b}\frac{\mathrm{d}}{\mathrm{d}\tau}\exp(\beta_3\tau + \beta_1 f_1(\tau) + \beta_2 g_1(\tau)). \tag{5.2.57}$$

To solve the leading-order energy equation (5.2.52) we note that it is exactly the same as problem (5.2.14) which was solved in order to find the early-time elastic temperature, with time $\tau > -\infty$ replacing $t \geq 0$, and the boundary heat flux given by (5.2.56). Therefore the leading-order outer solution is

$$T_1^O(Y,\tau) = \int_{-\infty}^{\tau}\left\{\frac{\lambda\dot{\gamma}_0(1+\hat{\omega}t_\mathrm{p})}{\beta_1 b}\exp\left[\beta_3\tau' + \beta_1 f_1(\tau') + \beta_2 g_1(\tau')\right] + \frac{\hat{A}_0}{b}\exp[a(\tau'-\tau_\mathrm{R}) + f_1(\tau') - f_1(\tau_\mathrm{R})]\right\} \times \exp\left[-\frac{Y^2}{4(\tau-\tau')}\right]\frac{\mathrm{d}\tau'}{[\pi(\tau-\tau')]^{1/2}}. \tag{5.2.58}$$

To find the outer stress we note that s_1^O satisfies a wave equation, as can be seen by differentiating (5.2.51) with respect to τ. We look for a solution using the ansatz $s_1^O(Y,\tau) = s_1^{O+}(\tau + \hat{\rho}_0^{1/2}Y) + s_1^{O-}(\tau - \hat{\rho}_0^{1/2}Y)$, and find that in order to satisfy the boundary condition (5.2.57) the solution must be

$$s_1^O(Y,\tau) = -\frac{\hat{\rho}_0^{1/2}\dot{\gamma}_0}{\beta_1 b} \times \exp\left[\beta_3(\tau - \hat{\rho}_0^{1/2}Y) + \beta_1 f_1(\tau - \hat{\rho}_0^{1/2}Y) + \beta_2 g_1(\tau - \hat{\rho}_0^{1/2}Y)\right]. \tag{5.2.59}$$

Imposing matching conditions between the inner and outer solution at $Y = 0$ gives a pair of coupled nonlinear equations for the leading-order temperature and stress perturbations in the shear band, namely

$$f_1(\tau) = \int_{-\infty}^{\tau}\left\{\frac{\lambda\dot{\gamma}_0(1+\hat{\omega}t_\mathrm{p})}{\beta_1 b}\exp\left[\beta_3\tau' + \beta_1 f_1(\tau') + \beta_2 g_1(\tau')\right] + \frac{\hat{A}_0}{b}\exp[a(\tau'-\tau_\mathrm{R}) + f_1(\tau') - f_1(\tau_\mathrm{R})]\right\}\frac{\mathrm{d}\tau'}{[\pi(\tau-\tau')]^{1/2}}, \tag{5.2.60}$$

$$g_1(\tau) = -\frac{\hat{\rho}_0^{1/2}\dot{\gamma}_0}{\beta_1 b}\exp\left[\beta_3\tau + \beta_1 f_1(\tau) + \beta_2 g_1(\tau)\right]. \tag{5.2.61}$$

These are to be solved in conjunction with (5.2.26) in order to determine the critical reaction time τ_R. We note that $f_1(\tau) \geq 0$ and $g_1(\tau) \leq 0$ which is consistent with the physical observation that plastic deformation leads to an increase in the temperature and a decrease in the stress [38]. In particular, rapid growth (decay) of the temperature (stress) is associated with the formation of a shear band, as seen

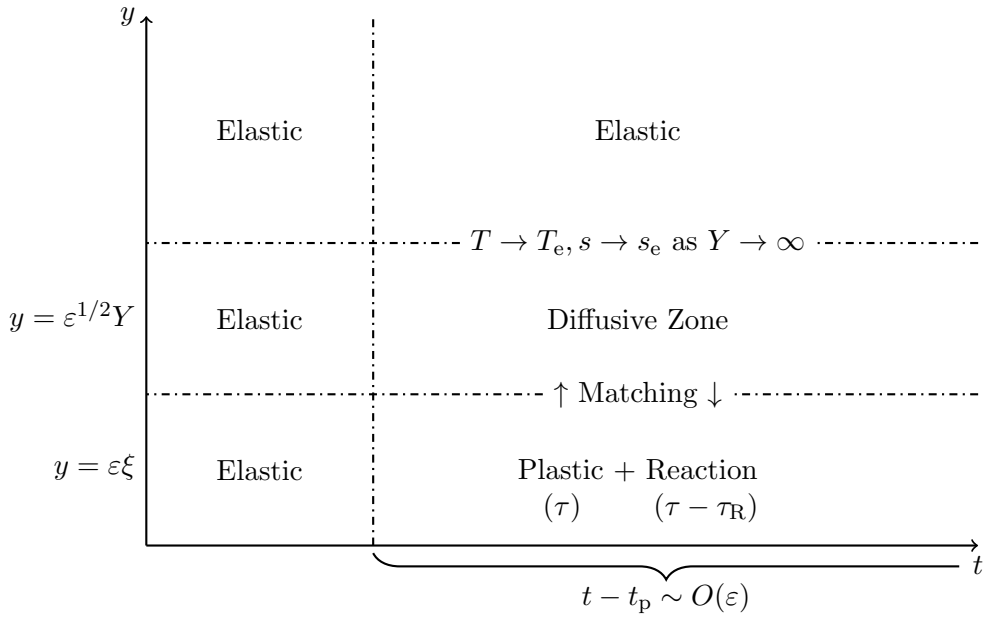

Figure 5.1: Sketch of the asymptotic structure used in Approach I. The up and down arrows at the matching interface between the shear band zone and the diffusive zone indicate that the problems are solved in conjunction with one another; the matching of the two solutions is necessary to obtain the behaviour of the centreline temperature and stress. The solution in the diffusive zone decays to the elastic solution as $Y \to \infty$.

in the red curves in Figure 5.2, which depicts typical solutions $T_1(\xi, \tau) = f_1(\tau)$ and $s_1(\xi, \tau) = g_1(\tau)$.

Figure 5.1 shows a sketch of the asymptotic structure used in Approach I. Note the inner band zone in which $y = \varepsilon\xi$, and the outer diffusive zone in which $y = \varepsilon^{1/2}Y$, which is used to match the solution in the shear band to the far-field elastic solution. In this approach we only introduce one new timescale, τ, as we approach the critical plastic time t_p. The solution in the band is determined by matching with the diffusive zone, so it is necessary to solve the problem in both the shear band and the diffusive zone in order to obtain the behaviour of the centreline temperature and stress; in some sense information is passed between the diffusive and shear band zones by the matching process, hence the arrows pointing both up and down in the sketch. Our solution in the diffusive zone decays to the elastic solution as $Y \to \infty$.

5.2.3 Onset of reactive shear band – Approach II

Here we consider the case in which the heating is first dominated by plastic work, and the heating due to reaction is asymptotically zero. This effectively splits the problem into three stages: an elastic stage; a plastic stage; and a plastic-reactive stage. The plastic stage problem is first solved using boundary-layer techniques, similar in fashion to the solution in the previous section. Here we assume that plastic work dominates until the critical reaction temperature is reached. We then introduce a new timescale which is suitable to describe the solution once the reaction has

commenced. This then leads to a system of two coupled ODEs which govern the behaviour of the stress and temperature in the band during the final stage of the process. This will be referred to as Approach II.

As in the previous section, we introduce boundary layer variables ξ and τ by (5.2.25), and look for a solution in terms of the expansions (5.2.27) and (5.2.28). However, we assume that the Arrhenius source term is asymptotically zero until the critical reaction temperature T_{R} is reached. The analysis for the plastic stage follows as in the previous section, but with the terms corresponding to the reaction set equal to zero. In fact, this part of the analysis is then identical to that in [38], with the result

$$T_1(\tau) = \int_{-\infty}^{\tau} \frac{\lambda\dot{\gamma}_0(1+\hat{\omega}t_{\mathrm{p}})}{\beta_1 b} \exp\left[\beta_3\tau' + \beta_1 f_1(\tau') + \beta_2 g_1(\tau')\right] \frac{\mathrm{d}\tau'}{[\pi(\tau-\tau')]^{1/2}}, \quad (5.2.62)$$

$$s_1(\tau) = -\frac{\hat{\rho}_0^{1/2}\dot{\gamma}_0}{\beta_1 b} \exp\left[\beta_3\tau + \beta_1 f_1(\tau) + \beta_2 g_1(\tau)\right]. \quad (5.2.63)$$

We observe that the solution in the plastic stage of the three-stage approximation (5.2.62)–(5.2.63) is simply the solution from the plastic-reactive analysis (5.2.60)–(5.2.61) with $\hat{A}_0 = 0$. Plots of typical solutions are shown in Figure 5.2, along with the results from the previous section. For the parameter values shown, we see that the magnitude of the stress perturbation increases much more rapidly compared with the magnitude of the temperature perturbation. This is particularly apparent for the solution with vanishing reaction rate ($\hat{A}_0 = 0$) shown in black. When the reaction rate is increased to $\hat{A}_0 = 10^{-2}$ we observe a dramatic increase in the growth rate of the temperature and stress, with the graphs of both T_1 and s_1, shown in red, becoming almost vertical around $\tau \sim 10$. This rapid growth is associated with the formation of a shear band, and, in particular, the rapid temperature rise may be associated with the onset of critical reaction or thermal runaway. It should be noted that only a modest increase in the reaction rate (in absolute terms) was required to obtain markedly different results, highlighting the strong influence a moderately growing reaction during the early stages of shearing can have on the formation of shear bands. In Section 5.5 we will investigate the solution of (5.2.60)–(5.2.61) in terms of new non-dimensional variables, allowing for the influence of key parameters on the formation of shear bands to be investigated. Extending the work on inert shear bands in [38], we will discuss a new criterion for the initiation of reactive shear bands.

We now proceed with the analysis and consider the plastic-reactive stage. The solutions (5.2.62) and (5.2.63) are both functions of time only, so we expect the critical reaction temperature to be reached simultaneously everywhere in the inner layer. Subsequent to sufficient heat being generated it is assumed that the inner, plastic layer transitions into an inner reaction zone, in which a new expansion about the critical temperature T_{R} is appropriate. Motivated by large activation energy

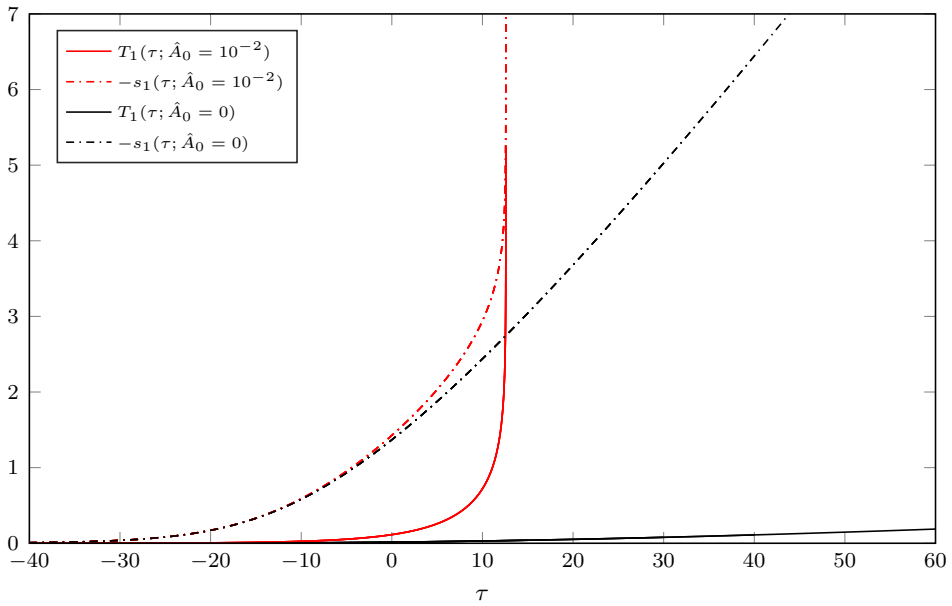

Figure 5.2: Typical results showing the magnitude of the temperature and stress perturbations with reaction $T_1(\tau;\hat{A}_0=10^{-2})$ and $-s_1(\tau;\hat{A}_0=10^{-2})$ shown in red, and without reaction $T_1(\tau;\hat{A}_0=0)$ and $-s_1(\tau;\hat{A}_0=0)$ shown in black. Here the parameter values used were $\hat{\rho}_0=10^{-1}$, $\lambda=10^{-3}$, $\dot{\gamma}_0=1$, $\hat{\omega}=10^{-2}$, $\hat{E}=10^3$, $a=0.1532$, $b=0.059$, $\beta_1=1$, $\beta_2=1$, $\beta_3=0.1632$.

asymptotics [68, 78], we assume that the critical reaction temperature is related to the activation energy by $\varepsilon^r = T_{\mathrm{R}}/\hat{E}^{1/2}$, where the exponent r is as-yet undetermined, and introduce a new time variable via the relation $\tau = \tau_{\mathrm{R}} + \varepsilon^r\hat{\tau}$. The reaction time is defined as the solution of

$$T_{\mathrm{R}} = T_{\mathrm{e}}(0, t_{\mathrm{p}} + \varepsilon\tau_{\mathrm{R}}) + \varepsilon T_1(\tau_{\mathrm{R}}) + o(\varepsilon), \tag{5.2.64}$$

which may then be used to define the stress at onset of reaction

$$s_R = s_e(0, t_{\mathrm{p}} + \varepsilon\tau_{\mathrm{R}}) + \varepsilon s_1(\tau_{\mathrm{R}}) + o(\varepsilon). \tag{5.2.65}$$

On the original timescale the reaction time is $t_{\mathrm{R}} = t_{\mathrm{p}} + \varepsilon\tau_{\mathrm{R}}$.

The independent variables in the reaction zone are

$$y = \varepsilon\xi, \quad t = t_{\mathrm{p}} + \varepsilon(\tau_{\mathrm{R}} + \varepsilon^r\hat{\tau}), \quad \xi > 0, \quad \hat{\tau} > -\frac{t_{\mathrm{R}}}{\varepsilon^{r+1}} \to -\infty, \tag{5.2.66}$$

and we expand the temperature and stress in the inner region as

$$T = T_{\mathrm{R}} + \varepsilon\theta(\xi,\hat{\tau}) + \cdots, \tag{5.2.67}$$

$$s = s_R + \varepsilon\psi(\xi,\hat{\tau}) + \cdots. \tag{5.2.68}$$

Substitution of the expansions (5.2.67) and (5.2.68) into the governing equations

gives

$$\varepsilon^{-r}\psi_{\hat{\tau}} = \frac{1}{\hat{\rho}_0}\int_{-\infty}^{\hat{\tau}} \varepsilon^{r-1}\psi_{\xi\xi}\,\mathrm{d}\hat{\tau} + \hat{\omega} - \dot{\gamma}, \tag{5.2.69}$$

$$\varepsilon^{-r}\theta_{\hat{\tau}} = \varepsilon^{-1}\theta_{\xi\xi} + \lambda(s_R + \varepsilon\psi + \cdots)\dot{\gamma} + \hat{\Omega}\hat{A}\exp\left(-\frac{\hat{E}}{T}\right), \tag{5.2.70}$$

where the asymptotic expansion of the plastic strain-rate function and Arrhenius source term are given by

$$\dot{\gamma} = \dot{\gamma}_0\varepsilon^{-1/2}\left\{\exp[\beta_3\tau_{\mathrm{R}} + \beta_1 T_1(\tau_{\mathrm{R}}) + \beta_2 s_1(\tau_{\mathrm{R}}) + \beta_1\theta + \beta_2\psi] + o(1)\right\}, \tag{5.2.71}$$

and

$$\hat{\Omega}\hat{A}\exp\left(-\frac{\hat{E}}{T}\right) = \hat{A}_0\varepsilon^{-r}\exp\{\theta\}. \tag{5.2.72}$$

To achieve a dominant balance between the time derivative of the temperature perturbation, the plastic work, and the reaction, we find $r = 1/2$. At $O(\varepsilon^{-1})$ we then have

$$\theta_{\xi\xi} = 0, \quad \theta_{\xi}(0,\hat{\tau}) = 0, \quad \theta(\xi,-\infty) = 0, \tag{5.2.73}$$

which has solution $\theta = \theta(\hat{\tau})$. Since θ is a function of time only, it follows that ψ is also a function of time only and the integral in (5.2.69) vanishes at $O(\varepsilon^{-1/2})$.

At $O(\varepsilon^{-1/2})$ we obtain a system of two coupled nonlinear ODEs which govern the first order corrections to the temperature and stress in the reaction zone:

$$\theta_{\hat{\tau}} = \lambda s_R\dot{\gamma}_0\exp\{\beta_3\tau_{\mathrm{R}} + \beta_1 T_1(\tau_{\mathrm{R}}) + \beta_2 s_1(\tau_{\mathrm{R}}) + \beta_1\theta + \beta_2\psi\} + \hat{A}_0\exp\{\theta\}, \tag{5.2.74}$$

$$\psi_{\hat{\tau}} = -\dot{\gamma}_0\exp\{\beta_3\tau_{\mathrm{R}} + \beta_1 T_1(\tau_{\mathrm{R}}) + \beta_2 s_1(\tau_{\mathrm{R}}) + \beta_1\theta + \beta_2\psi\}, \tag{5.2.75}$$

along with the initial conditions

$$\theta(-\infty) = 0, \quad \psi(-\infty) = 0. \tag{5.2.76}$$

Example solutions of the ODEs for $\theta(\tau)$ and $\psi(\tau)$ are given in Figure 5.3, with parameter values given in the caption. On the new τ timescale we see a rapid increase in the temperature and stress at the critical time $\tau_{\mathrm{R}} = 9.973$ ($\hat{\tau} \sim 15$) indicating thermal runaway. Using this three stage approximation it is found that localisation of plastic work must occur before a subsequent reaction can start. The reaction only affects the heating in the band once plastic work has caused the temperature in the band to reach the critical reaction temperature T_{R}. This means that the reaction is only accounted for once the Arrhenius source term becomes $O(1)$, and the analysis of Approach II neglects the slowly growing reaction during the early stages.

The difference between Approaches I and II is illustrated in Figure 5.4, which shows the temperature and stress along the centreline. The stages of each asymptotic

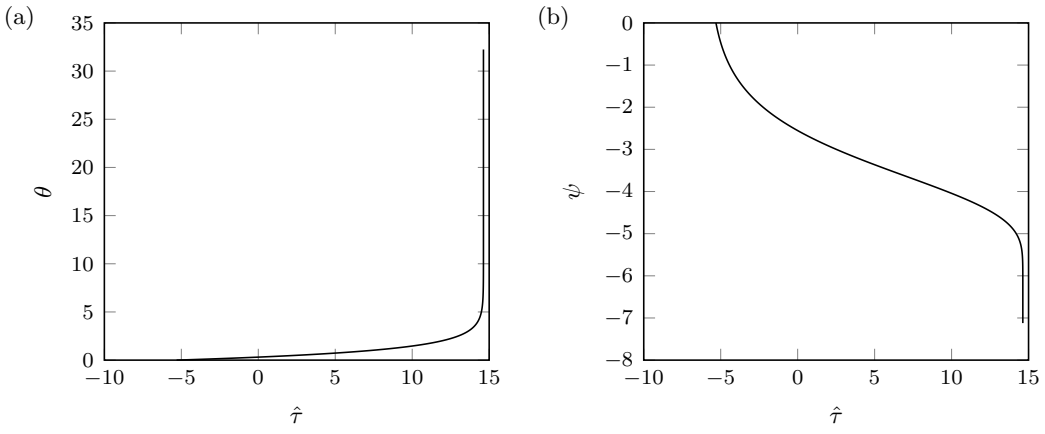

Figure 5.3: The centreline temperature and stress during the reaction stage on the $\hat{\tau}$ timescale. The the parameter values used were $\hat{\rho}_0 = 10^{-4}$, $\lambda = 10^{-3}$, $\dot{\gamma}_0 = 1$, $\hat{\omega} = 10^{-1}$, $\hat{A}_0 = 0.05$, $\hat{E} = 10^3$, $a = 0.1532$, $b = 0.059$, $\beta_1 = 1$, $\beta_2 = 1$ and $\beta_3 = 0.1632$. The critical reaction temperature was $T_{\mathrm{R}} = 1.02$, giving critical timescale $\tau_{\mathrm{R}} = 1.441$ and stress $s_R = 1.002$.

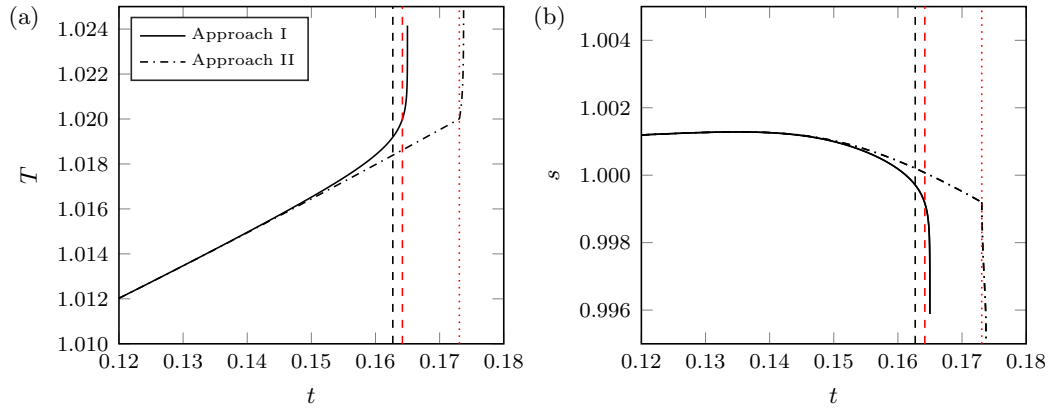

Figure 5.4: A comparison of the centreline temperature and stress as predicted by the reactive boundary layer models Approach I and Approach II. The parameter values used were $\hat{\rho}_0 = 10^{-4}$, $\lambda = 10^{-3}$, $\dot{\gamma}_0 = 1$, $\hat{\omega} = 10^{-2}$, $\hat{A}_0 = 0.05$, $\hat{E} = 10^3$, $a = 0.1532$, $b = 0.059$, $\beta_1 = 1$, $\beta_2 = 1$ and $\beta_3 = 0.1632$. This gave critical plastic time $t_{\mathrm{p}} = 0.1627$ (vertical black dashed line). The critical reaction temperature was $T_{\mathrm{R}} = 1.02$, predicting critical reaction time $t_{\mathrm{R_I}} = 0.1642$ using Approach I (vertical dashed red line), and $t_{\mathrm{R_{II}}} = 0.1730$ using Approach II (vertical dotted red line).

solution (elastic/plastic-reactive and elastic/plastic/plastic-reactive, respectively) have been matched together in order to give a complete history of the solution. The parameter values used give a critical plastic timescale $t_{\mathrm{p}} = 0.1627$, shown as a vertical black dashed line in Figure 5.4. The two approaches agree well in the early elastic stage. However, as the temperature is increased we begin to see the effect of the small, but growing, reaction. We observe that the temperature predicted by Approach I increases more rapidly as the critical plastic time is approached compared with the prediction of Approach II. Owing to thermal softening, a much more rapid drop in the stress is observed which ultimately leads to a shear band developing much sooner. The critical reaction time is reduced from $t_{\mathrm{R_{II}}} = 0.1730$ when using Approach II, to $t_{\mathrm{R_I}} = 0.1642$ when using Approach I which accounts for the reaction throughout the entire process.

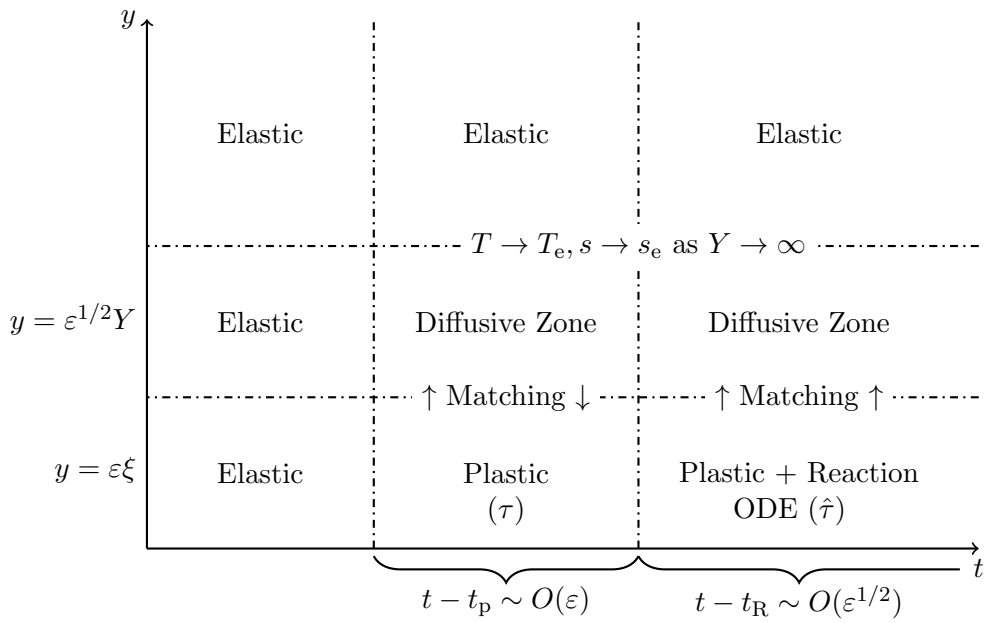

Figure 5.5: Sketch of the asymptotic structure used in Approach II. The up and down arrows at the matching interface between the shear band zone and the diffusive zone during the plastic stage indicate that the problems are solved in conjunction with one another. During the plastic-reactive stages the arrows only point upwards, as the solution in the band can be determined independently, and can be used to determine a boundary condition for the solution in the diffusive zone. The solution in the diffusive zone decays to the elastic solution as $Y \to \infty$.

Figure 5.5 shows a sketch of the asymptotic structure used in Approach II. In contrast to Approach I, see Figure 5.1, we introduce two new timecales: τ, which is used to describe the plastic stage; and $\hat{\tau}$, which is used to describe the plastic-reactive stage. As in Approach I, the solution in the band is determined by matching with the diffusive zone, but only during the plastic stage. During the final plastic-reactive stage, the leading-order temperature and stress in the band are functions of time only, and are solved independently of the diffusive zone. If one were to seek a solution in the diffusive zone in this final stage, then the boundary condition as $Y \to 0$ would be provided by the inner solution; hence the matching arrows pointing only upwards in the sketch, indicating that the information passes out of the shear band zone into the diffusive zone.

5.2.4 Onset of reactive shear band – Approach III

The thermal explosion theory presented in [80] considers a rigid-plastic material undergoing a shear deformation, which leads to a subsequent chemical reaction. The analysis identifies three distinct periods: an induction stage, during which spatially homogenous plastic work induces a temperature rise sufficient to trigger a significant reaction; a reaction period; and a post-reaction period. In this section we adapt our boundary layer analysis of the previous sections to mimic the induction and reaction stages as defined in [80]. In contrast to our critical reaction time t_R, the thermal

explosion theory identifies an induction time t^* corresponding to the time at which heating due to plastic work and reaction become comparable. The reaction stage, during which heating due to plastic work is assumed negligible, commences at time $t = t^*$. In this section we will use our model to obtain an induction time, and solve the subsequent reaction problem, in order to obtain a solution using the idea of the approximate thermal explosion theory [80].

In the [80] the induction time is estimated by solving the inert, spatially homogenous version of (5.2.2) to obtain an approximate (inner) solution $T_{\rm I}$ for the temperature. This solution is substituted into the plastic work and reaction terms, and the induction time is estimated as the time at which the two terms become equal. Our boundary layer analysis relies on retaining the spatial dependence of the variables. However, in the spirit of the analysis in [80] we can estimate the induction time by first solving the equations in the inert case (5.2.62)–(5.2.63), and substituting the result into the plastic work and reaction terms. As before, the governing equations are given by

$$\hat{\rho} v_t = s_y, \tag{5.2.77}$$

$$T_t = T_{yy} + \lambda s \dot{\gamma} + \hat{\Omega}\hat{A} \exp\left(-\frac{\hat{E}}{T}\right), \tag{5.2.78}$$

$$s_t = v_y - \dot{\gamma}, \tag{5.2.79}$$

with the plastic strain-rate given by (5.2.7). We solve the governing equations using the expansion about the elastic solution, as in the previous two sections. By evaluating the leading- and first-order terms in the expansions (5.2.27)–(5.2.28) at $\xi = 0$ ($y = 0$), and setting $\hat{A} = 0$, we obtain solution for the inert centreline temperature and stress

$$T_{\rm I}(t;\tau) = T_{\rm e}(0,t) + \varepsilon \int_{-\infty}^{\tau} \frac{\lambda \dot{\gamma}_0 (1 + \hat{\omega} t_{\rm p})}{\beta_1 b} \times \exp\left[\beta_3 \tau' + \beta_1 f_1(\tau') + \beta_2 g_1(\tau')\right] \frac{{\rm d}\tau'}{[\pi(\tau - \tau')]^{1/2}} + O(\varepsilon^{3/2}), \tag{5.2.80}$$

$$s_{\rm I}(t;\tau) = s_{\rm e}(0,t) - \varepsilon \frac{\hat{\rho}_0^{1/2} \dot{\gamma}_0}{\beta_1 b} \exp\left[\beta_3 \tau + \beta_1 f_1(\tau) + \beta_2 g_1(\tau)\right] + O(\varepsilon^{3/2}), \tag{5.2.81}$$

with $t = t_{\rm p} + \varepsilon\tau$. The induction time $t^* = t_p + \tau^*$ is estimated by equating the plastic work term

$$\lambda s \dot{\gamma} = \lambda s \dot{\gamma}_0 \varepsilon^{-1/2} \exp\{-\varepsilon^{-1}[\beta_1(T_{\rm p} - T) + \beta_2(s_{\rm p} - s)]\}, \tag{5.2.82}$$

to the Arrhenius reaction term

$$\hat{\Omega}\hat{A} \exp\left(-\frac{\hat{E}}{T}\right) = \hat{A}_0 \varepsilon^{-1/2} \exp\left(\frac{\hat{E}}{T_{\rm R}} - \frac{\hat{E}}{T}\right), \tag{5.2.83}$$

where $\varepsilon = T_{\mathrm{R}}^2/\hat{E}$. Hence t^* is found as the root of

$$\lambda s_{\mathrm{I}}(t^*)\dot{\gamma}_0 \exp\{-\varepsilon^{-1}[\beta_1(T_{\mathrm{p}} - T_{\mathrm{I}}(t^*)) + \beta_2(s_{\mathrm{p}} - s_{\mathrm{I}}(t^*))]\} = \hat{A}_0 \exp\left(\frac{\hat{E}}{T_{\mathrm{R}}} - \frac{\hat{E}}{T_{\mathrm{I}}(t^*)}\right). \tag{5.2.84}$$

As in the approximate thermal explosion theory [80], we assume a spatially homogenous solution during the reaction stage. The plastic work term is treated as negligible so that (5.2.78) is replaced by the ordinary differential equation

$$T_t = \hat{\Omega}\hat{A}\exp\left(-\frac{\hat{E}}{T}\right), \quad T(t^*) = T_{\mathrm{I}}(t^*), \tag{5.2.85}$$

which accounts solely for the heating due to reaction along the centre of the shear band. We further assume a constant strain-rate, giving a strain which depends linearly on time [80]

$$\dot{\gamma}(y,t) \approx \dot{\gamma}^*, \quad \gamma(y,t) \approx \dot{\gamma}^*(t - t^*) + \gamma_{\mathrm{I}}(t^*), \tag{5.2.86}$$

where the representative strain-rate $\dot{\gamma}^* = \dot{\gamma}(s_{\mathrm{I}}(t^*), T_{\mathrm{I}}(t^*))$ is calculated from the constitutive law (5.2.7), and γ_{I} is the strain computed using the inert ($\hat{A} = 0$) solution. An approximate time history of the stress in the band during the reaction stage may then be computed by rearranging (5.2.7) to give

$$s(t) = \frac{\beta_1}{\beta_2}(T_p - T) + s_p + \frac{\varepsilon}{\beta_2}\log\left(\frac{\dot{\gamma}^*}{\dot{\gamma}_0}\varepsilon^{1/2}\right). \tag{5.2.87}$$

Figure 5.6 gives a comparison of the centreline temperature and stress predicted by each of the three approaches. The vertical lines correspond to the critical plastic time t_{p}, induction time t^*, critical reaction time $t_{\mathrm{R_I}}$ predicted by Approach I, and critical reaction time $t_{\mathrm{R_{II}}}$ predicted by Approach II, respectively from left to right. As expected, the analysis of Approach I gives the most rapid rise (drop) in the temperature (stress) since it accounts for both heating due to plastic work and heating due to reaction. Approach II only accounts for heating due to plastic work up until time $t_{\mathrm{R_{II}}}$, at which point a sharp increase in temperature is observed due to the commencement of a rapid chemical reaction. Interestingly, both Approaches II and III predict that the temperature reaches the reaction temperature T_{R} at a comparable time, so both methods would provide a similar approximation for the time to runaway. This is likely only the case when we consider heating due to plastic work and reaction to be of a comparable size on a comparable timescale, as we do here. Approach I may be considered as the approximate sum of Approaches I and II up until the critical reaction time $t_{\mathrm{R_I}}$, most clearly seen in Figure 5.6 (c). Although the consideration of plastic work increases the heating due to the (nonlinear) reaction,

this effect is reasonably minimal when the temperature is less than the reaction temperature T_{R}.

An important distinction to make between the three approaches is that the dominant balance within the band in Approach I is between heat diffusion, plastic work and reaction (5.2.44). Solution of the problem then comes from matching with an outer region in which the temperature satisfies the usual one-dimensional heat equation with no heat sources (5.2.52). However, in the other two approaches there is a dominant balance between the time derivative of the temperature and either the plastic work and reaction in Approach II, or just the reaction in Approach III.

Figure 5.7 shows a sketch of the asymptotic structure used in Approach III. As with Approach II, see Figure 5.5, the problem is split into three stages. However, the final reactive stage now begins at the induction time $t = t^*$. As in Approaches I and II, the solution in the band during the plastic stage is determined by matching with the diffusive zone. In the final reactive stage the temperature is governed by the ODE (5.2.85) and is solved independently of the diffusive zone. As with Approach II, the inner solution can be used to provide the boundary condition in the diffusive zone as $Y \to 0$.

5.2.5 Localised reaction

Here we consider the case where the critical reaction temperature is much less than the critical plastic temperature, i.e. $T_{\mathrm{R}} \ll T_{\mathrm{p}}$ (which corresponds to $t_{\mathrm{R}} \ll t_{\mathrm{p}}$). In this regime the Arrhenius source term becomes $O(1)$ while the plastic strain-rate remains exponentially small everywhere. Since we have still imposed the heat flux inhomogeneity at $y = 0$, we still expect the reaction to first occur in a thin zone near to the centreline. In the absence of plastic work, we identify the small parameter through the relation $\varepsilon = T_{\mathrm{R}}^2/\hat{E}$. As in Section 5.2.2, new independent variables ξ and τ are introduced

$$y = \varepsilon\xi, \quad t = t_{\mathrm{R}} + \varepsilon\tau, \quad \xi > 0, \quad \tau > -\frac{t_{\mathrm{R}}}{\varepsilon} \to -\infty, \tag{5.2.88}$$

where the critical reaction time t_{R} is defined as the solution of

$$T_{\mathrm{e}}(0, t_{\mathrm{R}}) = t_{\mathrm{R}}. \tag{5.2.89}$$

Similarly, we define the stress at time of reaction as $s_R = s_e(0, t_{\mathrm{R}})$. Since the plastic strain-rate is exponentially small, the elastic solution for the stress $s_e(\varepsilon\xi, t_{\mathrm{R}} + \varepsilon\tau)$ is exact to all orders of ε. We expand the temperature as

$$T = T_{\mathrm{e}}(\varepsilon\xi, t_{\mathrm{R}} + \varepsilon\tau) + \varepsilon T_1(\xi, \tau) + \varepsilon^{3/2} T_2(\xi, \tau), \tag{5.2.90}$$

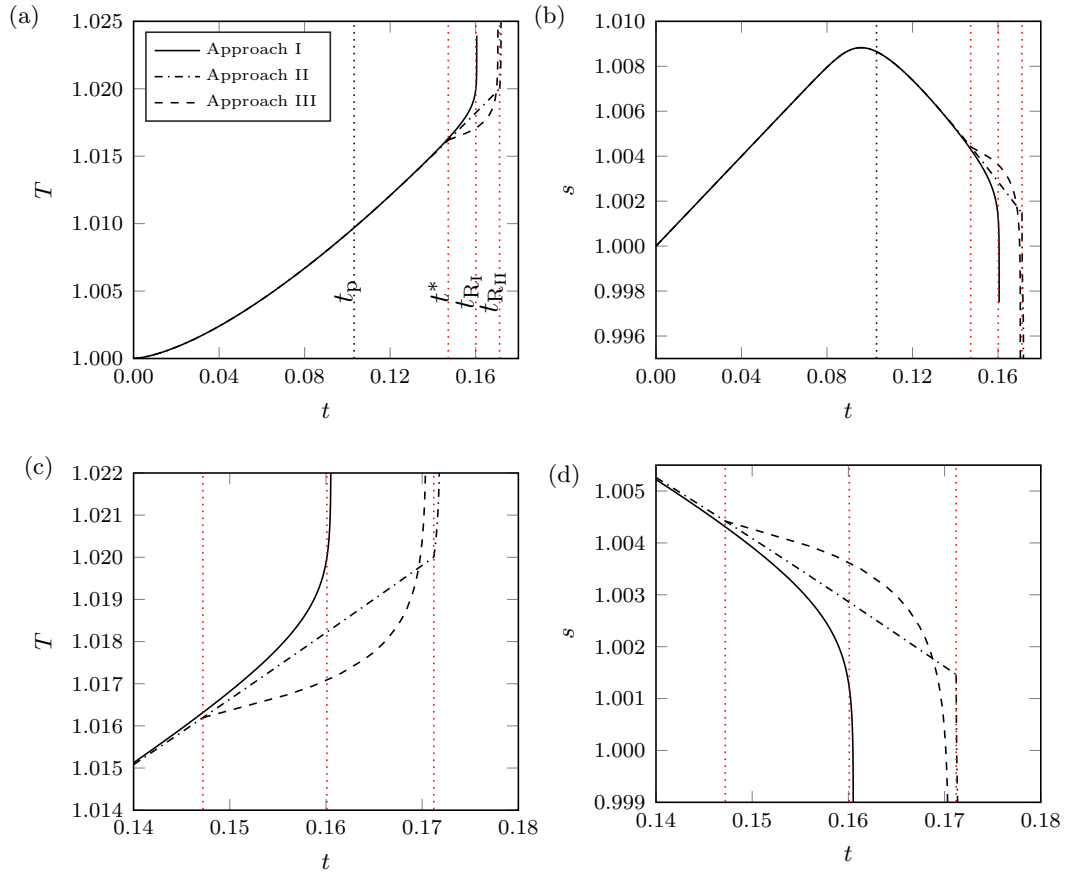

Figure 5.6: Comparison of the centreline temperature and stress as predicted by Approaches I, II and III. Panels (c,d) show in more details the later stages of the solutions depicted in panels (a,b), respectively. The parameter values used were $\hat{\rho}_0 = 10^{-4}$, $\lambda = 10^{-3}$, $\dot{\gamma}_0 = 1$, $\hat{\omega} = 10^{-2}$, $\hat{A}_0 = 0.05$, $\hat{E} = 10^3$, $a = 0.1532$, $b = 0.059$, $\beta_1 = 1$ and $\beta_2 = 1$. The vertical lines correspond to the critical plastic time $t_{\mathrm{p}} = 0.1032$, the induction time predicted by Approach III $t^* = 0.1472$, the critical reaction time predicted by Approach I $t_{\mathrm{R_I}} = 0.1601$, and the critical reaction time predicted by Approach II $t_{\mathrm{R_{II}}} = 0.1712$.

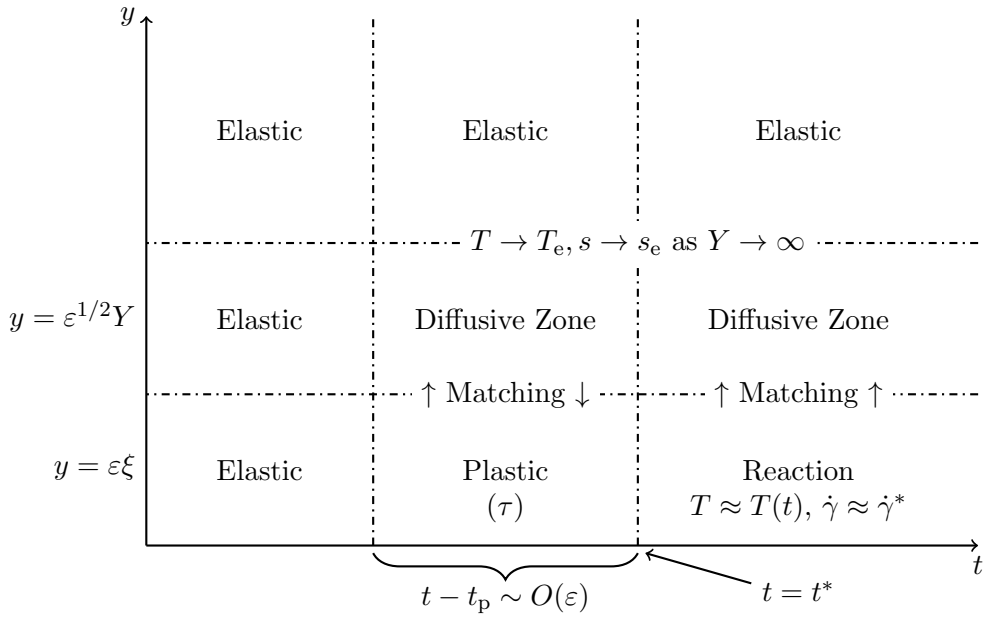

Figure 5.7: Sketch of the asymptotic structure used in Approach III. The solution in the elastic and plastic stages is the same as that in Approach II. However, at the induction time $t = t^*$ the temperature in the shear band zone is governed by an ODE which only accounts for reaction, and the strain-rate is assumed constant. The solution in the diffusive zone decays to the elastic solution as $Y \to \infty$.

where the elastic temperature may be expanded as

$$T_e(\varepsilon\xi, t_R + \varepsilon\tau) = T_R + \varepsilon(a\tau - b\xi) + o(\varepsilon), \tag{5.2.91}$$

where

$$a = T_{e_t}(0, t_R), \quad b = -T_{e_y}(0, t_R). \tag{5.2.92}$$

Substitution of (5.2.90) into the energy equation (5.2.2) gives

$$\Big[T_1 + \varepsilon^{1/2} T_2 + \cdots\Big]_\tau = \Big[\varepsilon^{-1} T_1 + \varepsilon^{-1/2} T_2 + \cdots\Big]_{\xi\xi} + \hat{A}_0 \varepsilon^{-1/2} \exp[a\tau - b\xi + T_1]. \tag{5.2.93}$$

At $O(\varepsilon^{-1})$ we have the problem

$$T_{1_{\xi\xi}} = 0, \quad T_{1_\xi}(0, \tau) = 0, \quad T_1(\xi, -\infty) = 0. \tag{5.2.94}$$

Integrating twice with respect to ξ and applying the boundary conditions we find

$$T_1(\xi, \tau) = f_3(\tau), \quad f_3(-\infty) = 0, \tag{5.2.95}$$

where the arbitrary function $f_3(\tau)$ is to be determine from matching with the outer solution.

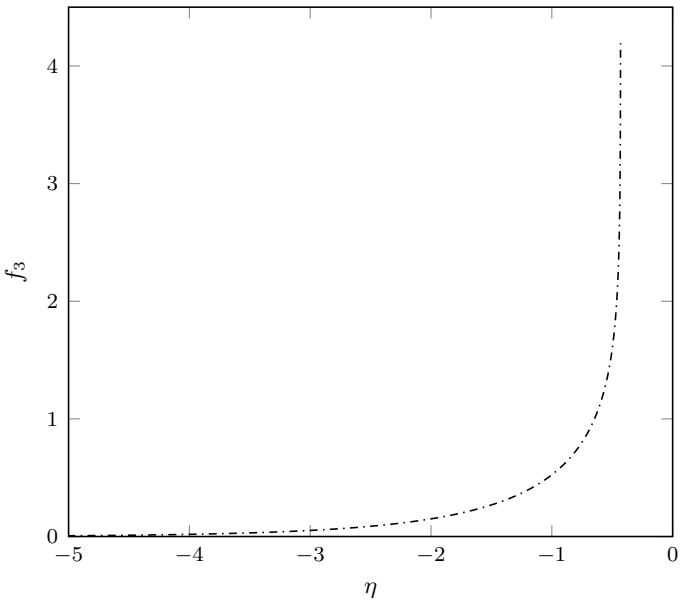

Figure 5.8: Magnitude of the temperature perturbation $f_3(\eta)$ during the reaction stage for $t_\mathrm{R} \ll t_\mathrm{p}$.

At $O(\varepsilon^{-1/2})$ we have the problem

$$T_{2_{\xi\xi}} = -\hat{A}_0 \exp\{a\tau - b\xi + f_3(\tau)\}, \tag{5.2.96}$$

$$T_{2_\xi}(0,\tau) = 0, \quad T_2(\xi,-\infty) = 0. \tag{5.2.97}$$

Integrating (5.2.96) directly gives

$$T_2(\xi,\tau) = -\frac{\hat{A}_0}{b}\left(\xi + \frac{\exp(-b\xi)}{b}\right)\exp[a\tau + f_3(\tau)] + f_4(\tau), \quad f_4(-\infty) = 0, \tag{5.2.98}$$

where f_4 is an as-yet undetermined function of τ.

As in Section 5.2.2 we introduce an outer expansion which results in a leading-order equation for the outer temperature identical to (5.2.52). The resulting matching conditions are

$$T_1^O(0,\tau) = f_3(\tau), \quad T_{1_Y}^O(0,\tau) = \frac{-\hat{A}_0}{b}\exp(a\tau + f_3(\tau)), \tag{5.2.99}$$

giving the first order correction to the outer temperature

$$T_1^O(Y,\tau) = \frac{\hat{A}_0}{b}\int_{-\infty}^{\tau}[\pi(\tau-\tau')]^{-1/2}\exp\left[a\tau' + f_3(\tau') - \frac{Y^2}{4(\tau-\tau')}\right]\mathrm{d}\tau'. \tag{5.2.100}$$

Application of the matching conditions yields an integral equation for the first order correction to the temperature in the reaction zone

$$f_3(\tau) = \frac{\hat{A}_0}{b}\int_{-\infty}^{\tau}[\pi(\tau-\tau')]^{-1/2}\exp\left[a\tau' + f_3(\tau')\right]\mathrm{d}\tau'. \tag{5.2.101}$$

Introducing a new variable $\eta = a\tau + \log(\hat{A}_0/(a^{1/2}b))$ we may remove the parameters from the equation for f_3, giving

$$f_3(\eta) = \int_{-\infty}^{\eta} [\pi(\eta - \eta')]^{-1/2} \exp\left[\eta' + f_3(\eta')\right] \mathrm{d}\eta'. \tag{5.2.102}$$

Asymptotic analysis by Olmstead [78] has shown that there is a critical value η^* for which f_3 becomes logarithmically unbounded as $\eta \to \eta^*$. In particular, it is shown that

$$f_3(\eta) = -\frac{1}{2}\log(\eta^* - \eta) - \left[\eta^* + \log\frac{2}{\pi^{1/2}}\right] + o(1), \quad \eta \to \eta^*, \tag{5.2.103}$$

with η^* being numerically evaluated as

$$\eta^* \approx -0.431. \tag{5.2.104}$$

The function f_3 was computed numerically, and is plotted in Figure 5.8.

5.3 Strain hardening effects

Strain hardening effects have been shown to be important in PBXs, and are included in a number of models for reactive shear bands [24, 80]. The strain hardening behaviour of a range of explosive simulants, including cure cast, melt cast, and pressed formulations, can be found in [23]. In order to investigate the effect strain hardening plays on the development of shear bands we adapt the plastic strain-rate function (5.1.18) to include dependence on the plastic strain γ. As a natural extension to the constitutive law (5.1.18) which includes hardening effects we propose a new model

$$\dot{\gamma} = \frac{\dot{\Gamma}^*}{\dot{\Gamma}_0} \exp\left\{-\left[\frac{\tilde{T}_0}{B_1}(T_p - T) + \frac{\tilde{s}_0}{B_2}(s_p - s) + \frac{\Gamma_0}{B_4}\gamma\right]\right\}, \tag{5.3.1}$$

where B_4 is an experimentally determined constant. In the analysis presented in this section we do not account for any chemical reaction occurring in the band; we simply wish to investigate how hardening affects the onset and development of plastic localisation. This offers a new extension to the work on inert shear bands [38].

As in Section 5.2.2 we introduce the boundary layer variables $y = \varepsilon\xi$ and $t = t_p + \varepsilon\tau$. Prior to the onset of plastic deformation, the plastic strain is naturally zero, so that the critical plastic time scale is still defined by (5.2.24). We introduce the $O(1)$ constant β_4 through the relation

$$\frac{B_4}{\Gamma_0} = \beta_4^{-1}\varepsilon^{1/2}, \tag{5.3.2}$$

so that (5.2.7) may be written

$$\dot{\gamma}(s,T,\gamma) = \dot{\gamma}_0 \varepsilon^{-1/2} \exp\{-\varepsilon^{-1}[\beta_1(T_p - T) + \beta_2(s_p - s)] - \varepsilon^{-1/2}\beta_4\gamma\}. \tag{5.3.3}$$

In terms of the boundary layer variables, the plastic strain is given by

$$\gamma = \dot{\gamma}_0 \varepsilon^{1/2} \int_{-\infty}^{\tau} \exp\{-\varepsilon^{-1}[\beta_1(T_p - T) + \beta_2(s_p - s)] - \varepsilon^{-1/2}\beta_4\gamma\}\,\mathrm{d}\tau. \tag{5.3.4}$$

To proceed with the analysis we use the expansions of the temperature and stress given by (5.2.27) and (5.2.28), respectively. The asymptotic expansion of the plastic strain-rate function (5.3.3) reads

$$\dot{\gamma} = \dot{\gamma}_0 \varepsilon^{-1/2} \left\{\exp[\beta_3\tau - \beta_1 b\xi + \beta_1 T_1 + \beta_2 s_1 - \beta_4\hat{\gamma}] + o(1)\right\}, \tag{5.3.5}$$

where the $O(1)$ variable $\hat{\gamma}(\xi,\tau) = \varepsilon^{-1/2}\gamma$ has been introduced.

At $O(\varepsilon^{-1})$ the problem remains unchanged from (5.2.39)–(5.2.40), with solution

$$T_1(\xi,\tau) = f_5(\tau), \quad f_5(-\infty) = 0, \quad s_1(\xi,\tau) = g_5(\tau), \quad g_5(-\infty) = 0, \tag{5.3.6}$$

where the functions f_5 and g_5 are to be determined by matching with an outer solution.

At $O(\varepsilon^{-1/2})$ we now have the problem

$$\int_{-\infty}^{\tau} s_{2_{\xi\xi}}\,\mathrm{d}\tau = \hat{\rho}_0\dot{\gamma}_0 \exp[\beta_3\tau - \beta_1 b\xi + \beta_1 f_5 + \beta_2 g_5 - \beta_4\hat{\gamma}], \tag{5.3.7}$$

$$s_{2_\xi}(0,\tau) = 0, \quad s_2(\xi,-\infty) = 0, \tag{5.3.8}$$

$$T_{2_{\xi\xi}} = -\lambda\dot{\gamma}_0(1 + \hat{\omega}t_p)\exp[\beta_3\tau - \beta_1 b\xi + \beta_1 f_5 + \beta_2 g_5 - \beta_4\hat{\gamma}], \tag{5.3.9}$$

$$T_{2_\xi}(0,\tau) = 0, \quad T_2(\xi,-\infty) = 0. \tag{5.3.10}$$

Integrating (5.3.9) twice with respect to ξ yields

$$\begin{aligned} T_2(\xi,\tau) = -\frac{\lambda\dot{\gamma}_0(1+\hat{\omega}t_p)}{\beta_1 b}\Bigg(&\xi\exp(-\beta_4\hat{\gamma}(0,\tau)) + \frac{\exp(-\beta_1 b\xi - \beta_4\hat{\gamma})}{\beta_1 b} \\ &+ \beta_4\int_0^{\xi}\frac{\exp(-\beta_1 b\xi - \beta_4\hat{\gamma})}{\beta_1 b}\hat{\gamma}_\xi\,\mathrm{d}\xi - \beta_4\int_0^{\xi}\int_0^{\xi}\exp(-\beta_1 b\xi - \beta_4\hat{\gamma})\hat{\gamma}_\xi\,\mathrm{d}\xi\,\mathrm{d}\xi\Bigg) \\ &\times\exp[\beta_3\tau + \beta_1 f_5(\tau) + \beta_2 g_5(\tau)] + f_6(\tau), \end{aligned} \tag{5.3.11}$$

where the arbitrary function f_6 satisfies $f_6(-\infty) = 0$. Similarly, integrating (5.3.7) twice with respect to ξ and differentiating the result with respect to τ gives

$$\begin{aligned} s_2(\xi,\tau) = \frac{\hat{\rho}_0\dot{\gamma}_0}{\beta_1 b}\Bigg(&\xi\exp(-\beta_4\hat{\gamma}(0,\tau)) + \frac{\exp(-\beta_1 b\xi - \beta_4\hat{\gamma})}{\beta_1 b} \\ &+ \beta_4\int_0^{\xi}\frac{\exp(-\beta_1 b\xi - \beta_4\hat{\gamma})}{\beta_1 b}\hat{\gamma}_\xi\,\mathrm{d}\xi - \beta_4\int_0^{\xi}\int_0^{\xi}\exp(-\beta_1 b\xi - \beta_4\hat{\gamma})\hat{\gamma}_\xi\,\mathrm{d}\xi\,\mathrm{d}\xi\Bigg) \end{aligned}$$

$$\times \frac{\mathrm{d}}{\mathrm{d}\tau}\{\exp[\beta_3\tau + \beta_1 f_5(\tau) + \beta_2 g_5(\tau)]\}$$
$$- \hat{\rho}_0\dot{\gamma}_0\beta_4 \int_0^\xi \int_0^\xi \exp(-\beta_1 b\xi - \beta_4\hat{\gamma})\hat{\gamma}_\tau \,\mathrm{d}\xi \,\mathrm{d}\xi$$
$$\times \exp[\beta_3\tau + \beta_1 f_5(\tau) + \beta_2 g_5(\tau)] + g_6(\tau), \tag{5.3.12}$$

where the arbitrary function g_6 satisfies $g_6(-\infty) = 0$.

In order to satisfy the boundary conditions as $y \to \infty$ we again introduce an outer layer layer, in which the appropriate independent variables are $y = \varepsilon^{1/2}Y, t = t_p + \varepsilon\tau$. To leading-order the outer problem remains unchanged from (5.2.51)–(5.2.52). Matching between the inner and outer solutions provides the boundary conditions

$$T_1^O(0,\tau) = f_5(\tau), \quad s_1^O(0,\tau) = g_5(\tau), \tag{5.3.13}$$
$$T_{1_Y}^O(0,\tau) = -\frac{\lambda\dot{\gamma}_0(1+\hat{\omega}t_p)}{\beta_1 b}\exp(\beta_3\tau + \beta_1 f_5(\tau) + \beta_2 g_5(\tau) - \beta_4\hat{\gamma}(0,\tau)), \tag{5.3.14}$$
$$s_{1_Y}^O(0,\tau) = \frac{\hat{\rho}_0\dot{\gamma}_0}{\beta_1 b}\frac{\mathrm{d}}{\mathrm{d}\tau}\exp(\beta_3\tau + \beta_1 f_5(\tau) + \beta_2 g_5(\tau) - \beta_4\hat{\gamma}(0,\tau)). \tag{5.3.15}$$

As in Section 5.2.2, solution of the leading-order equations (5.2.51)–(5.2.52) subject to the boundary and flux conditions gives

$$T_1^O(Y,\tau) = \frac{\lambda\dot{\gamma}_0(1+\hat{\omega}t_p)}{\beta_1 b}\int_{-\infty}^{\tau}[\pi(\tau-\tau')]^{-1/2}$$
$$\times \exp\left[\beta_3\tau' + \beta_1 f_5(\tau') + \beta_2 g_5(\tau') - \beta_4\hat{\gamma}(0,\tau') - \frac{Y^2}{4(\tau-\tau')}\right]\mathrm{d}\tau', \tag{5.3.16}$$

$$s_1^O(Y,\tau) = -\frac{\hat{\rho}_0^{1/2}\dot{\gamma}_0}{\beta_1 b}\exp\Big[\beta_3(\tau - \hat{\rho}_0^{1/2}Y) + \beta_1 f_5(\tau - \hat{\rho}_0^{1/2}Y)$$
$$+ \beta_2 g_5(\tau - \hat{\rho}_0^{1/2}Y) - \beta_4\hat{\gamma}(0, \tau - \hat{\rho}^{1/2}Y)\Big]. \tag{5.3.17}$$

Imposing matching conditions between the inner and outer solution at $Y = 0$ gives a pair of coupled nonlinear equations for the leading-order temperature and stress perturbations in the shear band, namely

$$f_5(\tau) = \frac{\lambda\dot{\gamma}_0(1+\hat{\omega}t_p)}{\beta_1 b}\int_{-\infty}^{\tau}\frac{\exp\left[\beta_3\tau' + \beta_1 f_5(\tau') + \beta_2 g_5(\tau') - \beta_4\hat{\gamma}(0,\tau')\right]}{[\pi(\tau-\tau')]^{1/2}}\,\mathrm{d}\tau', \tag{5.3.18}$$

$$g_5(\tau) = -\frac{\hat{\rho}_0^{1/2}\dot{\gamma}_0}{\beta_1 b}\exp\left[\beta_3\tau + \beta_1 f_5(\tau) + \beta_2 g_5(\tau) - \beta_4\hat{\gamma}(0,\tau)\right], \tag{5.3.19}$$

with the scaled centreline plastic strain given by

$$\hat{\gamma}(0,\tau) = \int_{-\infty}^{\tau}\dot{\gamma}_0\exp\left[\beta_3\tau' + \beta_1 f_5(\tau') + \beta_2 g_5(\tau') - \beta_4\hat{\gamma}(0,\tau')\right]\mathrm{d}\tau'. \tag{5.3.20}$$

We introduce the new variables

$$f(\eta) = \beta_1 f_5(\tau), \quad g(\eta) = -\beta_2 g_5(\tau), \quad k(\eta) = \beta_4 \hat{\gamma}(0,\tau),$$
$$\eta = \beta_3 \tau + \log\left[\frac{\lambda\dot{\gamma}_0(1+\hat{\omega}t_p)}{b\beta_3^{1/2}}\right], \tag{5.3.21}$$

and the parameters

$$\Lambda_{\mathrm{p}} = \frac{\beta_2(\hat{\rho}_0\beta_3)^{1/2}}{\beta_1\lambda(1+\hat{\omega}t_p)}, \quad \Lambda_{\mathrm{k}} = \frac{\beta_4 b}{\lambda(1+\hat{\omega}t_p)}, \tag{5.3.22}$$

which are known in terms of the material properties and applied shearing motion. Now (5.3.18)–(5.3.20) take the simplified form

$$f(\eta) = \int_{-\infty}^{\eta} [\pi(\eta-\eta')]^{-1/2} \exp\left[\eta' + f(\eta') - g(\eta') - k(\eta')\right] \mathrm{d}\eta', \tag{5.3.23}$$

$$g(\eta) = \Lambda_{\mathrm{p}} \exp\left[\eta + f(\eta) - g(\eta) - k(\eta)\right], \tag{5.3.24}$$

$$k(\eta) = \Lambda_{\mathrm{k}} \int_{-\infty}^{\eta} \exp\left[\eta' + f(\eta') - g(\eta') - k(\eta')\right] \mathrm{d}\eta'. \tag{5.3.25}$$

Figure 5.9 shows solutions of (5.3.23)–(5.3.25) for fixed $\Lambda_{\mathrm{p}} = 1$ and $\Lambda_{\mathrm{k}} = 0$, 0.1, 1 and 10. For the special case of no hardening, we have the exact solution $f(\eta) = 1 = g(\eta)$, all other curves were obtained numerically. In [38] the onset of shear banding is associated with the rapid growth of the magnitudes of the perturbations to the temperature and stress. Here we observe that increasing Λ_{k}, which directly corresponds to increasing the effects of strain hardening, slows the growth of temperature and stress. Indeed, for $\Lambda_{\mathrm{k}} = 10$ we see that the stress perturbation $g(\eta)$ has barely increased by the time the hardening variable $k(\eta)$ has increased by an order of magnitude ($\eta \approx 7.5$). From this analysis we may conclude that strain hardening may delay, or even entirely prevent, the onset of shear banding.

5.4 Comparison with numerical results

In this section we compare the asymptotic results from Approach I, see Section 5.2.2, with the numerical results found using the cohesive numerical scheme described in Section 4.2. In the preceding asymptotic analysis we made some assumptions about the scalings of various parameters, namely (5.2.5), (5.2.6), (5.2.8) and (5.2.9). In order to obtain a good comparison with the numerical solution we must ensure our parameters are within reasonable agreement with the desired scalings, else we may find ourselves in a different regime in which the onset of shear banding and reaction occur on vastly different timescales. It is also important to note that having parameters which respect the asymptotic scalings discussed in Section 5.2 does not necessarily guarantee that the critical times t_{p} and t_{R} are similar. The asymptotic

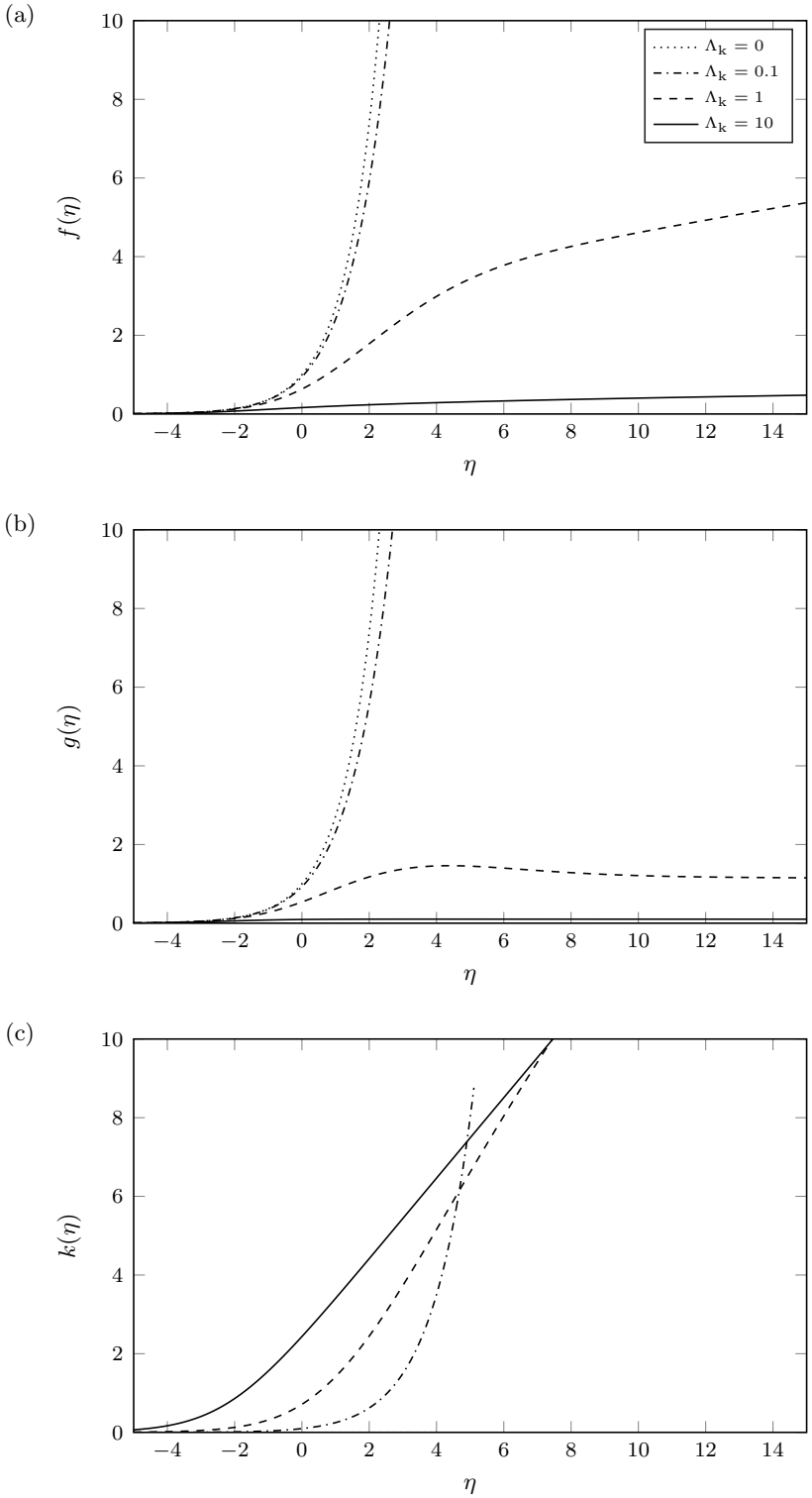

Figure 5.9: Magnitude of the perturbations to the temperature $f(\eta)$, stress $g(\eta)$ and plastic strain $k(\eta)$.

solution may be used to determine the critical plastic and reaction times to ensure the parameters chosen are in the correct regime. The parameter values used in the numerical simulations, and corresponding asymptotic solutions, are given in the figure captions.

Figure 5.10 compares the temperature and stress at the centre of the shear band for various values of the non-dimensional reaction rate $\hat{A}_0$. In each panel the exact elastic solution is shown as a dot-dashed line, the numerical solution as blue circles and the asymptotic solution as a solid black line. The critical plastic and reaction times predicted by the asymptotic analysis are shown using a vertical dashed black line and a vertical red dotted line, respectively. In each case the mechanical properties are held fixed so that the critical plastic time is always $t_{\mathrm{p}} = 0.1627$. An activation energy of $\hat{E} = 10^3$ and critical reaction temperature $T_{\mathrm{R}} = 1.02$ gives $\varepsilon = 10^{-3}$. Panels (a) and (b) show the results for the temperature and stress with $\hat{A}_0 = 0.01$, giving $t_{\mathrm{R}} = 0.1705$. In panels (c) and (d) the reaction rate is increased to $\hat{A}_0 = 0.05$, giving a reduced reaction time $t_{\mathrm{R}} = 0.1642$. In both cases the critical plastic time agrees well with the numerical solution, identified as the time at which the solution first differs from the elastic solution by $O(\varepsilon)$. This is most clearly observed in the plots of the stress. Further, the time at which significant heating due to reaction occurs is also well predicted. For the faster reaction rate $\hat{A}_0 = 0.05$ the reaction happens so quickly that the critical time t_{R} almost coincides exactly with the time at which the temperature becomes singular (i.e. thermal runaway). With such a fast reaction it is found that the stage during which heating due to reaction is negligible is virtually nonexistent, and as such the approximate three stage analysis of Approach II in Section 5.2.3 would give excellent agreement with the asymptotic analysis of Section 5.2.2 (Approach I), as well as the numerical results.

If the reaction rate is increased further to $\hat{A}_0 = 0.1$, see Figure 5.10 (e,f), then the reaction can occur before plastic work becomes significant. The numerical solution predicts $t_{\mathrm{R}} < t_{\mathrm{p}}$, and the incorrect critical plastic time predicted by the asymptotic solution is of little use; our definition of the t_{p} uses the elastic solution, and does not account for heating due to reaction. However, it is still found that the asymptotic solution agrees well with the numerical solution. In fact, when the critical times are such that $t_{\mathrm{R}} < t_{\mathrm{p}}$ the governing equations which resulted from the analysis in Section 5.2.2 reduce to the governing equation for the localised reaction (5.2.101) found in in Section 5.2.5.

Figure 5.11 shows the same results for an increased non-dimensional shear rate $\hat{\omega} = 10^{-1}$. In this case we observe that the stress increases much more rapidly, and the temperature is further from the critical reaction temperature T_{R} at the critical plastic time t_{p}; here the increasing stress plays a greater contributing role in the onset of shear banding. As a result we find that the separation between t_{p} and t_{R} is greater. However, it is still found that the asymptotic and numerical results show excellent agreement.

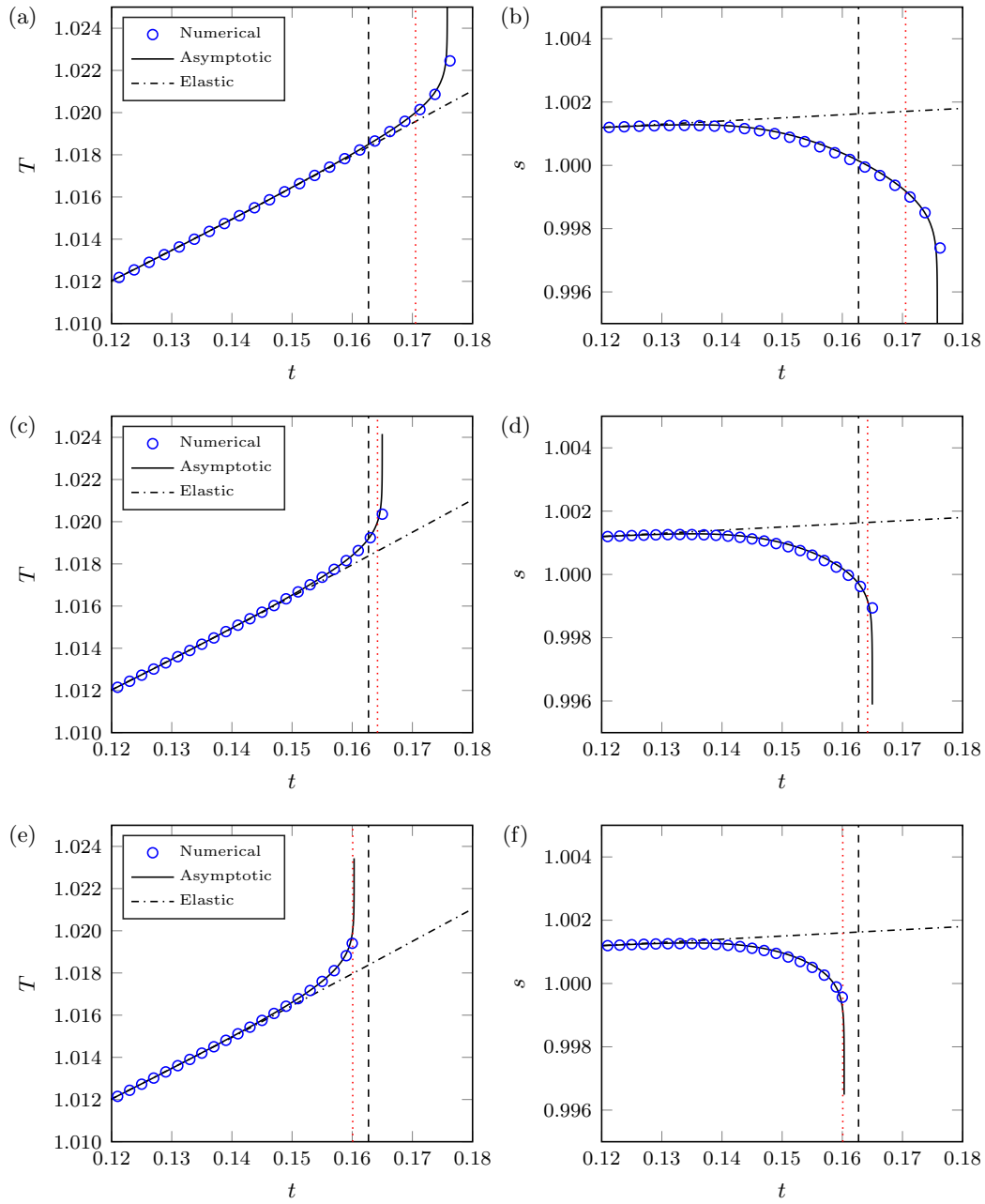

Figure 5.10: Comparison of the centreline temperature and stress as predicted by the asymptotic (Approach I) and numerical solutions with: (a,b) $\hat{A}_0 = 0.01$; (c,d) $\hat{A}_0 = 0.05$; and (e,f) $\hat{A}_0 = 0.1$. In each case the critical plastic time t_p is shown as a vertical black dashed line, and the critical reaction time t_R is shown as a vertical dotted red line. The parameter values used were $\hat{\rho}_0 = 10^{-4}$, $\lambda = 10^{-3}$, $\dot{\gamma}_0 = 1$, $\hat{\omega} = 10^{-2}$, $T_\mathrm{p} = 1.01$, $s_\mathrm{p} = 1.01$, $\hat{E} = 10^3$, $a = 0.1532$, $b = 0.059$, $\beta_1 = 1$ and $\beta_2 = 1$.

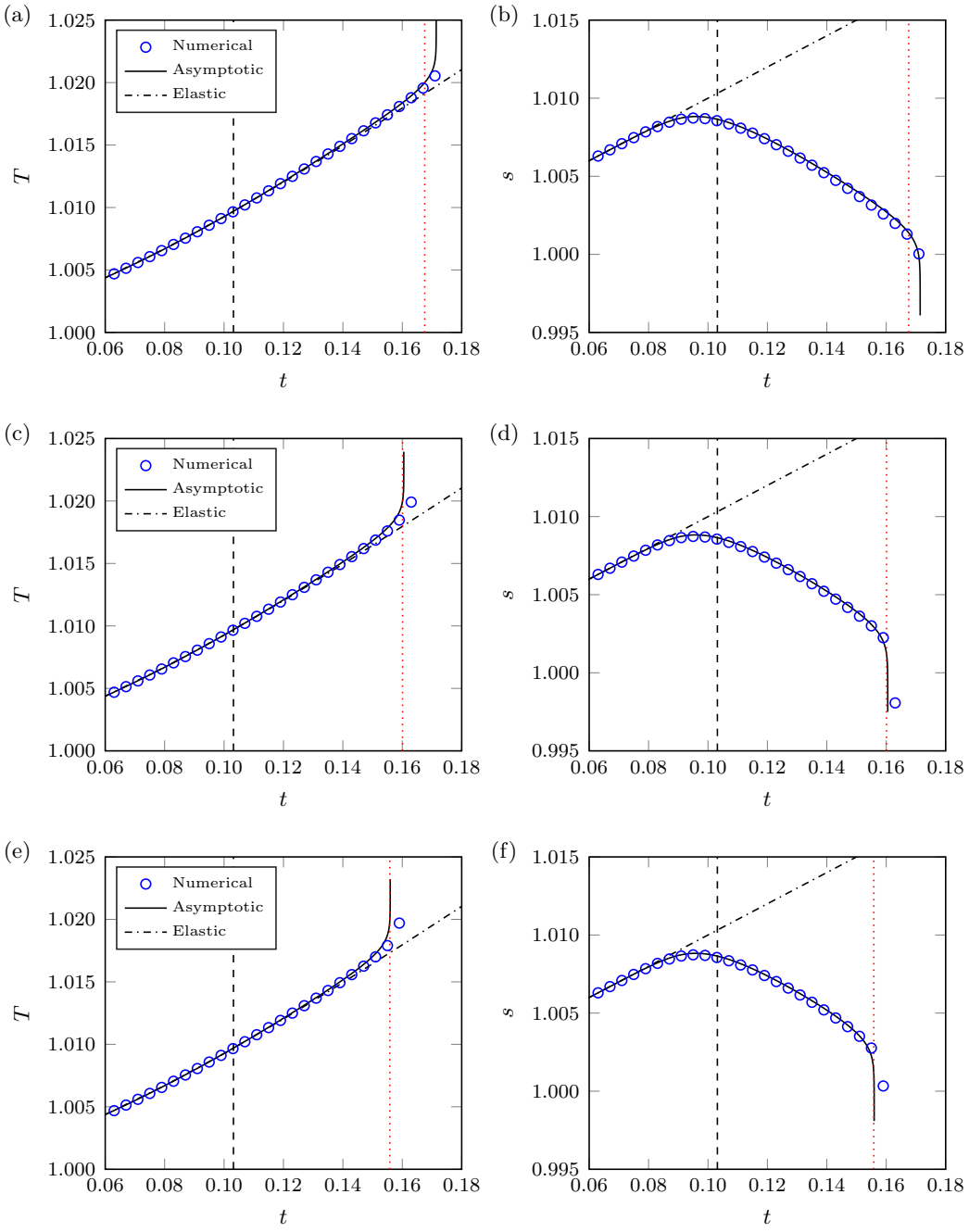

Figure 5.11: Comparison of the centreline temperature and stress as predicted by the asymptotic (Approach I) and numerical solutions with: (a,b) $\hat{A}_0 = 0.01$; (c,d) $\hat{A}_0 = 0.05$; and (e,f) $\hat{A}_0 = 0.1$. In each case the critical plastic time t_p is shown as a vertical black dashed line, and the critical reaction time t_R is shown as a vertical dotted red line. The parameter values used were $\hat{\rho}_0 = 10^{-4}$, $\lambda = 10^{-3}$, $\dot{\gamma}_0 = 1$, $\hat{\omega} = 10^{-1}$, $T_\mathrm{p} = 1.01$, $s_\mathrm{p} = 1.01$, $\hat{E} = 10^3$, $a = 0.1532$, $b = 0.059$, $\beta_1 = 1$ and $\beta_2 = 1$.

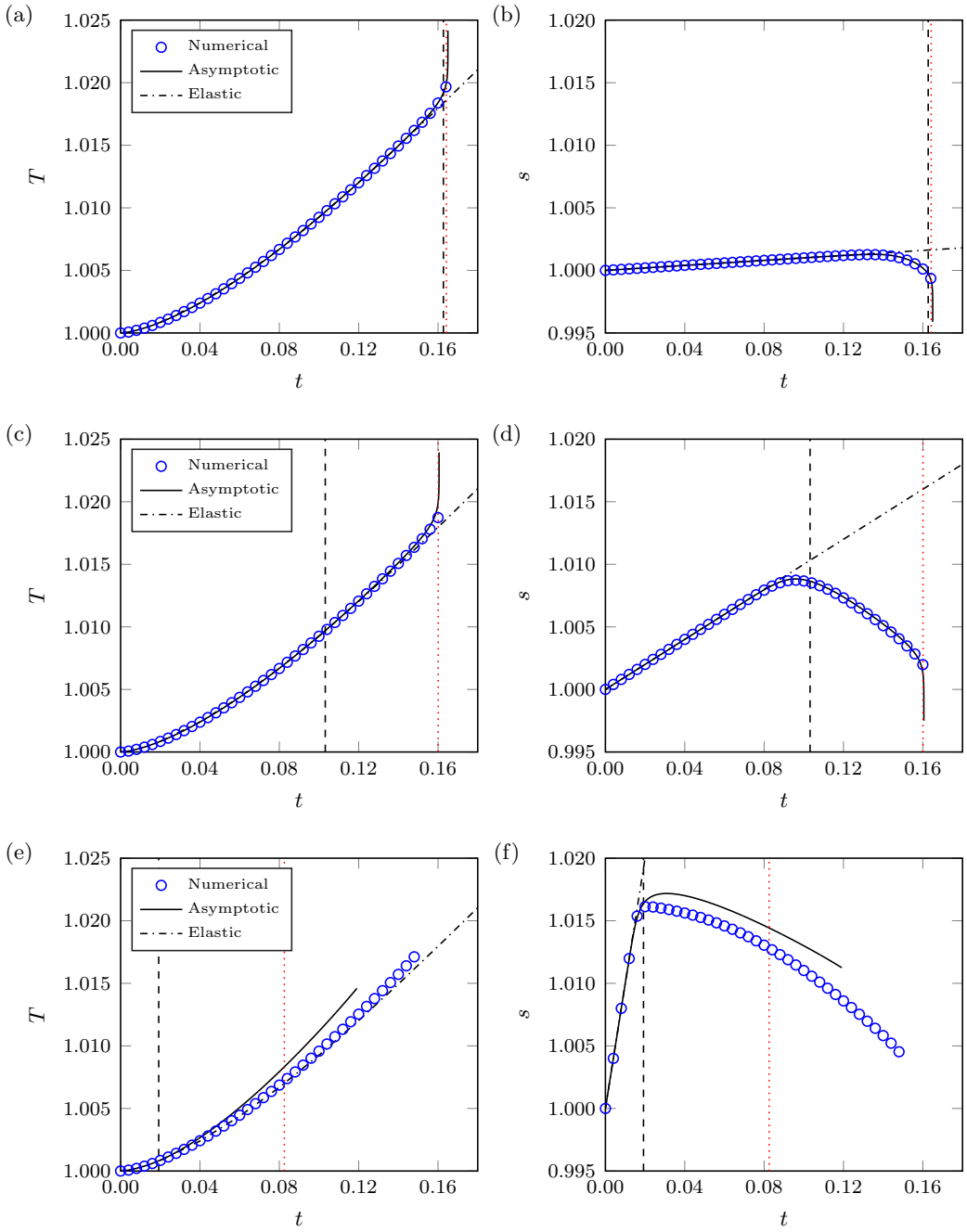

Figure 5.12: Comparison of the centreline temperature and stress as predicted by the asymptotic (Approach I) and numerical solutions with: (a,b) $\hat{\omega} = 0.01$; (c,d) $\hat{\omega} = 0.1$; and (e,f) $\hat{\omega} = 1$. In each case the critical plastic time t_{p} is shown as a vertical black dashed line, and the critical reaction time t_{R} is shown as a vertical dotted red line. The parameter values used were $\hat{\rho}_0 = 10^{-4}$, $\lambda = 10^{-3}$, $\dot{\gamma}_0 = 1$, $T_{\mathrm{p}} = 1.01$, $s_{\mathrm{p}} = 1.01$, $\hat{A}_0 = 0.05$, $\hat{E} = 10^3$, $a = 0.1532$, $b = 0.059$, $\beta_1 = 1$ and $\beta_2 = 1$.

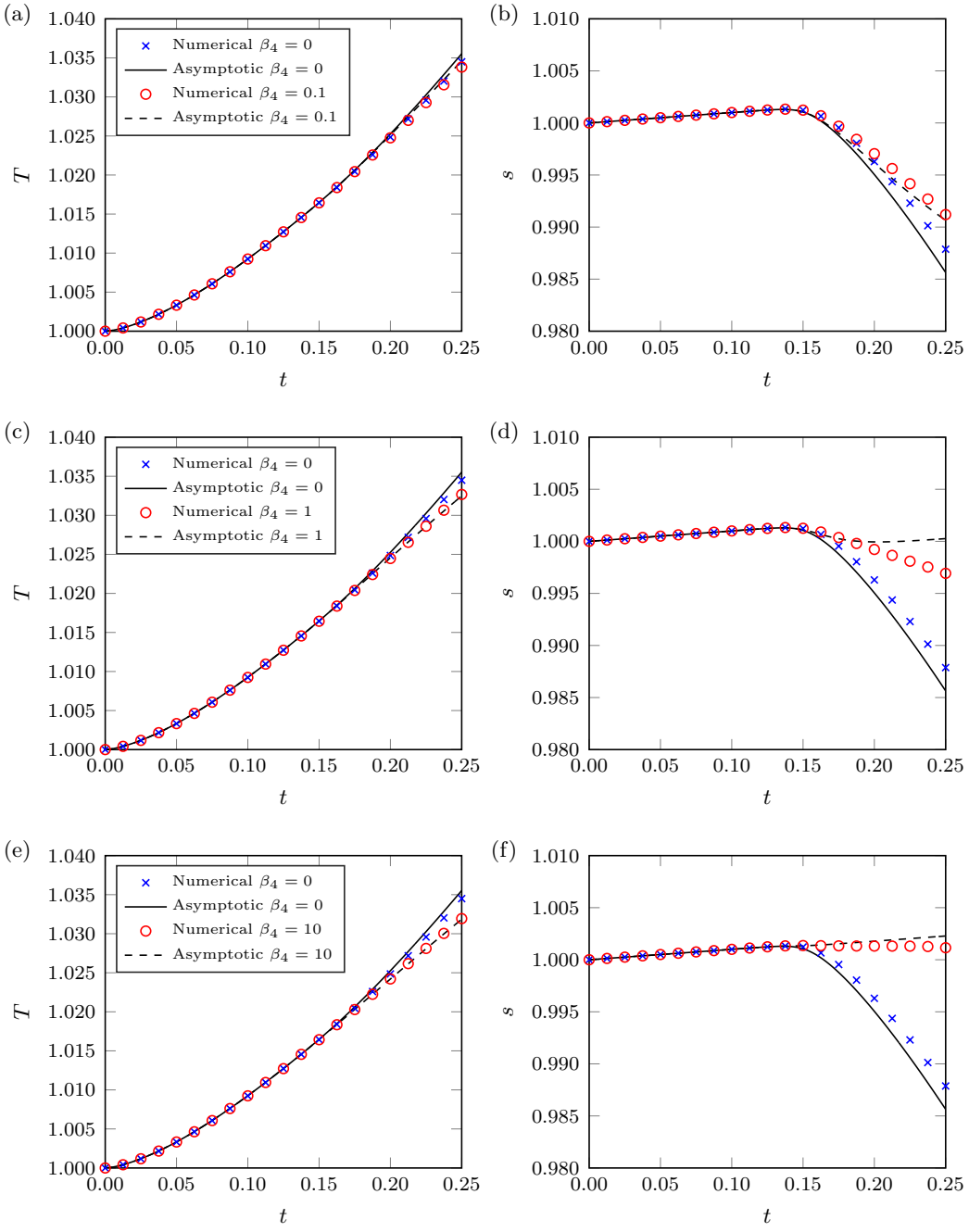

Figure 5.13: Comparison of the centreline temperature and stress as predicted by the asymptotic and numerical solutions with: (a,b) $\beta_4 = 0.1$; (c,d) $\beta_4 = 1$; and (e,f) $\beta_4 = 10$. The parameter values used were $\hat{\rho}_0 = 10^{-4}$, $\lambda = 10^{-2}$, $\dot{\gamma}_0 = 1$, $T_\mathrm{p} = 1.01$, $s_\mathrm{p} = 1.01$, $a = 0.1532$, $b = 0.059$, $\beta_1 = 1$ and $\beta_2 = 1$.

Figure 5.12 further explores the effect of varying $\hat{\omega}$, taking values 10^{-2} in panels (a,b), 10^{-1} in panels (c,d), and 1 in panels (e,f). As $\hat{\omega}$ is increased we see that the centreline stress increases more rapidly, leading to a reduction in the critical time t_{p}. For $\hat{\omega} = 1$ we find that the temperature has barely risen from its initial value at time t_{p}, whereas the stress has exceeded the critical plastic value $s_{\mathrm{p}} = 1.01$. Here the agreement between the asymptotic and numerical solutions is less good. However, in our analysis we assumed that the temperature would be close to the critical plastic and reaction temperature at time t_{p}, which is not the case here. In a scenario such as this, where the formation of the shear band is dominated by the stress, a new analysis would be needed which describes the formation of the shear band, allows it to develop, and then investigates the effect of a chemical reaction on a fully-formed band.

Figure 5.13 shows a comparison between the asymptotic analysis in Section 5.3 and numerical results which include strain hardening effects. As predicted by the asymptotic analysis, the onset of shear banding (associated with the drop in stress) is delayed as the hardening parameter is increased from $\beta_4 = 0.1$ in panels (a,b) to $\beta_4 = 1$ in panels (c,d). As the effect of hardening is increased further, to $\beta_4 = 10$ in panels (e,f), we find that the onset of a shear band is prevented entirely, and the stress continues to grow in time like the uniform shearing solution (5.2.13). For the parameter values used here we find that the heating is initially unaffected by the inclusion of hardening. In the later stages, once the stress has started to drop, we see that increasing the hardening parameter β_4 causes the temperature to rise more slowly. However, we note that even an order of magnitude increase in β_4 has little effect on the growth of the centreline temperature. From our extension to the plastic strain-rate function (5.3.3) we see that the hardening term is proportional to $\varepsilon^{-1/2}$, whereas the temperature and stress appear at $O(\varepsilon^{-1})$, so it is reasonable to see little difference in the heating as we change Λ_{k}; the change in the work term $\lambda s\dot{\gamma}$ primarily comes from the effect the hardening has on the stress.

5.5 Reactive Shear Band criterion

In order to analyse the coupled equations for the reactive shear bands (5.2.60) and (5.2.61) we use the new non-dimensional variables

$$f(\eta) = \beta_1 f_1(\tau), \quad g(\eta) = -\beta_2 g_1(\tau), \quad \eta = \beta_3 \tau + \log\left[\frac{\lambda\dot{\gamma}_0(1+\hat{\omega}t_{\mathrm{p}})}{b\beta_3^{1/2}}\right], \tag{5.5.1}$$

to re-write the problem on the η timescale. However, we now account for heating due to reaction, giving rise to three non-dimensional parameters in contrast to the single parameter found in the analysis of the plastic localisation stage. These parameters

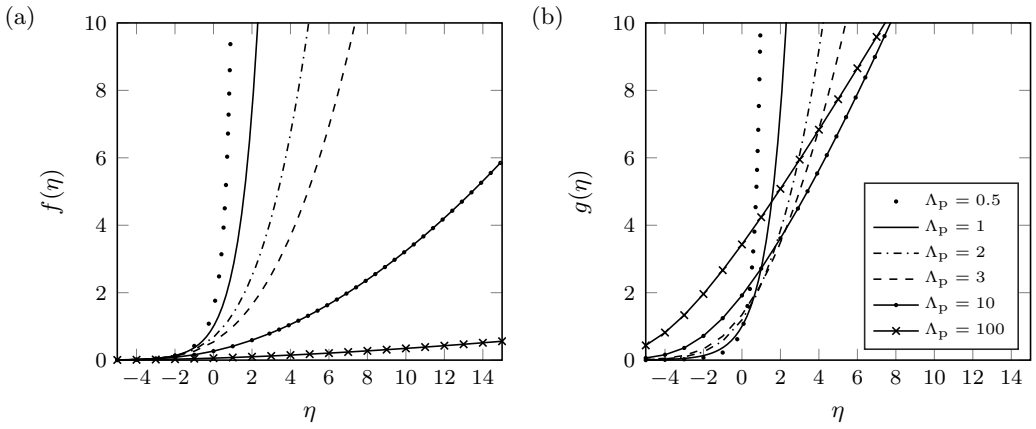

Figure 5.14: Magnitude of the perturbations to the temperature $f(\eta)$ and stress $g(\eta)$ for the plastic localisation stage (i.e. negligible reaction).

are

$$\Lambda_{\rm p} = \frac{\beta_2(\hat{\rho}_0\beta_3)^{1/2}}{\beta_1\lambda(1+\hat{\omega}t_{\rm p})}, \quad \Lambda_{\rm R} = \frac{\hat{A}_0}{b\beta_3^{1/2}}, \quad \Lambda_{\rm t} = \frac{a}{\beta_3}. \tag{5.5.2}$$

Now (5.2.60) and (5.2.61) take the simplified form

$$f(\eta) = \int_{-\infty}^{\eta} [\pi(\eta-\eta')]^{-1/2} \Big\{ \exp\left[\eta' + f(\eta') - g(\eta')\right] + \Lambda_{\rm R} \exp\left[\Lambda_{\rm t}(\eta'-\eta_R) + \beta_1^{-1}(f(\eta') - f(\eta_R))\right] \Big\} {\rm d}\eta', \tag{5.5.3}$$

$$g(\eta) = \Lambda_{\rm p} \exp\left[\eta + f(\eta) - g(\eta)\right], \tag{5.5.4}$$

and correspond to the magnitudes of the temperature and stress perturbations, respectively. The parameters $\Lambda_{\rm p}$ and $\Lambda_{\rm t}$ relate to the material properties, applied shearing motion and heat flux inhomogeneity, whereas the parameter $\Lambda_{\rm R}$ relates to the properties of the chemical reaction.

For the special case $\Lambda_{\rm p} = 1$ and $\Lambda_{\rm R} = 0$ we have the exact solution $f(\eta) = g(\eta) = e^{\eta}$ for all values of $\Lambda_{\rm t}$. For other values of the parameter $\Lambda_{\rm p}$ we may investigate the behaviour of f and g numerically, the results of which are shown in Figure 5.14, and are those found in [38].

In particular, we are interested in understanding how the inclusion of a chemical reaction in the model affects the tendency for a shear band to form when compared with the inert solution. In [38] a shear band criterion is developed by adopting the position that the perturbations should remain $O(1)$ at the critical plastic time for plastic work $t = t_{\rm p}$ ($\tau = 0$). For the parameter values quoted in [38] it is found that $\tau = 0$ corresponds to $\eta \sim 1$ to 7. For $\Lambda_{\rm p} < 10$ the perturbations become $O(10)$ at time $\eta \sim 7$, and it is argued that $\Lambda_{\rm p} < 10$ provides a useful threshold below which the formation of shear bands occurs. In the following we will assume that the parameters which appear in the definition of η $(5.5.1)_3$ are such that $\eta = 7$ corresponds to $\tau = 0$. This will allow for a direct comparison between the inert results in [38] and our

reactive shear band model.

In order to simplify the analysis to follow we note that $\beta_1 \sim O(1)$, and through an appropriate choice of scaling we can always set $\beta_1 = 1$. Further, we note that the parameter Λ_t, which is approximately the ratio of the growth rate of the centreline elastic solution to the non-dimensional shear rate, is typically $O(10^{-2})$. We choose to fix $\Lambda_t = 0.01$ and study a simplified two parameter system. Doing so allows us to focus on how the reaction properties affect the initiation of a shear band.

When $\Lambda_R \neq 0$ the equations governing the behaviour of $f(\eta)$ and $g(\eta)$ require numerical solution. The coupled equations (5.5.3) and (5.5.4) are to be solved using Newton's method, along with (5.2.26) to determine the critical reaction time $\eta_R = \beta_3\tau_R + \log[\lambda\dot{\gamma}_0(1+\hat{\omega}t_p)b^{-1}\beta_3^{-1/2}]$. The numerical results are shown in Figure 5.15, with the inert result shown as a thick dashed line. This dashed line illustrates our shear band criterion: if the solution grows more rapidly than the inert solution with $\Lambda_p = 10$ a shear band is formed; if it grows more slowly, then the temperature and stress perturbations remain $O(1)$ at the critical plastic time $t = t_p$ ($\tau = 0, \eta \sim 7$), and a shear band is not formed.

Panels (a) and (b) of Figure 5.15 show the behaviour of $f(\eta)$ and $g(\eta)$ for fixed $\Lambda_p = 10$ and varying Λ_R. Here we observe that increasing Λ_R has the effect of initiating a shear band at an earlier time. Increasing Λ_R beyond a value of approximately 10 we can initiate a shear band for $\eta < 0$. Panels (c) and (d) show the numerical results for an increased value of $\Lambda_p = 100$. For $\Lambda_R < 10$ we observe that the growth of the temperature perturbation is slow when compared with the inert result with $\Lambda_p = 10$, which corresponds to the critical value below which a shear band is formed in the inert analysis. For the results shown with $\Lambda_R \leq 10$, the magnitude of the stress perturbation is of a similar size at $\eta \sim 7$. However, as Λ_R is increased to 15 we see a significant increase in the growth rate of both the temperature and stress, clearly demonstrating that the inclusion of a chemical reaction can cause shear bands to initiate in a reactive material in conditions where no shear band would be seen in an inert material with similar material properties.

Figure 5.16 shows the outcome of a number of simulations in the $\Lambda_p - \Lambda_R$ plane, with fixed $\Lambda_t = 0.01$. In the plot, green triangles indicate that a shear band did not form, i.e. the perturbations remained $O(1)$ at the critical plastic time $t = t_p$. Red circles indicate that the perturbations to the temperature and stress were no longer $O(1)$ at time t_p, and therefore a shear band did form based on our criterion. As discussed in [38], for $\Lambda_p < 10$ a shear band is always initiated, irrespective of the reaction properties. However, the reaction may affect the growth rate of the temperature and stress perturbations once the band has formed. For $\Lambda_p > 10$ a shear band is not observed when there is no reaction, but it is found that a shear band may be initiated by sufficiently increasing Λ_R. That is, for a sufficiently strong/fast reaction a shear band may be initiated in a material which would not otherwise undergo shear banding under the same load. Initially, as Λ_p is increased we see that

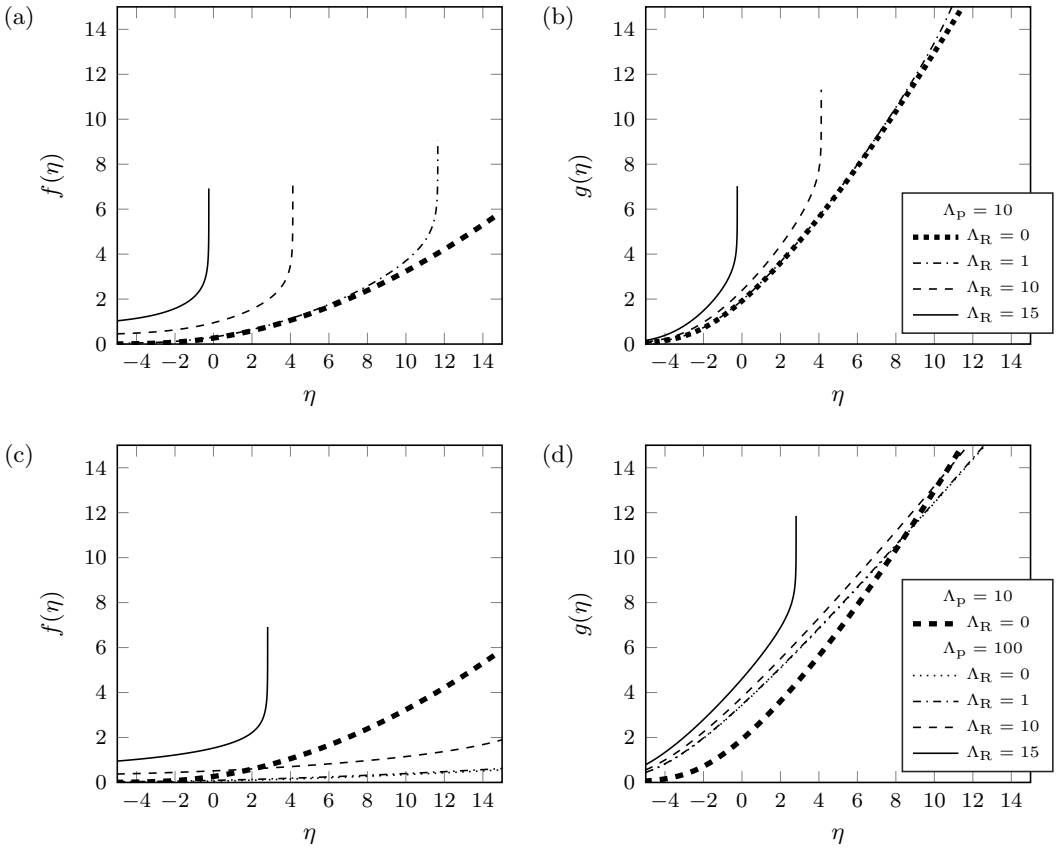

Figure 5.15: Magnitude of the perturbations to the temperature $f(\eta)$ and stress $g(\eta)$. Panels (a) and (b) show results for fixed $\Lambda_p = 10$ and various Λ_R, and panels (c) and (d) show results for fixed $\Lambda_p = 100$ and various Λ_R. In all panels the thick dashed line shows the solution associated with the inert shear band criterion $\Lambda_p = 10$, $\Lambda_R = 0 = \Lambda_t$ discussed in [38]. In some of the cases shown the computation ceased due to a minimum timestep threshold being reached. However, in such cases it is clear by inspection that the growth rate is rapid, and the perturbations will have ceased to remain $O(1)$ at $t = t_p$ ($\tau = 0, \eta \sim 7$).

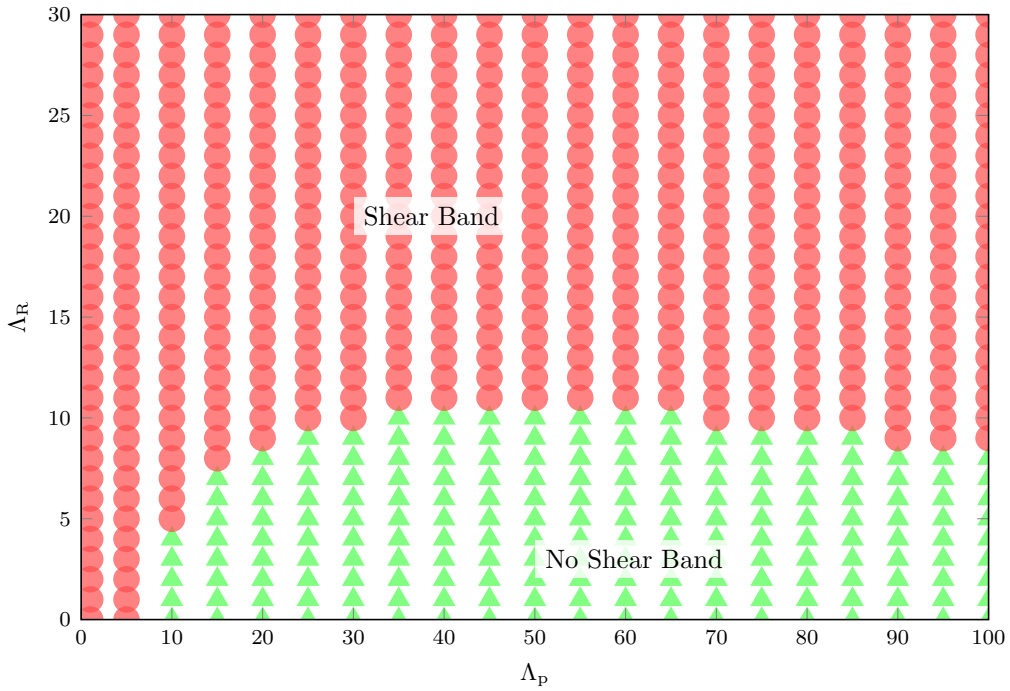

Figure 5.16: A sketch of the region in the $\Lambda_p - \Lambda_R$ plane in which a shear band is formed. The parameter Λ_t has been held fixed at a typical value of 0.01. Green triangles indicate that no shear band was formed, whereas red circles indicate a shear band was formed (based on our criterion).

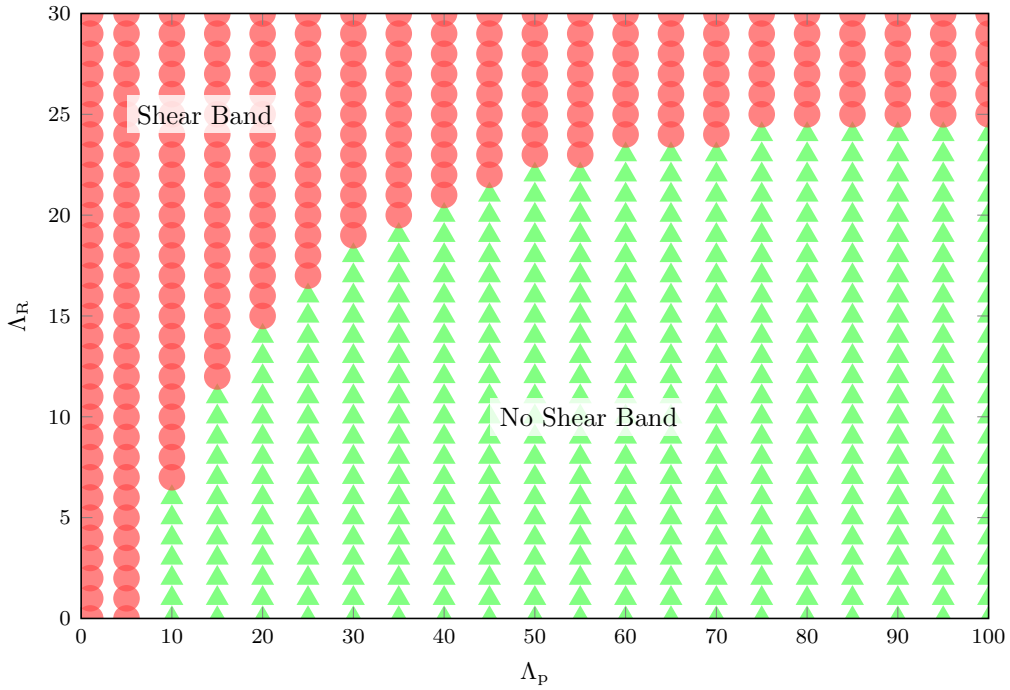

Figure 5.17: A sketch of the region in the $\Lambda_p - \Lambda_R$ plane in which a shear band is formed. The parameter is held fixed at the increased value $\Lambda_t = 0.1$. Green triangles indicate that no shear band was formed, whereas red circles indicate a shear band was formed (based on our criterion).

a greater value of Λ_R is required in order to initiate a shear band. However, for Λ_p large enough ($\Lambda_p > 70$) we see that the critical value of Λ_R required for shear band formation begins to decrease. This is best understood by referring back to Figure 5.14, which shows the inert results. We see that the stress perturbation $g(\eta)$ grows more slowly as Λ_p is increased from 0.5 through to 10, but begins to grow more rapidly again for $\Lambda_p = 100$. When we introduce the chemical reaction, the effects of thermal softening are increased which causes $g(\eta)$ to increase at an even faster rate, triggering the formation of a shear band.

In the results presented so far we fixed $\Lambda_t = 0.01$, based on approximate parameter values in [38, 80, 101]. Figure 5.17, shows the outcome of simulations in which Λ_t is increased to 0.1. Physically, this corresponds to a lower representative shear rate in the band compared to the timescale over which the elastic solutions grows. As expected, a faster reaction is required to initiate a shear band; the temperature increase due to plastic work is lower, owing to the reduced shear rate, and therefore a faster reaction is necessary to increase the temperature sufficiently to cause shear banding.

5.6 Discussion

In this chapter we have developed a model for shear bands occurring in reactive materials motivated by the boundary layer analysis of [38]. The analysis allows for the full system of governing equations to be reduced to three coupled equations used to describe the behaviour of the perturbations to the centreline temperature and stress, as well as the critical reaction time. In contrast to the inert case, we find that the initiation of shear banding is controlled by three parameters instead of one. The simplified equations allow for the parameter space to be explored, and a criterion for the initiation of shear bands based on known physical parameters has been suggested. This analysis has extended previous work on shear bands in reactive materials, and has identified three new parameters, which will help towards our aim set out in Chapter 2 of understanding how localised shearing operates as a hot spot mechanism.

The usefulness of this analysis is primarily in assessing the tendency of a reactive material to form shear bands, based on its material properties and the shear rate of the deformation. As an example we consider the reactive material LX-14 using the parameter values given in Section 5.1. By further assuming that $\tilde{T}_p \approx \tilde{T}_0$ and $\tilde{s}_p \approx \tilde{s}_0$, we find that $\Lambda_p \approx 1.4$ and $\Lambda_R \approx 10$, which is well within the range of values for which a shear band would be observed, even in the absence of any reaction. However, if the material were less sensitive to thermal softening, say $P = 0.1$, then we would find $\Lambda_p \approx 14$. In this case we would not expect a shear band if the material were inert, but we do expect a shear band when we take the reaction into consideration. From this we conclude that considering the behaviour of the reaction can be critical

in determining whether or not localised plastic deformation will occur in an explosive material. Since the non-dimensional parameters which govern the behaviour of the perturbations to temperature and stress are known in terms of material properties, the study could be used to inform the manufacture of new explosive materials: for instance, a different binder could be used to alter the bulk material properties in such a way to suppress shear banding. In Section 5.3 we demonstrated that strain hardening effects could delay or prevent the onset of shear bands. Altering the binder used in manufacturing could be especially useful in controlling the strain hardening behaviour of the material, and could therefore be an important consideration in the design of materials that are less susceptible to accidental ignitions due to shear banding.

In this study it was assumed that the critical temperature for plastic work and reaction were similar in magnitude, so that the reaction occurs soon after the band has formed. In fact, the scalings are such that the onset of significant plastic work and onset of reaction effectively occur simultaneously. In reality, this may not be the case and some adjustment to the analysis would be required. For the case where reaction occurs before significant plastic work (i.e. reactive materials which do not exhibit significant shear localisation) it was shown that the problem reduces to that of [78]. In this instance the reaction is confined to a thin zone around the centreline, and the problem is effectively equivalent to the heating of a half-space of material with the boundary layer playing the role of a thermal flux applied at the boundary. On the other hand, if the reaction is weak enough it may be observed that the shear band becomes fully developed before the reaction occurs. Solution of this problem would require imposing initial conditions consistent with those found inside a developed shear band and looking for a solution as perturbation about the critical reaction temperature.

Chapter 6

Hot Spot Generation in a Reactive Two-Dimensional Sheared Viscous Layer

In this chapter we consider the melting of a thin viscous layer of explosive material due to an applied shear. When an explosive sample is subject to a mechanical insult pre-existing, or new, microcracks will be in compression and shear. Such microcracks can grow in size if the local stress is great enough and, due to friction between solid surfaces, heat is released during the growth process [90]. Subsequent to sufficient heat release, the crack surface temperature will be raised to the solid melting point and a thin sheared melt layer will be formed, separating the solid surfaces [3]. This thin melt layer will continue to be heated through viscous dissipation, and is thought to be a prime location for hot spot generation [2, 3, 51]. Experiments show that lightly confined HMX-based explosives subject to impacts from blunt projectiles at velocities in the range 50 to 100 $\mathrm{m\,s^{-1}}$ undergo violent delayed reaction [72]. Samples which were below the threshold for violent reaction were recovered, and showed evidence of cracking and surface melt layers.

Starobin and Dienes [90] developed an ad-hoc one-dimensional model for the lateral melting and ignition of a thin, sheared, viscous layer of the reactive solid HMX. In their work, an analytical and numerical study of the melt front propagation, both with and without a chemical reaction, was presented. By assuming a melt layer of uniform width, and adopting a non-linear Arrhenius heat source term to capture the reaction, they demonstrated that shear melting in the one-dimensional geometry leads to an increase in the peak temperature relative to the melting point of HMX. In [90] all material properties were treated as constant, and, in particular, the assumption of constant viscosity led to a linear velocity profile across the layer. This in turn gave rise to uniform heating due to mechanical dissipation, and the model was therefore unable to predict any localised heating due to mechanical dissipation within the layer. Since the temperature across the layer varies from the melt temperature of

520 K to a peak temperature of well over 700 K, the assumption of constant material properties should be questioned. Inevitably this large increase in temperature will have some effect on the material properties. In particular, it is suggested that the viscosity may vary significantly across the layer, and the linearisation of the fluid velocity across the layer would break down.

A natural question arises: will the typically inhomogeneous structure found in explosive materials cause further localisation? Polymer bonded explosives are highly granular materials, and the constituent materials in the explosive will in general have different thermomechanical properties. Such spatial differences in material properties will inevitably create a non-uniform melt layer. In this chapter, we formally derive a two-dimensional model for the melting and ignition of a half space of explosive material, so that the effects of material inhomogeneity can be investigated. In the model, the molten layer of explosive remains thin in comparison to the bulk, unmolten material. In order to account for the possible non-uniform melting of material, we impose a shape on the melt front which is allowed to evolve in time. In particular, we demonstrate that even a small two-dimensional disturbance can lead to the generation of highly localised hot spots within the melt layer and greatly reduce the predicted time to runaway. Further, we allow the specific heat, viscosity, and thermal conductivity to vary with temperature and compare the results with those found in [90].

In Section 6.1 we derive a two-dimensional model describing the heating of thin molten layer of explosive undergoing shear. The thinness of the melt layer is exploited and a lubrication approximation is made. The resulting equations are transformed into front-fixed coordinates, which are particularly convenient for the numerical analysis to follow. In Section 6.2 we investigate the effects arising from the two-dimensionality of our model, and make the simplifying assumption of constant material properties. A linear stability analysis is conducted, considering small deviations from a melt layer of uniform width. It is demonstrated that the melt front is linearly stable in the absence of any chemical reaction, but stability is lost upon introduction of an Arrhenius heat source which models the chemical reactions occurring within the layer. In Section 6.2.4 we present an iterative numerical scheme which is used to determine the temperature field in the melt layer. Times to ignition are computed for various initial conditions, demonstrating the effect the imposed melt front shape has on the self heating in the layer. In Section 6.3 we investigate the effects of allowing the liquid specific heat, viscosity, and thermal conductivity to vary with temperature. We demonstrate a departure from the leading-order linear velocity profile found in [90], and show this leads to non-uniform mechanical heating across the layer. We conclude in Section 6.5, where we discuss the possible physical interpretations of the model and offer some suggestions for the conditions under which non-uniform melting may occur.

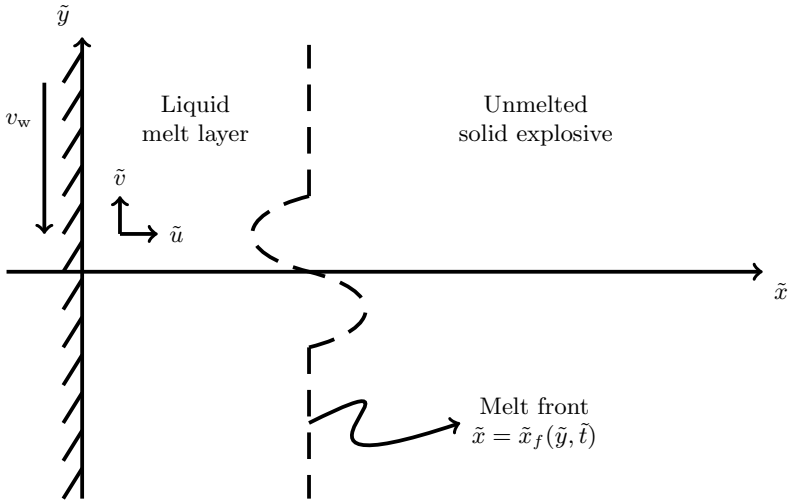

Figure 6.1: A solid block of explosive material occupies the region $\tilde{x} > 0$. At $\tilde{t} = 0$ the rigid wall located at $\tilde{x} = 0$ is impulsively moved downward, so that at $\tilde{t} = \tilde{t}_0$ a thin viscous liquid melt layer has already formed.

6.1 Model equations

We consider a semi-infinite solid block of explosive material occupying the region $\tilde{x} > 0$, with a rigid wall located at $\tilde{x} = 0$. At time $\tilde{t} = 0$ the wall moves impulsively downwards with speed v_w. The movement provides a shear force on the explosive sample, generating sufficient heat to melt the explosive sample near the wall, such that, at $\tilde{t} = \tilde{t}_0$, there already exists a thin viscous liquid melt layer adjacent to the wall, see Figure 6.1. The melt front, shown here as a dashed line, is located at $\tilde{x} = \tilde{x}_f(\tilde{y}, \tilde{t})$. In [51] a model for a one-dimensional reactive shear band is developed, and the explosive is assumed to be linearly viscoplastic, with shear stress

$$\tau = \mu \frac{\mathrm{d}v}{\mathrm{d}x} + \sigma, \tag{6.1.1}$$

where μ is the viscosity, v is the velocity and x is the spatial coordinate. The shear strength σ is independent of pressure and goes to zero at the melting point, so that the molten material behaves as a viscous fluid. Such a viscoplastic model, which includes strength, could be used to model the initial stages $\tilde{t} < \tilde{t}_0$.

A possible physical interpretation of the current work is to consider a scenario in which an internal crack develops, and two material planes slide against one another. In this case, the model is readily adapted to account for a symmetry condition at $\tilde{x} = 0$, as in [90]. The solid wall used in the current formulation may also be considered as a model for a piece of high melting point grit present in the explosive sample [96]. In either case, the heating mechanisms discussed here are still present.

The molten explosive in the melt layer is modelled as an incompressible viscous fluid with temperature dependent specific heat $\tilde{c}$, viscosity $\tilde{\mu}$, and thermal conductivity $\tilde{\kappa}$. However, the density ρ is assumed constant. Under these assumptions, the continuity

equation and Navier-Stokes equations, given here in dimensional form, are

$$\frac{\partial \tilde{u}}{\partial \tilde{x}} + \frac{\partial \tilde{v}}{\partial \tilde{y}} = 0, \tag{6.1.2}$$

$$\rho\left(\frac{\partial \tilde{u}}{\partial \tilde{t}} + \tilde{u}\frac{\partial \tilde{u}}{\partial \tilde{x}} + \tilde{v}\frac{\partial \tilde{u}}{\partial \tilde{y}}\right) = -\frac{\partial \tilde{p}}{\partial \tilde{x}} + 2\frac{\partial}{\partial \tilde{x}}\left(\tilde{\mu}\frac{\partial \tilde{u}}{\partial \tilde{x}}\right) + \frac{\partial}{\partial \tilde{y}}\left[\tilde{\mu}\left(\frac{\partial \tilde{u}}{\partial \tilde{y}} + \frac{\partial \tilde{v}}{\partial \tilde{x}}\right)\right], \tag{6.1.3}$$

$$\rho\left(\frac{\partial \tilde{v}}{\partial \tilde{t}} + \tilde{u}\frac{\partial \tilde{v}}{\partial \tilde{x}} + \tilde{v}\frac{\partial \tilde{v}}{\partial \tilde{y}}\right) = -\frac{\partial \tilde{p}}{\partial \tilde{y}} + 2\frac{\partial}{\partial \tilde{y}}\left(\tilde{\mu}\frac{\partial \tilde{v}}{\partial \tilde{y}}\right) + \frac{\partial}{\partial \tilde{x}}\left[\tilde{\mu}\left(\frac{\partial \tilde{u}}{\partial \tilde{y}} + \frac{\partial \tilde{v}}{\partial \tilde{x}}\right)\right], \tag{6.1.4}$$

where $(\tilde{u}, \tilde{v})$ are the horizontal and vertical components of the liquid velocity, respectively, and $\tilde{p}$ is the pressure. As in [90], we assume the molten explosive behaves as a viscous fluid, so appropriate conditions on the wall and liquid/solid boundary are the no-slip conditions:

$$\tilde{u}(0, \tilde{y}, \tilde{t}) = 0, \quad \tilde{v}(0, \tilde{y}, \tilde{t}) = -v_{\mathrm{w}}, \quad \tilde{u}(\tilde{x}_f, \tilde{y}, \tilde{t}) = 0, \quad \tilde{v}(\tilde{x}_f, \tilde{y}, \tilde{t}) = 0. \tag{6.1.5}$$

The explosive sample is initially heated by viscous dissipation in the melt layer and, once the temperature rise is sufficient, heated further by a consequent chemical reaction. We denote the temperature in the melt layer by $\tilde{T}(\tilde{x}, \tilde{y}, \tilde{t})$ and the solid temperature by $\tilde{T}_{\mathrm{sol}}(\tilde{x}, \tilde{y}, \tilde{t})$. The chemical reaction is modelled as a single-step Arrhenius reaction, expressed in terms of the (dimensionless) mass fraction α of gaseous products,

$$\frac{\partial \alpha}{\partial \tilde{t}} + \tilde{u}\frac{\partial \alpha}{\partial \tilde{x}} + \tilde{v}\frac{\partial \alpha}{\partial \tilde{y}} = A(1-\alpha)\exp\left(-\frac{E}{R\tilde{T}}\right), \tag{6.1.6}$$

where A is the pre-exponential factor, E is the activation energy, and R is the molar gas constant [34]. The viscous dissipation in the melt is given by

$$\tilde{\Phi} = \tilde{\mu}(\tilde{T})\left\{2\left[\left(\frac{\partial \tilde{u}}{\partial \tilde{x}}\right)^2 + \left(\frac{\partial \tilde{v}}{\partial \tilde{y}}\right)^2\right] + \left(\frac{\partial \tilde{v}}{\partial \tilde{x}} + \frac{\partial \tilde{u}}{\partial \tilde{y}}\right)^2\right\}. \tag{6.1.7}$$

In the presence of both viscous and chemical heating in the melt layer, the conservation of energy equations in the liquid and solid phases read, in dimensional form,

$$\rho\tilde{c}(T)\left(\frac{\partial \tilde{T}}{\partial \tilde{t}} + \tilde{u}\frac{\partial \tilde{T}}{\partial \tilde{x}} + \tilde{v}\frac{\partial \tilde{T}}{\partial \tilde{y}}\right) = \nabla\cdot(\tilde{\kappa}(\tilde{T})\,\nabla\tilde{T}) + \tilde{\Phi} + \Omega A(1-\alpha)\exp\left(-\frac{E}{R\tilde{T}}\right), \tag{6.1.8}$$

and

$$\rho\tilde{c}(\tilde{T}_{\mathrm{sol}})\frac{\partial \tilde{T}_{\mathrm{sol}}}{\partial \tilde{t}} = \nabla\cdot(\tilde{\kappa}(\tilde{T}_{\mathrm{sol}})\,\nabla\tilde{T}_{\mathrm{sol}}) + \Omega A(1-\alpha)\exp\left(-\frac{E}{R\tilde{T}_{\mathrm{sol}}}\right), \tag{6.1.9}$$

respectively, where Ω is the heat of reaction. The location of the melt front is determined by the Stefan condition, which equates the temperature flux discontinuity

across the melt front with the magnitude of the latent heat sink at the phase boundary,

$$L\rho\tilde{v}_f = -\left[\tilde{\kappa}(\tilde{T})\frac{\partial\tilde{T}}{\partial n}\right]_{\tilde{x}=\tilde{x}_f^-} + \left[\tilde{\kappa}(\tilde{T}_{\rm sol})\frac{\partial\tilde{T}_{\rm sol}}{\partial n}\right]_{\tilde{x}=\tilde{x}_f^+}, \tag{6.1.10}$$

where L is the latent heat of the material, $\tilde{v}_f$ is the normal velocity of the melt front, and $\partial\tilde{T}/\partial n$ is the normal derivative of the temperature. The normal velocity is given by

$$\tilde{v}_f = \frac{\frac{\partial\tilde{x}_f}{\partial\tilde{t}}}{\sqrt{1+\left(\frac{\partial\tilde{x}_f}{\partial\tilde{y}}\right)^2}}. \tag{6.1.11}$$

As in [90], the melting temperature is assumed constant, $\tilde{T} = \tilde{T}_{\rm m}$, and we make the equilibrium assumption at the solid-liquid interface, giving the condition

$$\tilde{T}(\tilde{x}_f(\tilde{y},\tilde{t}),\tilde{y},\tilde{t}) = \tilde{T}_{\rm sol}(\tilde{x}_f(\tilde{y},\tilde{t}),\tilde{y},\tilde{t}) = \tilde{T}_{\rm m}. \tag{6.1.12}$$

In the following we will assume that the wall acts as a insulating boundary, giving

$$\frac{\partial\tilde{T}}{\partial\tilde{x}}(0,\tilde{y},\tilde{t}) = 0. \tag{6.1.13}$$

In reality there will be some heat loss to the wall. However, any loss will be negligibly small owing to the very short typical timescale to ignition and comparatively large thermal diffusion time. Estimates for the reaction and thermal diffusion timescales, based on a melt width $\tilde{x}_f$ on the order of microns and typical initial wall temperature $\tilde{T} \approx 750\,\mathrm{K}$ [90], are

$$\tau_{\rm R} \approx \frac{\rho\tilde{c}}{\Omega A}\exp\left(\frac{E}{R\tilde{T}}\right) \sim O(10^{-5})\,\mathrm{s}, \quad \tau_{\rm th} = \tilde{c}\rho\tilde{x}_f^2/\tilde{\kappa} \sim O(10^{-5})\,\mathrm{s}, \tag{6.1.14}$$

so that the timescales are similar near to the wall during the very early stages. However, as the temperature is increased we find that the Arrhenius source term acts over a shorter timescale; for a temperature $\tilde{T} \approx 850\,\mathrm{K}$ the reaction time scale is $\tau_{\rm R} \sim O(10^{-7})$s. This reduction in reaction time scale with increasing temperature typically leads to an ignition time on the order of microseconds for the one-dimensional model [90] and on the order of a few hundreds of nanoseconds in the two-dimensional model. Note that if we were to consider a symmetric sheared layer, as in [90], the condition (6.1.13) would be applicable at the midpoint. In the far-field (i.e. away from the melt front) the temperature of the solid explosive material should decay to the ambient temperature, giving the condition

$$\tilde{T}_{\rm sol} \to \tilde{\tilde{T}} \quad \text{as} \quad \tilde{x} \to \infty, \tag{6.1.15}$$

where $\tilde{\tilde{T}} = 300\,\mathrm{K}$ is the dimensional ambient temperature.

Herein we restrict our attention to localised disturbances to the melt front, centred about $\tilde{y} = 0$, so that we recover the existing corresponding one-dimensional solution as we move away from the disturbance site. This provides the conditions

$$\frac{\partial \tilde{T}}{\partial \tilde{y}} \to 0, \quad \frac{\partial \tilde{T}_{\mathrm{sol}}}{\partial \tilde{y}} \to 0 \quad \text{and} \quad \frac{\partial \tilde{p}}{\partial \tilde{y}} \to 0 \quad \text{as} \quad \tilde{y} \to \pm\infty. \tag{6.1.16}$$

The equation for the mass fraction (6.1.6) is supplemented by the boundary conditions

$$\begin{aligned} \frac{\partial \alpha}{\partial \tilde{x}}(0, \tilde{y}, \tilde{t}) = 0, \quad \alpha(\tilde{x}_f^-, \tilde{y}, \tilde{t}) = \alpha(\tilde{x}_f^+, \tilde{y}, \tilde{t}), \quad \alpha \to 0 \quad \text{as} \quad \tilde{x} \to \infty, \\ \text{and} \quad \frac{\partial \alpha}{\partial \tilde{y}} \to 0 \quad \text{as} \quad \tilde{y} \to \pm\infty. \end{aligned} \tag{6.1.17}$$

The first condition states that no gaseous reaction products flow into the rigid wall at $\tilde{x} = 0$, the second condition states that the reaction progress is continuous across the melt front, the third condition states that far away from the melt front the room temperature solid is unreacted, and the final condition states that we recover the one-dimensional solution far away from the site of the disturbance in the melt front.

The two-dimensional melt model presented here accounts for the temperature dependence of the specific heat, viscosity, and thermal conductivity. We describe the specific heat $\tilde{c}$ using an Einstein relation. This particular functional form has been used by Austin et al. [3] to describe the heat capacity for the β phase of HMX, and it is therein assumed that the heat capacity of the liquid phase is identical to that of the solid phase. In the interest of simplicity we make the same assumption here so that the specific heat of liquid HMX is given by

$$\tilde{c}(\tilde{T}) = \frac{(\tilde{\theta}_1/\tilde{T})^2 \exp(\tilde{\theta}_1/\tilde{T})}{(\exp(\tilde{\theta}_1/\tilde{T}) - 1)^2}, \tag{6.1.18}$$

where $\tilde{\theta}_1 = 1000\,\mathrm{K}$. The temperature dependence of the viscosity $\tilde{\mu}$ is modelled using an Arrhenius law

$$\tilde{\mu}(\tilde{T}) = \exp\left(\frac{\tilde{\theta}_2}{\tilde{T}} - \frac{\tilde{\theta}_2}{\tilde{\theta}_3}\right), \tag{6.1.19}$$

where $\tilde{\theta}_2 = 7800\,\mathrm{K}$ and $\tilde{\theta}_3 = 800\,\mathrm{K}$ are experimentally determined constants [51, 72]. For the thermal conductivity $\tilde{\kappa}$ we fit data found in [11, 72] using an exponential law

$$\tilde{\kappa}(\tilde{T}) = \tilde{\theta}_4 + \tilde{\theta}_5 \exp(-\tilde{\theta}_6 \tilde{T}), \tag{6.1.20}$$

where $\tilde{\theta}_4 = 0.26\,\mathrm{W\,m^{-1}\,K^{-1}}$, $\tilde{\theta}_5 = 246.08\,\mathrm{W\,m^{-1}\,K^{-1}}$ and $\tilde{\theta}_6 = 0.0145\,\mathrm{K^{-1}}$.

The relevant material properties, their notation, and typical values for HMX, are shown in Table 6.1. In order to simplify the problem, all material properties are taken to be the same in both the solid and liquid regions. This assumption is consistent with [90], and has been used in other models for HMX [e.g. 3]; the analysis could be

Explosive Property	HMX
Density ρ /kg m^{-3}	1860
Reference Specific Heat c^* /J kg^{-1} K^{-1}	1034
Reference Thermal Conductivity κ^* /W m^{-1} K^{-1}	0.3884
Reference Viscosity μ^* /kg m^{-1} s^{-1}	5.5×10^{-3}
Melting Temperature T_m /K	520.6
Latent Heat L /J kg^{-1}	2.08×10^5
Activation Energy E /J mol^{-1}	2.2×10^5
Heat of Reaction Ω /J kg^{-1}	5.02×10^6
Molar Gas Constant R /J mol^{-1} K^{-1}	8.314
Pre-Exponential Constant A /s^{-1}	$5.011872336 \times 10^{19}$

Table 6.1: Material properties for HMX taken from [34, 72, 90].

extended in a straightforward manner to account for differing material properties. However, in the following lubrication analysis we only treat the liquid layer, and the properties of the solid phase do not appear explicitly at leading-order. As a result, the analysis presented would be unchanged.

6.1.1 Non-dimensional model equations

We now introduce non-dimensional variables, which are related to the dimensional variables by

$$\begin{aligned} x = \tilde{x}/l^*, \quad y = \tilde{y}/l^*, \quad u = \tilde{u}/v_\mathrm{w}, \quad v = \tilde{v}/v_\mathrm{w}, \quad p = \tilde{p}/(\mu^* v_\mathrm{w}/l^*), \\ T = \tilde{T}/\Delta T, \quad t = \tilde{t}/t^*, \quad c = \tilde{c}/c^*, \quad \mu = \tilde{\mu}/\mu^*, \quad \kappa = \tilde{\kappa}/\kappa^*, \end{aligned} \tag{6.1.21}$$

where l^*, v_w, t^*, ΔT, c^*, μ^*, and κ^* are a typical length scale, wall speed, typical time scale, typical temperature difference, and reference specific heat, viscosity, and thermal conductivity, respectively. The time scale used relates to a typical time to ignition in the layer, and is discussed in Section 6.2.4. The length scale may be given as the product of a time scale t^* and the typical wall speed v_w, i.e. $l^* = v_\mathrm{w} t^*$. Here we have chosen to scale the pressure with $(\mu^* v_\mathrm{w})/l^*$ in order to balance with the viscous terms. The non-dimensional specific heat, viscosity, and thermal conductivity are related to their dimensional counterparts through the scalings $c^* = 1034\,\mathrm{J\,kg^{-1}\,K^{-1}}$, $\mu^* = 5.5 \times 10^{-3}\,\mathrm{kg\,m^{-1}\,s^{-1}}$ and $\kappa^* = 0.3884\,\mathrm{W\,m^{-1}\,K^{-1}}$, respectively. For the viscosity we use the values given by Menikoff and Sewell [72], who state that at 800 K the viscosity of HMX drops to $5.5 \times 10^{-3}\,\mathrm{kg\,m^{-1}\,s^{-1}}$, whereas the scaling for the specific heat has been chosen to compare well with previous modelling. The scaling for the thermal conductivity was chosen using the data from [11], and is taken as the value at the melt temperature T_m.

In terms of the non-dimensional variables, the governing equations in the liquid

layer read

$$\frac{\partial u}{\partial x}+\frac{\partial v}{\partial y}=0, \tag{6.1.22}$$

$$\mathrm{Re}\left(\frac{\partial u}{\partial t}+u\frac{\partial u}{\partial x}+v\frac{\partial u}{\partial y}\right)=-\frac{\partial p}{\partial x}+2\frac{\partial}{\partial x}\left(\mu\frac{\partial u}{\partial x}\right)+\frac{\partial}{\partial y}\left[\mu\left(\frac{\partial u}{\partial y}+\frac{\partial v}{\partial x}\right)\right], \tag{6.1.23}$$

$$\mathrm{Re}\left(\frac{\partial v}{\partial t}+u\frac{\partial v}{\partial x}+v\frac{\partial v}{\partial y}\right)=-\frac{\partial p}{\partial y}+2\frac{\partial}{\partial y}\left(\mu\frac{\partial v}{\partial y}\right)+\frac{\partial}{\partial x}\left[\mu\left(\frac{\partial u}{\partial y}+\frac{\partial v}{\partial x}\right)\right], \tag{6.1.24}$$

$$c(T)\left(\frac{\partial T}{\partial t}+u\frac{\partial T}{\partial x}+v\frac{\partial T}{\partial y}\right)=\frac{1}{\mathrm{Pe}}\nabla\cdot(\kappa(T)\,\nabla T)+\frac{\mathrm{Ec}}{\mathrm{Re}}\Phi + \hat{\Omega}\hat{A}(1-\alpha)\exp\left(-\frac{\hat{E}}{T}\right), \tag{6.1.25}$$

$$\Phi=\mu(T)\left\{2\left[\left(\frac{\partial u}{\partial x}\right)^2+\left(\frac{\partial v}{\partial y}\right)^2\right]+\left(\frac{\partial v}{\partial x}+\frac{\partial u}{\partial y}\right)^2\right\}, \tag{6.1.26}$$

where $\mathrm{Re}=(\rho v^* l^*)/\mu^*$ is the Reynolds number, $\mathrm{Pe}=(c^*\rho v_\mathrm{w} l^*)/\kappa^*$ is the Péclet number, and $\mathrm{Ec}=v_\mathrm{w}^2/(c^*\,\Delta T)$ is the Eckert number.

In the solid region, the non-dimensional version of the energy equation is

$$c(T_\mathrm{sol})\frac{\partial T_\mathrm{sol}}{\partial t}=\frac{1}{\mathrm{Pe}}\nabla\cdot(\kappa(T_\mathrm{sol})\,\nabla T_\mathrm{sol})+\hat{\Omega}\hat{A}(1-\alpha)\exp\left(-\frac{\hat{E}}{T_\mathrm{sol}}\right), \tag{6.1.27}$$

In both the liquid and solid region, the mass fraction is governed by the non-dimensional counterpart of (6.1.6), which reads

$$\frac{\partial \alpha}{\partial t}+u\frac{\partial \alpha}{\partial x}+v\frac{\partial \alpha}{\partial y}=\hat{A}(1-\alpha)\exp\left(-\frac{\hat{E}}{T}\right), \tag{6.1.28}$$

where $\hat{\Omega}=\Omega/(c^*\,\Delta T)$ is the non-dimensional heat of reaction, $\hat{A}=t^*A=(l^*A)/v_\mathrm{w}$ is the non-dimensional pre-exponential factor, and $\hat{E}=E/(R\,\Delta T)$ is the non-dimensional activation energy.

The non-dimensional governing equations are to be solved subject to the boundary conditions

$$u(0,y,t)=0,\quad v(0,y,t)=-1\quad u(x_f,y,t)=0,\quad v(x_f,y,t)=0, \tag{6.1.29}$$

$$\frac{\partial T}{\partial x}(0,y,t)=0,\quad T_\mathrm{sol}\to\bar{T}\quad\text{as}\quad x\to\infty, \tag{6.1.30}$$

$$T(x_f(y,t),y,t)=T_\mathrm{sol}(x_f(y,t),y,t)=T_\mathrm{m}, \tag{6.1.31}$$

$$\frac{\partial \alpha}{\partial x}(0,y,t)=0,\quad \alpha(x_f^-,y,t)=\alpha(x_f^+,y,t),\quad \alpha\to 0\quad\text{as}\quad x\to\infty, \tag{6.1.32}$$

$$\frac{\partial T}{\partial y}\to 0,\quad \frac{\partial T_\mathrm{sol}}{\partial y}\to 0,\quad \frac{\partial P}{\partial y}\to 0,\quad \frac{\partial \alpha}{\partial y}\to 0\quad\text{as}\quad y\to\pm\infty, \tag{6.1.33}$$

where $\bar{T}$ is the non-dimensional ambient temperature, and T_{m} is the non-dimensional melt temperature. The boundary conditions are further supplemented by the Stefan condition:

$$v_f = D\left(-\frac{\partial}{\partial n}T(x,y,t)\bigg|_{x=x_f^-} + \frac{\partial}{\partial n}T_{\mathrm{sol}}(x,y,t)\bigg|_{x=x_f^+}\right), \tag{6.1.34}$$

where the non-dimensional diffusion coefficient is given by $D = \mathrm{Ste}\,/\,\mathrm{Pe}$, which is the ratio of the Stefan number to the Péclet number. The Stefan number is the ratio of the sensible heat to the latent heat $\mathrm{Ste} = (c^*\,\Delta T)/L$.

The non-dimensional counterparts of (6.1.18)–(6.1.20) are

$$c(T) = \frac{(\theta_1/T)^2\exp(\theta_1/T)}{(\exp(\theta_1/T)-1)^2}, \tag{6.1.35}$$

$$\mu(T) = \exp\left(\frac{\theta_2}{T} - \frac{\theta_2}{\theta_3}\right), \tag{6.1.36}$$

$$\kappa(T) = \theta_4 + \theta_5\exp(-\theta_6 T), \tag{6.1.37}$$

where the non-dimensional parameters are $\theta_1 = (1000\,\mathrm{K})/\Delta T$, $\theta_2 = (7800\,\mathrm{K})/\Delta T$, $\theta_3 = (800\,\mathrm{K})/\Delta T$, $\theta_4 = (0.26\,\mathrm{W\,m^{-1}\,K^{-1}})/\kappa^*$, $\theta_5 = (246.08\,\mathrm{W\,m^{-1}\,K^{-1}})/\kappa^*$ and $\theta_6 = (0.0145\,\mathrm{K^{-1}})\,\Delta T$.

6.1.2 Small-time behaviour of the melt layer model

Shortly after the onset of melting we expect a balance between the rate of change of temperature and the horizontal diffusion term in the liquid region, essentially reducing the problem to one which is locally one-dimensional. Here we show that we recover the model presented in [90] by considering the two-dimensional model at early times. We formally introduce the small parameter $\Delta \ll 1$ to allow us to investigate the behaviour at small times. For $t \ll 1$ and $x_f \ll 1$ we anticipate the following scalings

$$t \sim \Delta \ll 1, \quad x \sim \sqrt{t} \sim \Delta^{1/2} \ll 1, \quad u \sim \Delta^{1/2} \ll 1, \quad y \sim 1, \quad v \sim 1. \tag{6.1.38}$$

At early times it can be shown that the velocity field is linear $v = x/x_f - 1$, giving local viscous heating $(1/x_f)^2$. Note that the large Prandtl number $\mathrm{Pr} \approx 110$ indicates that thermal diffusion time is much greater than the momentum diffusion time, and validates our assumption that the velocity field is near the steady state [90]. Further, in the early stages of melting the temperature in the melt layer is not expected to be near the activation temperature for the reaction, so the Arrhenius source term is exponentially small.

Under these early time assumptions, and the assumption of constant material properties, the model equations have a solution for a parabolic advancement law for

the phase boundary $x_f = q\sqrt{t}$ which is equivalent to the one-dimensional solution presented in [90]. For mathematical convenience, the solutions in the liquid and solid region are given here in terms of the front-fixed variable $\xi = x/x_f = x/(q\sqrt{t})$.

In order to solve the problem, we introduce three functions: $h_1(\xi)$ and $h_2(\xi)$, which are self-similar and satisfy the time independent part of the problem in each phase, respectively; and $f(\xi, t)$ which is required to satisfy the transient part of the problem. Thus, the temperature in the liquid and solid region may be written

$$T(\xi, t) = f(\xi, t) + h_1(\xi), \quad T_{\text{sol}}(\xi, t) = f(\xi, t) + h_2(\xi). \tag{6.1.39}$$

As stated, the functions $h_i(\xi)$ satisfy the time-independent form of the governing equations,

$$h_1'' + \operatorname{Pe} \frac{q^2}{2} \xi h_1' = -\operatorname{Ec} \operatorname{Pr}, \quad h_2'' + \operatorname{Pe} \frac{q^2}{2} \xi h_2' = 0, \tag{6.1.40}$$

which may be integrated twice through the use of an integrating factor $e^{u\xi^2}$, where $u = \operatorname{Pe} q^2/4$. Application of the appropriate boundary conditions gives the solutions

$$\begin{aligned} h_1(\xi) = T_m + \operatorname{Ec} \operatorname{Pr} \frac{\sqrt{\pi}}{2u} \left(\operatorname{erf}(\sqrt{u}) \int_0^{\sqrt{u}} e^{q^2} \, \mathrm{d}q - \int_0^{\sqrt{u}} \operatorname{erf}(q) e^{q^2} \, \mathrm{d}q \right) \\ - \operatorname{Ec} \operatorname{Pr} \int_0^{\xi} e^{-u\xi_2^2} \int_0^{\xi_2} e^{u\xi_1^2} \, \mathrm{d}\xi_1 \, \mathrm{d}\xi_2, \qquad 0 < \xi < 1, \end{aligned} \tag{6.1.41}$$

and

$$h_2(\xi) = \bar{T} - (\bar{T} - T_m) \frac{\operatorname{erfc}(\sqrt{u}\xi)}{\operatorname{erfc}(\sqrt{u})}, \qquad \xi > 1, \tag{6.1.42}$$

respectively. The Stefan condition provides the equation for the propagation parameter u

$$\operatorname{Pe} x_f \dot{x}_f = 2u = \operatorname{Ste} \left(\operatorname{Ec} \operatorname{Pr} \frac{e^{-u}}{\sqrt{u}} \int_0^{\sqrt{u}} e^{q^2} \, \mathrm{d}q - \frac{2(T_{\mathrm{m}} - \bar{T})}{\sqrt{\pi}} \frac{e^{-u}\sqrt{u}}{\operatorname{erfc}(\sqrt{u})} \right). \tag{6.1.43}$$

The function $f(\xi, t)$ satisfies the equation

$$q^2 t \frac{\partial f}{\partial t} = \frac{\partial^2 f}{\partial \xi^2} + \frac{q^2}{2} \xi \frac{\partial f}{\partial \xi}, \tag{6.1.44}$$

and must have vanishing first derivative at the origin, decay at infinity, and be continuous at the melt front. It can be shown (see [90]) that f has the following form:

$$f(\xi, t) = f_0 \left(\frac{t_0}{t} \right)^{\beta^2/q^2} {}_1F_1 \left(\frac{\beta^2}{q^2}, \frac{1}{2}, -\frac{q^2}{4} \xi^2 \right), \tag{6.1.45}$$

where t_0 is the initial time, ${}_1F_1$ is a confluent hypergeometric function [1], β is a constant which is fixed by ensuring the $f(\xi, t)$ vanishes at $\xi = 1$ (thus satisfying the

boundary condition $T = T_{\mathrm{m}} = T_{\mathrm{sol}}$ at $\xi = 1$), and f_0 is fixed by imposing an initial temperature profile.

A number of other self similar solutions with a parabolic advancement law for the phase boundary are available. For discussion see Carslaw and Jaeger [22], for example.

6.1.3 Lubrication approximation

After an initial small time period a viscous melt layer will have formed between the moving wall and the solid explosive. The melt layer is expected to be thin in comparison to its length, so we adopt the lubrication approximation (see [77], for example). This essentially reduces the problem to a single-phase Stefan problem in which we are concerned with the temperature evolution in the liquid melt layer. To exploit this expected thinness of the melt layer, we adopt the usual scalings

$$x = \epsilon X, \quad u = \epsilon U, \quad p = \epsilon^{-2} P, \tag{6.1.46}$$

where ϵ is a small parameter such that X, U, P are $O(1)$ in the thin melt layer. The governing equations for the liquid melt layer read

$$\frac{\partial U}{\partial X} + \frac{\partial v}{\partial y} = 0, \tag{6.1.47}$$

$$\epsilon^4 \operatorname{Re}\left(\frac{\partial U}{\partial t} + U\frac{\partial U}{\partial X} + v\frac{\partial U}{\partial y}\right) = -\frac{\partial P}{\partial X} + 2\varepsilon^2 \frac{\partial}{\partial X}\left(\mu \frac{\partial U}{\partial X}\right) + \frac{\partial}{\partial y}\left[\mu\left(\epsilon^4 \frac{\partial U}{\partial y} + \epsilon^2 \frac{\partial v}{\partial X}\right)\right], \tag{6.1.48}$$

$$\epsilon^2 \operatorname{Re}\left(\frac{\partial v}{\partial t} + U\frac{\partial v}{\partial X} + v\frac{\partial v}{\partial y}\right) = -\frac{\partial P}{\partial y} + \epsilon^2 \frac{\partial}{\partial y}\left(\mu \frac{\partial v}{\partial y}\right) + \frac{\partial}{\partial X}\left[\mu\left(\epsilon^2 \frac{\partial U}{\partial y} + \frac{\partial v}{\partial X}\right)\right]. \tag{6.1.49}$$

Making the usual assumption that both $\epsilon \ll 1$ and $\epsilon^2 \operatorname{Re} \ll 1$ gives the leading-order governing equations in the melt layer

$$\frac{\partial U}{\partial X} + \frac{\partial v}{\partial y} = 0, \tag{6.1.50}$$

$$\frac{\partial P}{\partial X} = 0, \tag{6.1.51}$$

$$-\frac{\partial P}{\partial y} + \frac{\partial}{\partial X}\left(\mu(T)\frac{\partial v}{\partial X}\right) = 0. \tag{6.1.52}$$

Equations (6.1.50)–(6.1.52) are to be solved subject to no-slip boundary conditions on the wall and melt front, where the liquid melt layer will be in contact with the unmelted solid explosive. Since we are restricting our attention to localised disturbances we expect that far from the site of the two-dimensional disturbance the solution will resemble the one-dimensional solution, and that the pressure will be a function of time only.

Substitution of the lubrication layer scalings (6.1.46) into the energy equation for the melt layer (6.1.25) provides

$$c(T)\left(\frac{\partial T}{\partial t}+U\frac{\partial T}{\partial X}+v\frac{\partial T}{\partial y}\right)=\frac{1}{\mathrm{Pe}}\epsilon^{-2}\left(\frac{\partial \kappa(T)}{\partial X}\frac{\partial T}{\partial X}+\kappa(T)\frac{\partial^2 T}{\partial X^2}\right) + \frac{1}{\mathrm{Pe}}\left(\frac{\partial \kappa(T)}{\partial y}\frac{\partial T}{\partial y}+\kappa(T)\frac{\partial^2 T}{\partial y^2}\right)+\frac{\mathrm{Ec}}{\mathrm{Re}}\Phi+\hat{\Omega}\hat{A}(1-\alpha)\exp\left(-\frac{\hat{E}}{T}\right), \quad (6.1.53)$$

where the expansion of the mechanical dissipation is given by

$$\Phi=\mu(T)\left\{2\left[\left(\frac{\partial U}{\partial X}\right)^2+\left(\frac{\partial v}{\partial y}\right)^2\right]+\epsilon^{-2}\left(\frac{\partial v}{\partial X}\right)^2+\epsilon^2\left(\frac{\partial u}{\partial y}\right)^2+2\frac{\partial v}{\partial X}\frac{\partial U}{\partial y}\right\}. \quad (6.1.54)$$

The energy equation (6.1.53) is to be solved subject to the boundary conditions

$$\frac{\partial T}{\partial X}(0,y,t)=0, \quad T(X_f,y,t)=T_\mathrm{m}, \quad \frac{\partial T}{\partial y}\to 0 \text{ as } y\to\pm\infty. \quad (6.1.55)$$

The small parameter ϵ is fixed to obtain a dominant balance between convection, diffusion and dissipation terms in the melt layer. This amounts to ensuring the horizontal diffusion term in the energy equation (6.1.53) is $O(1)$, so that

$$\epsilon^2=\frac{1}{\mathrm{Pe}}. \quad (6.1.56)$$

For the material properties used in this study we find that the Péclet number is in the range $10^3<\mathrm{Pe}<10^6$, depending on wall speed v_w, so that ϵ is indeed small. Alternatively, one could choose to balance the diffusion with the reaction term, fixing $\epsilon=(\mathrm{Pe}\,\hat{\Omega}\hat{A})^{-1/2}$. In the modelling of shear bands, some authors [e.g. 54] account for a inner zone in which the source term (plastic work in the modelling of shear bands, but chemical reaction here) is balanced by diffusion. Such a dominant balance could be useful to describe the temperature profile near to the wall during the later stages of the melting process when the chemical reaction dominates.

We retain the leading-order terms, along with the reaction term which is initially small but grows rapidly as the temperature increases. The leading-order energy equation in the melt layer now reads

$$c(T)\left(\frac{\partial T}{\partial t}+U\frac{\partial T}{\partial X}+v\frac{\partial T}{\partial y}\right)=\frac{\partial \kappa(T)}{\partial X}\frac{\partial T}{\partial X}+\kappa(T)\frac{\partial^2 T}{\partial X^2} + \mathrm{Ec}\,\mathrm{Pr}\,\Phi+\hat{\Omega}\hat{A}(1-\alpha)\exp\left(-\frac{\hat{E}}{T}\right), \quad (6.1.57)$$

with $\Phi=\mu(T)\left(\partial v/\partial X\right)^2$. Here we have introduced the Prandtl number, defined as $\mathrm{Pr}=(c^*\mu^*)/\kappa^*$. Note that for heat transfer the Péclet number can be written as the product of the Reynolds number and the Prandtl number: $\mathrm{Pe}=\mathrm{Re}\,\mathrm{Pr}$. The rescaled

Stefan condition (6.1.34) reads

$$\epsilon\frac{\partial X_f}{\partial t}(y,t) = D\left(-\epsilon^{-1}\left.\frac{\partial T}{\partial X}\right|_{X=X_f^-} + \epsilon^{-1}\left.\frac{\partial}{\partial X}(\epsilon T'_{\rm sol}(X=X_f)+O(\epsilon^2))\right|_{X=X_f^+}\right), \tag{6.1.58}$$

where the solid temperature has been expanded about the melt front so that the size of its derivative may be properly determined with respect to ϵ. For the material properties quoted for HMX, and taking a typical temperature difference to be $\Delta T \sim O(100\,\mathrm{K})$, it is found that the Stefan number is typically $O(1)$. This makes the diffusion coefficient $D \sim O(\epsilon^2)$ so that the leading-order Stefan condition is given by

$$\frac{\partial X_f}{\partial t} = -\,\mathrm{Ste}\left.\frac{\partial T}{\partial X}\right|_{X=X_f^-}. \tag{6.1.59}$$

Note that, owing to the thinness of the melt layer, the melting only occurs laterally to leading-order in ϵ.

In our thin layer model we only treat the liquid layer, and the solid appears to be at the constant melt temperature $T_{\rm m}$ to leading-order in ϵ. It can be shown that at this fixed temperature, and over the timescale for reaction in the liquid layer, that the reaction progress in the solid is exponentially small, and therefore the solid region can be considered unreacted to leading-order. As a result, the boundary condition $(6.1.32)_2$ on the mass fraction α at the melt front is replaced with $\partial\alpha/\partial x = 0$ at $x = x_f$. This no-flux boundary condition has the physical interpretation that no gaseous products may flow into the unreacted solid explosive.

6.1.4 Front-fixing transformation

In Section 6.2.4 the governing equations in the liquid region (6.1.50)–(6.1.52), (6.1.57) and (6.1.59), along with the Arrhenius equation (6.1.28) are to be solved numerically. In order to facilitate this we introduce the front-fixed co-ordinate $\xi = X/X_f$. This significantly simplifies the numerical treatment, and formally recovers a fixed grid. The 3×3 Jacobian transformation matrix reads

$$\boldsymbol{J} = \frac{\partial(\xi,y,t)}{\partial(X,y,t)} = \begin{pmatrix} \frac{1}{X_f} & 0 & 0 \\ -\frac{\partial X_f}{\partial y}\frac{\xi}{X_f} & 1 & 0 \\ -\frac{\partial X_f}{\partial t}\frac{\xi}{X_f} & 0 & 1 \end{pmatrix}. \tag{6.1.60}$$

Under this coordinate transformation the moving phase boundary is located exactly at $\xi = 1$. The governing equations for the melt front take the following form in the front-fixing coordinates:

$$\frac{1}{X_f}\frac{\partial U}{\partial \xi} - \frac{\partial X_f}{\partial y}\frac{\xi}{X_f}\frac{\partial v}{\partial \xi} + \frac{\partial v}{\partial y} = 0, \tag{6.1.61}$$

$$\frac{1}{X_f}\frac{\partial P}{\partial \xi} = 0, \tag{6.1.62}$$

$$\frac{\partial X_f}{\partial y}\frac{\xi}{X_f}\frac{\partial P}{\partial \xi} - \frac{\partial P}{\partial y} + \frac{1}{X_f^2}\frac{\partial}{\partial \xi}\left(\mu(T)\frac{\partial v}{\partial \xi}\right) = 0, \tag{6.1.63}$$

$$\begin{aligned} c(T)\left(\frac{\partial T}{\partial t} + \frac{1}{X_f}\left(U - \frac{\partial X_f}{\partial t}\xi - v\frac{\partial X_f}{\partial y}\xi\right)\frac{\partial T}{\partial \xi} + v\frac{\partial T}{\partial y}\right) \\ = \frac{1}{X_f^2}\left(\frac{\partial \kappa(T)}{\partial \xi}\frac{\partial T}{\partial \xi} + \kappa(T)\frac{\partial^2 T}{\partial \xi^2}\right) + \mathrm{Ec}\,\mathrm{Pr}\,\Phi + \hat{\Omega}\hat{A}(1-\alpha)\exp\left(-\frac{\hat{E}}{T}\right), \end{aligned} \tag{6.1.64}$$

$$\Phi = \mu(T)\frac{1}{X_f^2}\left(\frac{\partial v}{\partial \xi}\right)^2, \tag{6.1.65}$$

$$\frac{\partial X_f}{\partial t} + \mathrm{Ste}\,\frac{1}{X_f}\frac{\partial T}{\partial \xi}\bigg|_{\xi=1^-} = 0, \tag{6.1.66}$$

$$\frac{\partial \alpha}{\partial t} + \frac{1}{X_f}\left(U - \frac{\partial X_f}{\partial t}\xi - v\frac{\partial X_f}{\partial y}\xi\right)\frac{\partial \alpha}{\partial \xi} + v\frac{\partial \alpha}{\partial y} = \hat{A}(1-\alpha)\exp\left(-\frac{\hat{E}}{T}\right), \tag{6.1.67}$$

where velocity components U and v, temperature T, and mass fraction α are all functions of ξ, y, t, and pressure P and melt front location X_f are functions of y and t only. This formulation of the problem will be used to obtain asymptotic results in Sections 6.2.1 and 6.3.

In the preceding analysis we have derived a two-dimensional model for the melting of HMX. The introduction of the lubrication approximation has reduced the problem to a single-phase Stefan problem, in which the melt front only propagates in the direction perpendicular to the wall located at $\xi = 0$ ($X = 0$). The solid region of unmelted explosive occupying the region $\xi > 1$ ($X > X_f$) is held fixed at the melting temperature T_m. In the absence of any y dependence the analysis in this section may be viewed as a formal derivation of the ad-hoc one-dimensional model for a thin shear-melted viscous layer presented in [90].

6.2 Shear melt model: constant material properties

In order to simplify the analysis, and to compare results with [90], the specific heat, viscosity, and thermal conductivity are treated as constant in this section, taking dimensional values $\tilde{c} = 989.25\,\mathrm{J\,kg^{-1}\,K^{-1}}$, $\tilde{\mu} = 4.6 \times 10^{-2}\,\mathrm{kg\,m^{-1}\,s^{-1}}$ and $\tilde{\kappa} = 0.404\,\mathrm{W\,m^{-1}\,K^{-1}}$, respectively. Since the material properties are assumed independent of temperature, the functions (6.1.35)–(6.1.37) are constant $c(T) = \mu(T) = \kappa(T) = 1$. This assumption will be relaxed in Section 6.3, where the effects of temperature dependent material properties will be investigated, and are shown to make only a minor qualitative difference to the hot spot generation mechanisms discussed here.

For constant material properties, the mechanical and thermal equations decouple and explicit expressions may be found for the velocity components. Equation (6.1.62)

immediately requires that the pressure in the lubrication layer is independent of ξ, i.e. $P = P(y,t)$. Integrating (6.1.63) directly with respect to ξ and applying boundary conditions we obtain an expression for the vertical velocity component

$$v(\xi,y,t) = \frac{1}{2}X_f^2\frac{\partial P}{\partial y}\xi\left(\xi-1\right) - \left(1-\xi\right). \tag{6.2.1}$$

The horizontal velocity component may then be calculated by integration of the continuity equation (6.1.61) a distance ξ across the layer

$$U(\xi,y,t) = \frac{1}{2}\frac{\partial X_f}{\partial y}\xi^2 + \frac{1}{12}\left(3X_f^2\frac{\partial X_f}{\partial y}\frac{\partial P}{\partial y}\xi^2 + 6X_f^3\frac{\partial^2 P}{\partial y^2}\left(\frac{\xi^2}{2}-\frac{\xi^3}{3}\right)\right). \tag{6.2.2}$$

Application of the no-slip boundary conditions then provides the standard Reynolds lubrication equation, relating the position of the melt front and the pressure gradient

$$\frac{\partial X_f}{\partial y} + \frac{\partial}{\partial y}\left(\frac{X_f^3}{6}\frac{\partial P}{\partial y}\right) = 0. \tag{6.2.3}$$

In Section 6.2.4 the above expressions will be substituted into the energy equation, which is solved numerically subject to the Stefan condition. The simplified system of equations that result from assuming constant material properties allows consideration of larger departures from a uniform melt front in our numerical analysis.

6.2.1 Asymptotic analysis for small disturbances to the melt front

In this section we consider small deviations from a flat melt front $X_{f0} = X_{f0}(t)$ for both reactive and non-reactive materials in order to assess the stability of the melt front in the presence and absence of any chemical reaction. The problem is linearised about X_{f0}, and formulated in terms of the leading-order front-fixed coordinate $\zeta = X/X_{f0}$ instead of $\xi = X/X_f$. It is demonstrated that the melt front is linearly stable to small disturbances in the absence of the chemical reaction, but linearly unstable upon inclusion of the Arrhenius source term. We look for a solution in terms of a perturbation series, writing

$$X_f = X_{f0}(t) + \delta X_{f1}(t)S(y) + O(\delta^2), \tag{6.2.4}$$

$$P(y,t) = P_0(t) + \delta P_1(y,t) + O(\delta^2), \tag{6.2.5}$$

$$[U,v,T,\alpha](\zeta,y,t) = [U_0,v_0,T_0,\alpha_0](\zeta,t) + \delta[U_1,v_1,T_1,\alpha_1](\zeta,y,t) + O(\delta^2), \tag{6.2.6}$$

where $0 < \delta \ll 1$ and $S(y)$ is a given function describing the shape of the localised disturbance in the melt front. Note that since we are only considering localised disturbances we require that $S \to 0$ as $y \to \pm\infty$. We further stipulate that this shape must be slowly varying in the y direction so that its derivatives may be neglected to a first approximation.

The expansions (6.2.4)–(6.2.6) are substituted into the governing equations (6.1.61)–(6.1.67) and terms with like powers of δ are collected to form a series of problems to be solved. At leading-order we have the problem

$$\frac{1}{X_{f0}}\frac{\partial U_0}{\partial \zeta} = 0, \tag{6.2.7}$$

$$\frac{1}{X_{f0}^2}\frac{\partial^2 v_0}{\partial \zeta^2} = 0, \tag{6.2.8}$$

$$\frac{\partial T_0}{\partial t} + \frac{1}{X_{f0}}\left(U_0 - \frac{\partial X_{f0}}{\partial t}\zeta\right)\frac{\partial T_0}{\partial \zeta} = \frac{1}{X_{f0}^2}\frac{\partial^2 T_0}{\partial \zeta^2} + \mathrm{Ec}\,\mathrm{Pr}\,\Phi_0 + \hat{\Omega}\hat{A}(1-\alpha_0)\exp\left(-\frac{\hat{E}}{T_0}\right), \tag{6.2.9}$$

$$\Phi_0 = \frac{1}{X_{f0}^2}\left(\frac{\partial v_0}{\partial \zeta}\right)^2, \tag{6.2.10}$$

$$\frac{\partial X_{f0}}{\partial t} = -\,\mathrm{Ste}\,\frac{1}{X_{f0}}\left.\frac{\partial T_0}{\partial \zeta}\right|_{\zeta=1^-}, \tag{6.2.11}$$

$$\frac{\partial \alpha_0}{\partial t} + \frac{1}{X_{f0}}\left(U_0 - \frac{\partial X_{f0}}{\partial t}\zeta\right)\frac{\partial \alpha_0}{\partial \zeta} = \hat{A}(1-\alpha_0)\exp\left(-\frac{\hat{E}}{T_0}\right), \tag{6.2.12}$$

with boundary conditions

$$U_0 = 0, \qquad v_0 = -1, \qquad \frac{\partial T_0}{\partial \zeta} = 0, \qquad \frac{\partial \alpha_0}{\partial \zeta} = 0 \qquad \text{on } \zeta = 0, \tag{6.2.13}$$

$$U_0 = 0, \qquad v_0 = 0, \qquad T_0 = T_\mathrm{m}, \qquad \frac{\partial \alpha_0}{\partial \zeta} = 0 \qquad \text{on } \zeta = 1. \tag{6.2.14}$$

At $O(\delta)$ we have the problem

$$\frac{1}{X_{f0}}\frac{\partial U_1}{\partial \zeta} + \frac{\partial v_1}{\partial y} = 0, \tag{6.2.15}$$

$$-\frac{\partial P_1}{\partial y} + \frac{1}{X_{f0}^2}\frac{\partial^2 v_1}{\partial \zeta^2} = 0, \tag{6.2.16}$$

$$\frac{\partial T_1}{\partial t} + \frac{1}{X_{f0}}\left(U_0 - \frac{\partial X_{f0}}{\partial t}\zeta\right)\frac{\partial T_1}{\partial \zeta} + \frac{1}{X_{f0}}\left(U_1 - \frac{\partial X_{f1}}{\partial t}S\zeta\right)\frac{\partial T_0}{\partial \zeta} + v_0\frac{\partial T_1}{\partial y} = \frac{1}{X_{f0}^2}\frac{\partial^2 T_1}{\partial \zeta^2} + \mathrm{Ec}\,\mathrm{Pr}\,\Phi_1 + \hat{\Omega}\hat{A}\left[(1-\alpha_0)\frac{\hat{E}}{T_0^2}T_1 - \alpha_1\right]\exp\left(-\frac{\hat{E}}{T_0}\right), \tag{6.2.17}$$

$$\Phi_1 = \frac{2}{X_{f0}^2}\frac{\partial v_0}{\partial \zeta}\frac{\partial v_1}{\partial \zeta}, \tag{6.2.18}$$

$$\frac{\partial X_{f1}}{\partial t} = -\,\mathrm{Ste}\,\left.\left(\frac{X_{f1}}{X_{f0}^2}\frac{\partial T_0}{\partial \zeta} + \frac{1}{X_{f0}}\frac{\partial T_1}{\partial \zeta}\right)\right|_{\zeta=1^-}, \tag{6.2.19}$$

$$\frac{\partial \alpha_1}{\partial t} + \frac{1}{X_{f0}}\left(U_0 - \frac{\partial X_{f0}}{\partial t}\zeta\right)\frac{\partial \alpha_1}{\partial \zeta} + \frac{1}{X_{f0}}\left(U_1 - \frac{\partial X_{f1}}{\partial t}S\zeta\right)\frac{\partial \alpha_0}{\partial \zeta} + v_0\frac{\partial \alpha_1}{\partial y}$$

$$= \hat{A}\left[(1-\alpha_0)\frac{\hat{E}}{T_0^2}T_1 - \alpha_1\right]\exp\left(-\frac{\hat{E}}{T_0}\right), \qquad (6.2.20)$$

with boundary conditions

$$U_1 = 0, \quad v_1 = 0, \quad \frac{\partial T_1}{\partial \zeta} = 0, \quad \frac{\partial \alpha_1}{\partial \zeta} = 0 \quad \text{on } \zeta = 0, \qquad (6.2.21)$$

$$\frac{X_{f1}}{X_{f0}}\frac{\partial U_0}{\partial \zeta} + U_1 = 0, \quad \frac{X_{f1}}{X_{f0}}\frac{\partial v_0}{\partial \zeta} + v_1 = 0 \quad \text{on } \zeta = 1,$$

$$\frac{X_{f1}}{X_{f0}}\frac{\partial T_0}{\partial \zeta} + T_1 = 0, \quad \frac{X_{f1}}{X_{f0}}\frac{\partial \alpha_0}{\partial \zeta} + \alpha_1 = 0 \quad \text{on } \zeta = 1. \qquad (6.2.22)$$

Integration of (6.2.16) twice with respect to ζ and application of the appropriate boundary conditions gives that $v_1 \sim S(y)$. By (6.2.15) it is then found that $U_1 \sim S'(y)$, so the horizontal velocity is neglected up to $O(\delta)$ in this analysis.

6.2.2 Linearised model: non-reactive material

Here we consider the heating solely due to mechanical dissipation in the melt layer. Naturally, we take $\hat{A} = 0$ since we are considering non-reactive materials. The leading-order problem is the same as that found in [90] and has an analytical solution, whereas the first-order problem is solved numerically using an iterative Crank-Nicolson scheme.

It is easily verified that a steady state velocity profile satisfies equations (6.2.7) and (6.2.8) for the leading-order velocity components

$$U_0(\zeta, t) = 0, \quad v_0(\zeta, t) = \zeta - 1, \qquad (6.2.23)$$

which, by equation (6.2.10), predicts uniform leading-order dissipative heating $\Phi_0(t) = 1/X_{f0}^2$. The same solution may be found by substitution of the expansions into equations (6.2.1)–(6.2.3). In the absence of any chemical reaction, the leading-order equations admit a self-similar analytical solution which has parabolic advancement of the melt front $X_{f0} = q\sqrt{t}$, with propagation parameter q. As in Section 6.1.2, we look for a solution which decomposes the temperature into two parts: a self-similar part which satisfies the time independent part of the problem; and a transient part which is required to satisfy the initial conditions. Thus, the leading-order temperature may be written

$$T_0(\zeta, t) = f(\zeta, t) + h(\zeta). \qquad (6.2.24)$$

The function $h(\zeta)$ which satisfies the time-independent form of (6.2.9), along with the appropriate boundary conditions, is given by

$$h(\zeta) = T_{\mathrm{m}} + \mathrm{Ec}\,\mathrm{Pr}\,\frac{\sqrt{\pi}}{2u}\left(\mathrm{erf}(\sqrt{u})\int_0^{\sqrt{u}} e^{q^2}\,\mathrm{d}q - \int_0^{\sqrt{u}} \mathrm{erf}(q)e^{q^2}\,\mathrm{d}q\right)$$

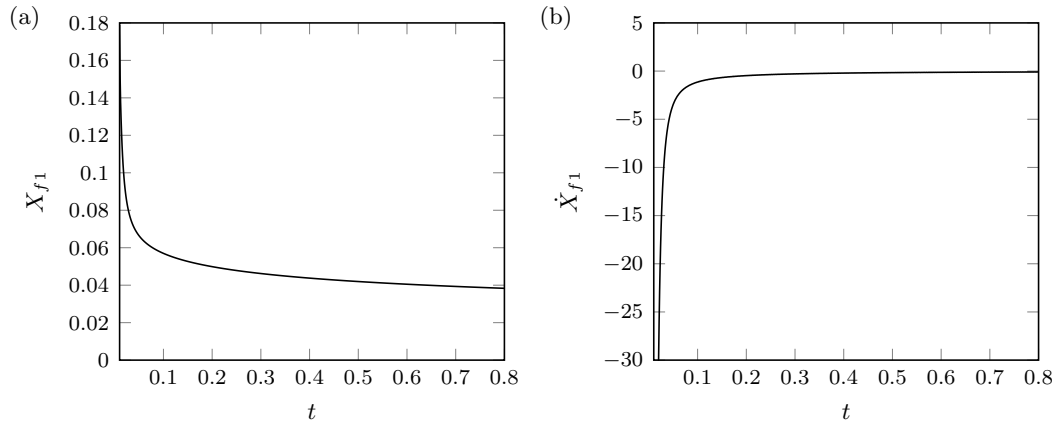

Figure 6.2: (a) Melt front correction X_{f1}; and (b) melt front correction propagation speed $\dot{X}_{f1}$ for an inert melt layer, both as a function of non-dimensional time t. In the absence of any chemical reaction, the melt front is shown to be linearly stable to small perturbations in shape.

$$- \operatorname{Ec}\operatorname{Pr}\int_0^{\zeta} e^{-u\zeta_2^2}\int_0^{\zeta_2} e^{u\zeta_1^2}\,\mathrm{d}\zeta_1\,\mathrm{d}\zeta_2, \tag{6.2.25}$$

with the propagation parameter $u = q^2/4$ satisfying

$$2u = \operatorname{Ste}\operatorname{Ec}\operatorname{Pr}\frac{e^{-u}}{\sqrt{u}}\int_0^{\sqrt{u}} e^{q^2}\,\mathrm{d}q. \tag{6.2.26}$$

The function $f(\zeta, t)$ satisfies the equation

$$q^2 t\frac{\partial f}{\partial t} = \frac{\partial^2 f}{\partial \zeta^2} + \frac{q^2}{2}\zeta\frac{\partial f}{\partial \zeta}, \tag{6.2.27}$$

and must have vanishing first derivative at $\zeta = 0$. We also require $f(1, t) = 0$ so that the temperature is equal to the melt temperature T_{m} at the melt front. As in Section 6.1.2, the the function $f(\zeta, t)$ has the form:

$$f(\zeta, t) = f_0\left(\frac{t_0}{t}\right)^{\beta^2/q^2} {}_1F_1\left(\frac{\beta^2}{q^2}, \frac{1}{2}, -\frac{q^2}{4}\zeta^2\right). \tag{6.2.28}$$

This leading-order solution is essentially the same as the small-time solution in Section 6.1.2. However, owing to the lubrication approximation, the influence of the solid temperature does not appear at this order.

Figure 6.2 shows the melt front correction X_{f1} and melt front propagation speed $\dot{X}_{f1}$ both as a function of time. It is found that small spatial variations in the melt front are linearly stable, always decaying back to the one-dimensional case for a non-reactive material. We observe that the propagation speed decays very rapidly, and we soon return to a solution close to the one-dimensional solution.

Figure 6.3 (a) shows the leading-order velocity, i.e. the linear profile, along with the velocity computed up to $O(\delta)$. We observe a small departure from the linear profile, which in turn creates some spatial variation in the mechanical heating across

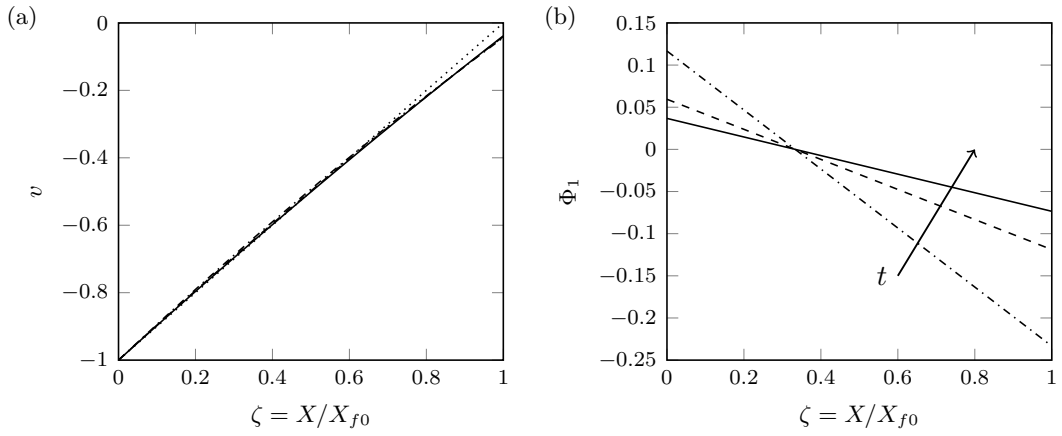

Figure 6.3: (a) The vertical velocity v correct up to $O(\delta)$; and (b) the (ζ, t) dependence of the first-order correction to the mechanical dissipation, i.e. $\Phi_1 = 4(X_{f1}/X_{f0}^3)(1-3\zeta)S(y)$ with fixed $S(y) = 1$. Both are plotted as a function of the leading-order front-fixed variable ζ at a series of increasing times. The dotted line $(\cdots)$ in (a) shows the leading-order linear velocity profile.

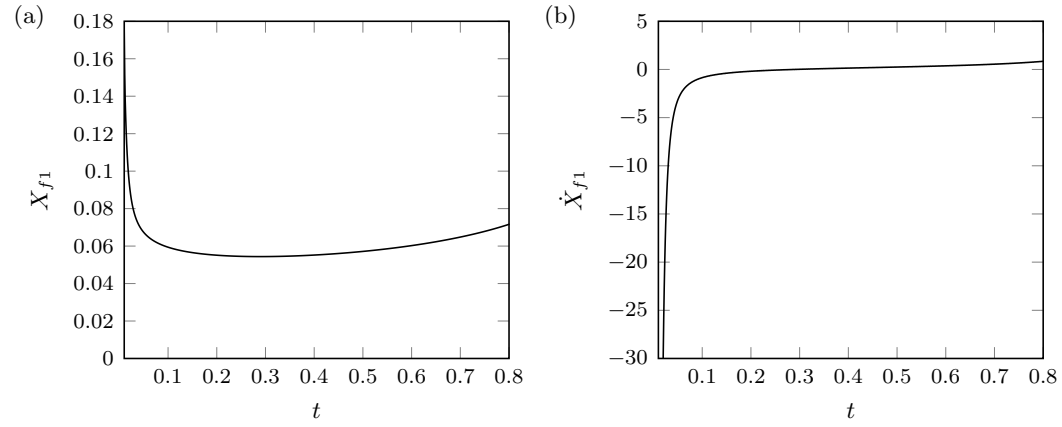

Figure 6.4: (a) Melt front correction X_{f1}; and (b) melt front correction propagation speed $\dot{X}_{f1}$ for a reactive melt layer, both as a function of non-dimensional time t. It is found that the inclusion of a chemical reaction in the melt layer has a destabilising effect; the melt front is no longer linearly stable to small perturbations in shape.

the melt layer, as seen in Figure 6.3 (b) which depicts the first-order correction to the dissipation at a series of increasing times. The correction to the mechanical dissipation may be calculated in terms of the melt front correction X_{f1} as

$$\Phi_1(\zeta, y, t) = 4\frac{X_{f1}}{X_{f0}}(1-3\zeta)S(y), \tag{6.2.29}$$

which has a root at $\zeta = 1/3$, so that we always observe an area of increased dissipative heating along with an accompanying area of decreased heating. The locations of these so-called "mechanical hot/cool spots" will depend on the sign of the shape function $S(y)$. Irrespective of the selected shape, Figure 6.3 shows clear localisation of mechanical dissipation which may serve as a source for hot spot generation.

The results of the perturbation analysis can be investigated for different melt front shapes and the key results are discussed here. For initial conditions which solely act

to widen the melt layer ($S(y) > 0$) we find increased dissipative heating adjacent to the moving wall and decreased heating on the opposite side of the melt layer, near the solid explosive. Localised dissipation is also witnessed in computations using initial conditions which perturb the melt front towards the wall ($S(y) < 0$). However, this heating happens adjacent to the unmelted solid explosive material, with an accompanying region close to the wall in which the dissipation is lower. In shapes which provide both positive and negative disturbances both heating mechanisms are present – we observe increased dissipative heating both near the wall where the melt layer widens and near the solid explosive where the melt layer narrows.

The locations of the mechanical hot, and accompanying cool, spots may be understood by consideration of the dissipation term near the sliding wall and melt front. Upon substitution of the analytical solution for the vertical velocity component (6.2.1) into the dissipation (6.1.65) we find

$$\Phi \sim \frac{1}{X_f^2}\left(1 + \frac{X_f^4}{4}\left(\frac{\partial P}{\partial y}\right)^2\right) - \frac{\partial P}{\partial y} \qquad \text{near } \xi = 0 \ (X = 0), \tag{6.2.30}$$

$$\Phi \sim \frac{1}{X_f^2}\left(1 + \frac{X_f^4}{4}\left(\frac{\partial P}{\partial y}\right)^2\right) + \frac{\partial P}{\partial y} \qquad \text{near } \xi = 1 \ (X = X_f). \tag{6.2.31}$$

We observe that the final correction term to the heating depends on the sign of the pressure gradient, which is negative for disturbances away from the wall and positive for disturbances towards the wall. The above considerations also explain why we always observe an accompanying mechanical cool spot on the opposite side of the melt layer to each hot spot.

Clearly the solution for the non-reactive material cannot make any predictions regarding time to thermal runaway or locations of increased chemical heating. However, a large temperature increase is required to start the chemical reaction, so the localisation of heating due to mechanical dissipation is an excellent indicator of possible hot spot locations.

6.2.3 Linearised model: reactive material

We now account for self-heating due to exothermic reaction in the melt layer. The non-dimensional rate constant $\hat{A} = t^* A$ is no longer taken to be zero, and we include an Arrhenius heat source, described by equations (6.2.12) and (6.2.20), in our analysis to account for the chemical reaction. In this case, both the leading- and first-order equations are solved numerically. Since the material properties are considered to be constant, the velocity profile remains unchanged, as does the mechanical heating in the layer. However, the heat generated by the chemical reactions affects the propagation of the melt front. Figure 6.4 shows the first-order correction to the melt front X_{f1} and its propagation speed $\dot{X}_{f1}$. In contrast to the non-reactive results we find that the perturbation begins to grow in time, i.e. the melt front is

found to be linearly unstable upon inclusion of the Arrhenius source term. This destabilising effect introduced by the chemical reaction may lead to the growth of local disturbances to the melt front, which in turn may lead to the formation of more violent hot spots.

6.2.4 Numerical results for a reactive material

We now return to the full problem described by (6.1.61)–(6.1.67), including the Arrhenius source term. The model equations for the liquid region in the front-fixing coordinates are solved numerically using an iterative Crank-Nicolson scheme, subject to the boundary conditions which are the front-fixed counterparts of conditions (6.1.55), which read

$$\frac{1}{X_f}\frac{\partial T}{\partial \xi}(0,y,t)=0, \quad T(1,y,t)=T_{\mathrm{m}}, \quad \frac{\partial T}{\partial y}\to 0 \text{ as } y\to\pm\infty, \tag{6.2.32}$$

where we have used the fact that we are studying localised shapes ($S \to 0$ as $y \to \pm\infty$) to remove the terms arising from the coordinate transformation in the final condition. We solve the problem on an $N_\xi \times N_y$ grid, with subscripts $i = 1, \ldots, N_\xi$ and $j = 1, \ldots, N_y$ indexing the position and superscript k denoting the time step. The convective terms were discretised using a standard two-point centred difference and the second order diffusive term was discretised using a three point centred difference, both of which are averaged over the current and subsequent time steps. For the time derivative a second order centred difference is used to evaluate the derivative at the point $(\xi_i, y_j, t_{k+1/2})$. The nonlinear terms were evaluated at the mid-level, in keeping with the rest of the scheme. This gives overall truncation error $O(\Delta\xi^2, \Delta y^2, \Delta t^2)$, where $\Delta\xi$, Δy and Δt are the grid and time spacing, respectively. Typically a grid spacing of $\Delta\xi = 0.02$ and $\Delta y = 0.06$ was used. For the time-stepping an adaptive scheme was used allowing for larger steps to be taken in the early stage of the simulation before the onset of rapid reaction.

The method uses an initial condition provided by the small time solution given in Appendix 6.1.2 and proceeds in the following way:

1. The current iterate of the temperature is computed using the discrete form of the energy equation (6.1.64) using the current melt front location.

2. The current melt front location is updated using the Stefan condition (6.1.66) with the current temperature iterate.

3. The current iterate of the pressure gradient is updated using (6.2.3).

This process is iterated until the melt front location converges. In practice it is found that 2 or 3 iterations is normally sufficient to meet a convergence threshold of 10^{-6} in the relative change in the melt front location.

To obtain a suitable initial condition for computations an initial time t_0 is selected, and the time-independent part of the analytical one-dimensional solution for non-reactive materials (6.2.25) is applied at each y station in the finite difference scheme. This approach is consistent with the assumption that the melt layer has already formed before being perturbed. The one-dimensional solution also determines the thickness of the melt layer at the initial time $X_f(t_0) = q\sqrt{t_0}$. The liquid speed at the wall will remain equal to the sliding speed for melt layers thicker than approximately 10 nm [90], so in order to apply the no-slip boundary condition used in this analysis we must select an initial time t_0 which provides an initial dimensional melt layer thickness of at least 10 nm. Typically an initial time of 10 ns was used. A selection of different initial times were taken, and the choice of t_0 was shown to have a negligible effect on the results below. At time $t = t_0^+$ the uniform melt front is perturbed via a shape function $S(y)$ so that it is now a function of space and time $X_f = X_f(y, t_0^+)$. The numerical scheme is then used to evolve the temperature field forward in time subject to the Stefan condition.

Results are presented for a sample of HMX subject to a uniform wall speed v_w. A number of melt front shapes were studied. Here we draw comparison between two initial shapes which describe the y dependence of the initial melt front $X_f(y, t_0^+)$, and are parametrised by δ: $S_1(\delta, y) = 1 + (\delta/2)e^{-y^2}$ and $S_2(\delta, y) = 1 + \delta e^{-2y^2}\sin(\pi y)$. For shape S_1 positive values of δ correspond to a local widening of the melt layer, whereas negative values of δ correspond to a local narrowing of the melt layer. Shape S_2 describes a localised sinusoidal perturbation the melt front shape. In the following, the time to ignition is defined as the time at which the peak temperature exceeds 1000 K.

Figure 6.5 compares the non-dimensional propagation constant q calculated from equation (6.2.26), with the numerically computed propagation constant for a flat melt front profile, i.e. $X_f = X_f(t)$. The agreement is shown to be good, with numerical and analytical values agreeing to within one percent, for grid sizes $\Delta\xi = 0.05$, $\Delta y = 0.05$ and timestep $\Delta t = 10^{-4}$. It is found in practice that the time scale t^* should decrease logarithmically from 10^{-4}s to 10^{-7}s over the range of wall speeds $v_\mathrm{w} = 50$–$80\,\mathrm{m\,s^{-1}}$. Figure 6.6 shows the time to ignition and maximum melt width for a sample of HMX with a uniform melt layer, which corresponds exactly to the one-dimensional model. As in [90], we observe an order of magnitude decrease in the ignition time and melt width as the wall speed is increased.

Somewhat counterintuitively, we find that making the melt layer locally wider, as in S_1 with $\delta > 0$, appears to be the most violent initial condition in the sense of decreasing time to runaway. It is found that the heating due to mechanical dissipation is greatest adjacent to the wall and opposite from the imposed disturbance in the melt front, see Figure 6.7 (a). The location of the hot spot is due to the sign of the pressure gradient induced by the perturbation to the melt front, see equation (6.2.31). The temperature rise here is sufficient to cause a local reaction, leading to

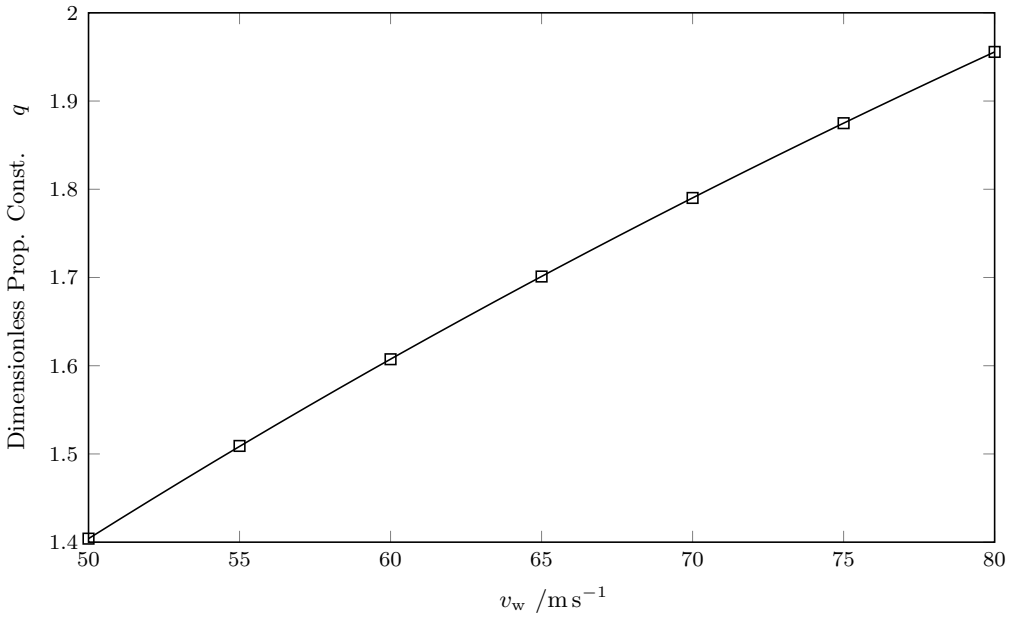

Figure 6.5: Dimensionless propagation constant q as a function of dimensional wall speed v_{w}.

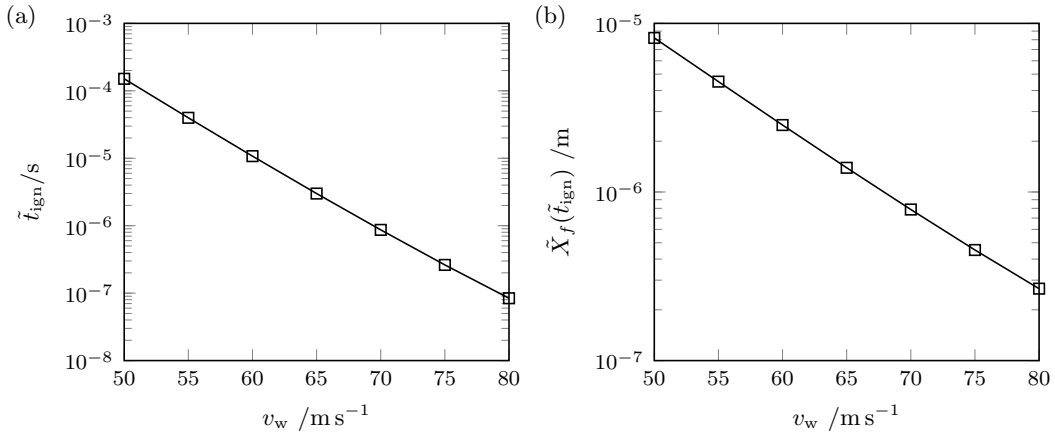

Figure 6.6: (a) Dimensional ignition time $\tilde{t}_{\mathrm{ign}}$; and (b) dimensional melt width at ignition $\tilde{X}_f(t_{\mathrm{ign}})$, both as a function of dimensional wall speed v_{w} for a melt layer of uniform width in HMX.

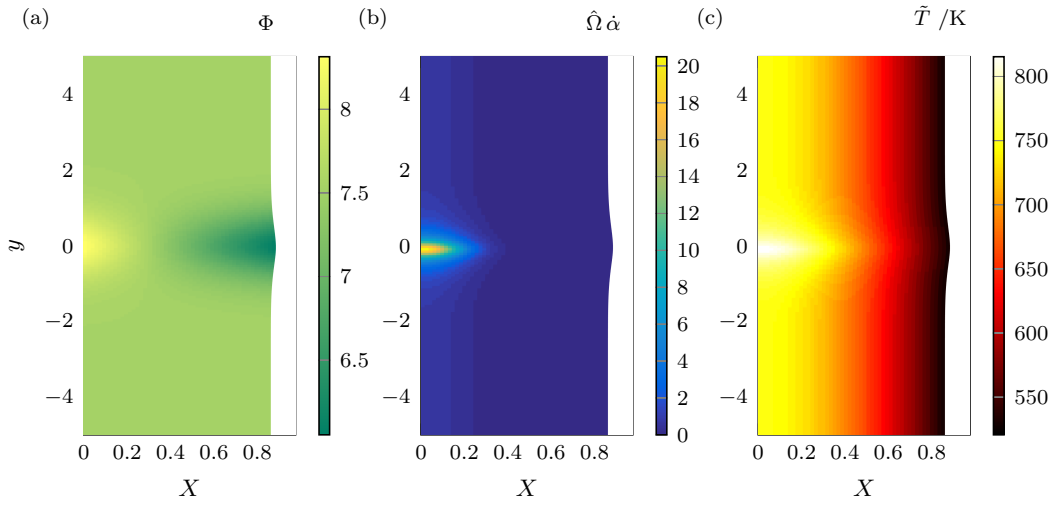

Figure 6.7: (a) Non-dimensional instantaneous energy increase due to mechanical dissipation; (b) non-dimensional instantaneous energy increase due to reaction; and (c) dimensional temperature $\tilde{T}$ of a sample of HMX at 90% of the time to runaway since t_0. An initial melt front shape $S_1(0.8, y)$ and wall speed $v_w = 70\,\mathrm{m\,s^{-1}}$ were used.

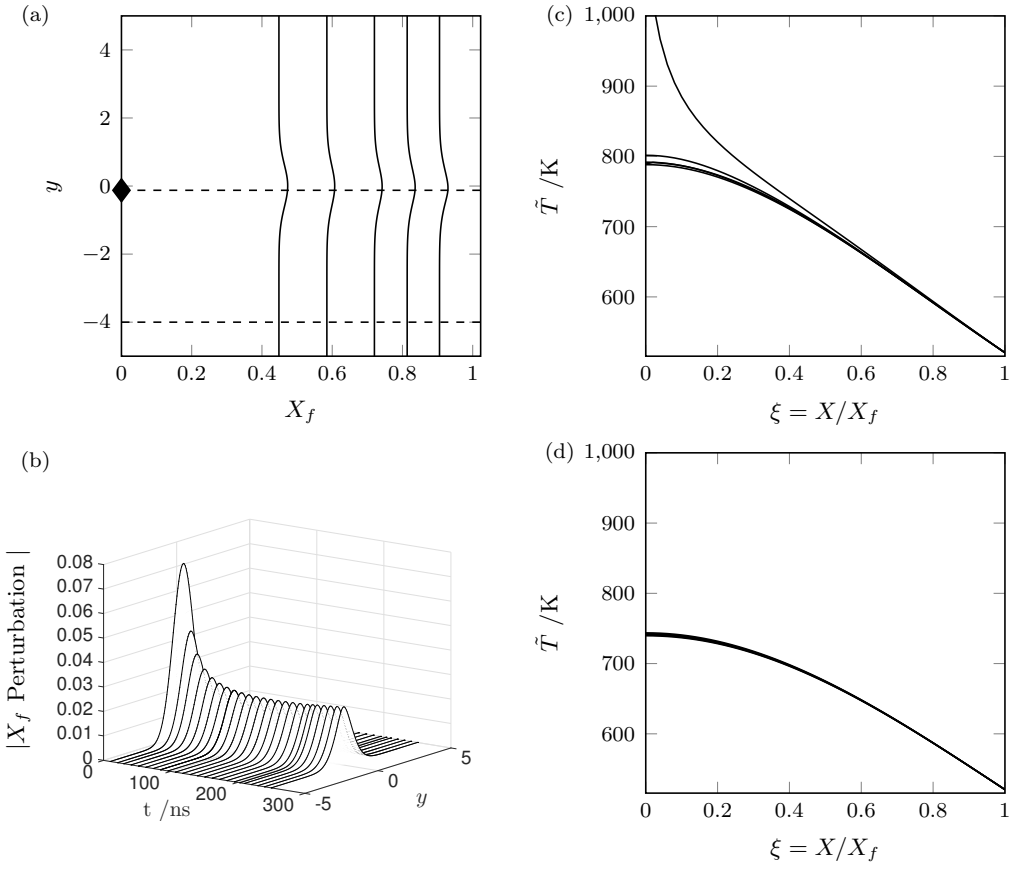

Figure 6.8: (a) Melt front location at dimensional times $\tilde{t} = 59, 108, 158, 207$ and 256 ns for a sample of HMX with initial melt front shape $S_1(0.8, y)$; and (b) the magnitude of the melt front perturbation at a series of increasing times. Also shown are temperature profiles across the melt width at the times depicted in (a), plotted at vertical coordinates: (c) $y = y_R$, where y_R is the vertical coordinate of the peak reaction site, and (d) $y = -4$. The filled diamond symbol shows the location of the peak reaction site at ignition. The dashed lines in (a) show the locations of the temperature profiles taken in (c) and (d). A wall speed $v_w = 70\,\mathrm{m\,s^{-1}}$ was used.

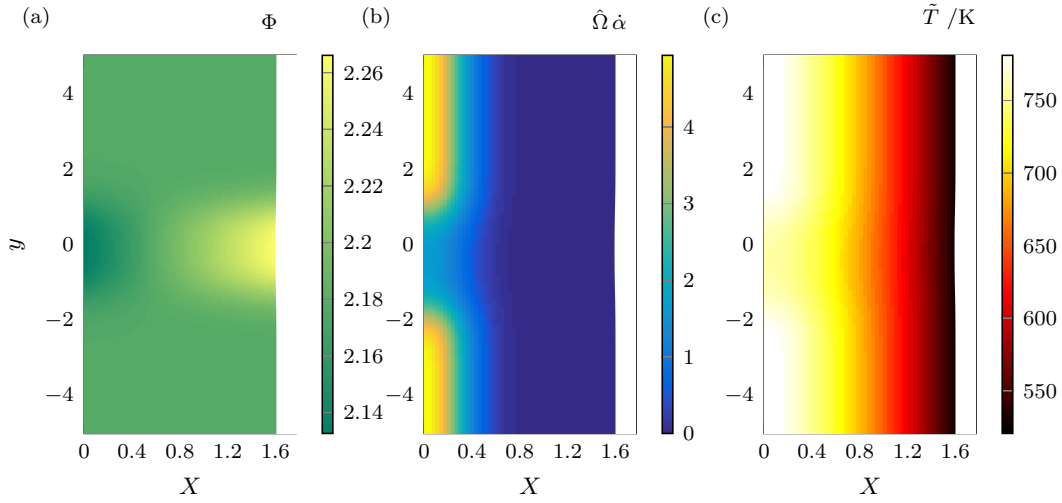

Figure 6.9: (a) Non-dimensional instantaneous energy increase due to mechanical dissipation; (b) non-dimensional instantaneous energy increase due to reaction; and (c) dimensional temperature $\tilde{T}$ of a sample of HMX at 90% of the time to runaway since t_0. An initial melt front shape $S_1(-0.8, y)$ and wall speed $v_w = 70\,\mathrm{m\,s^{-1}}$ were used.

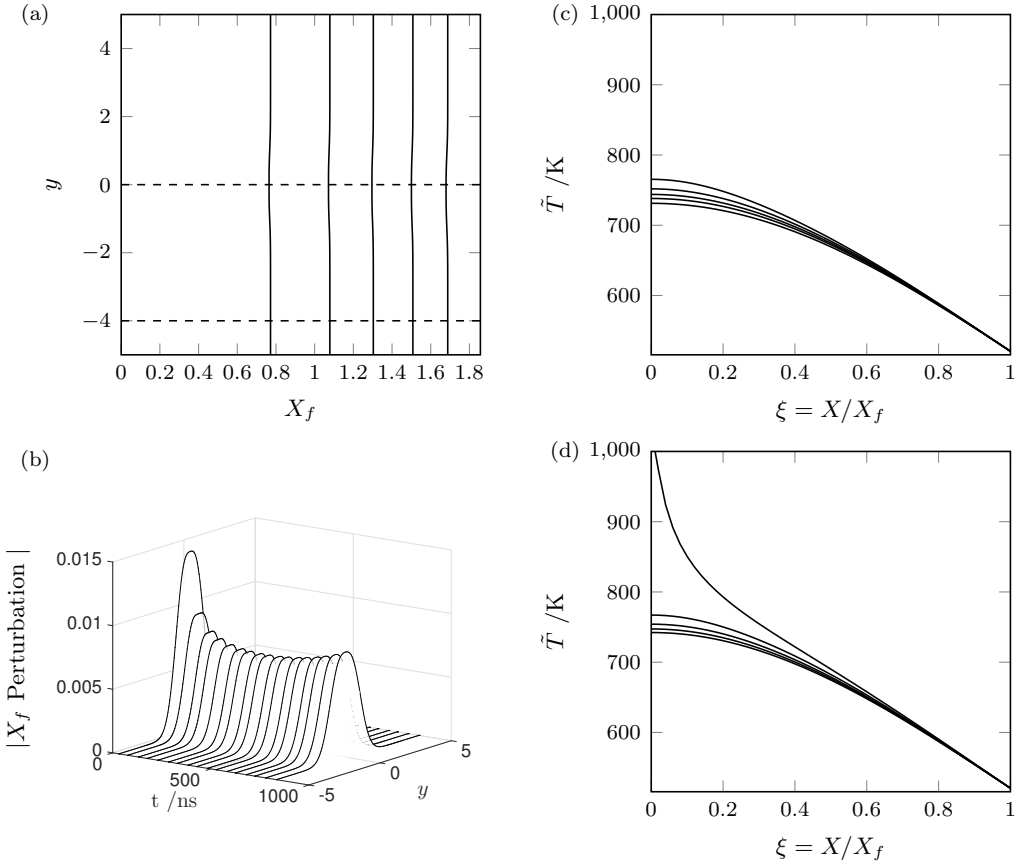

Figure 6.10: (a) Melt front location at dimensional times $\tilde{t} = 186, 357, 530, 704$ and $877\,\mathrm{ns}$ for a sample of HMX with initial melt front shape $S_1(-0.8, y)$; and (b) the magnitude of the melt front perturbation at a series of increasing times. Also shown are temperature profiles across the melt width at the times depicted in (a), plotted at vertical coordinates: (c) $y = 0$, and (d) $y = -4$. The dashed lines in (a) show the locations of the temperature profiles taken in (c) and (d). A wall speed $v_w = 70\,\mathrm{m\,s^{-1}}$ was used.

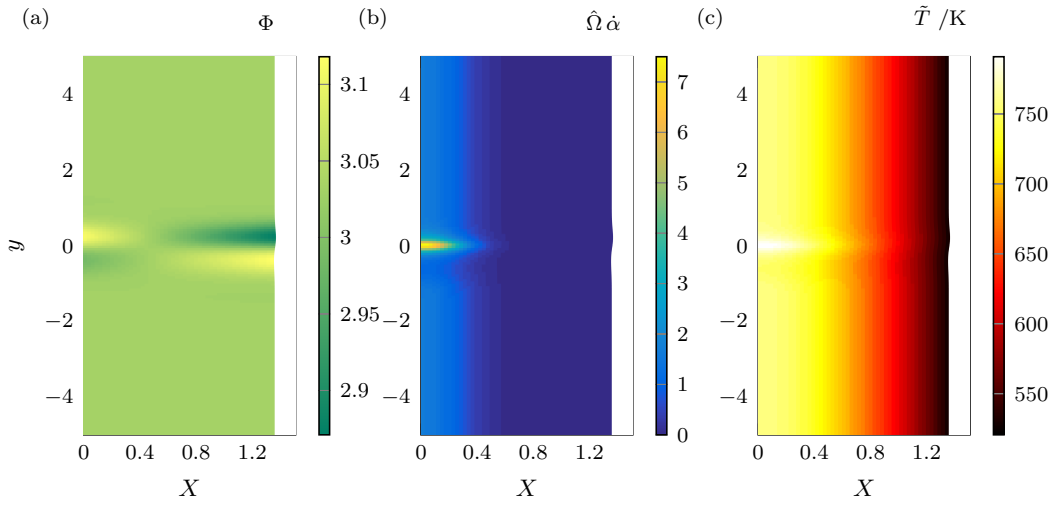

Figure 6.11: (a) Non-dimensional instantaneous energy increase due to mechanical dissipation; (b) non-dimensional instantaneous energy increase due to reaction; and (c) dimensional temperature $\tilde{T}$ of a sample of HMX at 90% of the time to runaway since t_0. An initial melt front shape $S_2(0.5, y)$ and wall speed $v_w = 70\,\mathrm{m\,s^{-1}}$ were used.

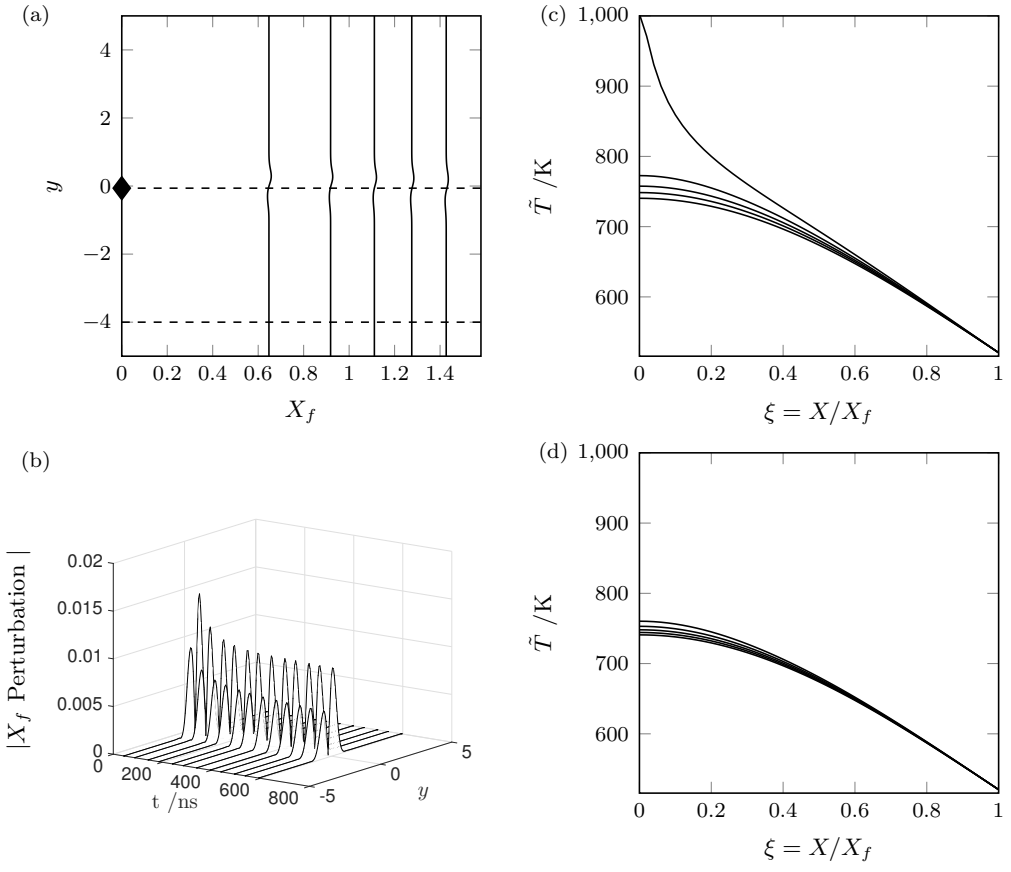

Figure 6.12: (a) Melt front location at dimensional times $\tilde{t} = 134, 258, 383, 507$ and 631 ns for a sample of HMX with initial melt front shape $S_1(-0.8, y)$; and (b) the magnitude of the melt front perturbation at a series of increasing times. Also shown are temperature profiles across the melt width at the times depicted in (a), plotted at vertical coordinates: (c) $y = y_R$, where y_R is the vertical coordinate of the peak reaction site, and (d) $y = -4$. The filled diamond symbol shows the location of the peak reaction site at ignition. The dashed lines in (a) show the locations of the temperature profiles taken in (c) and (d). A wall speed $v_w = 70\,\mathrm{m\,s^{-1}}$ was used.

a rapid rise in temperature. This has the resultant effect of causing the disturbance to grow in magnitude, causing further temperature localisation. Thus the overall time to runaway is reduced when compared with the one-dimensional case. The high contribution of heating due to reaction is clearly depicted in Figure 6.7.

The evolution of the melt front, along with the temperature profiles across the width of the melt layer, is shown in Figure 6.8. Looking at the temperature across the melt width, we observe a temperature rise of over 200 K near the reaction site. However, away from the reaction site we see that the temperature profile across the melt width has remained almost unchanged throughout the duration of the computation.

As in the linearised case in Section 6.2.1, it is found that upon reintroduction of the chemical reaction the melt front becomes unstable to small perturbations. This can be observed in Figure 6.8 (b) which depicts the perturbation from the uniform melt layer at a series of increasing times. We see that initially the disturbance decays, as in the non-reactive material, but towards the end of the computation the disturbance begins to grow again, albeit only by a small amount by the time the ignition threshold was reached. In particular this result demonstrates the ability of the chemical reaction to turn what was once a stable system into an unstable one.

In shapes which cause the melt layer to be locally narrower (i.e. S_1 with $\delta < 0$) we find the dissipation to be greatest at the melt front, see Figure 6.9 (a) and equation (6.2.30). The additional temperature increase near the unmelted explosive material causes the melt front to propagate more quickly at the disturbance site, so that the melt layer flattens, returning to a uniform width. We find that the hot spot generated by the narrowing of the melt layer is quenched to the melt temperature T_{m} by the unmelted solid explosive, so does not have the effect of decreasing the time to runaway. We conclude that a hot spot located on the melt front has little or no effect on the time to runaway. Indeed, we observe that the chemical reaction finally takes off on the wall, but away from the site of the localised disturbance owing to the corresponding mechanical cool spot, see Figure 6.9 (b). This is further illustrated in Figure 6.10, where we observe that the temperature increase is less near the disturbance, see Figure 6.10 (c), than it is away from the disturbance, see Figure 6.10 (d)). In this case the reaction takes longer commence, and we observe a noticeable temperature increase throughout the melt layer over the duration of the computation. Since the reaction occurs on the wall away from the perturbation, the bulk of the melt layer propagates ahead of the narrow area, resulting in the apparent growth of the perturbation in the later stages of melting.

Figures 6.11 and 6.12 show similar results for the localised sinusoidal disturbance S_2, which combines both effects seen in shape S_1 with positive and negative δ. As one might expect for such a small disturbance, we see no interaction between the two heating mechanisms and we observe two hot spots.

The time to ignition as a function of δ for both shapes $S_1(\delta, y)$ and $S_2(\delta, y)$ is shown

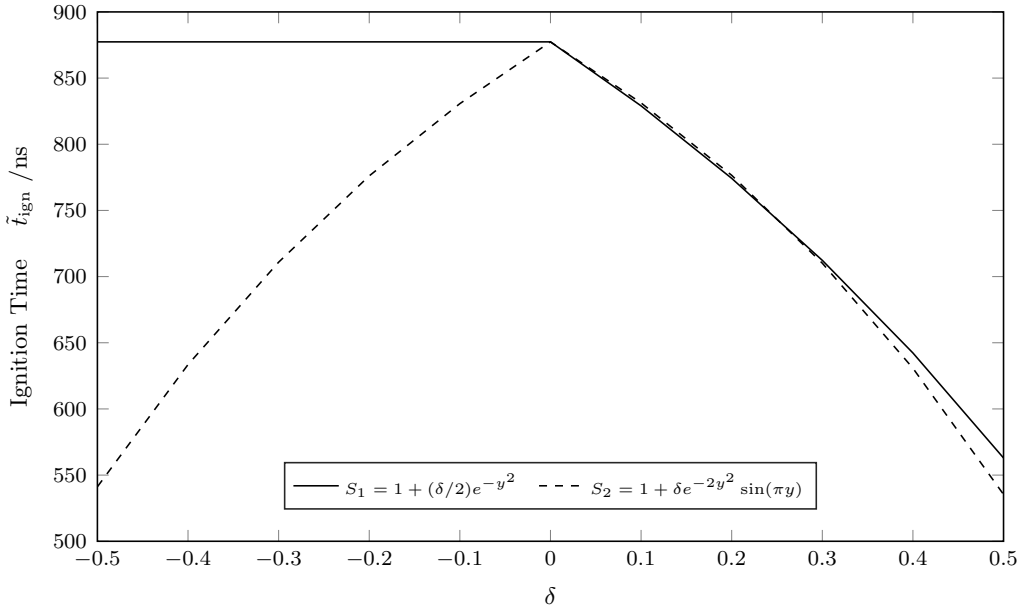

Figure 6.13: Dimensional time to ignition $\tilde{t}_{\text{ign}}$ as a function of δ for initial melt front shapes S_1 and S_2.

in Figure 6.13. The quenching behaviour is clearly demonstrated; for perturbations which only serve to narrow the melt width (shape $S_1, \delta < 0$), we see that the ignition time is unchanged from that of a uniform melt layer, whereas for positive disturbances ($\delta > 0$) the ignition time decreases as δ increases.

6.3 Shear melt model: temperature-dependent material properties

In this section we consider the effects of allowing the specific heat, viscosity, and thermal conductivity to vary with temperature. When the assumption of constant material properties is relaxed, the lubrication equations cannot be integrated directly, so we instead adopt an asymptotic approach. It is shown that the hot spot mechanisms discussed in Section 6.2 are still present when the assumption of constant material properties is relaxed. Full numerical solution of the coupled equations (6.1.61)–(6.1.67) would involve iteration between the mechanical and thermal equations and be more complicated than the analysis presented in Section 6.2.4. Since the results are found to be qualitatively similar in both the constant and non-constant material properties model, only the asymptotic results are presented here, and not the full numerical solution.

As in Section 6.2.1 we look for a solution in terms of a perturbation series as given by (6.2.4)–(6.2.6), with the additional expansions for the specific heat, viscosity, and

thermal conductivity

$$[c,\mu,\kappa](\zeta,y,t) = [c_0,\mu_0,\kappa_0](\zeta,t) + \delta[c_1,\mu_1,\kappa_1](\zeta,y,t) + O(\delta^2), \tag{6.3.1}$$

where $0 < \delta \ll \epsilon \ll 1$ is a small parameter characterising the size of the two-dimensional disturbance. As in the previous sections, we stipulate that this shape must decay in the far-field, so that our one-dimensional solution is applicable as $y \to \pm\infty$. It is recognised that the specific heat, viscosity, and thermal conductivity may be expressed in terms of the temperature expansion. However, the expansions (6.3.1) provide a useful notational convenience. The expansions (6.2.4)–(6.2.6) and (6.3.1) are substituted into the governing equations (6.1.61)–(6.1.67), to give the leading-order problem

$$\frac{1}{X_{f0}}\frac{\partial U_0}{\partial \zeta} = 0, \tag{6.3.2}$$

$$\frac{1}{X_{f0}^2}\frac{\partial}{\partial \zeta}\left(\mu_0\frac{\partial v_0}{\partial \zeta}\right) = 0, \tag{6.3.3}$$

$$\begin{aligned} c_0\left[\frac{\partial T_0}{\partial t} + \frac{1}{X_{f0}}\left(U_0 - \frac{\partial X_{f0}}{\partial t}\zeta\right)\frac{\partial T_0}{\partial \zeta}\right] &= \frac{1}{X_{f0}^2}\left(\frac{\partial \kappa_0}{\partial \zeta}\frac{\partial T_0}{\partial \zeta} + \kappa_0\frac{\partial^2 T_0}{\partial \zeta^2}\right) \\ &\quad + \mathrm{Ec}\,\mathrm{Pr}\,\Phi_0 + \hat{\Omega}\hat{A}(1-\alpha_0)\exp\left(-\frac{\hat{E}}{T_0}\right), \end{aligned} \tag{6.3.4}$$

$$\Phi_0 = \frac{\mu_0}{X_{f0}^2}\left(\frac{\partial v_0}{\partial \zeta}\right)^2, \tag{6.3.5}$$

$$\frac{\partial X_{f0}}{\partial t} = -\,\mathrm{Ste}\,\frac{1}{X_{f0}}\left.\frac{\partial T_0}{\partial \zeta}\right|_{\zeta=1^-}, \tag{6.3.6}$$

$$\frac{\partial \alpha_0}{\partial t} + \frac{1}{X_{f0}}\left(U_0 - \frac{\partial X_{f0}}{\partial t}\zeta\right)\frac{\partial \alpha_0}{\partial \zeta} = \hat{A}(1-\alpha_0)\exp\left(-\frac{\hat{E}}{T_0}\right), \tag{6.3.7}$$

with the boundary conditions given by (6.2.13)–(6.2.14).

At $O(\delta)$ we have the problem

$$\frac{1}{X_{f0}}\frac{\partial U_1}{\partial \zeta} + \frac{\partial v_1}{\partial y} = 0, \tag{6.3.8}$$

$$-\frac{\partial P_1}{\partial y} + \frac{1}{X_{f0}^2}\frac{\partial}{\partial \zeta}\left(\mu_0\frac{\partial v_1}{\partial \zeta} + \mu_1\frac{\partial v_0}{\partial \zeta}\right) = 0, \tag{6.3.9}$$

$$\begin{aligned} &c_0\left[\frac{\partial T_1}{\partial t} + \frac{1}{X_{f0}}\left(U_0 - \frac{\partial X_{f0}}{\partial t}\zeta\right)\frac{\partial T_1}{\partial \zeta} + \frac{1}{X_{f0}}\left(U_1 - \frac{\partial X_{f1}}{\partial t}S\zeta\right)\frac{\partial T_0}{\partial \zeta} + v_0\frac{\partial T_1}{\partial y}\right] \\ &\qquad + c_1\left[\frac{\partial T_0}{\partial t} + \frac{1}{X_{f0}}\left(U_0 - \frac{\partial X_{f0}}{\partial t}\zeta\right)\frac{\partial T_0}{\partial \zeta}\right] \\ &\quad = \frac{1}{X_{f0}^2}\left(\frac{\partial \kappa_0}{\partial \zeta}\frac{\partial T_1}{\partial \zeta} + \kappa_0\frac{\partial^2 T_1}{\partial \zeta^2} + \frac{\partial \kappa_1}{\partial \zeta}\frac{\partial T_0}{\partial \zeta} + \kappa_1\frac{\partial^2 T_0}{\partial \zeta^2}\right) \end{aligned}$$

$$+ \operatorname{Ec}\operatorname{Pr}\Phi_1 + \hat{\Omega}\hat{A}\left[(1-\alpha_0)\frac{\hat{E}}{T_0^2}T_1 - \alpha_1\right]\exp\left(-\frac{\hat{E}}{T_0}\right), \quad (6.3.10)$$

$$\Phi_1 = \frac{2}{X_{f0}^2}\left(2\mu_0\frac{\partial v_0}{\partial\zeta}\frac{\partial v_1}{\partial\zeta} + \mu_1\frac{\partial^2 v_0}{\partial\zeta^2}\right), \quad (6.3.11)$$

$$\frac{\partial X_{f1}}{\partial t} = -\operatorname{Ste}\left(\frac{X_{f1}}{X_{f0}^2}\frac{\partial T_0}{\partial\zeta} + \frac{1}{X_{f0}}\frac{\partial T_1}{\partial\zeta}\right)\Bigg|_{\zeta=1^-}, \quad (6.3.12)$$

$$\frac{\partial\alpha_1}{\partial t} + \frac{1}{X_{f0}}\left(U_0 - \frac{\partial X_{f0}}{\partial t}\zeta\right)\frac{\partial\alpha_1}{\partial\zeta} + \frac{1}{X_{f0}}\left(U_1 - \frac{\partial X_{f1}}{\partial t}S\zeta\right)\frac{\partial\alpha_0}{\partial\zeta} + v_0\frac{\partial\alpha_1}{\partial y}$$
$$= \hat{A}\left[(1-\alpha_0)\frac{\hat{E}}{T_0^2}T_1 - \alpha_1\right]\exp\left(-\frac{\hat{E}}{T_0}\right), \quad (6.3.13)$$

with boundary conditions given by (6.2.21)–(6.2.22).

First we present the leading-order solutions, demonstrating a departure from the linearised velocity profile used by Starobin and Dienes [90] and the resulting localisation in the mechanical heating across the layer. The leading-order solutions correspond to the one-dimensional case, that is an unperturbed melt front of uniform width. Comparison of the leading-order results with the one-dimensional model presented in [90] allows for the identification of heating mechanisms due solely to modelling the temperature dependence of material properties. We then present an example two-dimensional solution computed up to $O(\delta)$ in the analysis and observe that the localisation mechanisms discussed in the previous section persist when we relax the assumption of constant specific heat, viscosity, and thermal conductivity. The leading and first-order problems were solved using the front-fixed coordinate system and iterative Crank-Nicolson scheme presented in Section 6.2.4. In the interest of brevity we only present a single two-dimensional solution to illustrate the effects of temperature dependent material properties, but similar conclusions hold for the other melt front shapes discussed in this chapter.

Equation (6.3.2) along with the appropriate boundary conditions gives that the horizontal velocity is zero to leading-order. Since the viscosity is temperature dependent, the momentum and energy equations do not decouple, as is normally the case in lubrication theory. However, we may integrate (6.3.3) twice with respect to ζ to obtain the following expression for the leading-order vertical velocity component

$$v_0(\zeta,t) = \left(\int_0^1 \frac{1}{\mu_0(T(\zeta',t))}\,\mathrm{d}\zeta'\right)^{-1}\int_0^\zeta \frac{1}{\mu_0(T(\zeta',t))}\,\mathrm{d}\zeta' - 1. \quad (6.3.14)$$

Figure 6.14 shows the leading-order vertical velocity and mechanical dissipation across the melt layer. As predicted in [90], we see an increase in the velocity gradient near the sliding surface and as the temperature increases the velocity profile moves further away from the linear profile. We now observe that the leading-order dissipation is no longer constant in the melt layer, owing to the departure from the linear velocity

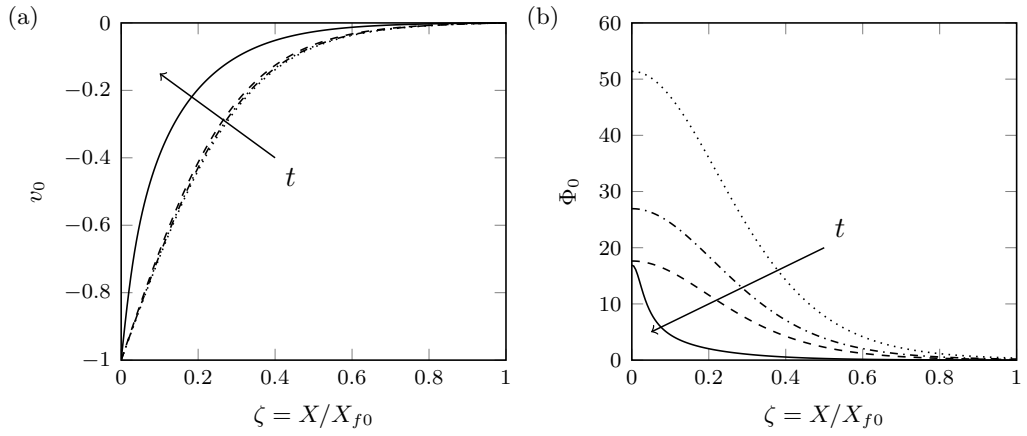

Figure 6.14: (a) The leading-order vertical velocity profile v_0 across the melt layer at dimensional times $\tilde{t} = 117, 223, 330$ and 436 ns; and (b) The non-dimensional leading-order energy increase due to viscous dissipation across the melt layer shown at the same times.

profile. The dissipation term is computed as

$$\Phi = \mu_0 \left(\frac{\partial v_0}{\partial \zeta}\right)^2 + \delta \left[2\mu_0 \frac{\partial v_0}{\partial \zeta}\frac{\partial v_1}{\partial \zeta} + \mu_1 \left(\frac{\partial v_0}{\partial \zeta}\right)^2\right] + O(\delta^2), \tag{6.3.15}$$

where we note that in the leading-order term both μ_0 and $\partial v_0/\partial\zeta$ are now functions of ζ and t. This may be contrasted with the constant materials properties result in which the leading-order mechanical dissipation is a function of time only $\Phi = (1/X_{f0}(t))^2 + O(\delta)$, see Section 6.2.1.

Figure 6.15 shows the leading-order specific heat, viscosity, and thermal conductivity across the melt layer at a series of increasing times. Figure 6.15 (d) shows the temperature dependence of each of the three properties, scaled by their values at a reference temperature of 750 K. We observe that the specific heat increases with temperature, with the shape of the plot looking much like a typical temperature profile across the layer. Conversely, both the viscosity and thermal conductivity decrease with temperature, thus taking their smallest values adjacent to the moving wall where the temperature is greatest. Interestingly we see very little change in the viscosity and specific heat as functions of time, with all snapshots virtually coinciding. The temperature profile used as an initial condition is such that we already observe a dramatic decrease in the viscosity and specific heat across the melt layer, and the local changes in temperature have relatively little effect on both of these properties as time proceeds. Note that since the leading-order equations reduce to one spatial dimension, the observed effects are entirely due to the temperature dependence of the material properties and not the result of any geometrical disturbance to the melt front.

Figure 6.16 shows a comparison of the leading-order temperature and magnitude of the reaction source term for the constant material properties simulation (dashed red) and temperature dependent material properties simulations (solid black). In panels

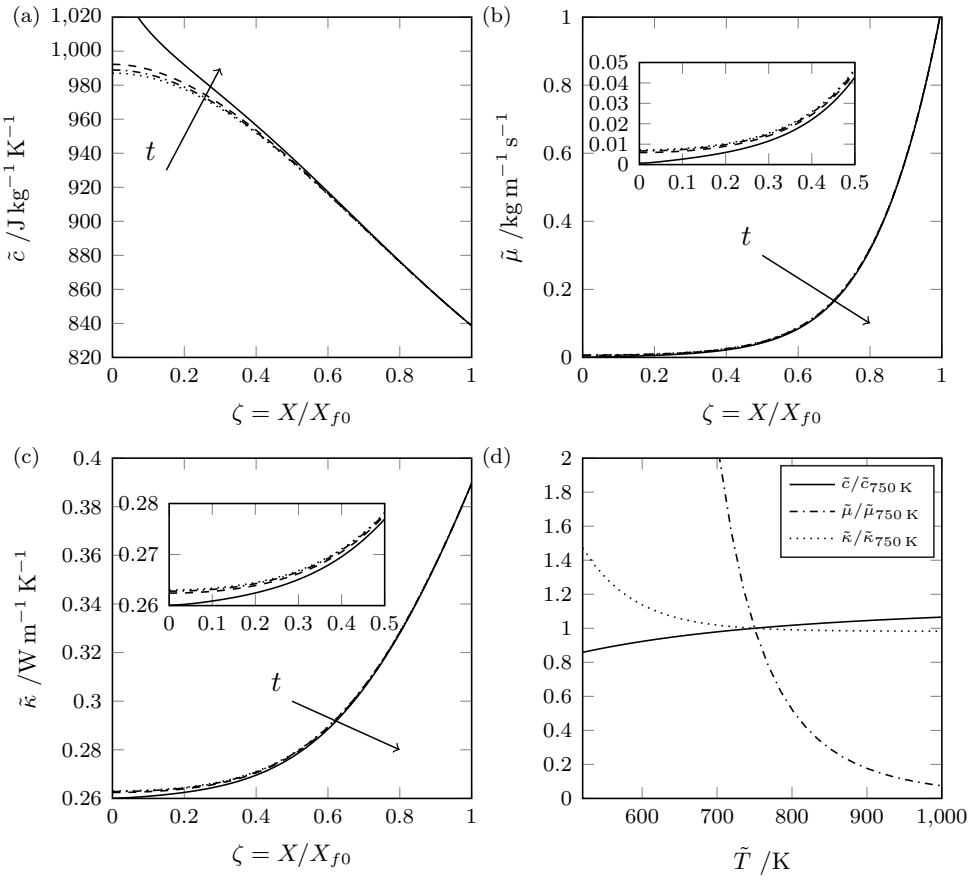

Figure 6.15: (a) The leading-order dimensional specific heat $\tilde{c} = c^* c_0$; (b) the leading-order dimensional viscosity $\tilde{\mu} = \mu^* \mu_0$; and (c) the leading-order dimensional thermal conductivity $\tilde{\kappa} = \kappa^* \kappa_0$ across the melt layer at dimensional times $\tilde{t} = 117, 223, 330$ and 436 ns. Panel (d) shows the material properties as a function of temperature, scaled by their values at a temperature of 750 K.

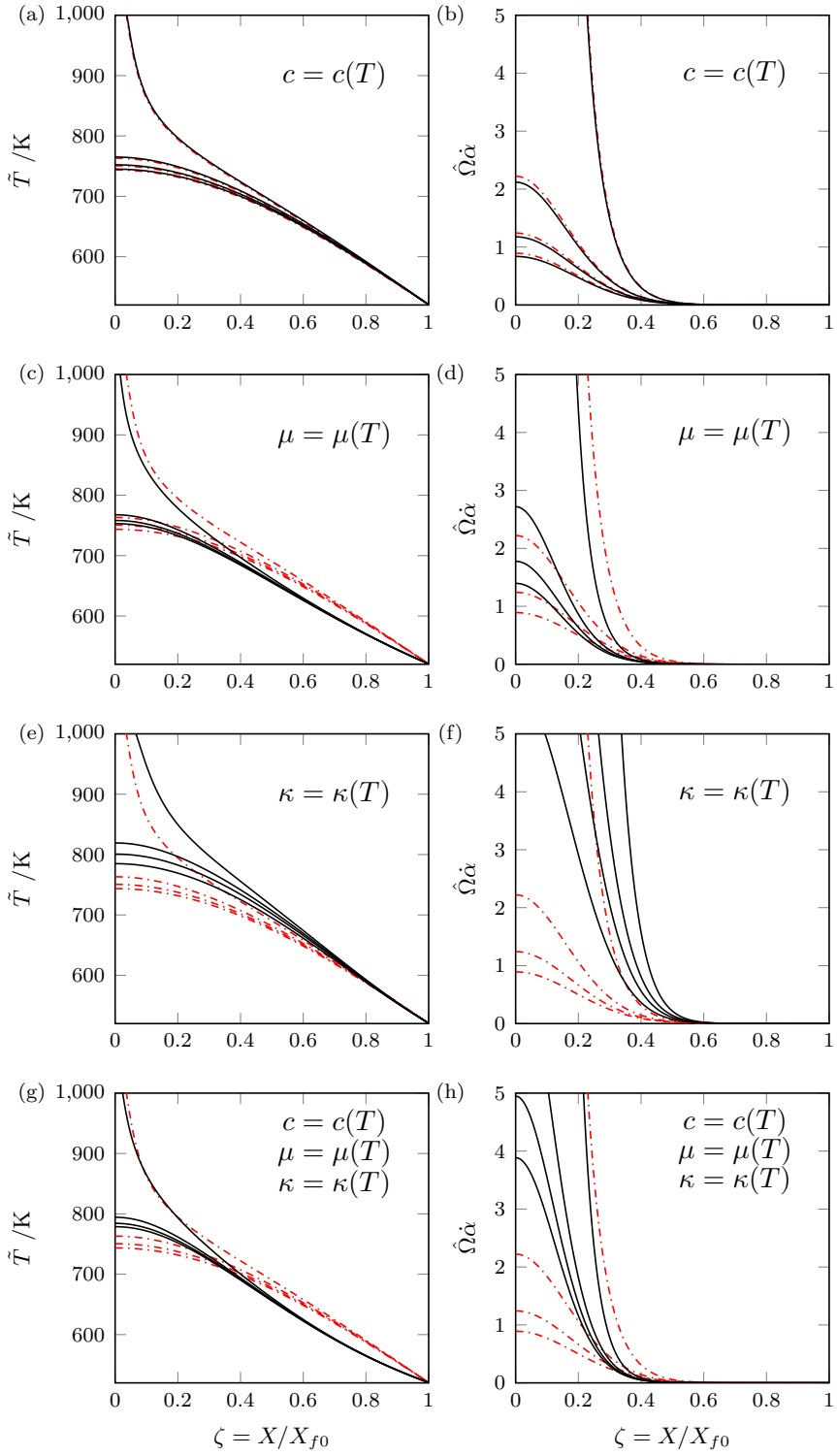

Figure 6.16: (a,c,e,g) The dimensional leading-order temperature across the melt layer; and (b,d,f,h) the non-dimensional leading-order energy increase due to chemical reaction across the melt layer. The dashed red line shows results with constant material properties in each plot. The solid black line shows results for: (a,b) temperature dependent specific heat; (c,d) temperature dependent viscosity; (e,f) temperature dependent thermal conductivity; and (g,h) temperature dependent specific heat, viscosity and thermal conductivity. The plots show snapshots at dimensional times $\tilde{t} = 226, 441, 657$ and 872 ns for the constant material properties simulation. For the temperature dependent plots the times shown are: (a,b) $\tilde{t} = 206, 403, 599$ and 795 ns; (c,d) $\tilde{t} = 326, 643, 959$ and 1276 ns; (e,f) $\tilde{t} = 31, 52, 73$ and 94 ns; and (g,h) $\tilde{t} = 117, 223, 330$ and 436 ns.

(a–f) we only allow one of the material properties to vary with temperature, allowing us to see how each property affects the shape of the leading-order temperature profile across the layer. Since the ignition times are changing, the plots are shown at approximately 25%, 50%, 75% and 100% of the time to thermal runaway, allowing the shapes of the temperature profiles to be compared. For the constant material properties simulation this corresponds to times $\tilde{t} = 226, 441, 657$ and 872 ns. For the temperature dependant plots times are: $\tilde{t} = 206, 403, 599$ and 795 ns for temperature dependent specific heat only; $\tilde{t} = 326, 643, 959$ and 1276 ns for temperature dependent viscosity only; $\tilde{t} = 31, 52, 73$ and 94 ns for temperature dependent thermal conductivity only; and $\tilde{t} = 117, 223, 330$ and 436 ns for temperature dependent specific heat, viscosity, and thermal conductivity. Considering the large variation in time to runaway for each of the cases studied, it may be concluded that accurate modelling of the temperature dependence of the material properties is vital for making reasonable predictions about the time to runaway. However, in this chapter we are concerned with how perturbations to the melt front, as well as the temperature dependence of the material properties, affect the spatial distribution of the temperature within the layer, and are less concerned with making predictions about runaway times.

Figure 6.16 (a) compares the temperature in the melt layer in the case of constant material properties with the solution found for temperature dependent specific heat. It is observed that the shape of the temperature profile remains nearly unchanged, due to the weak dependence of the specific heat on the temperature. However, we observe in Figures 6.16 (c,d) and (e,f) that allowing the viscosity and specific heat to vary with temperature alters the shape of the temperature profile. When $\mu = \mu(T)$ it is found that the hot spot is confined to a thinner region near the wall when compared with the constant material properties solution. This is due to the increased velocity gradient near the wall, see Figure 6.14. In contrast, when $\kappa = \kappa(T)$ the zone in which significant reaction occurs is comparatively much wider. This may seem counterintuitive, as one might expect decreased thermal conductivity lead to a more localised hot spot. However, in the early stages on melting, when the heating is dominated by viscous dissipation, it is found that the heat diffuses across the layer leading to more rapid melting in the constant material properties case. When we account for the temperature dependence of the specific heat, the timescales are such that there isn't enough time for the temperature to diffuse across the entire layer before the reaction commences, leading to a wider region adjacent to the wall in which the temperature is elevated, ultimately leading to a wider reaction zone.

Figure 6.17 shows the temperature profiles across the melt layer at a series of increasing times for the model with: (a) temperature dependent thermal conductivity; (b) temperature dependent specific heat, viscosity, and thermal conductivity; (c) temperature dependent specific heat; and (d) temperature dependent viscosity. The times shown correspond to the ignition times in each case, respectively. The temperature profiles are plotted as a function of the lubrication X co-ordinate, not

the front-fixed co-ordinate ζ. The melt width X_f can be inferred from the X value at which the temperature is equal to the melt temperature 520.6 K (i.e. by looking at where the curve crosses the horizontal axis) at each of the times shown. As discussed, for the parameter values taken in this study, we see a reasonable variation in the time to runaway in each of the four cases shown. The dotted line shows the temperature in each of the models at the time corresponding to ignition in the model with temperature dependent thermal conductivity only. We observe that in all other models the temperature is still below 800 K – this temperature is great enough to exceed the activation energy required for reaction, but the reaction may continue to proceed for some time (over 1000 ns shown in panel (d)) before runaway commences. In each of the cases we see that the propagation speed of the melt front is affected by the temperature dependence of the material properties. This is most apparent in panel (c), where we observe a non-dimensional melt width of nearly 1.3 at time $\tilde{t} = 436$ ns, compared with melt widths of less than 1 in panels (b) and (d). This change in melt front propagation speed is accompanied by a change in the shape of the temperature profile across the layer, and highlights how accounting for the temperature dependence of material properties is important in accurately determining the correct spatial dependence of the temperature field inside such melt layers.

It is found that the introduction of temperature dependence in the specific heat, viscosity, and thermal conductivity does not suppress the localisation mechanisms induced by perturbing the melt front, and it is still the case that the melt front may be unstable to small perturbations in the presence of chemical reaction. As an example case, Figure 6.18 shows results for HMX with an initial melt shape $S_1(y)$ with $\delta = 0.2$. As found in the previous section, the imposed disturbance in the melt front causes a mechanical hot spot adjacent to the moving wall. This is most clearly seen in the middle pane which shows the magnitude of the reaction source term in the melt layer – we see that the reaction is starting all along the wall, owing the the increased mechanical heating near $X = 0$, but there is clearly a localised hot spot opposite the site of the disturbance in the melt front. This highly localised heating ultimately leads to a substantial temperature increase and the time to ignition is significantly decreased when compared with the corresponding one-dimensional (or, equivalently, uniform width) case. As in the constant material properties case, it is found that the substantial temperature increase due to chemical reaction causes the initially decaying perturbation to the melt front to grow in time.

6.4 An idealised model for surface roughness or grit

Another scenario of physical interest is that of a rough surface sliding against a bare explosive. In such a scenario, frictional heating may lead to the development of a melt layer as studied here. Frictional heating has been the subject of a number of

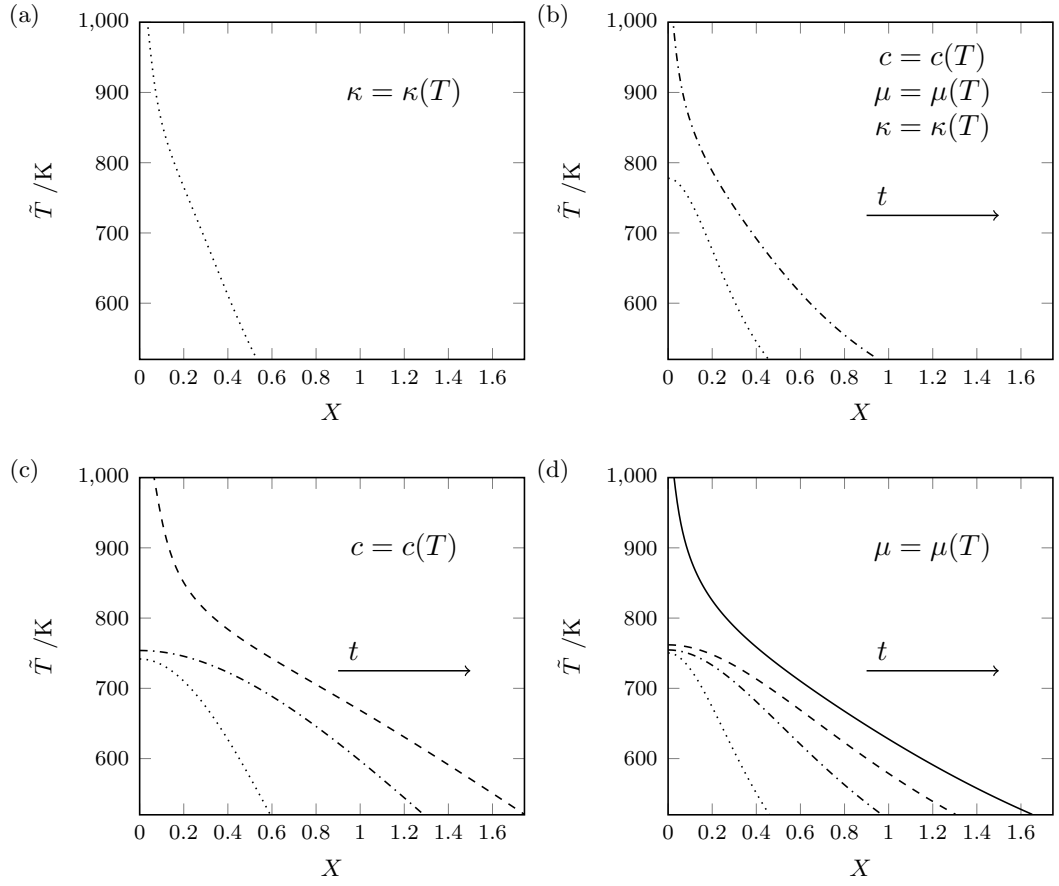

Figure 6.17: Leading-order temperature profiles across the layer in the temperature dependent material properties melt model. In each panel, the line styles indicate temperature profiles taken at times $\tilde{t} = 94$ ($\cdots$), 436 ($\cdot-$), 795 ($--$) and 1276 ns ($-$), which correspond to the times to runaway for the model with: temperature dependent thermal conductivity only; temperature dependent specific heat, viscosity, and thermal conductivity; temperature dependent specific heat only; and temperature dependent viscosity only. For the simulation shown in panel (a), thermal runaway commenced at the first snapshot time $\tilde{t} = 94$ ns and the simulation was terminated, hence only one temperature profile is plotted. Similarly, for panel (b) thermal runaway commenced at the second snapshot time, so only two temperature profiles are plotted, and so on for panels (c) and (d). The width of the melt layer grows in time, which can be inferred by observing the increasing in time X coordinate at the melt temperature $\tilde{T} = 520.6$ K.

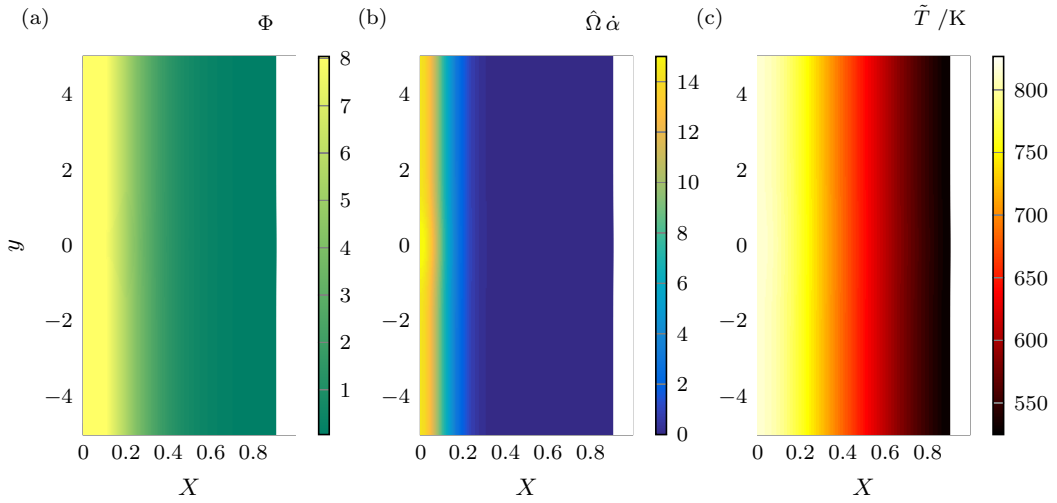

Figure 6.18: (a) Non-dimensional instantaneous energy increase due to mechanical dissipation; (b) non-dimensional instantaneous energy increase due to reaction; and (c) dimensional temperature $\tilde{T}$ of a sample of HMX at 90% of the time to runaway since t_0, as predicted by the analysis which includes temperature dependent specific heat, viscosity and thermal conductivity. An initial melt front shape $S_1(0.2, y)$ and wall speed $v_\mathrm{w} = 70\,\mathrm{m\,s^{-1}}$ were used.

experimental works, for example [14, 16, 18, 96]. In [51] a model for the initiation of an explosive by rapid shear is developed, and frictional heating of the explosive due to sliding past a hard, irregular surface is discussed. The study makes a comparison between shear banding and friction, arguing that frictional heating and heating within a shear band are only superficially different. On a microscopic level, frictional heating is caused by viscoplastic work at surface irregularities which deform as the two surfaces slide past one another [51]. From this perspective, frictional heating at a sliding interface is similar to that in a shear band; in the former deformation is localised because the interface is the weakest region, whereas in the latter the localisation is due to thermal softening overcoming work hardening.

As an idealised model for a melt layer generated by sliding past a rough surface, or a smooth surface contaminated with grit, we can impose a shape on the solid wall. In this model, the boundary conditions applied at $x = 0$ are instead applied at $x = S_\mathrm{w}(y, t)$, where S_w is an imposed wall shape. As in Section 6.1.3 we make the lubrication approximation. The model is then formulated in terms of the front-fixed co-ordinate, now defined as

$$\xi = \frac{X - S_\mathrm{w}}{X_f - S_\mathrm{w}}, \tag{6.4.1}$$

with Jacobian

$$\boldsymbol{J} = \frac{\partial(\xi, y, t)}{\partial(X, y, t)} = \begin{pmatrix} \frac{1}{X_f - S_\mathrm{w}} & 0 & 0 \\ \frac{\frac{\partial S_\mathrm{w}}{\partial y}(1-\xi) - \frac{\partial X_f}{\partial y}\xi}{X_f - S_\mathrm{w}} & 1 & 0 \\ \frac{\frac{\partial S_\mathrm{w}}{\partial t}(1-\xi) - \frac{\partial X_f}{\partial t}\xi}{X_f - S_\mathrm{w}} & 0 & 1 \end{pmatrix}. \tag{6.4.2}$$

The front-fixed equations in the liquid layer (6.1.61)–(6.1.67) are then replaced with

$$\frac{1}{X_f - S_\mathrm{w}}\left[\frac{\partial U}{\partial \xi} + \left(\frac{\partial S_\mathrm{w}}{\partial y}(1-\xi) - \frac{\partial X_f}{\partial y}\xi\right)\frac{\partial v}{\partial \xi}\right] + \frac{\partial v}{\partial y} = 0, \tag{6.4.3}$$

$$\frac{1}{X_f - S_\mathrm{w}}\frac{\partial P}{\partial \xi} = 0, \tag{6.4.4}$$

$$-\frac{\frac{\partial S_\mathrm{w}}{\partial y}(1-\xi) - \frac{\partial X_f}{\partial y}\xi}{X_f - S_\mathrm{w}}\frac{\partial P}{\partial \xi} - \frac{\partial P}{\partial y} + \frac{1}{(X_f - S_\mathrm{w})^2}\frac{\partial}{\partial \xi}\left(\mu(T)\frac{\partial v}{\partial \xi}\right) = 0, \tag{6.4.5}$$

$$c(T)D[T] = \frac{1}{(X_f - S_\mathrm{w})^2}\left(\frac{\partial \kappa(T)}{\partial \xi}\frac{\partial T}{\partial \xi} + \kappa(T)\frac{\partial^2 T}{\partial \xi^2}\right) + \mathrm{Ec}\,\mathrm{Pr}\,\Phi + \hat{\Omega}\hat{A}(1-\alpha)\exp\left(-\frac{\hat{E}}{T}\right), \tag{6.4.6}$$

$$\Phi = \mu(T)\frac{1}{(X_f - S_\mathrm{w})^2}\left(\frac{\partial v}{\partial \xi}\right)^2, \tag{6.4.7}$$

$$\frac{\partial X_f}{\partial t} + \mathrm{Ste}\,\frac{1}{X_f - S_\mathrm{w}}\frac{\partial T}{\partial \xi}\bigg|_{\xi=1^-} = 0, \tag{6.4.8}$$

$$D[\alpha] = \hat{A}(1-\alpha)\exp\left(-\frac{\hat{E}}{T}\right), \tag{6.4.9}$$

where

$$D[\cdot] := \frac{\partial \cdot}{\partial t} + \frac{1}{X_f - S_\mathrm{w}}\left[U + \frac{\partial S_\mathrm{w}}{\partial t}(1-\xi) - \frac{\partial X_f}{\partial t}\xi + v\left(\frac{\partial S_\mathrm{w}}{\partial y}(1-\xi) - \frac{\partial X_f}{\partial y}\xi\right)\right]\frac{\partial \cdot}{\partial \xi} + v\frac{\partial \cdot}{\partial y}.$$

If we make the assumption of constant material properties, the velocity components may be computed explicitly:

$$\begin{aligned} U(\xi,y,t) = {} & \frac{1}{2}\left(\frac{\partial X_f}{\partial y} - \frac{\partial S_\mathrm{w}}{\partial y}\right)\left(\xi + \frac{2\xi}{X_f - S_\mathrm{w}}\right) - \left(\frac{\partial X_f}{\partial y}S_\mathrm{w} - X_f\frac{\partial S_\mathrm{w}}{\partial y}\right)\frac{\xi}{X_f - S_\mathrm{w}} \\ & + \frac{1}{2}\Bigg\{\Bigg[3\left(\frac{\partial X_f}{\partial y} + \frac{\partial S_\mathrm{w}}{\partial y}\right)(\xi^2(X_f - S_\mathrm{w})^2 + 2\xi(X_f - S_\mathrm{w})) \\ & \quad - 6\left(\frac{\partial X_f}{\partial y}S_\mathrm{w} + X_f\frac{\partial S_\mathrm{w}}{\partial y}\right)\xi(X_f - S_\mathrm{w})\Bigg]\frac{\partial P}{\partial y} \\ & \quad + \Bigg[-2(\xi^3(X_f - S_\mathrm{w})^3 + 3\xi(X_f - S_\mathrm{w})^2 + 3\xi(X_f - S_\mathrm{w})S_\mathrm{w}^2) \\ & + 3(S_\mathrm{w} + X_f)(\xi^2(X_f - S_\mathrm{w})^2 + 2\xi(X_f - S_\mathrm{w})) - 6X_f S_\mathrm{w}\xi(X_f - S_\mathrm{w})\Bigg]\frac{\partial^2 P}{\partial y^2}\Bigg\}, \end{aligned} \tag{6.4.10}$$

$$v(\xi,y,t) = \frac{1}{2}(X_f - S_\mathrm{w})^2\frac{\partial P}{\partial y}\xi\,(\xi - 1) - (1-\xi)\,. \tag{6.4.11}$$

Integration of (6.4.3) across the layer and application of the no-slip boundary conditions gives the following relation between the pressure, wall shape and melt

front shape

$$\frac{\partial}{\partial y}(X_f + S_\mathrm{w}) + \frac{\partial}{\partial y}\left(\frac{(X_f - S_\mathrm{w})^3}{6}\frac{\partial P}{\partial y}\right) = 0. \tag{6.4.12}$$

Figure 6.19 shows the numerical results of (6.4.3)–(6.4.9) with an initial wall shape $S_\mathrm{w}(y,0) = \sin(10\pi)$, which may be considered as an idealised rough surface. We observe that the heating due to mechanical dissipation is heightened behind the "bumps" in the wall, with a corresponding decrease in mechanical heating on the opposite side of the layer, Figure 6.19 (a). This leads to a subsequent chemical reaction trailing behind the tip of each "bump" in the wall, Figure 6.19 (b). Figure 6.20 shows temperature profiles at fixed horizontal coordinates (a) $\xi = 0$, (b) $\xi = 1/3$, and (c) $\xi = 2/3$, corresponding to the wall, a distance 1/3 of the way across the melt layer, and a distance 2/3 of the way across the melt layer, respectively. The reaction sites are clearly visible in Figure 6.20 (a), where we see localised hot spots with temperature increases of around 300 K compared with the "bulk" wall temperature. Figures 6.21 and 6.22 show the same results but for a localised initial wall shape $S_\mathrm{w} = e^{-4y^2}$, which could be considered as a model for a piece of grit sliding past an explosive. Again we observe that a localised reaction occurs just above the perturbation to the wall shape.

For the results shown the initial melt front shape was taken to be flat so that the effect of the wall shape could be observed independently. If both a wall shape and melt front shape were imposed multiple mechanical hot and cool spots may be formed in the layer, with their location being dependent on the imposed shapes. This may lead to either a competition between heating mechanisms, or a compounded effect where a single hot spot is generated due to the shape of the wall and the shape of the melt front.

Here we have demonstrated how the model may be extended to serve as an idealised model for grit. In practice we may look to experiments or literature in order to determine a more suitable wall shape S_w which is more representative of the roughness or grit that may be present in a real life accident scenario.

6.5 Discussion

The numerical results presented here indicate that perturbations from a uniform width melt layer can cause localised heating due to mechanical dissipation. In particular, it has been demonstrated that accounting for the non-uniform melting behaviour through the introduction of spatial dependence in the melt front location can reduce the time to ignition compared with the corresponding one-dimensional model of melting.

In order to model the non-uniform melting, highly idealised melt front shapes were selected for analysis. The shapes chosen captured both of the possible important disturbances: those which locally increase the width of the melt layer, corresponding

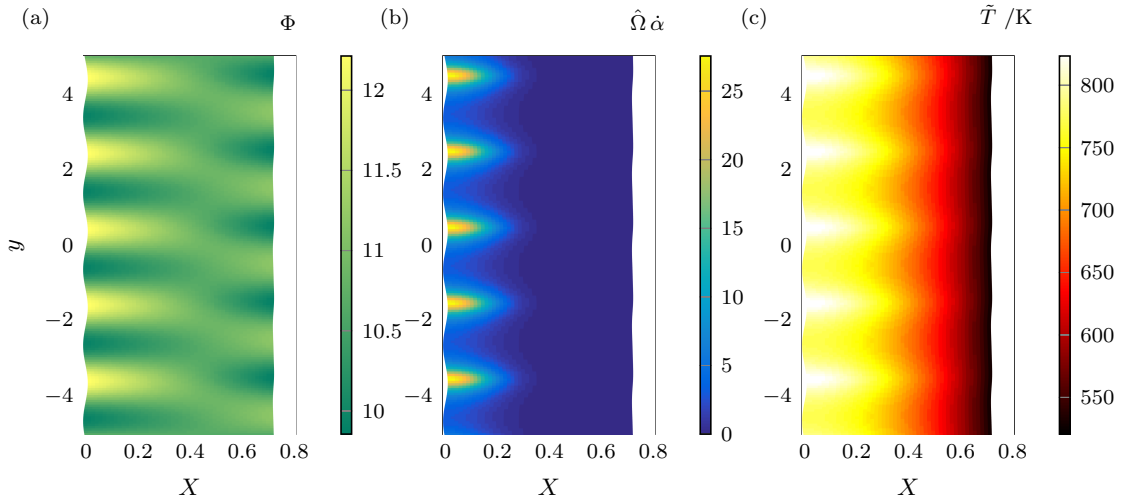

Figure 6.19: (a) Non-dimensional instantaneous energy increase due to mechanical dissipation; (b) non-dimensional instantaneous energy increase due to reaction; and (c) dimensional temperature $\tilde{T}$ of a sample of HMX at 90% of the time to runaway since t_0, as predicted by the analysis which includes temperature dependent specific heat, viscosity and thermal conductivity. An initial wall shape $S_w = \sin(\pi y)$ and wall speed $v_w = 70\,\mathrm{m\,s^{-1}}$ were used.

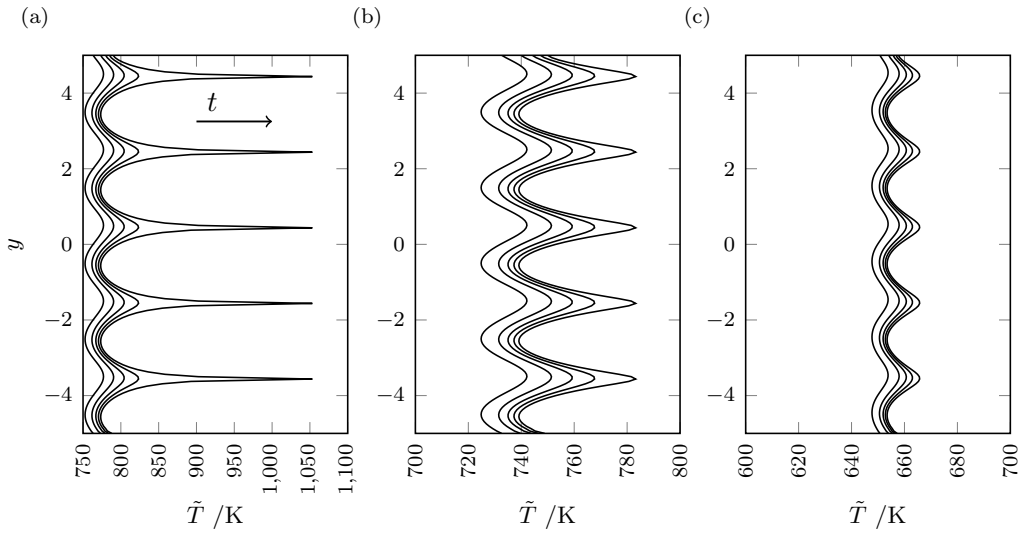

Figure 6.20: Temperature profiles at fixed horizontal coordinates (a) $\xi = 0$, (b) $\xi = 1/3$, and (c) $\xi = 2/3$, corresponding to the wall, a distance 1/3 of the way across the melt layer, and a distance 2/3 of the way across the melt layer, respectively. Profiles are show at a series of increasing times $\tilde{t} = 44$, 78, 112, 133 and 145 ns. An initial wall shape $S_w = \sin(\pi y)$ and wall speed $v_w = 70\,\mathrm{m\,s^{-1}}$ were used. Note the different scale in the $\tilde{T}$ axis in panel (a) compared to panels (b,c).

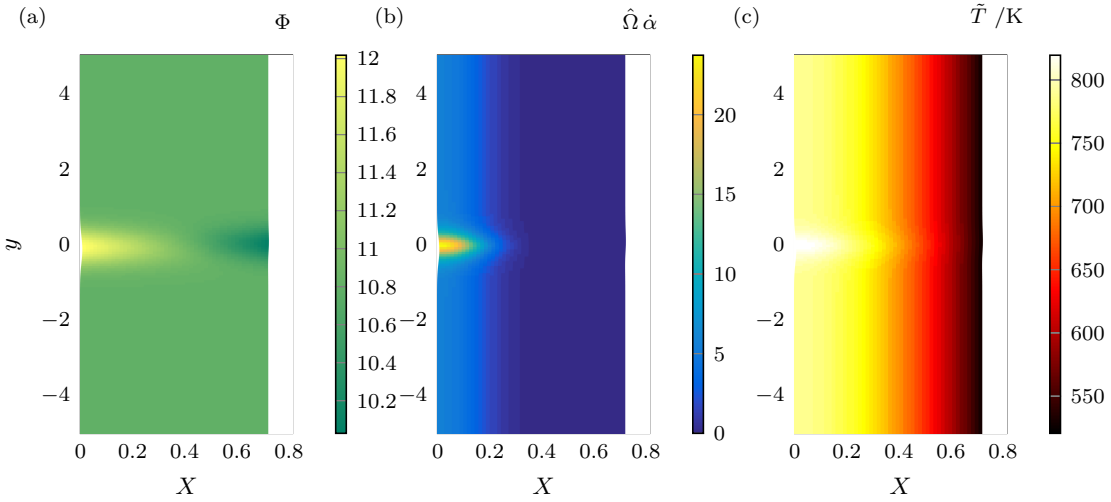

Figure 6.21: (a) Non-dimensional instantaneous energy increase due to mechanical dissipation; (b) non-dimensional instantaneous energy increase due to reaction; and (c) dimensional temperature $\tilde{T}$ of a sample of HMX at 90% of the time to runaway since t_0, as predicted by the analysis which includes temperature dependent specific heat, viscosity and thermal conductivity. An initial wall shape $S_\mathrm{w} = e^{-4y^2}$ and wall speed $v_\mathrm{w} = 70\,\mathrm{m\,s^{-1}}$ were used. Note that for the time shown here the "bump" in the wall is small compared with the melt width.

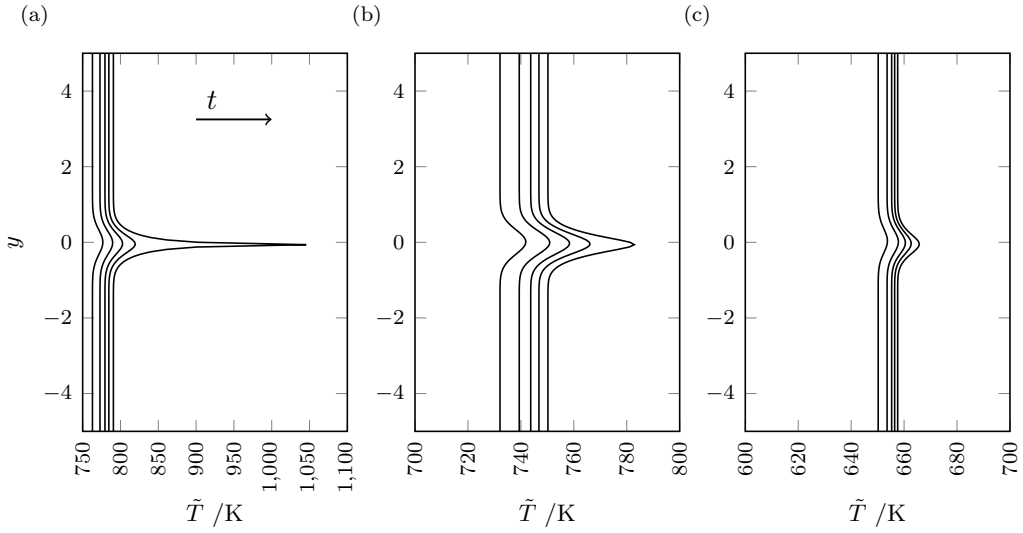

Figure 6.22: Temperature profiles at fixed horizontal coordinates (a) $\xi = 0$, (b) $\xi = 1/3$, and (c) $\xi = 2/3$, corresponding to the wall, a distance 1/3 of the way across the melt layer, and a distance 2/3 of the way across the melt layer, respectively. Profiles are show at a series of increasing times $\tilde{t} = 45$, 80, 114, 135 and 148 ns. An initial wall shape $S_\mathrm{w} = e^{-4y^2}$ and wall speed $v_\mathrm{w} = 70\,\mathrm{m\,s^{-1}}$ were used. Note the different scale in the $\tilde{T}$ axis in panel (a) compared to panels (b,c).

to areas which initially melted more quickly, and those which locally reduce the width of the melt layer, corresponding to areas which initially melted more slowly. One possible physical interpretation of this would be a scenario in which the melt temperature of the unmelted solid explosive material varies locally in space. This would result in a non-constant melt temperature, which would be accounted for in equation (6.1.12). This would affect the propagation of the melt front, causing some areas to melt rapidly, thus introducing some shape in the melt front. In our modelling it is assumed that the melt layer has already formed at time t_0, and it is reasoned that the initial melt front shape we impose could be generated by the mechanism described above. Local differences in other thermo-mechanical properties would operate in a similar fashion to give rise to non-uniform melting.

For certain disturbances it was shown that the time to ignition may be considerably reduced. For instance, the results in Figure 6.8 predicted an ignition time of 256 ns compared with an ignition time on the microsecond timescale for the corresponding one-dimensional simulation. The possibly reduced time to ignition predicted by the two-dimensional model increases the range of physical scenarios in which the shear melting hot spot mechanism is plausible.

For example, we may consider the physical scenario of an internal microcrack. In their analysis, Starobin and Dienes [90] find that for sliding speeds below $50\,\mathrm{m\,s^{-1}}$ the ignition time predicted by the one-dimensional model exceeds a millisecond. Over this time period the slip would be greater than 5 cm, a distance much larger than the HMX grain size found in a PBX, meaning the shear crack would cross the grain boundary [90]. The crossing of the boundary would likely change the crack propagation direction and the model with lateral melting would no longer be appropriate. However, due to local inhomogeneities in the material properties, the ignition time may be significantly reduced, even to the nanosecond timescale, meaning that the shear melting mechanism may lead to ignition in this model well before the slip length becomes an issue.

For the initial part of this study many material properties, such as viscosity, were assumed constant with respect to pressure and temperature. Later these assumptions were relaxed, and the the specific heat, viscosity, and thermal conductivity were allowed to vary with temperature. As suggested by Starobin and Dienes [90], it was shown that the leading-order velocity profile was no longer linear, with most of the slip being supported in the region of the melt layer adjacent to the wall. This in turn introduced spatial dependence into the leading-order mechanical dissipation term. The pressure dependence of the material properties may also be studied. For example, Menikoff and Sewell [72] propose a modified form of the viscosity which increases with pressure, which may go some way to offset the drop in viscosity associated with the temperature increase across the layer.

Future work may include computation of numerical solutions for the fully-coupled governing equations, accounting for temperature (and possibly pressure) dependence

of the material properties. This would allow for consideration of larger departures from the uniform melting case, but we would expect the results would be qualitatively similar to those found here. We would certainly expect the hot spot mechanisms introduced by the shape in the melt front to persist.

Chapter 7

Conclusion

7.1 Summary of thesis

In Chapter 1 we motivated the mathematical study of accidental ignitions by describing the everyday scenarios, such as handling and transport, during which low energy stimuli, or 'insults', may lead to disastrous consequences. We also gave a brief outline of the background mathematics needed to model the constitutive behaviour of explosive materials, and discussed simple chemical decomposition models.

In Chapter 2 we discussed a range of hot spot mechanisms suggested in the literature, the majority of which were evidenced by experimental work at the Cavendish laboratory by Field and colleagues [45–48, 58, 91]. We gave an overview of the types of experiments conducted, in particular noting which of the more simple geometries, for instance the drop-weight test, could prove useful in our analytical models. As well as discussing each of the main hot spot mechanisms in some detail, we also listed the most common types of insults that explosives may be subject to during typical use, and highlighted tests currently used at AWE to examine explosive response [5]. We then went on to describe how accidental ignition is investigated through the use of numerical hydrocode models, with a focus on the HERMES ignition parameter. An example numerical simulation was shown, illustrating that the regions in which ignition is expected to occur during a drop-weight test suffered from severe mesh deformation. The chapter closed by establishing the aims of the thesis.

We considered the pinching of an explosive material between two rough, rotating plates in Chapter 3. This model was motivated in part by drop-weight type experiments [e.g. 45, 48] and the simple pinch model of Curtis [33]. The consideration of a combined squeezing and rotating plate was motivated by wanting to study a simplified geometry that was somewhat representative of the more complicated deformations seen in real life, which inevitably comprise of combined normal and shear deformations. The roughness of the plates was accounted for using

a Tresca boundary condition, which prescribed the shear stress at the boundary to be a fraction of the yield stress. The mechanical analysis offered a novel extension to the squeeze flow problem analysed by Sherwood and Durban [88], by including a partial-slip boundary condition in the θ–z direction. An asymptotic solution based on a correction to a uniform shearing motion was sought in the form of a series in the ratio of sample height to sample radius h/r. One drawback of this approach was that the solution failed in a thin region near the axis $r = 0$: unphysical negative velocities were predicted near the axis, identifying the need for consideration of an inner asymptotic region. This problem was also present in the analysis of Sherwood and Durban [88]. While we did not consider such an inner region, we commented on how it could physically be explained by an unyielded core [44]. It was demonstrated that the solution in the bulk of material could be obtained by truncating the computational domain at some minimum radius $r_{\min}$, and that the solution was largely unchanged by the choice of boundary condition applied there.

In the absence of inertia, analytical solutions for the corrections to the velocities and stress away from the axis could be obtained for varying 'stress fractions' m and n. A region of increased heating due to mechanical dissipation was identified near to the impacting plates, agreeing with what is observed in experiments and numerical simulations [33, 35, 59]. When the inertial terms were retained it was shown that the corrections to the velocity components could be obtained through the solution of a set of couple ordinary differential equations, and the results could then be used to reconstruct the stresses, strains and mechanical dissipation. For parameter values typical of PBXs it was shown that the solution which neglected inertial effects provided a good approximation to the full problem. Subsequently, the thermal problem was solved, and it was demonstrated that the reaction took place close to the plates. The strong agreement in qualitative behaviours predicted by the simple pinch model of Chapter 3, numerical simulations, and experimental work illustrated the usefulness of idealised mathematical models in investigating explosive response. We concluded by discussing the limitations of the simple rigid-plastic behaviour assumed in the model, particularly noting the lack of coupling between the mechanical and thermal problems. Some ideas for extensions to the pinch model will be given in Section 7.2.

In Chapter 4 we introduced a one-dimensional model for an explosive material undergoing a unidirectional shearing motion, with a view to understanding how the presence of a chemical reaction affects the development of shear bands. The material was modelled as an elastic-plastic, with an as-yet unprescribed constitutive law for the plastic strain-rate, allowing some freedom in the modelling of the material behaviour. Through selection of an appropriate function for the strain-rate, the shear band model can account for important physical effects such as thermal softening, strain and strain-rate hardening. We extended the so-called 'cohesive' scheme of Zhou et al. [107] to include heating due to chemical reaction, and typical results illustrating the

formation of a shear band in the explosive material LX-14 were presented. Owing to the large ratio of elastic shear modulus to yield stress in shear, it was expected that the results for the elastic-plastic model would be well approximated by a rigid-plastic model. We formally took the limit of infinite elastic modulus, and recovered a one-dimensional model analogous to the axisymmetric model for shear banding studied by Powers and Caspar [23, 24, 80]. Through a comparison of numerical results we confirmed that the rigid-plastic model was able to capture the key features and timescales present in the elastic-plastic model.

We went on to seek an asymptotic solution for the rigid-plastic model, which used the uniform shearing solution as the leading-order term. In order to make analytical progress in the inner shear band region, it was necessary to neglect the effects of strain hardening. This was also found to be the case in a similar analysis of inert shear bands by Edwards and French [42]. Simply setting the strain hardening exponent to zero in our constitutive law resulted in the early onset of plastic work compared to what is observed in experiments; clearly more consideration is needed to select an appropriate function, or appropriate parameters, for the plastic strain-rate in the absence of hardening. We then considered a model in which the activation energy was reduced, allowing for the investigation of the onset of shear banding in a material which reacts at a temperature similar to the critical temperature for which plastic work becomes important. In this case, our asymptotic solution was able to capture the initial growth of the temperature within the shear band, in the presence of both mechanical and chemical heating.

Motivated by the numerical results of the previous chapter, and by the experimental observation that shear bands are typically very thin [e.g. 101], we developed a boundary layer analysis for the onset of reactive shear bands in Chapter 5. The analysis built on the inert model of DiLellio and Olmstead [38], and looked for a solution as a perturbation to the elastic solution. A small parameter ε was identified through model parameters relating to thermal softening and strain-rate hardening. To simultaneously account for the heating due to plastic work and chemical reactions occurring within the developing zone of localisation, we further exploited the large activation energy. This led to a novel system of governing equations for the behaviour of the temperature and stress at the centre of the band. Efforts to model the processes of plastic localisation and reaction led to the identification of three different asymptotic structures: Approach I, which accounted for heating due to plastic work and reaction throughout the entire process of shear band formation; Approach II, which assumed the heating due to reaction to be negligible during the initial stages; and Approach III, based on the Thermal Explosion Theory of Powers [80], which effectively split the problem into separate stages in which either heating due to plastic work or heating due to reaction dominated. The predictions of the three different approaches were compared, and it was concluded that accounting for the slowly growing reaction during the early stages of deformation is important in accurately

predicting the critical time at which significant reaction takes place. The asymptotic results from Approach I were compared with the numerical results using the cohesive scheme of Chapter 4, demonstrating an excellent agreement between the temperature and stress within the band.

In order to account for the important effect of strain hardening we suggested a new model for the plastic strain-rate, based on an exponential formulation [38]. It was demonstrated that strain hardening can delay the onset of shear banding and, in the most extreme cases, prevent it entirely. Another interesting observation came from considering the limit of heating due to plastic work going to zero, i.e. the regime $T_{\mathrm{R}} \ll T_{\mathrm{p}}$, where T_{R} is the critical reaction temperature and T_{p} the critical plastic temperature. In this limit, the model we developed for describing reactive shear bands reduces to a model for the ignition of a half space due to heating at the boundary [78], prompting the analogy of considering a developed shear band as a line source.

The chapter concluded by recasting the governing equations in terms of new non-dimensional variables, resulting in a system governed by just three non-dimensional parameters which are known in terms of material properties, the applied shearing motion, and properties of the chemical reaction. This lead to the discussion of a new criterion for the onset of reactive shear bands. By a comparison with the inert analysis by DiLellio and Olmstead [38], we were able to show that the introduction of an Arrhenius source term into the model can cause shear bands to form where they otherwise would not have. An important consequence of this is that it is necessary to account for the presence of a chemical reaction when determining if a shear band is likely to form. Perhaps even more importantly, we may conclude that the material behaviour observed in experiments on inert simulants of explosive materials may well be different to the behaviour of the actual explosive if the temperatures are such that the reaction has commenced, at least in the case of shear banding.

In Chapter 6 we considered a model of a molten layer of explosive material between two sliding surfaces. By considering perturbations in the width of the melt layer we were able to investigate the effect of non-uniform melting caused by, for example, material inhomogeneity. A linear stability analysis revealed that the melt front is stable to perturbations in the absence of chemical reaction, but becomes unstable upon introduction of an Arrhenius heat source. The one-dimensional analysis of Starobin and Dienes [90] predicted uniform mechanical heating throughout the layer, with the reaction first occurring along the entire centreline of the layer (corresponding to the rigid wall at $x = 0$ in our model). In our two-dimensional model we were able to predict highly localised regions of mechanical heating due to non-uniform melting, which had the potential to reduce the time to ignition considerably. Numerical results revealed that the location, size and sign of the perturbation to the melt front are all important in determining whether or not the localised mechanical heating leads to a critical hot spot where a reaction initiates: mechanical hot spots near to the melt

front were quenched to the melt temperature, whereas hot spots near the sliding wall were allowed to persist, ultimately causing ignition.

The model developed in Chapter 6 also accounted for the temperature dependence of the thermal conductivity, viscosity and specific heat. In terms of hot spot generation, the temperature dependent viscosity appears to be most important, causing a non-linear velocity profile, and therefore spatially non-uniform mechanical heating, even when the melt layer is of a uniform width. We ended the chapter by discussing how, by allowing a shape to be imposed on the sliding wall, the melt model could be interpreted as a model for the sliding of a rough surface or piece of grit past a bare explosive. Results indicated that surface roughness could lead to the generation of localised hot spots within the molten layer.

7.2 Future work

Owing to the large number of hot spot mechanisms suggested in the literature, see Chapter 2, there is a great deal of scope for new modelling work. Even when considering a single hot spot mechanism the number of modelling considerations is vast: there are many potentially interesting geometries suggested by both experimental set-ups and real life problems; the constitutive response of explosive materials is complex; and the modelling of the chemical reaction could be far more complicated than considered here. In this section, we discuss some ideas for future work that could be considered as direct extensions of the models in this thesis, or relate more closely to our aims laid out at the end of Chapter 2.

7.2.1 Heating due to friction

Though the pinch model of Chapter 3 considered the roughness of the plates, it did not specifically account for heating due to friction: any additional heating predicted was due entirely to changes in the stresses and strains when allowing for partial slip. As discussed, we could add a heat source term at the boundary to model the effect of friction at the surfaces. A model in a different geometry, perhaps simple shear, would likely be useful in more carefully addressing the effects of friction while avoiding the problems present in the pinch model, such as issues near the axis of symmetry. Such a model may also be able to describe the early stages of melting during sliding. In our shear melt model described in Chapter 6, we assumed that a thin layer of molten material already existed at the initial time. In reality, the two sliding surfaces would rub past one another, heating due to friction and/or shear banding, subsequently causing a molten layer to form. A good starting point for this may be the simple model of Frey [51] which describes the deformation of a linearly viscoplastic material with a shear strength that goes to zero at the melting temperature. Though the model derived by Frey is simple, the physical description

given of the analysis, explaining the heating due to a hard, rough material sliding past an explosive, could form the basis of a more detailed mathematical model. In order to retain an analytical approach, one could exploit the thin shear boundary layers as observed during pinch, see Figure 2.7 and [4, 33, 59].

7.2.2 Localised impacts

Of particular interest is the study of localised impacts, with a typical modelling example being the normal impact of a spigot on a bare explosive, see Figure 2.4. Localised impacts are of greater physical importance than the more uniform deformations observed in the pinch model studied in Chapter 3, and a much more representative of the type of mechanical insults that might threaten explosives during handling. In the Spigot test, high values of the HERMES ignition parameter are seen at the leading edge of the spigot – an area in which high shear deformations are taking place. One approach to modelling localised impacts analytically may be to look for an asymptotic solution near to the impact site, which could be matched on to a more simple solution in the far-field. Such an approach would require the identification of appropriate length scales over which important physical features occur.

Motivated by a squeeze-film analogy, one could consider a two-dimensional slab of explosive material which is impacted on by a flat plate whose width is less than the initial sample width, see Figure 7.1. The material initially occupies the space $-L \leq x \leq L$ and $0 \leq y \leq h_0$, and a pressure is applied on the upper surface in the region $-l \leq x \leq l$. The upper surface $y = h(x,t)$ is allowed to vary in space and time as the impacter squeezes the material. A similar squeeze film model is considered by Poole [79] in the study of the tip jet region in a shaped charge. There, the material is assumed to behave as an elastic-plastic, and a solution is sought based on the assumptions that the material sample is thin, and that the pressure applied by the impacter is sufficient enough so that all of the material underneath it can be treated as plastic. This leads to a problem in which three regions are identified: a plastic region; a 'plasticised' necking region, which contains material with residual plastic stresses; and a fully elastic region, which moves horizontally as a rigid body. Owing to the assumed thinness, the leading-order stresses and strains are independent of the vertical co-ordinate y. More importantly, the plastic shear stress is also zero to leading order. Experimental and numerical evidence suggest that during localised impacts the material shears considerably near to the leading edge of the impacter. Motivated by this observation, we note that it is important to consider a small region local to the corner of the upper plate in our simple model, see the boxed region in Figure 7.1. By identifying the appropriate scalings, a local, asymptotic solution could be sought which aims to capture the shear deformations seen in experiments. It is possible this region could be matched onto the more simple squeeze film solution,

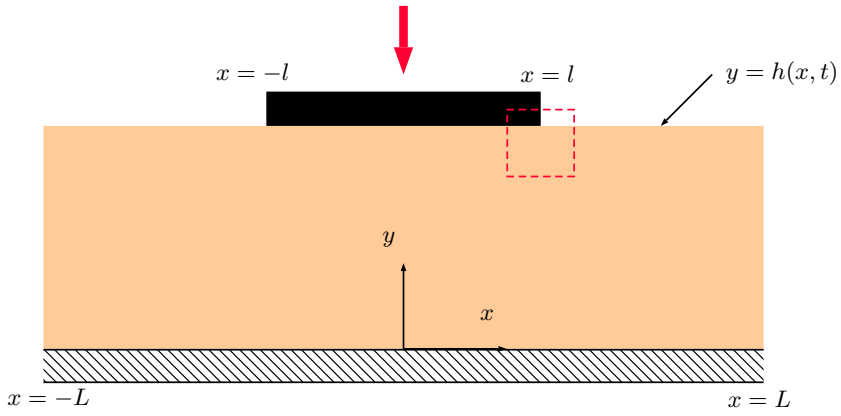

Figure 7.1: Schematic of the localised pinching of an explosive between two flat plates.

and we suggest that such an approach might be a useful first step in developing an analytical model of spigot impact.

An alternative numerical approach was also considered which may be useful in obtaining qualitative behaviours in more complicated geometries, such as those representative of localised impacts. The so-called Method of Fundamental Solutions (MFS) is a mesh-free numerical method, whose most important advantage is its simple implementation in complex geometries [27, 30]. The method obtains an approximate solution in terms of a linear combination of fundamental solutions, expressed in terms of singularities which lie on a fictitious boundary placed outside the physical boundary, see Figure 7.2. Many examples of this type of solution can be found in the literature, with a large collection of problems given by Chen et al. [27, 30]. As a particular example, we were motivated by the study of Jankowska and Kolodziej [64], who considered the deformation of a notched elastic-plastic plate. This problem shared some similarities with our idealised spigot model, see Figure 7.1, in that it had mixed boundary values, and considered the material to behave as elastic plastic. While this problem in particular did not consider a free surface, the MFS can be be used in free boundary problems, with examples from potential flow theory given in [27]. The elastic-plastic problem may be reformulated in terms of an Airy stress function ψ, see [e.g. 62], which satisfies a biharmonic equation

$$\nabla^4 \psi = b(x, y, \psi, \psi_{xx}, \psi_{yy}, \psi_{xy}, \psi_{xxx}, \psi_{yyy}, \psi_{xxy}, \psi_{xyy}), \tag{7.2.1}$$

where x and y are the horizontal and vertical co-ordinates, respectively, and the function b on the right hand side is due to the plastic behaviour of the material; if the material is purely elastic we have $b \equiv 0$. The boundary conditions are accounted for through a series of collocation points, as is the forcing term b. The problem is solved by first assuming $b = 0$, i.e. the elastic case, and then iterating, using the previous iteration in the forcing term b. The solution procedure is stopped once the boundary conditions are satisfied to within some user selected tolerance. In both trying to

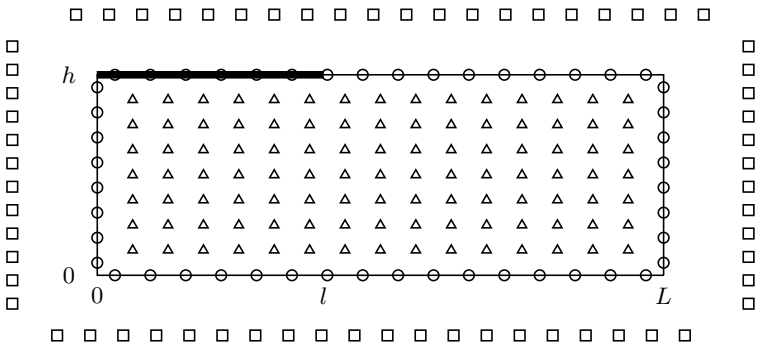

Figure 7.2: Schematic of the simple spigot model. Here the sample initially has width $2L$ and height h, and is impacted by a flat plate of width $2l$, shown as a thick line. Owing to symmetry, only the right half of the sample is shown. The squares represent the locations of the source points, which are located a short distance from the physical boundary. The boundary collocation points are shown as circles, and the points used to interpolate the right hand side function b are shown as triangles.

reproduce the solution in [64], and in subsequently applying the method to our spigot problem, it was found that the accuracy of the method was extremely sensitive to the number and location of source and collocation points. The problem of choosing "good" source points is often discussed in the MFS literature [e.g. 27], and is an issue which needs further consideration. Often the solution procedure is repeated multiple times, with some optimisation algorithm being used to adaptively choose the source points in order to minimise the error in satisfying the boundary conditions. We feel that this numerical method may have some use in providing approximate solutions for the stresses and strains experienced by an explosive material in a wide range of, potentially, very complex geometries. However, further investigation of the literature is required in order to better understand how to implement the method and ensure accurate solution.

7.2.3 Microstructure

Explosive materials are heterogeneous in nature, made up of explosives crystals bound together with a polymer binder. While all of the models developed aim to describe the influence of some physical inhomogeneity, for instance, a temperature perturbation in the modelling of shear bands, or a perturbation to the width of a molten shear layer, they do not explicitly account for the explosive microstructure. The perturbations we chose to impose in our modelling were used in order to investigate behaviours representative of explosive materials; in reality these perturbations would likely be caused by local variations in the microstructure. One method that could be useful in

accounting for the influence of the explosive microstructure in analytical models is the method of multiple scales, or homogenisation. By assuming that the scale over which the insults are acting can be separated (asymptotically) from the scale of the microstructure, one can obtain a solution for the response of the explosive on the macroscale, which accounts for the smaller scale features such as grains, voids, grit etc.

An interesting model, the analysis of which we applied to the pinch model (see Chapter 3 for discussion), is that of Burns [21], who studied the onset of shear bands in ductile metals due to small perturbations to a uniform shearing deformation. The material was considered to be viscoplastic with a strain, strain-rate and temperature dependent dynamic flow stress. Through a multiple scales argument it was shown that the growth rate of perturbations to the displacement and temperature is governed by the ratio of the slope of the homogeneous stress-strain curve to the strain-rate sensitivity of the material. This type of approach may allow for the development of analytical models of hot spot mechanisms which are triggered by changes to the microstructural response, and may shed more light on the early stages of hot spot generation. An obvious extension to, say, the reactive shear band models presented in this thesis, would be to consider some small, periodic features representative of the structure of an explosive, and investigate how this may lead to the triggering of plastic localisation.

7.3 Discussion

Through a combination of asymptotic and numerical techniques a number of different hot spot mechanisms have been investigated, with a particular focus on our aims of better understanding the localisation of plastic heating due to friction and shear banding, as outline in Chapter 2. The modelling of the constitutive behaviour has been necessarily simple, but we have still retained important features such as strain-rate hardening and thermal softening in the modelling of shear bands, for example.

Analysis of an improved model for pinch has led to the consideration of how friction affects the plastic flow and corresponding mechanical heating within the material, and may provide a useful basis for the consideration of more realistic geometries such as that of localised spigot impact. The pinch model could be improved further, particularly in conjunction with an experimental study, such as that of Field et al. [45, 48] or Williamson [98], to account for a range of different material behaviours. It is not certain how much analytical progress could be made should a more complicated material model be included, but we have been able to demonstrate via asymptotic techniques that informative conclusions can be drawn from the simple geometry the pinch test offers.

The boundary layer analysis of reactive shear bands demonstrated the importance

of considering the modelling of chemical reactions during localised plastic deformation. The simple one-dimensional shearing geometry provides a mathematically convenient framework for the analysis of shear bands and could be exploited further to improve the understanding of plastic localisation as a hot spot mechanism. Further insight could be gained by extending the analysis of Chapter 5 to incorporate additional important physical effects, possibly accounting for the influence of the explosive grains themselves. In order to get the most benefit, it would be useful to conduct more experiments on explosives undergoing uniform shear, thus helping to identify which features to include and investigate in the modelling. One of the most important outcomes of the boundary layer analysis was the identification of key parameters which control the growth and development of shear bands in reactive materials. In particular, it was demonstrated that strain hardening effects could delay the development of shear bands; this could be extremely useful as a design feature, possibly allowing for the manufacturing of explosive materials that are less sensitive to mechanical insults. For instance, the strain hardening behaviour of the material may be controlled by altering the type of binder used.

Novel insight into the behaviour of sheared molten layers was gained in Chapter 6, and, again, the importance of considering the heterogeneous nature of explosive materials was highlighted. Owing to the incredibly small length scales, experiments trying to investigate such melt layers would be difficult. The melting process is discussed in the literature, not only in the context of shear bands directly resulting from mechanical insults [37, 90], but also in shear localisation resulting from pore collapse in shocked HMX [3]. The analysis demonstrated the utility of exploiting the disparate length scales often observed in hot spot mechanisms, and motivates the continued analytical study within the broad field of accidental ignition.

Appendix A

Computational coordinates used in the model for pinch

Here we give details of the computational variables introduced to solve the thermal part of the problem in Chapter 3. We first note that the problem is axisymmetric, and then introduce non-dimensional variables $\hat{r}$ and $\hat{z}$, which map the problem onto the square domain $0 \leq \hat{r} \leq 1$, $-1/2 \leq \hat{z} \leq 1/2$, as follows

$$r = \hat{R}(\hat{z}, t)\hat{r}, \quad z = h(t)\hat{z}, \tag{A.1}$$

where the position of the outer surface $R(z,t)$ of the explosive sample may be calculated using the free surface condition

$$u - \frac{\partial R}{\partial t} - w\frac{\partial R}{\partial z} = 0. \tag{A.2}$$

For some given arbitrary function φ defined in the physical space (r,z) we define its counterpart $\hat{\varphi}$ is the computational space as

$$\varphi(r,z) = \varphi(\hat{R}\hat{r}, h\hat{z}) =: \hat{\varphi}(\hat{r},\hat{z}). \tag{A.3}$$

We may write the derivatives with respect to the computational variables as follows

$$\frac{\partial \varphi}{\partial r} = \frac{1}{\hat{R}}\frac{\partial \hat{\varphi}}{\partial \hat{r}}, \tag{A.4}$$

$$\frac{\partial \varphi}{\partial z} = \frac{1}{h}\frac{\partial \hat{\varphi}}{\partial \hat{z}} - \frac{\hat{r}}{h\hat{R}}\frac{\partial \hat{R}}{\partial \hat{z}}\frac{\partial \hat{\varphi}}{\partial \hat{r}}, \tag{A.5}$$

$$\frac{\partial \varphi}{\partial t} = \frac{\partial \hat{\varphi}}{\partial t} + \frac{\hat{r}}{\hat{R}}\left[-\frac{\partial \hat{R}}{\partial t} + \frac{\mathrm{d}h}{\mathrm{d}t}\frac{\hat{z}}{h}\frac{\partial \hat{R}}{\partial \hat{z}}\right]\frac{\partial \hat{\varphi}}{\partial \hat{r}} - \frac{\mathrm{d}h}{\mathrm{d}t}\frac{\hat{z}}{h}\frac{\partial \hat{\varphi}}{\partial \hat{z}}. \tag{A.6}$$

Appendix B

Comparison of exponential and power-law models for plastic strain rate

Here we compare the exponential and power-law models for the explosive material LX-14. The non-dimesnsional plastic strain rate models to be compared read

$$\dot{\gamma}(s,T) = \dot{\gamma}_0 \varepsilon^{-1/2} \exp\{-\varepsilon^{-1}[\beta_1(T_\mathrm{p} - T) + \beta_2(s_\mathrm{p} - s)]\}, \tag{B.1}$$

and

$$\dot{\gamma}(s,T) = s^{1/m} T^{-l/m}, \tag{B.2}$$

respectively. The parameters used in the power-law model are available LX-14, taking values $l = -1.28$ and $m = 0.08$ [80]. Here we use the power model as a surrogate for experimental data, and here investigate the fit of the exponential model to the power-law "data". The values of the parameters β_1 and β_2 are given by

$$\beta_1 = \varepsilon \left(\frac{\partial \log \dot{\gamma}}{\partial T} \right)_s \quad \text{and} \quad \beta_2 = \varepsilon \left(\frac{\partial \log \dot{\gamma}}{\partial s} \right)_T, \tag{B.3}$$

whereas the power-law parameters l and m are given by the relations

$$-\frac{l}{m} = \left(\frac{\partial \log \dot{\gamma}}{\partial \log T} \right)_s \quad \text{and} \quad \frac{1}{m} = \left(\frac{\partial \log \dot{\gamma}}{\partial \log s} \right)_T. \tag{B.4}$$

The critical plastic temperature T_p and stress s_p are assumed to take values approximately equal to the reference temperature T_0 and stress s_0. In the interest of simplicity the critical plastic values are fixed in the following, and fitting is achieved through the parameters β_1, β_2 and $\dot{\gamma}_0$.

Figure B.1 shows the stress–strain-rate curves for the power-law model and exponential model for a series of isothermal tests over the range 300 K to 500 K. When the temperature is held fixed the exponential law the stress is a linear

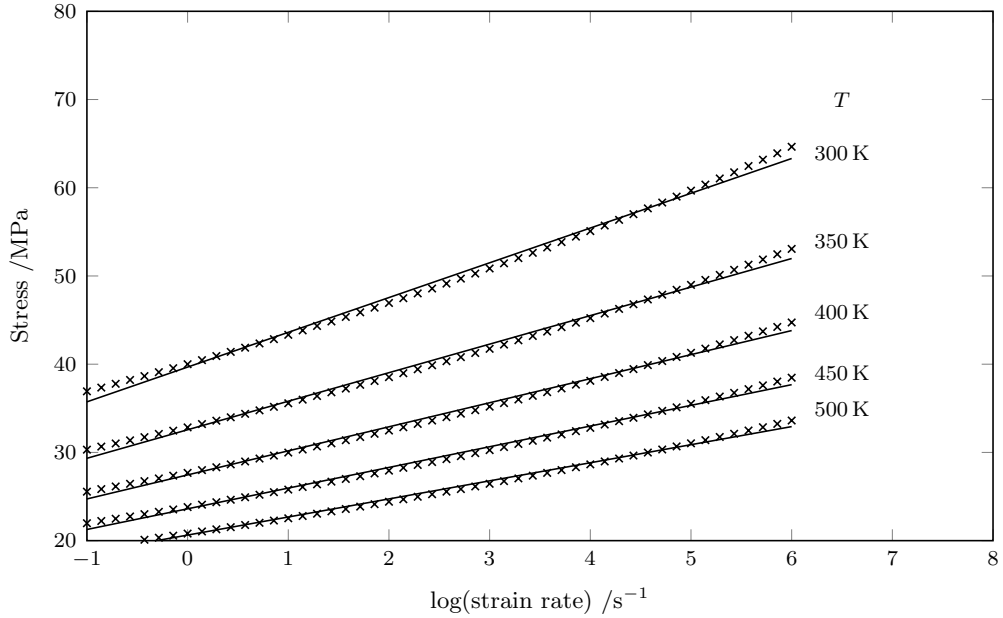

Figure B.1: Stress-strain-rate curves for the power-law model (×) and exponential model (−) for a series of isothermal tests.

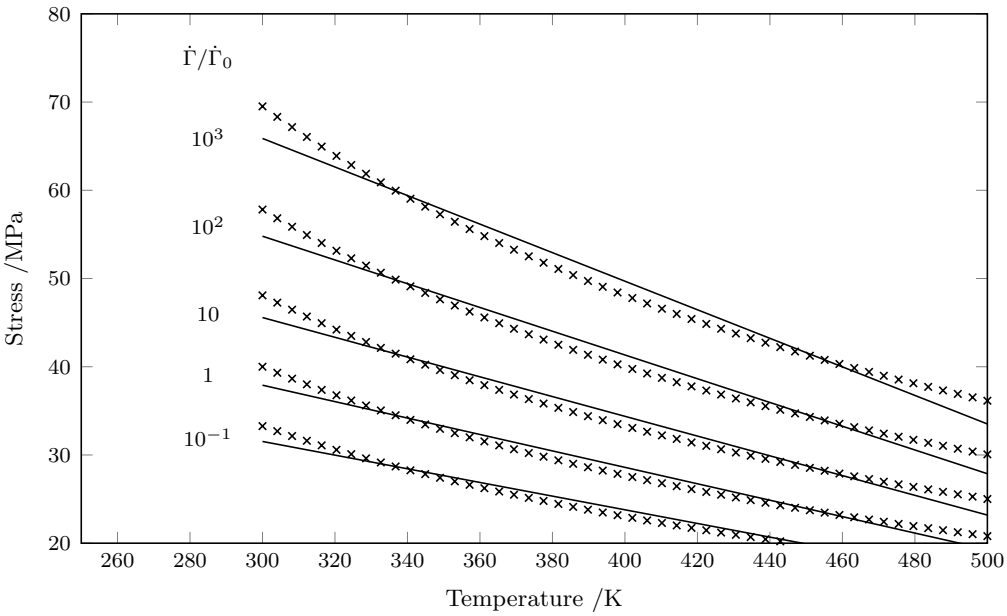

Figure B.2: Temperature-stress curves for the power-law model (×) and exponential model (−) for a series of constant strain-rate tests.

function of the logarithm of the strain rate

$$s = \frac{\varepsilon}{\beta_2} \log \dot{\gamma} + c_1, \tag{B.5}$$

where β_2 and $c_1 = s_\mathrm{p} + (\beta_1/\beta_2)(T_\mathrm{p} - T) - (\varepsilon/\beta_2)\log(\dot{\gamma}_0 \varepsilon^{-1/2})$ are found by a least-squares fit to the power-law model. It is found that β_2 varies in the range 0.1-0.2 as the temperature varies. However, the constant c_1 varies more significantly owing to its dependence on the temperature. Clearly, a better fit would be achieved by using different parameter values at higher and lower values of the strain rate. If a range of suitable strain-rates could be identified *a priori* then the parameters could be selected to give the best fit over the given range.

Similarly, at fixed strain-rate the exponential model predicts a linear relation between stress and temperature

$$s = -\frac{\beta_1}{\beta_2} T + c_2, \tag{B.6}$$

where β_1/β_2 and $c_2 = s_\mathrm{p} + (\beta_1/\beta_2)T_\mathrm{p} + (\varepsilon/\beta_2)(\log(\dot{\gamma}) - \log(\dot{\gamma}_0 \varepsilon^{-1/2}))$ are found by a least-squares fit to the power-law model. The results are shown in Figure B.2 for a series of tests which span five decades of the non-dimensional strain-rate $\dot{\Gamma}/\dot{\Gamma}_0$. In this case, the ratio β_1/β_2 varies with the strain-rate, as well as the fitting constant c_2. Again, it is observed that a better fit may be achieved if attention was restricted to a particular temperature range. For example, the linear fit through the range $300\,\mathrm{K} < T < 600\,\mathrm{K}$ would be considerably different from the linear fit through temperatures greater than 600 K.

Equations (B.1) and (B.2) do not account for the effects of strain hardening. It is posited that the exponential model for plastic strain rate, accounting for hardening effects, may be written

$$\dot{\gamma}(s, T, \gamma) = \dot{\gamma}_0 \varepsilon^{-1/2} \exp\{-\varepsilon^{-1}[\beta_1(T_\mathrm{p} - T) + \beta_2(s_\mathrm{p} - s)] - \varepsilon^{-1/2}\beta_4 \gamma\}, \tag{B.7}$$

with β_4 fitted to experimental data. The power-law model which accounts for hardening is given by

$$\dot{\gamma}(s, T, \gamma) = \gamma^{-n/m} s^{1/m} T^{-l/m}, \tag{B.8}$$

and is well used in the literature, e.g. Powers [80].

Figures B.3 and B.4 show stress–strain curves for a series of isothermal and constant strain-rate tests, respectively. When the effects of hardening are included we see there is good agreement between the two models across a range of reasonable strains.

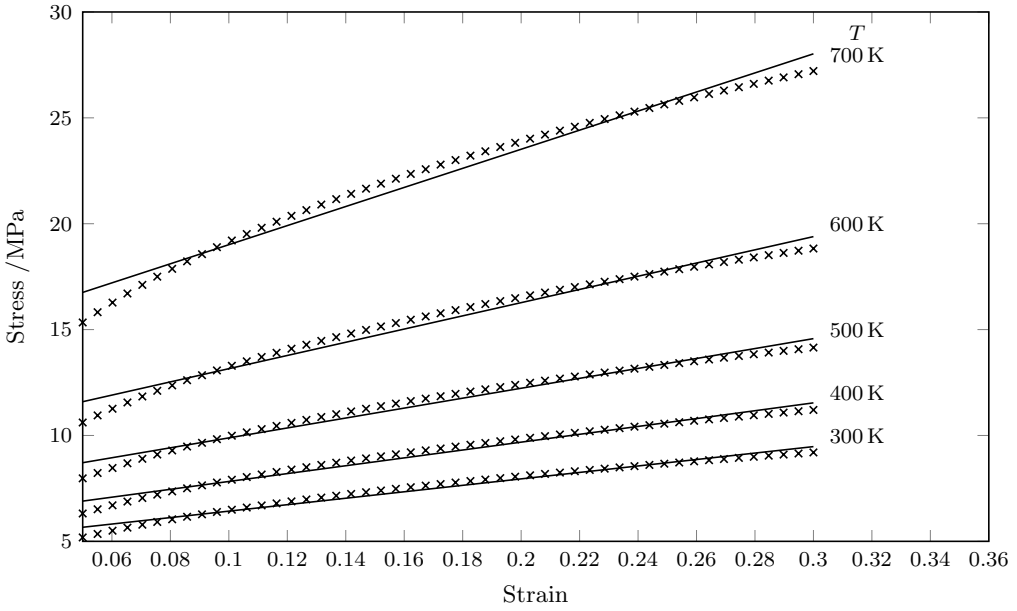

Figure B.3: Stress-strain-rate curves for the power-law model (×) and exponential model (−) for a series of isothermal tests, accounting for the effects of strain hardening. The strain-rate is held fixed at the reference strain-rate for each test, i.e. $\dot{\Gamma}/\dot{\Gamma}_0 = 1$.

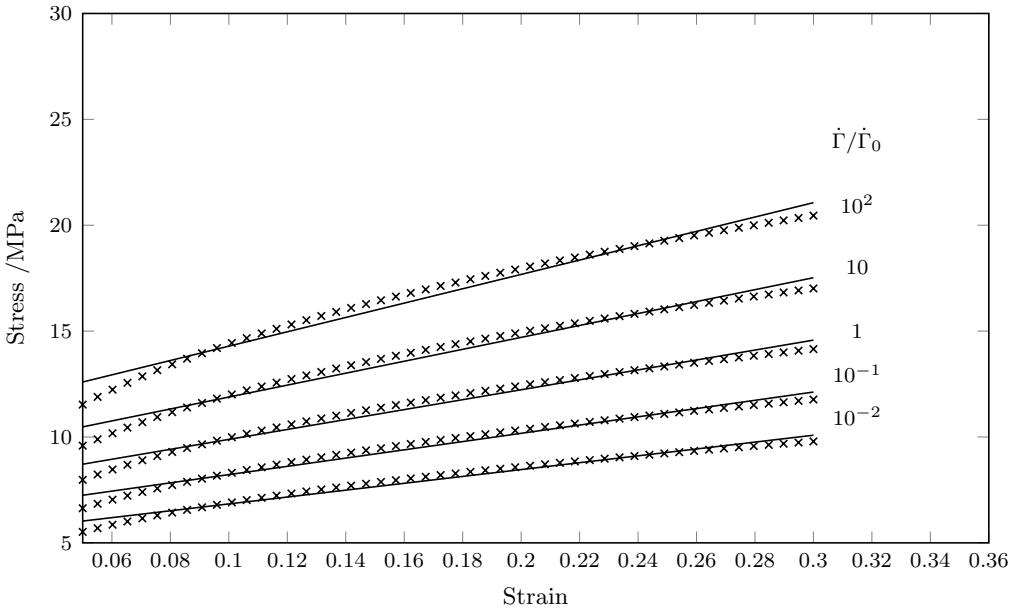

Figure B.4: Temperature-stress curves for the power-law model (×) and exponential model (−) for a series of constant strain-rate tests, accounting for the effects of strain hardening. The temperature is held fixed at 500 K in each test.

Bibliography

[1] M. Abramowitz and I. Stegun. Handbook of mathematical functions. *Applied Mathematics Series 55, National Bereau of Standards, Gaithersburg, MD*, 55: 62, 1966.

[2] G.T. Afanas'ev and V.K. Bobolev. *Initiation of solid explosives by impact.* Israel Program for Scientific Translations, 1971.

[3] R.A. Austin, N.R. Barton, J.E. Reaugh, and L.E. Fried. Direct numerical simualtion of shear localization and decomposition reactions in shock-loaded HMX crystal. *Journal of Applied Physics*, 117, 2015.

[4] AWE. Unpublished AWE Report. 2007.

[5] AWE. Discovery 25. *The Science and Technology Journal of AWE*, 25:29–33, 2014.

[6] M.R. Baer and J.W. Nunziato. A two-phase mixture theory for the deflagration-to-detonation transition (DDT) in reactive granular materials. *International Journal of Multiphase Flow*, 12(6):861–889, 1986.

[7] Y. Bai and B. Dodd. Adiabatic shear localization: Occurrence, theories, and applications. *Pergammon Press, Oxford, UK*, 1992.

[8] Y.L. Bai. Thermo-plastic instability in simple shear. *Journal of the Mechanics and Physics of Solids*, 30(4):195–207, 1982.

[9] A. Barua, Y. Horie, and M. Zhou. Microstructural level response of HMX–estane polymer-bonded explosive under effects of transient stress waves. *Proc. R. Soc. Lond. A*, 468(2147):3725–3744, 2012.

[10] J.F. Baytos. Specific heat and thermal conductivity of explosives, mixtures and plastic-bonded explosives determined experimentally. Technical report, Los Alamos Scientific Laboratory, NM, USA, 1979.

[11] D. Bedrov, G.D. Smith, and T.D. Sewell. Thermal conductivity of liquid octahydro-1,3,5,7-tetranitro-1,3,5,7-tetrazocine (HMX) from molecular dynamics simulations. *Chemical Physics Letters*, 324(1):64–68, 2000.

[12] J.D. Blackwood and F.P. Bowden. The initiation, burning and thermal decomposition of gunpowder. *Proc. R. Soc. Lond. A*, 213(1114):285–306, 1952.

[13] L.G. Bolkhovitinov and P.F. Pokhil. Calculation of the lower limit of the explosion frequency curve. *Doklady Akademii Nauk SSSR*, 123(4):637–638, 1958.

[14] F.P. Bowden and O.A. Gurton. Initiation of solid explosives by impact and friction: The influence of grit. *Proc. R. Soc. Lond. A*, 198(1054):337–349, 1949.

[15] F.P. Bowden and O.A. Gurton. Birth and growth of explosion in liquids and solids initiated by impact and friction. *Proc. R. Soc. Lond. A*, 198(1054): 350–372, 1949.

[16] F.P. Bowden and A.D. Yoffe. *Initiation and growth of explsoions in liquids and solids*. Cambridge University Press, Cambridge, UK, 1952.

[17] F.P. Bowden, M.F.R. Mulcahy, R.G. Vines, and A. Yoffe. The detonation of liquid explosives by gentle impact. The effect of minute gas spaces. *Proc. R. Soc. Lond. A*, 188(1014):291–311, 1947.

[18] F.P. Bowden, M.A. Stone, and G.K. Tudor. Hot spots on rubbing surfaces and the detonation of explosives by friction. *Proc. R. Soc. Lond. A*, 188(1014): 329–349, 1947.

[19] V. Boyle, R. Frey, and O. Blake. Combined pressure shear ignition of explosives. In *9th Symposium (International) on Detonation*, page 3. Office of Naval Research, 1989.

[20] J.K. Brennan, M. Fermen-Coker, and L. Tran. Physics-based multi-scale modeling of shear initiated reactions in energetic and reactive materials. Technical report, Army Research Lab Aberdeen Proving Ground Md Weapons And Materials Research Directorate, 2010.

[21] T. Burns. Approximate linear stability analysis of a model of adiabatic shear band formation. *Quarterly of Applied Mathematics*, 1985.

[22] H.S. Carslaw and J.C. Jaeger. *Conduction of heat in solids*. Oxford Clarendon Press, Oxford, UK, 1959.

[23] R.J. Caspar. *Experimental and numerical study of shear localization as an initiation mechanism in energetic solids*. PhD thesis, University of Notre Dame, Indiana, USA, 1996.

[24] R.J. Caspar, J.M. Powers, and J.J. Mason. Investigation of reactive shear localization in energetic solids. *Combustion Science and Technology*, 136(1-6): 349–371, 1998.

[25] M.M. Chaudhri. Stab initiation of explosions. *Nature*, 263(121–122), 1976.

[26] M.M. Chaudhri and J.E. Field. The role of rapidly compressed gas pockets in the initiation of condensed explosives. *Proc. R. Soc. Lond. A*, 340(1620): 113–128, 1974.

[27] C.S. Chen, A. Karageorghis, and Y.S. Smyrlis. *The method of fundamental solutions: a meshless method*. Dynamic Publishers Atlanta, 2008.

[28] G. Chen, Z. Feng, Y. Zhu, and Q. Shi. An alternative frictional boundary condition for computational fluid dynamics simulation of friction stir welding. *Journal of Materials Engineering and Performance*, 25(9):4016–4023, 2016.

[29] H.C. Chen, V.F. Nesterenko, J.C. LaSalvia, and M.A. Meyers. Shear-induced exothermic chemical reactions. *Le Journal de Physique IV*, 7(C3):C3–27, 1997.

[30] Wen Chen, Zhuo-Jia Fu, and Ching-Shyang Chen. *Recent advances in radial basis function collocation methods*. Springer Science & Business Media, 2013.

[31] R.J. Clifton. *Adiabatic shear banding*, chapter 8, page 129. National Materials Advisory Board (NRC) Washington, DC, 1980.

[32] G.D. Coley and J.E. Field. The role of cavities in the initiation and growth of explosion in liquids. *Proc. R. Soc. Lond. A*, 335(1600):67–86, 1973.

[33] J.P. Curtis. A model of explosive ignition due to pinch. In *38th International Pyrotechnics Seminar, Denver, Colorado, USA*, pages 207–216, 2012.

[34] J.P. Curtis. Explosive ignition due to adiabatic shear. In *39th International Pyrotechnics Seminar, Valencia, Spain*, 2013.

[35] J.P. Curtis and J.E. Reaugh. Modelling the ignition of explosives by pinch with the HERMES model. In *42nd International Pyrotechnics Seminar, Grand Junction, Colorado, USA*, 2016.

[36] J.P. Curtis et al. The influence of an air gap on the response of an explosive to spigot impact. In *European Study Group with Industry 91, Bristol 2013*, 2013.

[37] J.K. Dienes. On reactive shear bands. *Physics Letters A*, 118(9):433–438, 1986.

[38] J.A. DiLellio and W.E. Olmstead. Shear band formation due to a thermal flux inhomogeneity. *SIAM Journal on Applied Mathematics*, 57(4):959–971, 1997.

[39] J.A. DiLellio and W.E. Olmstead. Temporal evolution of shear band thickness. *Journal of the Mechanics and Physics of Solids*, 45(3):345–359, 1997.

[40] D. Durban. Drawing of tubes. *Journal of Applied Mechanics*, 47:736–740, 1980.

[41] D. Durban and B. Budiansky. Plane-strain radial flow of plastic materials. *Journal of the Mechanics and Physics of Solids*, 26:303–324, 1979.

[42] D.A. Edwards and D.A. French. Asymptotic and computational analysis of large shear deformations of a thermoplastic material. *SIAM Journal on Applied Mathematics*, 59(2):700–724, 1998.

[43] F.R. Eirich and D. Tabor. Collisions through liquid films. In *Mathematical Proceedings of the Cambridge Philosophical Society*, volume 44, pages 566–580. Cambridge University Press, 1948.

[44] J. Engmann, C. Servais, and A.S. Burbidge. Squeeze flow theory and applications to rheometry: A review. *J. Non-Newtonian Fluid Mech.*, 132:1–27, 2005.

[45] J.E. Field, G.M. Swallowe, and S.N. Heavens. Ignition mechanisms of explosives during mechanical deformation. *Proc. R. Soc. Lond. A*, 382(1782):231–244, 1982.

[46] J.E. Field, S.J.P. Palmer, P.H. Pope, R. Sundarajan, and G.M. Swallowe. Mechanical properties of PBX's and their behaviour during drop weight impact. In *8th Symposium (International) on Detonation*, page 635. Office of Naval Research, 1985.

[47] J.E. Field, M.A. Parry, S.J.P. Palmer, and J.M. Huntley. Deformation and explosive properties of HMX powders and polymer bonded explosives. In *9th Symposium (International) on Detonation*, page 886. Office of Naval Research, 1989.

[48] J.E. Field, N.K. Bourne, S.J.P. Palmer, S.M. Walley, J. Sharma, and B.C. Beard. Hot-spot ignition mechanisms for explosives and propellants [and discussion]. *Phil.Trans. of the R. Soc. Lond. A*, 339(1654):269–283, 1992.

[49] P.G. Fox. The explosive sensitivity of the metal azides to impact. *Journal of Solid State Chemistry*, 2(4):491–502, 1970.

[50] D.A. Frank-Kamenetskii. On the mathematical theory of thermal explosions. *Acta Physiocochimica URSS*, 16:357, 1942.

[51] R.B. Frey. The initiation of explosive charges by rapid shear. Technical report, DTIC Document, 1980.

[52] R.B. Frey. Cavity collapse in energetic materials. In *8th Symposium (International) on Detonation*, pages 68–80. Office of Naval Research, 1985.

[53] W.E. Garner. Thermal decomposition, inflammation and detonation. *Proc. R. Soc. Lond. A*, 246(1245):203–206, 1958.

[54] G. Gioia and M. Ortiz. The two–dimensional structure of dynamic boundary layers and shear bands in thermoviscoplastic solids. *Journal of the Mechanics and Physics of Solids*, 44(2):251–292, 1996.

[55] D.A. Gorham. Measurement of stress-strain properties of strong metals at very high rates of strain. *Inst. Phys. Conf. Ser.*, (47):16–25, 1979.

[56] C. Gruau, D. Picart, R. Belmas, E. Bouton, F. Delmaire-Sizes, J. Sabatier, and H. Trumel. Ignition of a confined high explosive under low velocity impact. *International Journal of Impact Engineering*, 36(4):537–550, 2009.

[57] S.N. Heavens. *The initiation of explosion by impact.* PhD thesis, University of Cambridge, Cambridge, UK, 1973.

[58] S.N. Heavens and J.E. Field. The ignition of a thin layer of explosive by impact. *Proc. R. Soc. Lond. A*, 338(1612):77–93, 1974.

[59] P.D. Hicks et al. Modelling of the effects of friction and compression on explosives. In *European Study Group with Industry 80, Cardiff*, 2011.

[60] R. Hill. *The Mathematical Theory of Plasticity.* Oxford University Press, Oxford, UK, 1950.

[61] P.M. Howe, G. Gibbons Jr, and P.E. Webber. An experimental investigation of the role of shear in initiation of detonation by impact. Technical report, DTIC Document, 1986.

[62] P. Howell, G. Kozyreff, and J. Ockendon. *Applied solid mechanics.* Cambridge University Press, Cambridge, UK, 2009.

[63] P.C. Hsu, G. Hust, M. Howard, and J.L. Maienschein. The ODTX system for thermal ignition and thermal safety study of energetic materials. In *14th Symposium (International) on Detonation*, pages 11–16, 2010.

[64] M. A Jankowska and J.A. Kolodziej. On the application of the method of fundamental solutions for the study of the stress state of a plate subjected to elastic–plastic deformation. *International Journal of Solids and Structures*, 67: 139–150, 2015.

[65] H. Kolsky. *Stress waves in solids*, volume 1098. Courier Corporation, 1963.

[66] M. Kornfeld and L. Suvorov. On the destructive action of cavitation. *Journal of Applied Physics*, 15(6):495–506, 1944.

[67] C.J. Lawrence and G.M. Corfield. Non-viscometric flow of viscoplastic materials: squeeze flow. *Dynamics of Complex Fluids*, pages 379–393, 1998.

[68] A. Linan and F.A. Williams. Theory of ignition of a reactive solid by constant energy flux. *Combustion Science and Technology*, 3(2):91–98, 1971.

[69] C.L. Mader. Initiation of detonation by the interaction of shocks with density discontinuities. *The Physics of Fluids*, 8(10):1811–1816, 1965.

[70] G. A. Maugin. *The thermomechanics of plasticity and fracture*, volume 7. Cambridge University Press, Cambridge, UK, 1992.

[71] R.R. McGuire and C.M. Tarver. Chemical-decomposition models for the thermal explosion of confined HMX, TATB, RDX, and TNT explosives. Technical report, Lawrence Livermore National Laboratory, CA, USA, 1981.

[72] R. Menikoff and T.D. Sewell. Constituent properties of HMX needed for mesoscale simulations. *Combustion Theory and Modelling*, 6(1):103–125, 2002.

[73] V. Krishna Mohan and J.E. Field. Impact initiation of hexanitrostilbene. *Combustion and Flame*, 56(3):269–277, 1984.

[74] V. Krishna Mohan, J.E. Field, and G.M. Swallowe. Effects of physical inhomogeneities on the impact sensitivity of solid explosives: A high-speed photographic study. *Combustion Science and Technology*, 40(5-6):269–278, 1984.

[75] V. Krishna Mohan, V.C. Jyothi Bhasu, and J.E. Field. Role of adiabatic shear bands in initiation of explosives by drop-weight impact. In *9th Symposium (International) on Detonation*, pages 1276–1283. Office of Naval Research, 1989.

[76] A. Molinari and R.J. Clifton. Analytical characterization of shear localization in thermoviscoplastic materials. *Journal of Applied Mechanics*, 54(4):806–812, 1987.

[77] H. Ockendon and J.R. Ockendon. *Viscous flow*, volume 13. Cambridge University Press, Cambridge, UK, 1995.

[78] W.E. Olmstead. Ignition of a combustible half space. *SIAM Journal on Applied Mathematics*, 43(1):1–15, 1983.

[79] C. Poole. *Penetration of a shaped charge*. PhD thesis, University of Oxford, Oxford, UK, 2005.

[80] J.M. Powers. Thermal explosion theory for shear localizing energetic solids. *Combustion Theory and Modelling*, (3):103–122, 1999.

[81] J.E. Reaugh. Progress in model development to quantify high explosive violent response (HEVR) to mechanical insult. Technical report, Lawrence Livermore National Laboratory, CA, USA, 2008.

[82] J.E. Reaugh. Modifications and applications of the HERMES model. Technical report, Lawrence Livermore National Laboratory, NM (USA), 2010.

[83] J.E. Reaugh and A.G. Jones. Mechanical damage, ignition, and burn: Experiment, model development, and computer simulations to study High-Explosive Violent Response (HEVR). In *14th Symposium (International) on Detonation*, page 909, 2010.

[84] J.E. Reaugh, B.W. White, J.P. Curtis, and H.K. Springer. Theory, solution methods, and implementation of the HERMES model. Technical report, Lawrence Livermore National Laboratory, CA, USA, 2017.

[85] E.K. Rideal and A.J.B. Robertson. Thermal decomposition of Pentaerythritol Tetranitrate, Nitroglycerin, Ethylenediamine Dinitrate, and Ammonium Nitrate. *Proc. R. Soc. Lond. A*, 195:135, 1948.

[86] W. Schroeder and D.A. Webster. Press-forging thin sections-effect of friction, area, and thickness on pressures required. *Journal of Applied Mechanics*, 16 (3):289–294, 1949.

[87] T.D. Sewell, D. Bedrov, R. Menikoff, and G.D. Smith. Elastic properties of HMX. In *AIP Conference Proceedings*, volume 620, pages 399–402. AIP, 2002.

[88] J.D. Sherwood and D. Durban. Squeeze flow of a power–law viscoplastic solid. *J. Non-Newtonian Fluid Mech.*, 62(1):35–54, 1996.

[89] J. Starkenberg. Ignition of solid high explosive by the rapid compression of an adjacent gas layer. In *7th Symposium (International) on Detonation*, pages 3–16, 1981.

[90] A.J. Starobin and J.K. Dienes. One-dimensional thermomechanical model for lateral melting and ignition of a thin sheared viscous layer. *Combustion Theory and Modelling*, 10(6):885–905, 2006.

[91] G.M. Swallowe and J.E. Field. The ignition of a thin layer of explosive by impact; the effect of polymer particles. *Proc. R. Soc. Lond. A*, 379(1777): 389–408, 1982.

[92] T.B. Tang and M.M. Chaudhri. Electron-induced decomposition and time-dependent breakdown of ionic solids: An experimental study on silver azide. *Physical Review B*, 30(10):6154, 1984.

[93] A.S. Tappan, A. Renlund, J. Stachowiak, J. Miller, and M. Oliver. Mechanical properties determination by real-time ultrasonic characterization of thermally damaged energetic materials. In *12th Symposium (International) on Detonation*, pages 356–362, 2002.

[94] W. Taylor and A. Weale. The mechanism of the initiation and propagation of detonation in solid explosives. *Proc. R. Soc. Lond. A*, 138(834):92–116, 1932.

[95] H. Tresca. Mémoire sur l'écoulement des corps solides soumis à de fortes pressions. *C. R. Acad. Sci. Paris*, 59:754, 1864.

[96] A.R. Ubbelohde. Part iii. (4) Mechanical and thermal processes of initiation. *Phil. Trans. of the R. Soc. Lond. A*, 241(831):280–286, 1948.

[97] R. von Mises. Mechanik der festen körper im plastisch-deformablen zustand. *Nachrichten von der Gesellschaft der Wissenschaften zu Göttingen, Mathematisch-Physikalische Klasse*, (4):582–592, 1913.

[98] D.M. Williamson et al. Temperature–time response of a polymer bonded explosive in compression (EDC37). *J. Physics D: Applied Physics*, 41(8): 085404, 2008.

[99] R.E. Winter and J.E. Field. The role of localized plastic flow in the impact initiation of explosives. *Proc. R. Soc. Lond. A*, 343(1634):399–413, 1975.

[100] T.W. Wright. Approximate analysis for the formation of adiabatic shear bands. *Journal of the Mechanics and Physics of Solids*, 38(4):515–530, 1990.

[101] T.W. Wright. *The physics and mathematics of adiabatic shear bands*. Cambridge University Press, Cambridge, UK, 2002.

[102] T.W. Wright and J.W. Walter. On stress collapse in adiabatic shear bands. *Journal of the Mechanics and Physics of Solids*, 35(6):701–720, 1987.

[103] R.M. Wyatt, P.W. Moore, G.K. Adams, and J.F. Sumner. The ignition of primary explosives by electric discharges. *Proc. R. Soc. Lond. A*, 246(1245): 189–196, 1958.

[104] A. Yoffe. Influence of entrapped gas on initiation of explosion in liquids and solids. *Proc. R. Soc. Lond. A*, 198(1054):373–388, 1949.

[105] F.J. Zerilli and R.W. Armstrong. Dislocation-mechanics-based constitutive relations for material dynamics calculations. *Journal of Applied Physics*, 61(5): 1816–1825, 1987.

[106] F. Zhou, J.F. Molinari, and K.T. Ramesh. Effects of material properties on the fragmentation of brittle materials. *International Journal of Fracture*, 139 (2):169–196, 2006.

[107] F. Zhou, T.W. Wright, and K.T. Ramesh. A numerical methodology for investigating the formation of adiabatic shear bands. *Journal of the Mechanics and Physics of Solids*, 54(5):904–926, 2006.